Purdue University

Purdue e-Pubs

Open Access Dissertations   Theses and Dissertations

5-2018

Multi-Hazard In-Plane Response of Steel-plate Composite (SC) Walls: Out-of-plane and Accident Thermal Loadings

Saahastaranshu R. Bhardwaj
Purdue University

Follow this and additional works at: https://docs.lib.purdue.edu/open_access_dissertations

MULTI-HAZARD IN-PLANE RESPONSE OF STEEL-PLATE COMPOSITE (SC) WALLS: OUT-OF-PLANE AND ACCIDENT THERMAL LOADINGS
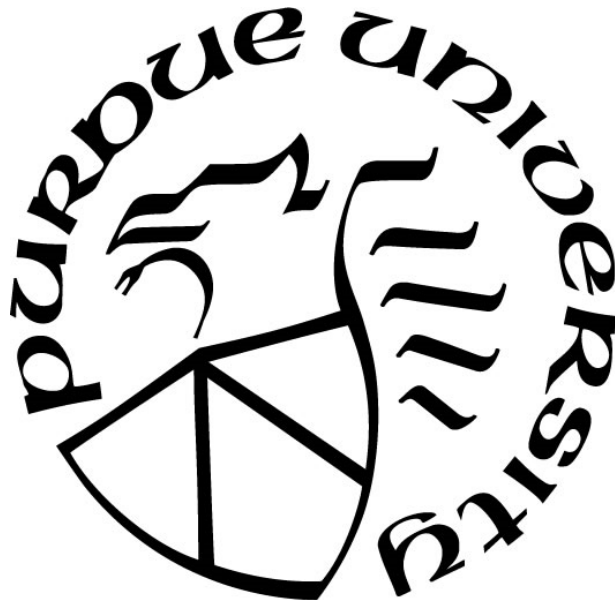
by

Saahastaranshu R. Bhardwaj

A Dissertation

Submitted to the Faculty of Purdue University

In Partial Fulfillment of the Requirements for the degree of

Doctor of Philosophy

Lyles School of Civil Engineering

West Lafayette, Indiana

May 2018

THE PURDUE UNIVERSITY GRADUATE SCHOOL

STATEMENT OF COMMITTEE APPROVAL

Dr. Amit H. Varma, Chair

      Department of Civil Engineering

Dr. Mark D. Bowman

      Department of Civil Engineering

Dr. Robert J. Connor

      Department of Civil Engineering

Dr. Vikas Tomar

      Department of Aeronautics and Astronautics

Approved by:

      Dr. Dulcy M. Abraham

            Head of the Graduate Program

To Renu Dalal, for constantly 'nagging' me to be a better person!

ACKNOWLEDGMENTS

Spring of 2013, and I came to Purdue University with hopes and dreams, but not sure how things would pan out. I was exploring my options when I met Dr. Amit H. Varma, and he agreed to be my Ph.D. advisor. Over these years, we have had countless stimulating discussions, and he has been an inspiration, both professionally and personally. I would like to thank him for providing me the opportunity to conduct research, teaching me the nuances of structural engineering and experimentation, and working patiently with through all these years. I would also like to thank my committee, Dr. Mark D. Bowman, Dr. Robert J. Connor, and Dr. Vikas Tomar, for their valuable inputs during our interactions. Special thanks are due to Dr. Andrew Whittaker, who was a co-principal investigator on the experimental projects, and Dr. Sanjeev R. Malushte, who spent numerous hours working with me on a variety of topics.

My desire to pursue doctoral research stemmed from my mother Seeta Devi who is a teacher, and who demonstrated the importance of constantly striving to acquire and disperse knowledge. My father Ganesh Dutt has always encouraged me to go all-in for my dreams, and his advice came in handy during my Ph.D. journey. This journey is incomplete without thoroughly thanking my partner-in-crime Renu Dalal, who too jumped into the stormy waters of a Ph.D. to make sure I had company. Throughout my stay at Purdue University, I have been lucky to have the company of Nikhil Sangwan, who is an amazing person and has always gone out of his way to help me, and who in fact also read this document for any grammatical or typographical errors. I would also like to thank my brother Amanpreet Rattan for his constant love and support.

The day I stepped foot onto the lab floor, I realized experimental research is a whole different ball game. And for this reason, I am grateful to Thomas Bradt for always coming up with innovative and efficient ways to get stuff done on the lab floor. I have received support and encouragement

TABLE OF CONTENTS

LIST OF TABLES

LIST OF FIGURES

LIST OF SYMBOLS

A_c	Cross-sectional area of concrete infill
A_c^{uncr}	Area of uncracked portion of concrete
A_g	Gross cross-sectional area of the wall
A_s	Cross-sectional area of steel plates
A_s^F	Cross-sectional area of steel plates in tension due to flexure
A_v	Cross-sectional area of shear reinforcement (ties)
E_c, E_{ci}	Concrete modulus of elasticity
EI_{cr}	Cracked in-plane flexural stiffness
EI_{uncr}	Uncracked flexural stiffness
EI_{eff}^{ip}	Effective in-plane flexural stiffness
EI_{eff}^{oop}	Effective out-of-plane flexural stiffness
E_s	Steel modulus of elasticity
F_n	Estimated in-plane strength of the specimen (for load cycles)
F_y	Steel yield stress
F_{yt}	Shear reinforcement yield strength
GA_{cr}	Cracked shear stiffness
GA_{eff}	Effective in-plane shear stiffness
GA_{cr}^{TAN}	Cracked tangent shear stiffness
GA_{cr}^{AISC}	Cracked secant shear stiffness (per AISC N690s1)
GA_{uncr}	Uncracked shear stiffness
G_c	Shear modulus of concrete

G_F	Fracture energy
G_s	Shear modulus of steel
I_c	Moment of inertia of concrete infill
I_s	Moment of inertia of steel plates
K_{cr}	Cracked wall stiffness
K_{in}	Initial stiffness of the specimen
K_s	Shear stiffness contribution from steel
K_{SC}	Shear stiffness contribution from composite SC behavior
K_{sec}	Secant wall stiffness
K_{uncr}	Uncracked wall stiffness
K_{xy}^{cr}	Cracked tangent shear stiffness
K_{xy}^{uncr}	Uncracked shear stiffness
M_{base}, M_u, M_{exp}	Moment at the base of the wall
$M_{cr\text{-}oop}$	Out-of-plane moment corresponding to concrete cracking
$M_{n\text{-}ACI}$	Nominal out-of-plane flexural strength per ACI 349
M_n^{AISC}	Out-of-plane flexural strength per AISC N690s1
$M_n^{AISC\text{-}P}$	Out-of-plane flexural strength per AISC N690s1, accounting for $P\text{-}M$ interaction.
$M_{n\text{-}fiber}$	Nominal flexural strength obtained from fiber model
M_{ny}	Nominal in-plane yield strength of SC wall
M_{oop}	Out-of-plane moment at the base due to out-of-plane force
M_p	Plastic moment capacity of SC wall piers

$M_{Vn\text{-}oop}$	Out-of-plane moment corresponding to out-of-plane shear strength
M_{yc}	Compression yield moment capacity for SC wall piers
P_n	Nominal axial compressive strength per AISC N690s1
P_y	In-plane load corresponding to expected strength
S	Spacing of shear reinforcement (ties)
S_{cr}	Cracking threshold force for in-plane shear
S_{p1}	Principal tensile stress
S_x, S_y	In-plane membrane forces
S_{xy}	In-plane shear force
$S_{xy}{}^{Y}$	In-plane shear force corresponding to Von-Mises yielding of faceplates
T	Temperature
T	SC Wall thickness
T_{max}	Maximum surface temperature
T_ε	Strain transformation matrix
T_σ	Stress transformation matrix
V_{app}	Applied in-plane load
V_{base}, V_u	Shear at the base of the wall
V_c	Concrete contribution to out-of-plane shear strength
V_{Myc}	In-plane load corresponding to compression yield moment capacity
V_{Mp}	In-plane load corresponding to plastic moment capacity

$V_n{}^{ACI}$	Nominal out-of-plane shear strength of SC walls (per ACI)
$V_{n\text{-}ip}$	Experimental in-plane capacity
$V_n{}^{AISC}$	Nominal in-plane shear strength per AISC N690s1
V_{oop}	Out-of-plane shear force
V_s	Contribution of shear reinforcement to out-of-plane shear strength
a/h	Shear span-to-depth ratio
b	Largest unsupported length between rows of studs or ties
c	Cohesion for concrete
c_p	Neutral axis location, from extreme compression fiber, corresponding to plastic moment capacity for SC wall piers
c_{yc}	Neutral axis location, from extreme compression fiber, corresponding to compression yield moment capacity for SC wall piers
c_2	Coefficient for effective out-of-plane flexural stiffness (per AISC N690s1)
d	Wall thickness
d_{tie}	Tie diameter
f'_c, f_{cm}	Uniaxial compressive strength of concrete
f_{ctm}	Mean tensile strength of concrete
f_{yf}	Flangeplate yield strength
f_{yp}	Faceplate yield strength
f_{yv}	Shear reinforcement yield strength

h	Specimen height
l_w	Length of wall
s	Shear stud spacing
t	time
t_c	Thickness of concrete infill
t_f	Flangeplate thickness
t_p	Faceplate thickness
t_{sc}	SC wall thickness
w_c	Crack width corresponding to zero tensile stress
$\alpha_{concrete}$	Coefficient of thermal expansion of concrete
α_{steel}	Coefficient of thermal expansion of steel
β_1	Factor for concrete compression block, per ACI 318
γ_{xy}	In-plane shear strain
σ	Normal stress
τ	Shear strength of concrete
ΔT	Change in temperature
Δ_y	Yield displacement
$\Delta_{u\text{-}ip}^{corr}$	Corrected peak drift ratio
ϕ	Angle of internal friction, curvature
κ	Calibration factor for in-plane shear strength (per AISC N690s1)
$\mu\varepsilon$	Micro strain
ν_s	Poisson's ratio for steel

ε_{cent}	Centroidal strain
ε_{cr}	Critical buckling strain
ε_{mech}	Mechanical strain
ε_{oop}	Faceplate strain due to out-of-plane loading
ε_{th}	Thermal strains
ε_{tot}	Total strain
ε_{y}	Steel yield strain
ρ	Reinforcement ratio
$\bar{\rho}$	Strength normalized reinforcement ratio
ρ_{w}	Longitudinal tensile reinforcement ratio

ABSTRACT

Author: Bhardwaj, Saahastaranshu, R., Ph.D.
Institution: Purdue University
Degree Received: May 2018
Title: Multi-Hazard In-plane Response of Steel-plate Composite (SC) Walls: Out-of-plane and Accident Thermal Loadings
Major Professor: Amit H. Varma

Steel-plate composite (SC) walls have been used for the third generation of nuclear power plants, and are being considered for small modular reactors of the future. Modular SC walls are also being considered for commercial applications, owing to their structural efficiency and construction economy. Walls in important structures may be subjected to a combination of loadings due to cascading hazards. Experimental and numerical studies were conducted to evaluate the in-plane response of SC walls (with boundary elements) and wall piers (without boundary elements) subjected to out-of-plane and accident thermal loadings.

First series of experiments comprised of four SC wall pier specimens. One control specimen was subjected to in-plane loading (no out-of-plane loading). Three specimens were subjected to different magnitudes of out-of-plane loading in combination with in-plane loading. Experimental results indicate that the in-plane response of wall piers with aspect ratios greater than or equal to 0.6 is flexure dominated. Introducing an out-of-plane force results in out-of-plane shear and moment in the wall piers. Wall piers subjected to out-of-plane shear equal to their nominal shear strength (per US codes) develop flexural yielding and failure due to interaction between the in-plane and out-of-plane moments. Shear failure does not occur for these wall piers. The wall pier specimen subjected to an out-of-plane shear force that is 2.5 times the nominal shear strength (per US codes) was forced into a shear failure mode by the interaction of in-plane shear and out-of-plane shear.

The second series of experiments involved subjecting one SC wall and one SC wall pier specimen to different magnitudes and durations of accident temperatures in combination with in-plane loading. Experimental results indicate that typical accident temperatures (up to 232°C) do not result in significant reduction in in-plane strength of walls and wall piers. The strength for accident temperatures can be estimated using existing strength equations (per US codes). However, accident thermal loads result in a significant reduction in the stiffness of wall and wall piers. The reduction is primarily due to concrete cracking and depends on the magnitude of accident temperature. Stiffness reductions of up to 40% of the ambient stiffness were observed.

Three-dimensional finite element models were developed for the two series of experiments. Additionally, a fiber-based model was developed to evaluate biaxial moment interaction for SC wall piers. The fiber model was then updated to include axial force-moment interaction and vector shear failure. Results from the numerical models compare favorably with experimental observations and provide additional insights into the behavior of the specimens.

Experimental and numerical results formed the basis of strength and stiffness recommendations for SC walls and wall piers subjected to combined in-plane and accident thermal loading. The results were also employed to recommend an interaction surface for in-plane and out-of-plane moments. The recommendations are intended to help designers consider the simultaneous presence of multiple demands due to cascading hazards.

1. INTRODUCTION

This dissertation discusses studies conducted to evaluate the in-plane response of steel-plate composite (SC) walls and wall piers subjected to multiple hazards. Two series of experiments were conducted: (a) SC wall piers subjected to biaxial (in-plane and out-of-plane) loading, and (b) SC wall and wall pier subjected to combined seismic (in-plane) and accident thermal loading (due to postulated high-energy pipe break events). Based on the experimental results, the biaxial interaction of SC wall piers, and the effect of thermal loads on the in-plane strength and stiffness of SC structures were evaluated. Benchmarked numerical and analytical models were developed to estimate the in-plane response of SC structures subjected to these combinations of hazards. Recommendations for analysis and design of SC structures for biaxial loading or combination of seismic and thermal loading were provided.

This chapter introduces SC structural systems and their advantages over conventional reinforced concrete (RC) systems. Since the study comprises of SC wall (with boundary elements) and wall pier (no flanges or boundary elements) specimens, a discussion of applicability and behavioral differences in walls and wall piers is presented. The motivation and need for this research is then presented followed by the research objectives. Research plan and methods are listed. Scope and limitations of the research are discussed. The significance of knowledge acquired through this research is described. The chapter then presents the organization of the rest of the document, mentioning the topics covered in various chapters.

1.1   SC Walls

Nuclear structures involve heavy concrete construction to provide adequate radiation shielding and resistance to severe and extreme loads. High-rise commercial construction may also require heavy

concrete shear walls to satisfy high wind loads, seismic loads, or other design requirements. This results in longer construction durations and large field labor force requirements. Generic modular construction, especially modular steel-plate composite (SC) construction, can minimize schedule and labor requirements. In SC construction, concrete walls are reinforced with two steel faceplates attached to concrete using steel anchors, such as steel-headed shear studs, and connected to each other using steel tie bars. Figure 1.1 illustrates a typical SC wall section. Steel anchors enable composite action between faceplates and concrete. Ties provide structural integrity, prevent delamination of the plain concrete core, and serve as shear reinforcement. The SC walls may have sleeves for penetrations, and embed plates for commodity attachments.

Behavior of SC walls under axial tension and compression [1], out-of-plane flexure [2] and out-of-plane shear ([3], [4]) is similar to that of reinforced concrete (RC) walls. However, behavior of SC walls under in-plane shear ([5]–[7]), combined in-plane forces and out-of-plane moments [8] can be significantly different from that of RC walls. Additionally, specific limit states such as faceplate local buckling [1], interfacial shear failure ([3], [4]) between the faceplates and concrete infill, and section delamination through the concrete infill [9] need to be adequately considered in the design of SC walls. These limit states are discussed in AISC Design Guide 32 [10], along with section detailing provisions to prevent them from limiting the design.

Advantages of SC construction include modularity and minimized construction schedule [11], structural strength and safety for seismic and accident thermal loading combinations ([12]–[14]) and resilience to impactive [15] and impulsive [16] loading. Presence of faceplates in SC walls eliminates the need for rebar and formwork. Use of faceplates facilitates fabrication of large empty modules in the shop. These modules can then be shipped to the site and assembled in the field.

Figure 1.2 presents the comparison between modular RC and SC construction. The schedule contraction achieved by modular SC construction is illustrated in Figure 1.3.

Steel faceplates in SC walls provide better shielding behavior than conventional concrete. Compared to RC walls, the faceplates act as a barrier to incident radiation and reduce the intensity of radiation passing through to the concrete infill. The improved performance may enable up to a 10% reduction in wall thickness due to reduction in the volume of concrete required for radiation shielding. SC walls do not have problems associated with rebar congestion or moisture loss due to evaporation. Faceplates in SC walls prevent moisture loss thus eliminating the need for concrete curing. With proper use of concrete lifts, the quality of placed concrete is generally superior to that in RC construction. Existence of faceplates makes it easier to incorporate major attachments such as large bore pipe supports during the initial construction. Additional minor attachments can also be easily handled during the service life of the structure. Similarly, the walls can be detailed during construction to accommodate any penetrations. SC walls have improved resistance to out-of-plane loads, such as bending and shear, that may be due to seismic or accident thermal events. The faceplates also provide better leak-tightness behavior, which reduces the loss of stored water. The leak-tightness also protects the concrete during the service life of the structure. SC construction has additional benefits in terms of resilience and sustainability of the structure. Some of the considerations for resilience and improved sustainability are discussed in Malushte and Varma [17] and Varma et al. [11].

Due to their numerous advantages, SC structures are increasingly being used in the third generation of nuclear power plants, and are also being considered for small modular reactors (SMRs) of the future. Modular SC walls are being considered for commercial applications, owing to their structural efficiency and construction economy. There has been recent research on the commercial

building application of SC walls with boundary elements ([18]–[21]). ASCE 7 [22] and AISC 341 [23] seismic provisions permit the use of composite-plate shear walls (C-PSW), with and without boundary elements, in seismic regions.

1.1.1 SC Flanged Wall and Wall Piers

SC construction may involve SC wall with boundary elements (or flanges), or without boundary elements (known as SC wall piers). In this document, walls with flanges are called SC walls, and walls without flanges are called SC wall piers. SC wall construction is employed for labyrinthine structures (with cross-walls serving as flange walls) typical to nuclear structures. SC wall piers (SC construction without any flange walls) are typically used as shear walls in Department of Energy (DOE) type nuclear facilities and commercial construction. SC wall piers are also inherently present in safety-related nuclear facilities where the walls have large openings. Commercial applications of SC structures may also involve SC walls (with boundary elements). The presence (or absence thereof) of flanges governs the lateral (in-plane) load resistance mechanism of the SC structures. Lateral force transfer mechanisms for SC walls and wall piers are presented in Figure 1.4. Lateral loads on SC structures will result in a base shear (V_{base}) and a base moment (M_{base}). The presence of flanges in SC walls means that the flexural stresses due to base moment will be resisted primarily by flanges as axial compression and tension. The base shear will primarily be resisted by the web of the wall. However, in SC wall piers the lack of boundary elements (or flanges) means that both the base moment and the base shear need to be resisted by the pier (web).

1.2 Research Motivation

SC walls in important structures (e.g., safety-related nuclear facilities) may be subjected to a combination of loads due to multiple hazards. The interaction of these loads is expected to adversely affect the lateral load (in-plane) response of SC walls. Fukushima nuclear accident of 2011 emphasized the need for designing walls for combination of accident thermal scenarios, and design basis and beyond design basis shaking. Although the probability of multiple design level events occurring simultaneously is low, severe impact of one hazard may trigger other ones, e.g., earthquake shocks may lead to accident thermal (high-energy pipe break) events. Additionally, subsequent aftershocks (potentially as intense as the main shock) may occur during the accident thermal event. Combination of accident thermal loading and safe shutdown earthquake (SSE) also presents a significant design challenge for Small Modular Reactors (SMRs) and Advanced Light Water Reactors (ALWRs) since postulated accident scenarios may cause higher elevated temperatures for longer durations in their small constrained spaces.

In case the seismic event occurs simultaneously with accident thermal event, the SC structures will be subjected to out-of-plane forces in combination with in-plane forces (in addition to accident temperature loads). Earthquake shaking, by itself, may also generate out-of-plane forces due to the inertial forces of the wall, and equipment and attachment loads. Nuclear structures are generally designed considering 100% of the design seismic force in one direction and 40% of the design seismic force in the other two orthogonal directions [24]. Additionally, the combination of out-of-plane and in-plane forces is an expected loading environment for SC walls at horizontal connections to foundations and floors, and vertical connections to other walls.

ACI 349 [25] and AISC N60s1 [26] require that the structural walls in safety-related facilities be designed for combination of abnormal loads (loads generated by a postulated high-energy pipe break accident) and safe shutdown earthquake loads. However, current design codes and standards

offer limited procedural guidance for including the effects of accident thermal loads or out-of-plane loads on the in-plane behavior (stiffness, strength, ductility or reserve margin) of structures. Existing research focus on the individual effects of in-plane, out-of-plane, or accident thermal loading, but not the combination of these loads. There is a need to evaluate (a) effect of accident temperature loads, (b) effect of out-of-plane loads, on the in-plane response of SC walls.

1.3 Research Objectives

The experimental data for SC structures subjected to multiple hazard loading is currently lacking. Therefore, the primary objective of the research was to experimentally evaluate the effect of loads due to multiple hazards (out-of-plane loads and accident temperature loads) on the in-plane strength, stiffness, and post-peak response of SC structures. Benchmarked numerical and analytical models were developed to supplement the experimental observations. Recommendations for analysis and design are provided based on the experimental and numerical results. The knowledge and recommendations derived from the experimental and numerical results are being made publicly available through reports, research articles, and possible inclusion into US design codes.

1.4 Research Plan and Methods

The research objectives were achieved by the following major tasks:

1.4.1 Design of Test Setup

Since the combined in-plane and out-of-plane loading tests were first of a kind, designing the test-setup that can apply high magnitude biaxial loading while accommodating orthogonal deformations was an important task. For tests involving combined in-plane and accident

temperature loading, designing the heating equipment that could enable surface temperature control at a specific magnitude for a specified duration was important.

1.4.2   Experimental Studies

Experimental program was the primary task of this research. Two series of experiments were conducted. Experiments were conducted to evaluate the in-plane response of SC wall piers subjected to different magnitudes of out-of-plane loading. Three specimens subjected to simultaneous in-plane and out-of-plane loading were tested. The second series of experiments involved testing SC wall and wall pier specimens to combination of accident temperature and in-plane loading. The in-plane response of specimens was quantified for different magnitudes and durations of accident thermal loading.

1.4.3   Benchmarked Models

Benchmarked analytical and numerical models were developed based on the experimental results. A finite-difference based cross-section model was developed to evaluate the interaction of biaxial moments and shears for SC wall piers. The interaction surface was compared with experimental and numerical results. Detailed finite element results were developed to numerically evaluate the in-plane response of SC walls and wall piers subjected to (a) out-of-plane loads, (b) typical accident temperature loads. The finite element results were benchmarked to experimental results, and can be employed for parametric studies to explore the effect of variation in parameters (e.g., the out-of-plane loading location, the accident temperature magnitude) on the in-plane response of structures.

1.4.4   Analyses and Design Recommendations

Based on the experimental results, recommendations for analysis and design of SC structures subjected to loads due to multiple hazards are provided. The recommendations are intended to provide designers with tools to more efficiently consider the effect of additional loads on the in-plane strength and stiffness of SC structures.

1.5   Research Scope and Limitations

Research presented in this dissertation includes experimental, numerical and analytical investigation of SC structures subjected to (a) biaxial loading, and (b) combined seismic and accident thermal loading. The first series of experiments (biaxial loading) was conducted to evaluate the effect of out-of-plane flexure and shear loading on the in-plane strength and behavior of SC wall piers. The tests were conducted on SC wall piers because it is simpler to apply and measure the in-plane and out-of-plane shear forces to SC wall piers without flanges. The proportion of in-plane and out-of-plane shear forces carried by the web in SC walls with flanges is variable and extremely difficult to measure or quantify. Some of the scaled specimens were pre-cracked to consider the size effects on the out-of-plane behavior of SC wall piers. The second series of experiments (seismic and thermal loading) was conducted to evaluate the effect of thermally induced cracking and stresses on the in-plane response of scaled SC wall and wall piers. An extensive loading and heating protocol was developed to investigate the effect of typical accident temperatures and durations.

Specimens were not subjected to any axial compression demands, as axial compression (expected to be less than the balance point or 40% of the axial capacity for these bulky walls) will increase the moment capacity of the sections. Therefore, it was conservative to not consider the axial demands.

Since typical SC structures in safety-related nuclear facilities have capacities that are almost impossible to replicate in a laboratory setup, scaling of the specimens was necessary. The design failure limit state in SC structures is generally ductile failure of steel, so the scaling of steel sections would not adversely affect these limit states. For concrete, pea-gravel aggregates were used in consideration of the scale effects of concrete. Additionally, some of the biaxially loaded specimens were cracked in the out-of-plane direction to try and address the size effects. For specimens subjected to combination of seismic and thermal loading, the duration of heating was scaled to obtain through-thickness temperature profiles similar to those observed in physical structures.

Numerical and analytical models were developed and benchmarked to experimental results. Since the benchmarked models are based on a limited number of experiments, they need to be validated with similar experiments that may be conducted in the future. The benchmarked models can be employed to conduct parametric studies. The parametric studies will further validate (and refine, if necessary) the analysis and design recommendations provided (based on the experimental results).

1.6 Research Significance

The experiments conducted as a part of this research are first of the kind. Currently, no data exists for SC specimens subjected to combination of in-plane and out-of-plane loading. Primary reason for that is the difficulty in designing a test setup where high magnitude of biaxial loads can be applied while accommodating orthogonal displacements. The test setup designed for this series of experiments can be employed to perform similar experiments on SC walls and RC walls.

Heating equipment employed for the second series of experiments (combined thermal and seismic) has been successfully used for conducting fire testing of structural elements (CFT columns, beam-columns, slabs, and connections) at Purdue University in the past ([27]–[31]) However, this is the

first time it was employed for wall tests. The successful completion of these tests means the setup can be employed for testing RC walls for similar loading. Wall tests for fire loading conditions can also be performed using the test setup designed.

The experimental data obtained from the research conducted fills a critical gap in SC wall knowledge database. The experimental results quantify the effect of additional forces (out-of-plane and thermal) on the in-plane response of SC walls. Based on the results, procedural guidance for analysis and design for these multiple hazard loads is provided. Since the US codes require designing the SC structures for extreme and abnormal load combinations, the guidance provided will enable engineers and designers to more thoroughly address multiple hazard loading on SC structures.

1.7 Organization

This dissertation is organized into the following chapters.

- Chapter 2 is the literature review section. This chapter provides a brief discussion on the history of SC construction. A listing of research on SC behavior is provided. The chapter then presents a discussion of current SC design provisions per US codes. A detailed review of research relevant to this study is provided. The review includes SC wall and wall pier behavior for in-plane and out-of-plane flexure and shear loads. Material and structural response to thermal loading in then discussed. The review of relevant research lays a foundation for the chapters that follow.

- Chapter 3 discusses the design of experiments for SC wall piers subjected to combined in-plane and out-of-plane loadings. The rationale for design of test matrix and test setup is described. Basis and type of instrumentation is presented. The chapter then describes the

construction of the specimens and the test setup. Finally, the testing procedure and loading protocol followed for the experiments is discussed.

- Chapter 4 presents detailed experimental results for SC wall piers subjected to combined in-plane and out-of-plane loading. Behavior of the wall piers specimens for biaxial loading is evaluated based on the experimental results.

- Chapter 5 discusses the design of experiments for SC wall and wall pier specimens subjected to combined in-plane and accident temperature loadings. The rationale for design of test matrix, loading and heating protocol, and test setup is described. The basis and type of instrumentation is presented. The chapter then describes the construction of the specimens and the test setup.

- Chapter 6 presents detailed experimental results for SC wall and wall pier specimens subjected to combined in-plane and accident temperature loadings. The in-plane strength and stiffness response of the specimens is evaluated based on the experimental results.

- Chapter 7 discusses the development of a fiber-model to evaluate biaxial moment-shear interaction for SC wall piers. The results obtained from benchmarked fiber model are compared with experimental results, and additional finite element results to establish the conservatism of the fiber model.

- Chapter 8 discusses the development and benchmarking of numerical finite element models for the specimens tested. The model parameters and details of finite element models are presented. Numerical results are compared with experimental results, and any limitations of the finite element models are discussed.

- Chapter 9 summarizes the research presented and enlists the conclusions drawn. Recommendations for analysis and design are also listed. Potential limitations of the results are discussed. Finally, future directions of research are discussed.
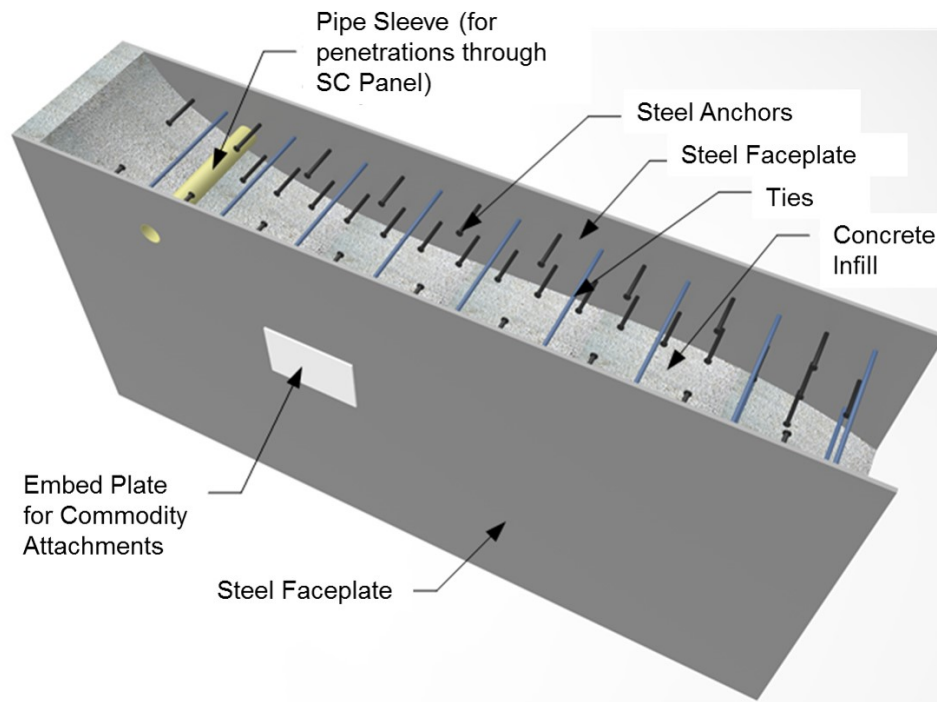
Figure 1.1 Typical SC wall configuration (from [10])
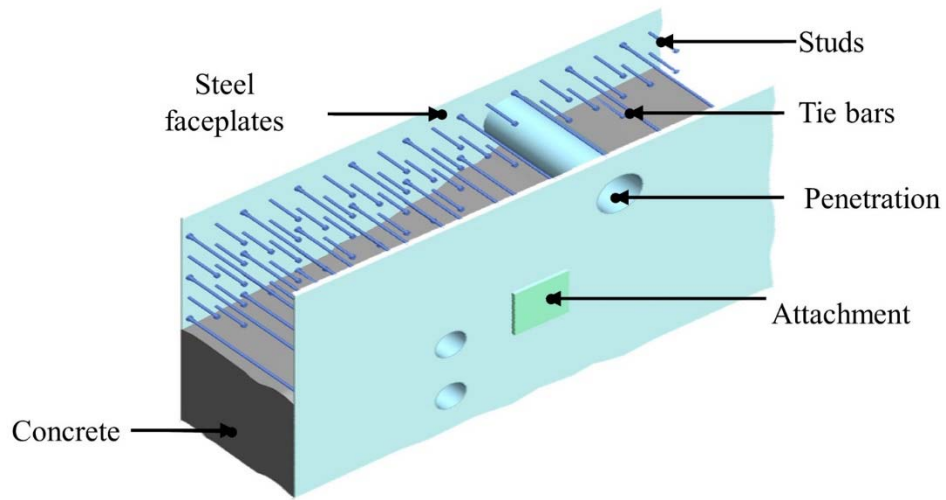
a) Modular SC construction
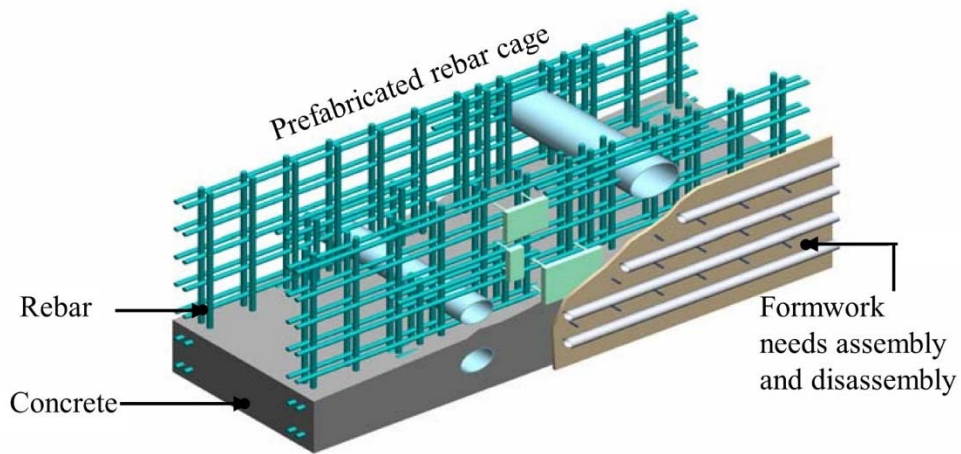
b) Modular RC construction

Figure 1.2 Typical modular SC and RC wall configurations (from [32])
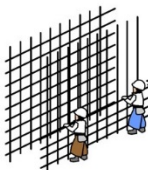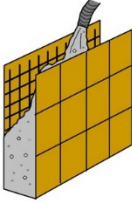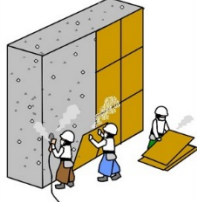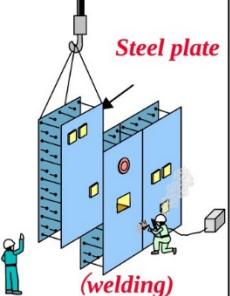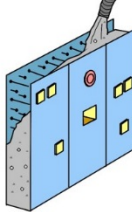
Structure \ Work	Rebar arrangement	Form work (assembling	Placing concrete	Form work (removal)
RC		Wooden form		
28days	13days	7days	4days	4days
SC	—	Steel plate (welding)		—
14days	—	10days	4days	—

Figure 1.3 Schedule contraction by means of SC construction (from [32])
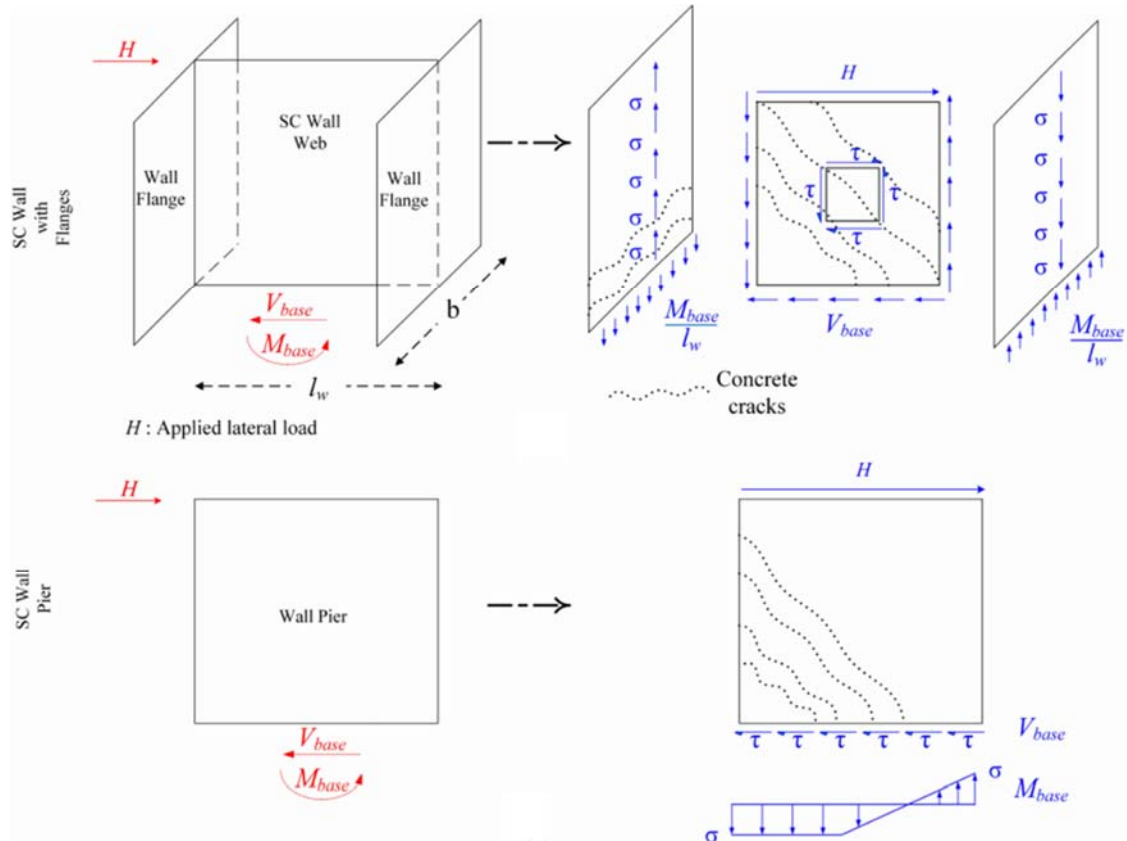
Figure 1.4 Difference in SC wall and wall pier lateral force transfer mechanisms (from [33])

2. BACKGROUND

This chapter presents the review of literature related to SC structures. The chapter is organized into following sections.

- SC construction and research background: Initial applications and relevant research for SC structures are listed. Research conducted on the non-commercial applications of SC walls is mentioned. SC construction and research history for nuclear applications is listed. The section summarizes SC construction and research history.

- US design provisions for SC structures: A brief discussion of organization and layout of Appendix N9 to AISC N690s1 [26] addressing the analysis and design of modular composite construction is provided in the section. Organization of AISC's recently published design guide on modular composite construction [10] is also presented.

- SC Detailing Provisions: AISC N690s1 [26] provisions to ensure that the non-ductile failure modes (e.g., faceplate buckling, splitting failure) do not govern the failure of SC walls are presented in this section. Faceplate slenderness requirement is discussed in detail.

- SC wall pier behavior: Relevant research on in-plane and out-of-plane behavior of SC wall piers is discussed in detail in this section.

- SC wall behavior: Research on the in-plane shear response of SC walls is described.

- Thermal loading: This section discusses the material and structural response to typical accident temperature loads.

2.1 SC Construction and Research Background

Initial application of SC walls was in non-nuclear commercial projects to resist extreme events in large structures. SC walls were expected to provide better resistance to extreme blast and

earthquake events. Other non-nuclear applications of SC walls included submerged tube tunnels [34], offshore oil rigs [35], and ship building [36]. Experimental and numerical studies were conducted in the UK (and Europe) on SC beams to investigate the effect of various parameters (e.g., partial composite action, stud spacing, steel faceplate thickness, etc.) on the out-of-plane flexure and shear response of the specimens ([37]–[42]). Recently, there has been research on the commercial building application of SC walls with boundary elements ([18]–[21]).

The need for construction schedule reduction, and better constructability and performance aspects of SC walls in comparison to RC walls led to the consideration of their use in safety-related nuclear facilities [32]. Some of the early studies on nuclear power plant type structures composed of SC walls were conducted in Japan. For example, the seismic behavior of a containment internal structure (CIS) composed entirely of SC walls was evaluated experimentally by testing a 1/10th scale model of the entire structure by Akiyama et al. [43]. The structure was subjected to a cyclic loading history with load control cycles in the elastic range and displacement control cycles in the inelastic range. The cyclic response of the structure included events such as concrete cracking, steel yielding, local buckling, shear buckling, and eventual fracture failure of the steel plates. The cyclic lateral load-displacement responses and hysteresis loops indicated that the structure had excellent stiffness, strength, and ductility. The equivalent viscous damping factor, obtained from the hysteresis loops, was about 5% before steel yielding and increased significantly thereafter due to yielding and inelasticity. Sener et al. [12] recently developed and verified a 3D nonlinear inelastic finite element model of the 1/10th scale test structure. They used the model to predict, further evaluate and gain insight into the seismic response of the SC structure. Both the experimental and numerical results confirmed that the seismic response including the stiffness, strength, and drift capacity was governed by the in-plane shear behavior and corresponding

concrete cracking and yielding of the steel plates of the SC walls. The lateral load ultimate strength was governed by the in-plane shear strength and failure of the SC walls parallel to the lateral loading direction. The final fracture occurred in regions where transverse shear reinforcement—web plates—in the SC walls were discontinued abruptly. The overturning moment at the base also contributed to inelastic deformations with extensive concrete cracking and yielding in the SC walls at the exterior outer regions of the CIS.

Akiyama et al. [43] compared the cyclic response of the SC structure with that of an equivalent RC structure that had been tested earlier using a similar size model by Kato et al. [44]. Akiyama et al. concluded that: (1) The ultimate strength of the SC structure was much higher than the corresponding RC structure due to the significant contribution of the steel plates. (2) Cyclic loading causes some stiffness degradation in the elastic range due to concrete cracking. This degradation was about 30% for the SC structure as compared to about 65% for the RC structure. (3) The SC structure was more ductile as the corresponding RC structure lost capacity rapidly after peak load due to shear failure. It is important to note that these conclusions were limited to specific SC and RC structures that were tested by Akiyama et al. and Kato et al., and the corresponding design, reinforcement and connection details. These conclusions cannot be generalized, but they motivated extensive research and studies in Japan, China, South Korea, the U.S. and Europe to establish rational design provisions, codes, and standards for SC structures.

Significant research on the behavior of SC walls for various loading conditions, both in-plane and out-of-plane, has been performed in Japan ([7], [45]–[48]), China ([49]–[51]), and in South Korea ([52]–[57]). The research in Japan and South Korea has been the basis for design standards for SC construction in the respective countries ([58], [59]).

In the U.S., extensive research has been conducted over the past decade to evaluate the behavior of SC walls and connections and to develop consensus design standards such as Appendix N9 to AISC N690s1 [26]. For example:

- The behavior of SC walls subjected to accident thermal and mechanical loading was evaluated by Booth et al. [60], Varma et al. [61], Varma et al. [62], and Booth et al. [63].

- The out-of-plane shear behavior and design of SC walls was evaluated by Varma et al. [64], Sener and Varma [3], and Sener et al. [65]. The out-of-plane flexure behavior of SC walls was analyzed by Sener et al. [2].

- The in-plane behavior and design of SC walls was evaluated by Varma et al. [6] and Seo et al. [66]. In-plane behavior of SC wall piers (without boundary elements) was analyzed by Epackachi et al. ([67], [68]) and Kurt et al. [69].

- The local buckling behavior of steel faceplates in SC walls and the composite action between steel plates and concrete infill was evaluated by Varma et al. [62], Zhang et al. [1], Zhang [70], and Bhardwaj and Varma ([71], [72]).

- The behavior and design of SC walls subjected to combined in-plane forces and out-of-plane flexure was presented by Varma et al. ([73], [8]).

- The missile impact behavior and design of SC walls was evaluated by Bruhl et al. ([15], [74]). The effects of impulsive loading on the design of SC walls was also evaluated by Bruhl and Varma ([75], [76]).

- The behavior and design of non-contact lap splices between the steel plates of SC walls and rebar of RC components were evaluated by Varma et al. [77], and Seo and Varma [78]. The direct shear strength of rebar coupler anchor systems for SC walls was evaluated by Kurt et al. [79].

- The behavior, design and shear strength of SC wall-to-wall T-joints and corner or L-joints were evaluated by Seo et al. [80], Seo [81]and Seo et al. [82].

- The design and detailing of faceplates, steel anchors and ties of SC walls to prevent local buckling, interfacial shear failure, and section delamination failure were presented in Bhardwaj et al. [9]. This paper also presented the design of steel anchors and ties to account for the effect of combined shear forces.

- The lateral load capacity of SC walls with boundary elements was evaluated by Booth et al. [83]. The lateral load capacity of SC wall piers (without boundary elements) was evaluated by Epackachi et al. ([67], [68]) and Kurt et al. [69].

SC walls are being increasingly used in nuclear facilities. GE Hitachi Nuclear Energy and Toshiba have used SC walls for advanced boiling water reactor (ABWR) Kashiwazaki-Kariwa Units 6 and 7 in Japan. These units were opened in 1996-97. Tokyo Electric Power Company (TEPCO) used SC walls in ABWR Fukushima 7 and 8 units. These units began commercial operation in 2007-08. Westinghouse Electric Corporation (WEC) has incorporated SC modules for walls and floors of its AP1000 plant internal structures. A typical wall module panel for the AP1000 plant containment internal structure is shown in Figure 2.1. Figure 2.2 presents a preassembled internal structure SC module. WEC also extended the use of SC modules to the AP1000 shield building to make it resilient against aircraft impact, a stipulated beyond-design-basis event. Construction of several AP1000 units is underway in the U.S. (South Carolina and Georgia) and China (Sanmen and Haiyang). Korea Hydro and Nuclear Power (KHNP) is incorporating SC construction in its advanced pressurized reactor (APR+) standard plant. Mitsubishi Heavy Industries (MHI) is doing the same for its advanced pressurized water reactor (APWR) standard plant. The use of SC construction in small modular reactors (SMR) is also currently being explored. Commercial

applications of SC wall piers—known as composite-plate shear walls—with and without boundary elements are also being considered in building construction.

2.2 US Design Provisions for SC Structures

Previously, the use of SC construction in the United States had been hindered by the absence of a U.S.-based design code for SC walls. However, in 2006 American Institute for Steel Construction (AISC) formed a subcommittee on modular composite construction under the Committee on Specifications Task Committee 12 for nuclear structures. Over the next nine years, from 2006 to 2015, a specification for the design of SC walls in safety-related nuclear facilities was developed and finalized as an appendix (Appendix N9) to AISC N690 [26]. The new appendix was based on research conducted in the US and elsewhere (discussed in the previous sections), and was incorporated into AISC N690 as Supplement No. 1. An outline of Appendix N9 and a brief discussion of how the provisions of the appendix may be used for the design of SC walls and connections are provided in Bhardwaj et al. [84] and Varma et al. [85].

2.2.1 Appendix N9 to AISC N690s1

Appendix N9 is applicable to the design of SC walls and their connections and anchorages. The experimental database that forms the basis of the provisions is discussed in AISC Design Guide 32 [10], and commentary to Appendix N9. The appendix is limited to SC walls with two faceplates on exterior surfaces and no additional reinforcing bars. General requirements of the appendix specify the conditions necessary for applicability of the provisions. Detailing requirements of the appendix address SC-specific limit states of local buckling, interfacial shear failure, and section delamination. The appendix discusses the analysis procedures and presents the guidelines for analysis. The demand types and available strengths for individual demands are presented. The

appendix also presents the interaction surfaces for combinations of demands. Connection design philosophy, detailing for regions around openings, design for impactive and impulsive loads, and quality assurance checks are other topics addressed by N690s1 [26].

2.2.2   AISC Design Guide 32

In 2017, AISC published Design Guide 32 [10] to facilitate the design of SC walls for safety-related nuclear facilities. The Design Guide:

- Addresses SC walls that meet the requirements of Appendix N9 to AISC N690s1 [26]

- Provides supplementary recommendations for the design of modular SC structures using the provisions of Appendix N9

- Discusses the design of SC wall connections, including design philosophies and typical connection details

- Presents illustrations explaining the tolerance requirements for construction and fabrication of SC walls

AISC N690s1 provides procedural recommendations for the design of SC wall connections. The Design Guide addresses the design of connections in detail. Different connection philosophies, force transfer mechanisms, and types of connections are discussed with illustrations. The implementation of the provisions of Appendix N9 is illustrated using a design example, where an SC wall from a compartment of a typical safety-related nuclear facility is designed. The design of SC wall and SC wall-to-basemat connection is presented based on Appendix N9 provisions.

2.3   SC Detailing Requirements

SC walls have some non-ductile failure modes (e.g., faceplate buckling, splitting failure) that should not be the governing failure modes. AISC N690s1 [26] provides SC detailing provisions

that ensure that these failure modes do not govern the behavior of the SC walls. Bhardwaj et al. [9] discuss the basis of these SC detailing provisions. The detailing provisions include:

a) the faceplate slenderness requirement (limits stud spacing to ensure faceplates yield in compression before buckling),

b) requirements for composite action (limit stud spacing to ensure that the interfacial shear strength is greater than the out-of-plane shear strength, and the interfacial shear strength is greater than the yield strength of the faceplates), and

c) shear reinforcement (tie) requirements to ensure that limit state of splitting or delamination failure is prevented (also based on the contribution of shear reinforcement to out-of-plane shear strength).

2.3.1 Faceplate Slenderness Requirement

When subjected to compressive stresses, the steel faceplates of SC walls can undergo local buckling between the steel anchors. This local buckling behavior of steel faceplates was investigated experimentally by Akiyama and Sekimoto [86], Usami et al. [87], Kanchi [88], Choi and Han [89], and Zhang [70]. These experimental studies evaluated the effects of the faceplate slenderness ratio—defined as the shear stud spacing, s, divided by the faceplate thickness, t_p, and the yield stress, F_y, on local buckling of faceplates. Zhang et al. [1] summarized these experimental studies and conducted additional numerical analyses to confirm and expand the experimental database. Figure 2.3 shows the relationship between the normalized critical buckling strain, buckling strain/steel yield strain, $\varepsilon_{cr}/\varepsilon_y$, and the normalized faceplate slenderness ratio, $s/t_p \times F_y/E_s$; where E_s is the steel modulus of elasticity. As shown, ε_{cr} is reasonably consistent with Euler's column buckling curve with partially fixed (K= 0.7) end conditions. Additionally, no data points

are located in the shaded region, which implies that yielding in compression occurs before local buckling for a normalized slenderness ratio less than 1.0.

Based on this investigation, AISC N690s1 [26] limits the slenderness ratio-the width-to-thickness ratio of the faceplates- as given by Equation 2.1 (Equation A-N9-2 of AISC N690s1), where b is the largest unsupported length between rows of studs or ties.

$$\frac{b}{t_p} \leq 1.0 \sqrt{\frac{E_s}{F_y}}$$

Equation 2.1

2.4   SC Wall Pier Behavior

Since the SC wall construction for safety-related nuclear facilities in typically labyrinthine, majority of the research conducted for in-plane (lateral) response of SC structures was for SC walls with flanges. However, SC walls without boundary elements (SC wall piers) may have applications as shear walls in DOE type nuclear facilities and commercial construction. Kurt et al. [69], and Epackachi et al. ([67], [68]) conducted experimental and numerical studies to evaluate the in-plane response of SC wall piers. The out-of-plane response of SC wall piers will be similar to that of SC walls. The in-plane and out-of-plane behavior of SC wall piers are discussed in this section.

2.4.1   In-plane Behavior

As discussed in Section 1.1.1, the in-plane behavior of SC wall piers is different from that of labyrinthine SC walls. While the SC walls (with flanges) resist the in-plane flexure through the flanges and in-plane shear through the web, SC wall piers are subject to the combination of in-plane moment and in-plane shear (since there are no flanges). Kurt et al. [69] and Epackachi et al. [68] conducted experimental and numerical studies to evaluate the in-plane shear behavior of SC wall piers. The authors tested eight SC wall pier specimens subjected to in-plane quasi-static cyclic loading. The experimental investigations focused on squat SC wall piers with aspect ratios ranging

from 0.6 to 1.0. In-plane response and failure mechanism for all the specimens was flexure controlled. The specimens underwent flexural cracking of infill concrete, followed by flexural yielding of faceplates at tension end (toe). Compression buckling at faceplate toe was observed after the faceplates yielded in tension and compression. The specimens failed in the inelastic cycles due to concrete spalling and crushing, and faceplate ductile fracture. While the in-plane flexure governed the behavior and failure mechanism of the specimens, corresponding in-plane shear was resisted by diagonal compression in concrete infill and horizontal shear stress in the faceplates. However, the shear did not govern the failure mechanism of the wall piers.

Since the in-plane response of SC wall piers with aspect ratios greater than or equal to 0.6 was governed by their in-plane flexural behavior, the lateral load capacity of the wall piers can be estimated by the flexural capacity of the wall piers [69]. The authors developed design equations for SC wall piers based on the plastic moment (M_p) and the compression yield moment capacity (M_{yc}, based on first compression yield of faceplates).

The plastic moment capacity of the wall pier cross-section at base was calculated considering (a) full plastification of faceplates, and (b) rectangular stress block in concrete based on ACI 318 [90]. The stress blocks assumed are shown in Figure 2.4. The plastic neutral axis location, c_p, from extreme compression fiber, and the plastic moment capacity, M_p, can be calculated by Equation 2.2 and Equation 2.3 respectively [69], where l_w is the length of the wall pier, t_c is the thickness of concrete infill, f'_c is the uniaxial compressive strength of concrete, and β_1 is as defined in ACI 318 [90].

$$c_p = (2t_p F_y l_w) / (4t_p F_y + 0.85\beta_1 f'_c t_c) \qquad \text{Equation 2.2}$$

$$M_p = F_y t_p (l_w^2 - 2l_w c_p + 2c_p^2) + \frac{0.85\beta_1 f'_c t_c c_p^2}{2} \qquad \text{Equation 2.3}$$

Kurt et al. [69] defined the yield moment capacity of the wall piers, M_{yc}, as the moment corresponding to initiation of compression yielding of the faceplates. Since the faceplate slenderness requirement of AISC N690s1 [26] ensures that the faceplates will yield in compression before buckling, M_{yc} can be used as a lower-bound estimate of the flexural strength of flexure-controlled wall piers. The authors calculated M_{yc} using lower bound theorem of plasticity, and admissible stress blocks shown in Figure 2.5. Faceplates were considered to undergo significant yielding and plastification in tension, and just reach yielding in compression. The concrete on the compression side was assumed to remain linear elastic, with concrete compressive stress limited to $0.70f'_c$. The neutral axis location, c_{yc}, from extreme compression fiber, and the yield moment capacity, M_{yc}, can be calculated by Equation 2.4 and Equation 2.5 respectively [69].

$$c_{yc} = (2t_p F_y l_w)/(4t_p F_y + 0.35 f'_c t_c) \qquad \text{Equation 2.4}$$

$$M_{yc} = F_y t_p (l_w^2 - 2l_w c_{yc} + \frac{4}{3} c_{yc}^2) + \frac{0.70 f'_c t_c c_{yc}^2}{3} \qquad \text{Equation 2.5}$$

Kurt et al. [69] developed benchmarked finite element models for all the wall pier specimens in commercial software packages LS-Dyna [91] and ABAQUS [92]. The authors conducted parametric studies to evaluate the influence of different aspect ratios (0.6, 0.75, 1.0, 1.5, and 3.0) and wall thicknesses (230, 305, and 457 mm) on the lateral load capacity of the wall piers. The parametric studies confirmed that SC wall piers (with aspect ratios greater than or equal to 0.6) failed in in-plane flexure. As the aspect ratio decreased, the base shear corresponding to lateral load capacity of the wall piers increased. While the base shear did not reach the yield strength of faceplates in shear ($0.6F_y A_s$, where A_s is the area of the faceplates), it did reduce the flexure capacity of the wall piers from M_p to M_{yc}.

Based on the experimental and analytical studies, the authors recommended that for wall piers with an aspect ratio equal to 0.5, the flexural capacity can be considered as equal to M_{yc}. For aspect

ratios greater than or equal to 1.5, the flexural capacity can be considered to be equal to M_p. For aspect ratios between 0.5 and 1.5, the authors recommended linear interpolation for flexural capacity (between M_p and M_{yc}) while accounting for wall thickness. The proposed equations compared favorably with experimental and analytical results. However, the validity of proposed equations was limited to the extent of parameters considered in experimental and analytical studies and needs to be verified for a wider range of parameters.

2.4.2   Out-of-plane Behavior

The out-of-plane shear force resisting mechanisms for SC walls (and wall piers) are similar to those for reinforced concrete beams, but with some differences [93]. Out-of-plane shear resistance is primarily provided by (a) concrete infill, and (b) shear reinforcement (ties) if provided. ACI 349 [25] estimates the out-of-plane strength (V_n) of the walls as the sum of concrete (V_c) and shear reinforcement (V_s) contributions. Per ACI 349, the shear strength can be calculated using Equations 2.6 to 2.8 (in SI units), where ρ_w is the longitudinal tensile reinforcement ratio (t_p/d for SC walls), $M_u/V_u d$ is the shear span-to-depth ratio, d is the beam section depth (wall thickness for SC walls), f_{yw} is the shear reinforcement (ties) yield strength, and A_v is the cross-sectional area of shear reinforcement (ties) at a spacing S. The equations are applicable for shear span-to-depth ratio larger than 1.0. V_c^{ACI} can also be calculated by a more commonly used expression, $0.17\sqrt{f_c'}\,A_c\;(2\sqrt{f_c'}\,A_c,\text{in psi units})$. V_s^{ACI} is considered only when shear reinforcement (ties) are spaced at not greater than half the section thickness.

$$V_n^{ACI} = V_c^{ACI} + V_s^{ACI} \qquad\qquad \text{Equation 2.6}$$

$$V_c^{ACI} = (0.16\sqrt{f_c'} + 17\rho_w \frac{V_u d}{M_u})A_c \leq 0.29\sqrt{f_c'}\,A_c \qquad\qquad \text{Equation 2.7}$$

$$V_s^{ACI} = A_v f_{yt} \frac{d}{S} \leq 0.66\sqrt{f_c'} b_w d \qquad\qquad \text{Equation 2.8}$$

The out-of-plane shear strength equations in AISC N690s1 [26] are based on ACI 349 equations

with V_c reduced to $0.13\sqrt{f_c'} A_c$ $(1.5\sqrt{f_c'} A_c, \text{in psi units})$ to account for size effects. Additionally,

AISC N690s1 permits the shear reinforcement to be spaced at greater than half the section

thickness, in which case V_n is equal to the greater of V_c and V_s. For the series of experiments in

this dissertation, ACI 349 equations were employed to calculate V_c, as those have been traditionally

used by engineers and practitioners.

Experimental investigations were conducted in Japan [46], S. Korea [57], China [94], and the US

([93], [95]) to determine the out-of-plane shear behavior and strength of SC walls. Sener et al. [3]

compiled the database of out-of-plane shear tests for SC walls. The authors used the experimental

database to evaluate the conservatism of the ACI 349 equations in calculating the out-of-plane

shear strength of SC walls. Figure 2.6 presents the experimentally observed out-of-plane shear

strengths normalized with V_n^{ACI}. The normalized strengths are plotted against (a) shear span-to-

depth ratio and (b) section depth. The authors observed that out-of-plane shear strength decreases

with the shear span-to-depth ratio, and the lower bound shear strength occurs for ratios in the range

of 3.0-3.5. The strength also decreased with increased section depth. Additionally, it was observed

that the ACI equations estimated the lower-bound out-of-plane shear strength of SC wall beam

specimens reasonably (as seen in Figure 2.6). Sener et al. [65] also compiled the out-of-plane

database of SC beam specimens without shear reinforcement and determined that V_c^{ACI} reasonably

estimated the strength of unreinforced specimens.

The out-of-plane flexure behavior of SC walls is governed by the faceplate limit state of flexural

yielding (provided the specimen meets the faceplate slenderness requirements of AISC N690s1).

Per AISC N690s1, the out-of-plane flexural capacity of the specimen can be calculated using

Equation 2.9 (Equation A-N9-18 in AISC N690s1), where $A_s{}^F$ is the area of the faceplate in tension

due to flexure, and t_{sc} is the wall thickness. The commentary to out-of-plane flexural strength

section in AISC N690s1 states that the strength can also be calculated using provisions of ACI 349

(Section 10.2) [25]. Sener et al. [2] compiled the experimental database for out-of-plane flexural

strength for SC beams. The database comprised of experiments conducted in Japan [46], S. Korea

[57], China [96], and the US [3]. In Figure 2.7, normalized experimental out-of-flexural capacity,

M_{exp}, (normalized with $M_{n.ACI}$) is plotted against the section depth for all the specimens. The

authors observed that ACI 349 provisions predicted the experimental strength accurately, but were

marginally unconservative for some specimens.

$$M_n^{AISC} = F_y\left(A_s^F\right)(0.9t_{sc})$$
<div align="right">Equation 2.9</div>

2.5 SC Wall In-Plane Behavior

For SC walls, in-plane flexure forces are primarily resisted by the boundary elements (flanges).

In-plane shear forces are resisted primarily by the web of the wall (as shown in Figure 1.4). The

in-plane shear behavior of SC walls was developed by Ozaki et al. [7] and extended by Varma et

al. [6]. Varma et al. [8] developed and verified a mechanics-based model (MBM) for estimating

the response of SC walls subjected to in-plane membrane normal forces (S_x and S_y) and in-plane

membrane shear force (S_{xy}) per unit width. The model was employed to develop pure in-plane

shear behavior of SC walls. Summary of the MBM application for pure in-plane shear is presented

in Figure 2.8. Part a of the figure shows a unit width of the SC specimen (width equal to thickness,

T) subjected to pure in-plane shear loading (S_{xy}). The membrane normal forces (S_x and S_y) are zero.

The principal direction for pure shear case will be 45˚, and the principal stresses will be equal and

opposite in magnitude. Figure 2.8b shows the principal stress distribution in concrete infill. The

concrete will crack in direction perpendicular to principal-1 (principal tension) direction when S_{p1} (principal tensile stress in direction principal-1) exceeds S_{cr} (cracking threshold). S_{cr} corresponds to a concrete tensile stress, $2\sqrt{f_c'}$ (in psi units). The cracking tensile stress is reduced to account for locked-in shrinkage strains, and slip between steel and concrete. S_{cr} can be calculated using Equation 2.10 (in SI units).

$$S_{cr} = \frac{0.17\sqrt{f_c'}}{E_c}(E_s A_s + E_c A_c) \qquad\qquad \text{Equation 2.10}$$

Post-cracking, the concrete loses stiffness in principal tension direction (perpendicular to direction of cracking). The concrete stresses in xy plane can be obtained by using transformation matrices for stress (T_σ) and strains (T_ε) as shown in Figure 2.8c. The steel stress-strain relationship can be defined using plane stress stiffness matrix (as shown in Figure 2.8d). The strains (and then stresses) in steel and concrete infill can be calculated from S_{xy} by establishing force equilibrium for SC wall panel (as shown in Figure 2.8e). The principal stresses in steel faceplates can be used to calculate Von-Mises stress of steel. The in-plane shear force ($S_{xy}{}^Y$) corresponding to Von-Mises yielding of faceplates can then be calculated.

Based on the MBM discussion, the in-plane behavior can be estimated as the tri-linear shear force–strain (S_{xy}-γ_{xy}) curve. The tri-linear curve is shown in Figure 2.9. The in-plane behavior was idealized in 3 parts.

(i) Before concrete cracking, where concrete and steel plates are elastic and perfect bond between them can be assumed. The stiffness corresponding to this branch (GA_{uncr}) can be calculated using Equation 2.11.

$$GA_{uncr} = K_{xy}^{uncr} = G_s A_s + G_c A_c \qquad\qquad \text{Equation 2.11}$$

(ii) Post-cracking but before faceplate yielding. Concrete cracks when S_{xy} exceeds S_{cr} (calculated using Equation 2.10). The tangent stiffness for region 2, $GA_{cr}{}^{TAN}$, can be calculated using Equation 2.12. The equation is based on MBM, considering orthotropic cracked concrete and plane stress steel properties.

$$GA_{cr}^{TAN} = K_{xy}^{cr} = K_s + K_{SC} = G_s A_s + \cfrac{1}{\cfrac{4}{0.7 E_c A_c} + \cfrac{2(1-\nu_s)}{E_s A_s}} \qquad \text{Equation 2.12}$$

(iii) Post-yield, where faceplates undergo Von-Mises yielding. The in-plane shear strength (based on Von-Mises yielding of faceplates, $V_n{}^{MBM}$) can be calculated using Equation 2.13. The equation is based on MBM.

$$V_n^{MBM} = S_{xy}^Y = \frac{K_s + K_{sc}}{\sqrt{3K_s^2 + K_{sc}^2}} \left(A_s F_y \right) \qquad \text{Equation 2.13}$$

The in-plane shear strength and stiffness requirements in AISC N690s1 [26] are based on the trilinear MBM developed by Varma et al. [8]. Per AISC N690, if the in-plane shear force demand is less than S_{cr}, the effective stiffness is equal to GA_{uncr} (as calculated in Equation 2.11). However, AISC N690s1 uses shear moduli instead of elastic moduli (in Equation 2.10) to calculate S_{cr}. This will result in a lower value of cracking threshold force in comparison to the value obtained from MBM (Equation 2.10). If the in-plane shear force demand is greater than $2S_{cr}$, the effective in-plane shear stiffness can be considered as GA_{cr}. Per AISC N690s1, GA_{cr} can be calculated using Equation 2.14 and Equation 2.15 and is calibrated to the secant stiffness for the tri-linear MBM. For in-plane force demands between S_{cr} and $2S_{cr}$, effective shear stiffness can be linearly interpolated between GA_{uncr} and $GA_{cr}{}^{AISC}$. For accident thermal combinations, effective stiffness is considered to be cracked, irrespective of the magnitude of in-plane shear force.

$$GA_{cr}^{AISC} = 0.5 \rho^{-0.42} G_s A_s \qquad \text{Equation 2.14}$$

where,

$$\bar{\rho} = \frac{A_s F_y}{12 A_c \sqrt{f_c'}}$$

Equation 2.15

The in-plane shear strength of SC walls per AISC N690s1 can be calculated using Equation 2.16 and Equation 2.17. Equation 2.16 is calibrated to the in-plane shear force corresponding to Von-Mises yielding of faceplates (based on MBM, Equation 2.13) where κ is the calibration factor calculated using Equation 2.17.

$$V_{ni}^{AISC} = \kappa F_y A_s$$

Equation 2.16

where,

$$\kappa = 1.11 - 5.16\bar{\rho} \le 1.0$$

Equation 2.17

Seo et al. [66] compiled an experimental database of the in-plane shear tests conducted in Japan, S. Korea, and the US ([6], [7], [45], [97]–[99]). The authors observed that the in-plane shear strength of the wall (normalized with $A_g f'_c$) increased linearly with faceplate reinforcement ratio. A comparison of experimentally observed in-plane shear strengths with V_{ni}^{AISC} indicated that the in-plane strength of SC walls can be conservatively estimated by using AISC N690s1 [26] provisions.

Booth et al. [100] proposed that the SC walls would have additional in-plane strength post the Von-Mises yielding of faceplates. The additional post-yield shear resistance is provided by the concrete compression strut (concrete arch action) that anchors into the boundary elements. The reserve strength would depend on the additional force resisted by concrete in diagonal compression, which in turn would depend on the strength of the boundary elements and the strength of the connection between the wall (web) and boundary elements.

2.6   Thermal Loading

Safety-related nuclear facilities need to be designed for load combinations considering operating and accident thermal loading (from postulated high-energy pipe break scenarios) ([26], [25]). Operating thermal loads are a consequence of the normal operation of the facility and include thermal loads associated with changes in ambient and weather conditions for exposed surfaces of walls. Operating thermal loads typically develop over a long duration of time (several days of operation) and consequently produce steady-state temperatures with linear variation through the thickness of the walls. The surface temperatures of the walls are same as the ambient air temperature within the respective compartment. Typically, no concrete cracking is associated with these steady-state temperatures and linear variations through the thickness of the wall. The thermal accidents may subject structures to accident pressure and accident temperature loading. These loadings result in thermal deformations. Restraints to thermal deformations may produce significant stresses and forces, which may need to be considered in the design. Since this dissertation evaluates the effect of accident temperature loading on the in-plane response of SC walls, research and code provisions for accident temperature loading are discussed in this section. Thermal-hydraulic analyses are conducted to simulate the effects of high-energy pipe break events. The results include the temperature histories (*T-t* plots) for exposed surfaces of the walls. These temperature histories (surface *T-t* plots) define the accident temperature loads for structural analysis and design. Sener et al. [101] identified typical accident temperature-time histories for the containment internal structure (CIS) nuclear power plants (NPPs) using envelopes of *T-t* from publicly available Design Control Documents ([102], [103]). Envelope temperature-time histories were obtained for each major NPP compartment; e.g., reactor cavity, steam generator, refueling water storage pit (RWSP), containment walls. The envelope *T-t* histories for these compartments are presented in Figure 2.10 to Figure 2.13. As shown, a thermal accident results in a steep increase

in the surface temperatures to peak value (typically around 140˚C to 180˚C), followed by cooling due to dissipation of heat throughout the CIS. The elevated temperatures are typically sustained over several days (approximately 15 days), but the curves were cut-off at 14 hours for clarity.

The accident event may subject the two surfaces of a wall to slightly different temperature histories. For example, Figure 2.14 shows idealized but representative temperature histories (*T-t* curves) for the surfaces (exterior and interior) of a compartment open at the top and subjected to high-energy pipe break event [104]. As shown, both surfaces of the walls have slightly different temperature histories, and the interior surface temperature leads the exterior surface temperature for a few hours. Figure 2.15 shows the *T-t* history zoomed into the first 10 hours after the accident. The inner surface temperature increases to 149˚C (300˚F) from the operating temperature 38˚C (100˚F) over the first 10 to 20 minutes of the event. The outer surface also reaches the peak temperature in about 3 hours, and the accident energy spreads. The temperatures reduce to about 100˚C over the next day (24 hours), and then reduce slowly to about 80˚C over the next ten days (240 hours). The specific details of the *T-t* curves will vary depending on the details of the compartment and the accident event.

The temperature histories (*T-t* curves) for various sections through the thickness of the wall, and the temperature profiles through the thickness of the wall at different times are calculated by performing heat transfer analysis through the cross-section. The steel faceplates may be considered, or conservatively ignored for heat-transfer analysis. For example, Figure 2.16 shows sample temperature profiles that were calculated through the thickness of a 1.22-m (48 in.) thick SC wall subjected to the surface temperature histories (*T-t* curves) shown in Figure 2.14. The temperature histories (*T-t* curves) for points through the thickness were obtained by performing heat transfer analysis using the heat conduction equation (heat loss through convection or radiation

was not considered) and concrete thermal and material properties (from [105], thermal and mechanical properties for steel and concrete are discussed in detail in the following section). The thermal gradient through the wall thickness is significantly nonlinear for several hours (almost up to one day) after the event. The temperatures become relatively uniform through the thickness after several (three to four) days. Specific details of the thermal gradients and their evolution over time will depend on the details of the wall and the surface temperature histories (*T-t* curves) generated by the accident event.

Based on the discussion in this section, typical accident temperatures for NPPs are around 150˚C. A high non-linear gradient exists through the cross-section of walls for initial few hours post the accident. Non-linearity of the thermal gradient reduces as time since the accident increases. Higher magnitudes of temperatures (up to around 225 ˚C) and higher accident durations maybe expected for Small Modular Reactors (SMRs) and Advanced Light Water Reactors (ALWRs) due to their small constrained spaces.

2.6.1 Material Behavior

Thermal and mechanical properties of steel and concrete will be influenced by accident temperatures. Significant research has been conducted for evaluating the change in thermal and mechanical properties of steel and concrete at elevated temperatures (typically for fire loading) ([106]–[115]). The research includes experimental evaluations, and comparisons with existing code provisions for fire design in the US ([116]–[118]) and Europe [119] However, the fire temperatures (up to 1100˚C) are significantly higher than typical accident temperatures (up to 225 ˚C). The material properties are not expected to change drastically for typical accident temperatures. Therefore, the research on fire-related material behavior is not discussed in this section. Instead, the AISC N690s1 [26] and Eurocode 3 [119] provisions for material properties

for the range of typical accident thermal temperatures are discussed and compared. Magnitude of change in the material properties will provide insight into the contribution of material behavior in structural response to combined seismic and thermal loading.

2.6.1.1 Steel

Temperature-dependent thermal and mechanical properties (for fire loading) are presented in Eurocode ([119]). Temperature-dependent properties in AISC N690s1 [26] are consistent with Eurocode properties. The density of steel is considered to be independent of temperature.

2.6.1.1.1 Coefficient of Thermal Expansion

The coefficient of thermal expansion of steel (α_{steel}) increases marginally for the range of accident thermal temperatures (Figure 2.17). Per Eurocode, the increase is about 20% as the temperature changes from ambient (20˚C) to 300˚C. For temperatures above 66˚C, AISC N690s1 recommends the α_{steel} value of $1.4x10^{-5}$/˚C (Eurocode also permits this value for simple calculations).

2.6.1.1.2 Specific Heat Capacity

Specific heat capacity of steel increases for the range of accident thermal temperatures (Figure 2.18). Per Eurocode, the increase in about 30% as the temperature changes from ambient (20˚C) to 300˚C. For simple calculations, Eurocode recommends a specific heat value independent of the steel temperature (600 J/Kg/K). However, this value is on the higher end for accident thermal temperature ranges (as seen in Figure 2.18).

2.6.1.1.3 Thermal Conductivity

The thermal conductivity of steel decreases for the range of accident thermal temperatures (Figure 2.19). Per Eurocode, the decrease is about 20% as the temperature changes from ambient (20˚C) to 300˚C. For simple calculations, Eurocode recommends a thermal conductivity value

independent of the steel temperature (45 W/m/K). However, this value is on the lower end for accident thermal temperature ranges (as seen in Figure 2.19).

2.6.1.1.4 Uniaxial Stress-strain behavior

Eurocode provides a series of equations to determine the temperature-dependent uniaxial stress-strain relationships for steel. Retention factors that vary with increase in temperatures are provided to adjust the ambient stress-strain curves. Similar retention coefficients (consistent with Eurocode) are provided in AISC N690s1. Figure 2.20 presents the temperature dependent steel stress-strain relationship for typical accident temperatures (for measured F_y of 393 MPa). For accident temperature range, the yield and tensile strength values are not reduced. However, a non-linearity is introduced into the stress-strain curve just before the yielding plateau, and this non-linearity increases with the increase in temperature. The modulus of elasticity of steel reduces by about 20% as steel temperature increases from ambient (20˚C) to 300˚C.

2.6.1.2 Concrete

Effect of temperatures on the thermal and mechanical properties of concrete depends on the type of concrete (light-weight or normal-weight) and aggregates (calcareous or siliceous). The values for normal-weight concrete, with siliceous aggregates, are discussed in this section.

2.6.1.2.1 Density

The density of concrete reduces marginally for the range of accident thermal temperatures (Figure 2.21). The density does not change up to temperatures of about 100˚C. The reduction in density for higher temperatures is due to loss of evaporable water (up to 150˚C) followed by chemically bound water (200˚C and above). The reduction in density for temperatures up to 300˚C is about 2.5%.

2.6.1.2.2   Coefficient of Thermal Expansion

The coefficient of thermal expansion of concrete ($\alpha_{concrete}$) increases significantly for the range of accident thermal temperatures (Figure 2.22). Per Eurocode, the increase is about 40% as the temperature changes from ambient (20˚C) to 300˚C. For temperatures above 66˚C, AISC N690s1 recommends the $\alpha_{concrete}$ value of 1.8×10^{-5}/˚C (the Eurocode also permits this value for simple calculations). However, the value is on the higher end for typical accident temperatures.

2.6.1.2.3   Specific Heat Capacity

The specific heat capacity of concrete depends on the moisture content. For oven dried concrete, the change in specific heat for typical accident temperatures is marginal (Figure 2.23, w/o moisture effect). When moisture effect is considered, the specific heat almost doubles for temperature range of 100˚C to 200˚C. Per Eurocode, the increase in dry specific heat in about 15% as the temperature changes from ambient (20˚C) to 300˚C. For simple calculations, Eurocode recommends a dry specific heat value independent of the concrete temperature (1000 J/Kg/K). The recommended value is close to the average for accident thermal temperature ranges (as seen from Figure 2.23).

2.6.1.2.4   Thermal Conductivity

The thermal conductivity of concrete decreases for the range of accident thermal temperatures (Figure 2.24). Per Eurocode, the decrease is about 30% as the temperature changes from ambient (20˚C) to 300˚C. For simple calculations, Eurocode recommends a thermal conductivity value independent of the concrete temperature (1.6 W/m/K). The recommended value is close to the average for accident thermal temperature ranges (as seen from Figure 2.24).

2.6.1.2.5 Uniaxial Compression Stress-Strain Behavior

Eurocode provides a series of equations to determine the temperature-dependent uniaxial compression stress-strain relationships for concrete. Retention factors that vary with increase in temperatures are provided to adjust the ambient stress-strain curves. Similar retention coefficients (consistent with Eurocode) are provided in AISC N690s1. Figure 2.25 presents the temperature dependent concrete stress-strain relationship for typical accident temperatures (for measured f'_c of 40 MPa). Unlike steel, the concrete compression strength reduces considerably for accident thermal temperature range. While there is no reduction for temperature of 100˚C, the compressive strength reduces by 5% for 200˚C, and by 15% for 300˚C. Additionally, the reduction in initial modulus of elasticity is higher for concrete than that for steel. The modulus of elasticity of concrete reduces by about 40% as concrete temperature increases from ambient (20˚C) to 300˚C.

2.6.1.2.6 Uniaxial Tensile Strength and Fracture Energy

Eurocode permits the tensile strength to be conservatively assumed as zero. However, if tension strength is considered, it should not exceed the values based on CEB-FIP model code [120]. However, the available data show that tensile strength reduces with increasing temperatures more rapidly than compressive strength [108]. Bazant and Prat [115] indicated that the fracture energy of concrete reduces with temperature. In the absence of Eurocode recommendations, Selden [30] obtained the reduction in tensile strength, fracture energy, and rupture strain based on the reduction in concrete compressive strength for accident thermal temperatures. The reduction in tensile strength and fracture energy was marginal for typical accident temperatures.

2.6.2 Structural Behavior

Operating thermal loads produce linear thermal gradients through the thickness of the structural element. These temperature changes induce thermal deformations due to expansion (or contraction)

of the concrete and steel materials in the structural member. If these thermal deformations are restrained by end conditions or connected members, restraining forces are induced in the structural elements. If these restraining forces are membrane tension, concrete will crack, relieve these forces and undergo the associated thermal deformation. If the restraining forces are membrane compression, they will be resisted by the concrete and steel together. If these restraining forces are membrane shear, out-of-plane shear, or out-of-plane flexure, there will be some concrete cracking, but the restraining forces will not be relieved. The restraining forces will depend on stiffness of the member subjected to thermal loads and the relative stiffness of the restraining member or structure.

The structural behavior of walls subjected to accident thermal loading can be complicated and variable over the duration of the event. As discussed previously, during the first few hours (up to one day) of the accident, structural members are subjected to significantly nonlinear thermal gradients over the thickness. These nonlinear thermal gradients induce significant concrete cracking due to internal or self-restraint. This is illustrated in Figure 2.26, which shows the qualitative behavior of an SC wall cross-section subjected to nonlinear thermal gradient (ΔT). Thermal strains (ε_{th}) are calculated directly as the thermal expansion coefficient (α) multiplied by ΔT. As a result, thermal strains have the same nonlinearity as the thermal gradient. Since plane sections remain plane, total strains (ε_{tot}) vary linearly over the thickness, which produces internal or self-restraint. Mechanical strains (ε_{mech}) are equal to the total strains (ε_{tot}) minus the thermal strains (ε_{th}). As shown in Figure 2.26, a significant portion of the member thickness is subjected tensile mechanical strains, which causes cracking of the concrete. The total strains (ε_{tot}), which depend on the centroidal strain (ε_{cen}) and curvature (φ), can be calculated by establishing force equilibrium over the cross-section. Thus, during the first few hours (up to one day) of the accident

event, there is significant cracking through the thickness of the concrete member due to self-restraint.

After the first few hours (up to one day) of the accident, the thermal gradients become relatively uniform through the thickness as shown in Figure 2.16. The concrete cracks, produced during the first few hours due to self-restraint, may close due to the uniformity of the temperatures through the thickness. The uniform temperatures are lower than the maximum values reached earlier. However, the concrete will never regain its uncracked stiffness for mechanical loads. In the rare situation of the thermal expansion being fully restrained, there will be no concrete cracking, even for the case with nonlinear thermal gradients. The membrane axial compression associated with full restraint will be equal to the integration of the thermal stresses ($E\,\varepsilon_{th}$) over the member area. This structural response to thermal loads was numerically validated by Bhardwaj et al.[104], by subjecting 1.22 m (48 in.) thick RC wall structures to idealized $T\text{-}t$ curves. The response was also experimentally verified for RC structures by studies conducted by Vecchio and Sato [121] on RC portal frame structure that was subjected to surface temperatures up to 80°C from one side. The experimental results demonstrated that the internal forces, strains and deformations (demands) induced by thermal loading were maximized shortly after the peak surface temperatures were attained when the nonlinearity in the thermal gradient was greatest. The thermally induced demands gradually reduced as the through-depth thermal gradient became uniform with continued heating. The test results also verified that thermally induced concrete cracking was observed in the externally unrestrained sections of the portal frame due to the internal restraints acting against thermal expansion caused by the nonlinear gradient. The mechanical load test results performed following the thermal load showed that the frame response was in accordance with the cracked section stiffness, and uncracked section stiffness overestimated the response significantly.

Recently, Kitajima et al. [122] carried out experimental and numerical studies on the seismic behavior of SC walls subjected to accident thermal loading. The researchers conducted tests of SC wall specimens that failed in in-plane shear mode. The tested specimens were 1/7 scale SC walls. The specimens had a wall thickness of 285 mm, steel faceplate thickness of 2.3 mm, and end (flange) plate thickness of 22 mm. The test results showed that the lateral load capacities of the specimens were reduced by 15-25% due to the thermal loading. Additionally, significant reduction (up to 50%) in the pre-yielding stiffness response was observed due to the thermal loading.

2.7 Chapter Summary

This chapter presented the SC construction and research history and background. SC related research conducted in the US and other countries was enlisted. US code provisions for design of modular SC walls were discussed (AISC N690s1 and AISC DG 32). Existing research relevant to the topic of this dissertation was discussed in detail. In-plane and out-of-plane behavior of SC wall piers was discussed. In-plane behavior of SC walls was presented. Typical accident thermal temperatures and results for thermal analysis were mentioned. The chapter then discussed the existing code provisions for material (steel and concrete) response to typical accident temperatures. Fundamentals of structural response to typical thermal loads were described, supplemented by existing numerical and experimental studies.
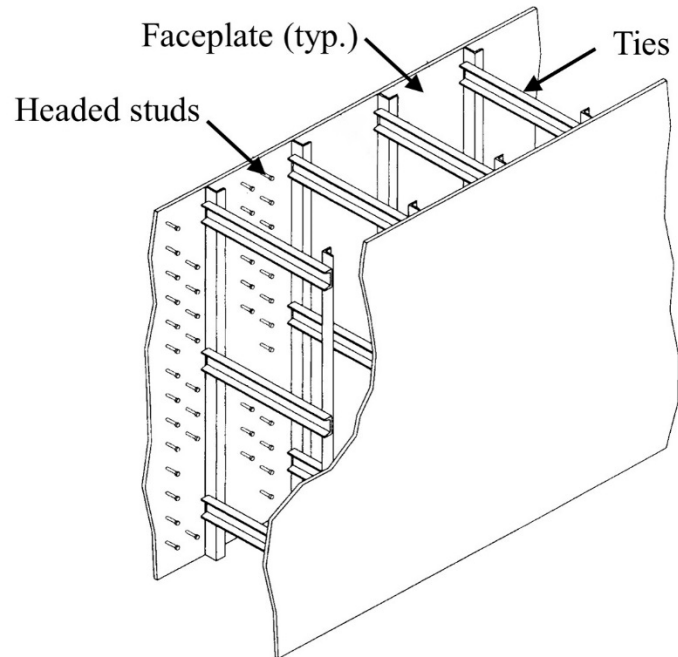
Figure 2.1 Typical structural wall module in AP1000 plant (from [102]) (©Westinghouse Electric Company, LC. All rights reserved).
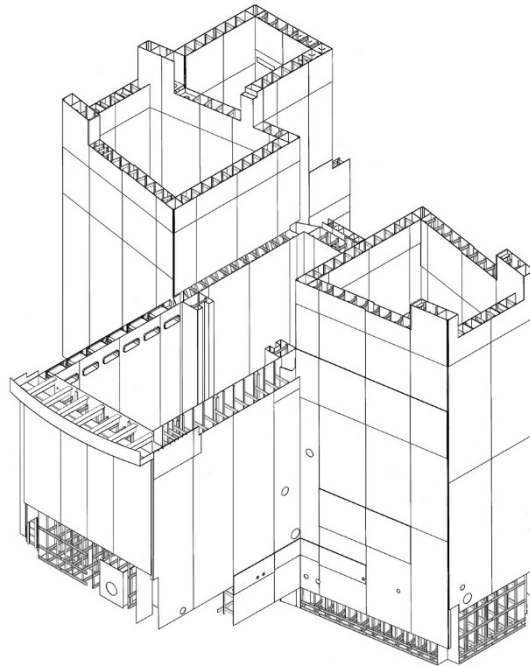
Figure 2.2 Example of large preassembled module in AP1000 plant (from [102]) (©Westinghouse Electric Company, LC. All rights reserved).
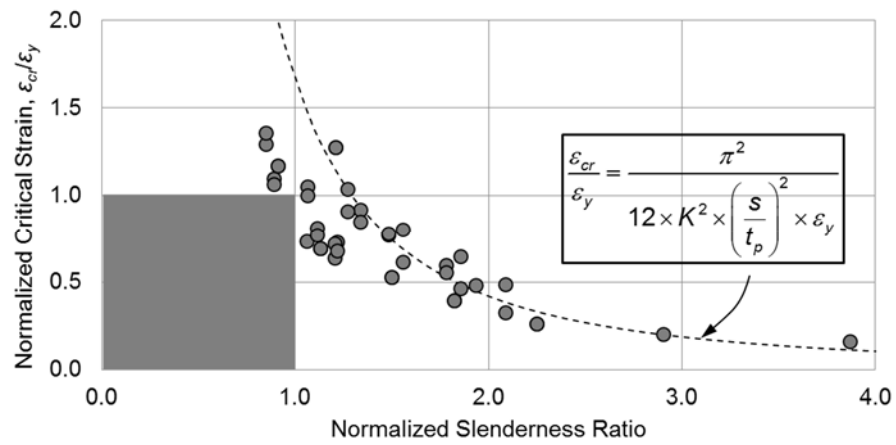
Figure 2.3 Relationship between buckling strain and normalized slenderness ratio, K=0.7 (from [9])
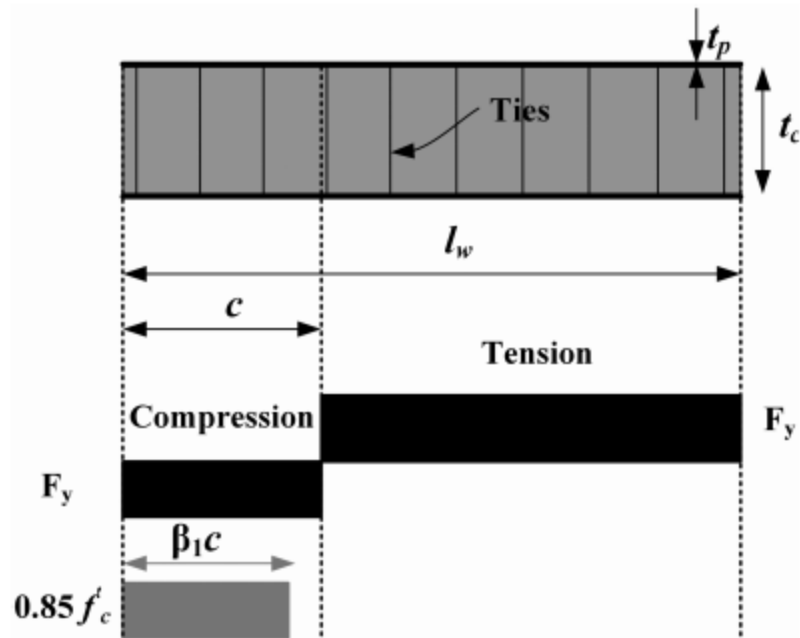
Figure 2.4 Stress distribution assumed in faceplates and concrete infill of SC wall piers for calculation of plastic moment capacity, M_p (from [33])
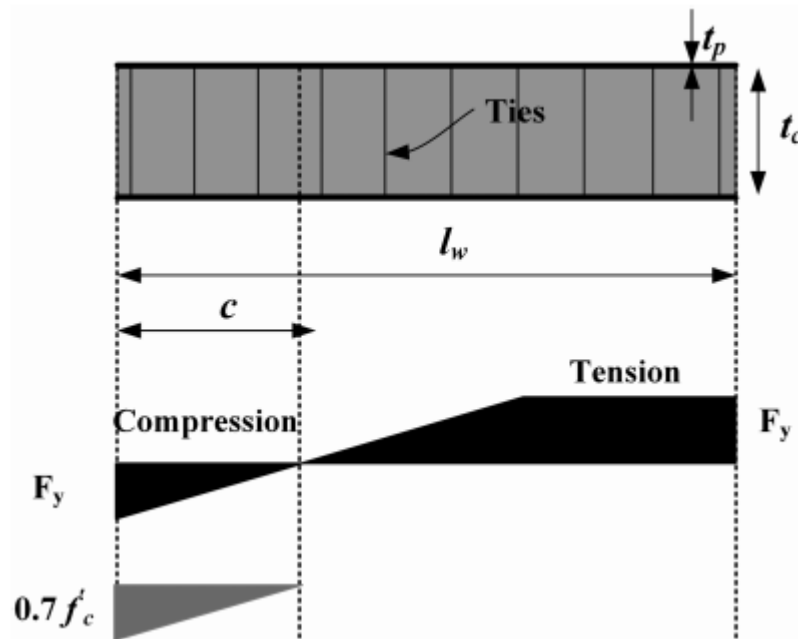
Figure 2.5 Stress distribution assumed in faceplates and concrete infill of SC wall piers for calculation of yield moment capacity, M_{yc} (from [33])
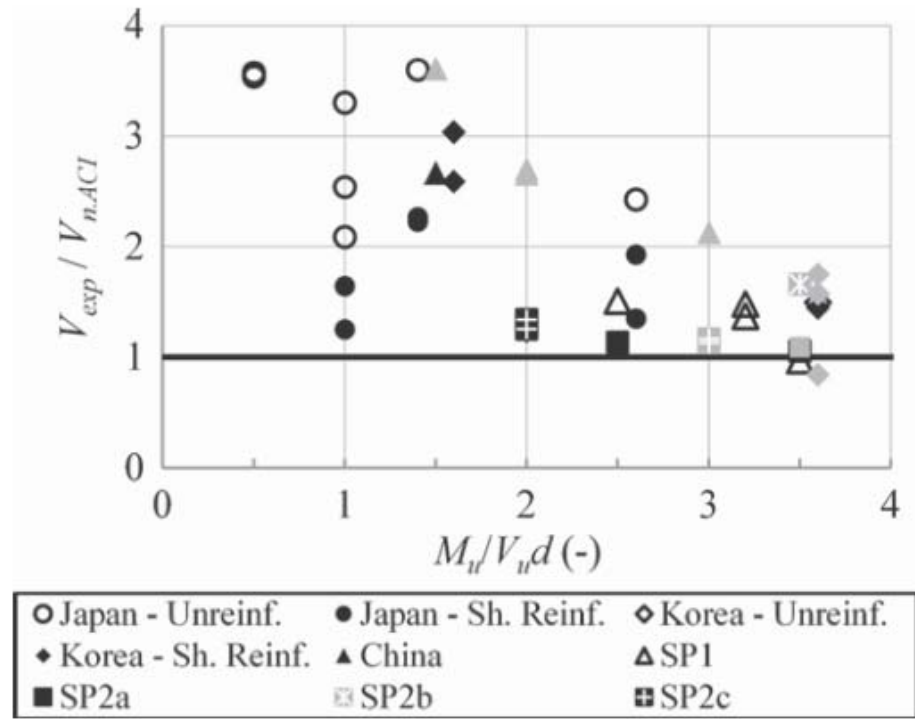
a) Variation with shear span-to-depth ratio
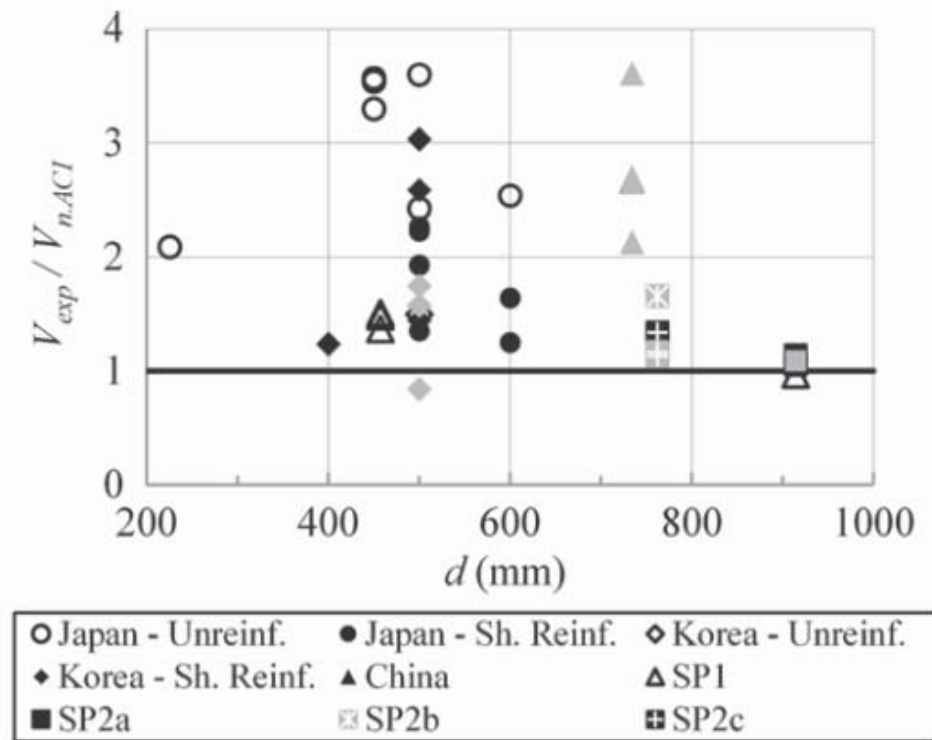
b) Variation with section depth

Figure 2.6 Normalized out-of-plane shear strengths (from [3])
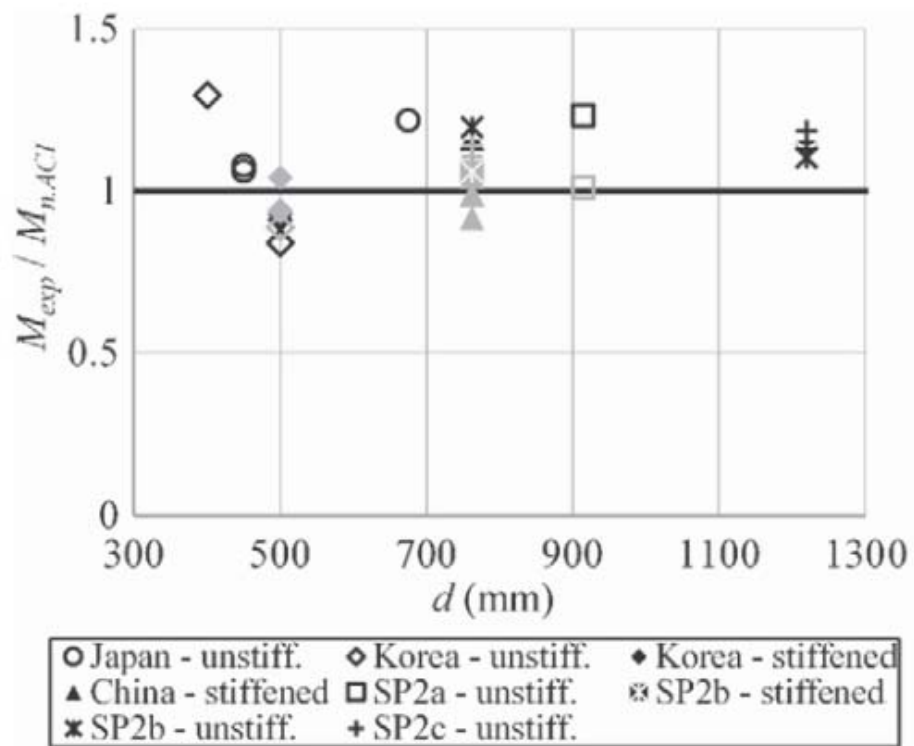
Figure 2.7 Normalized experimental out-of-plane flexural strength (from [2])
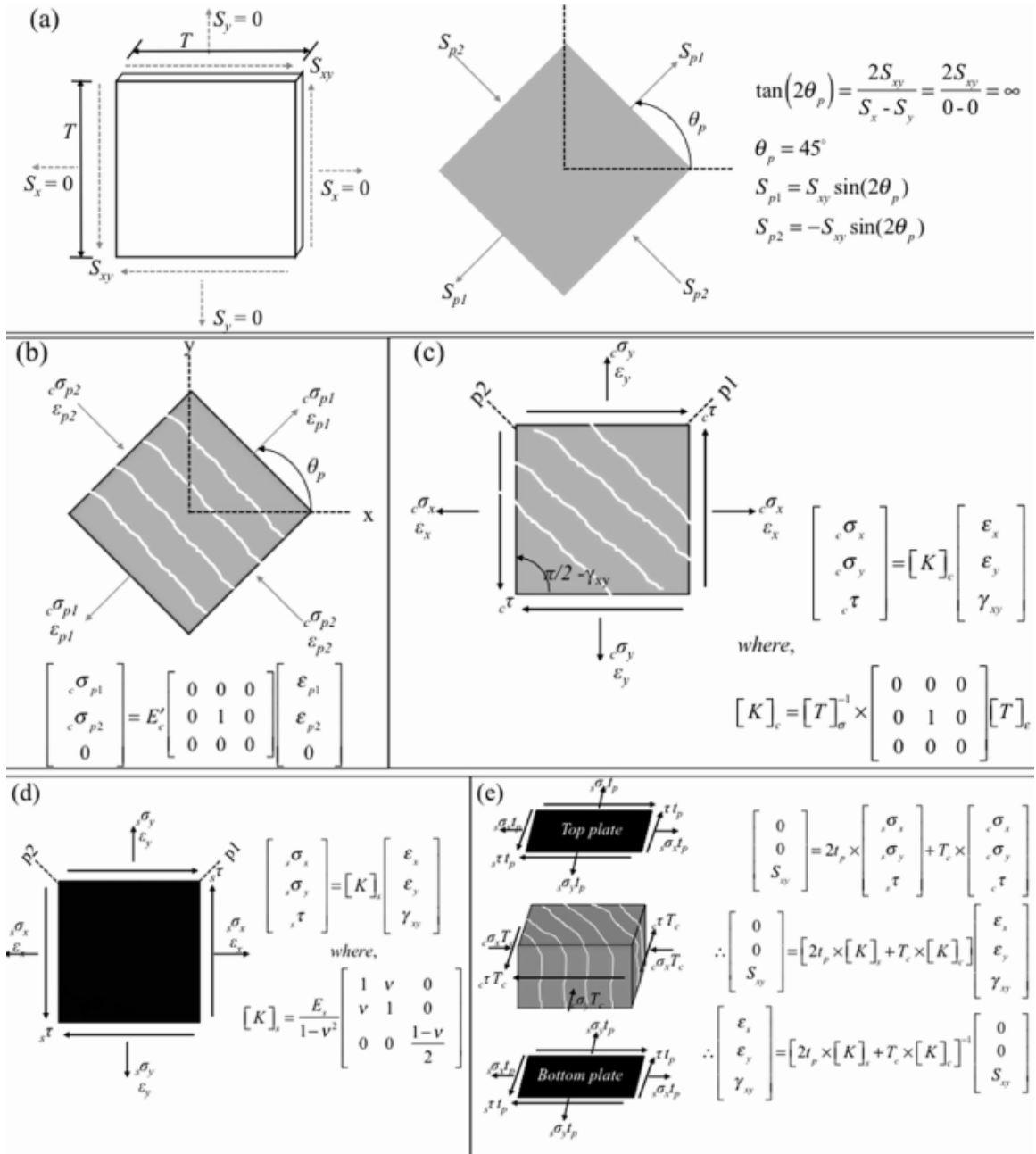
Figure 2.8 Summary of in-plane shear behavior theory (from [8])
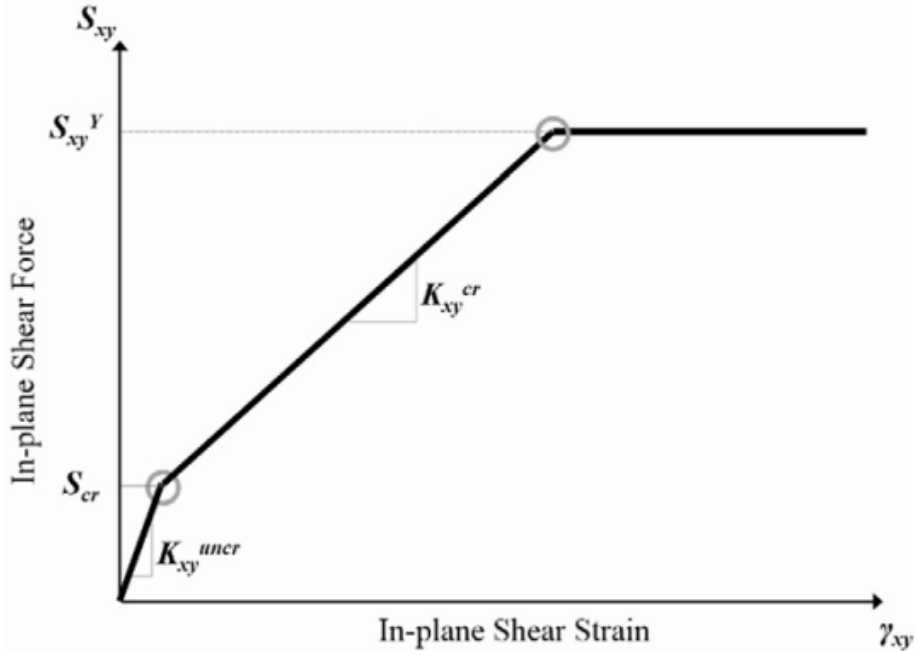
Figure 2.9 MBM based in-plane shear force-shear strain behavior tri-linear model (from [26])
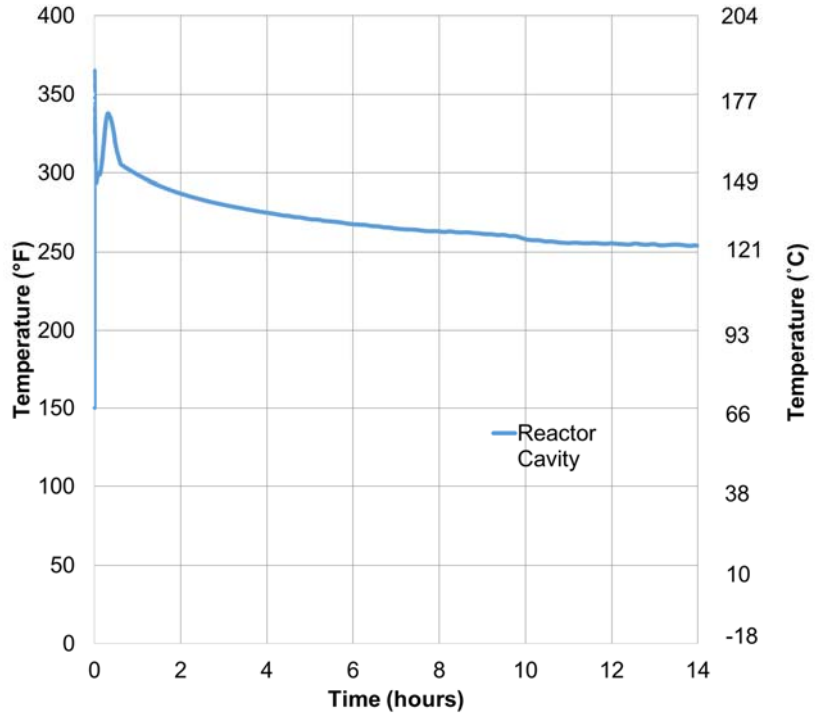
Figure 2.10 Envelope Temperature-time (T-t) history for Reactor Cavity (based on [102], [103])
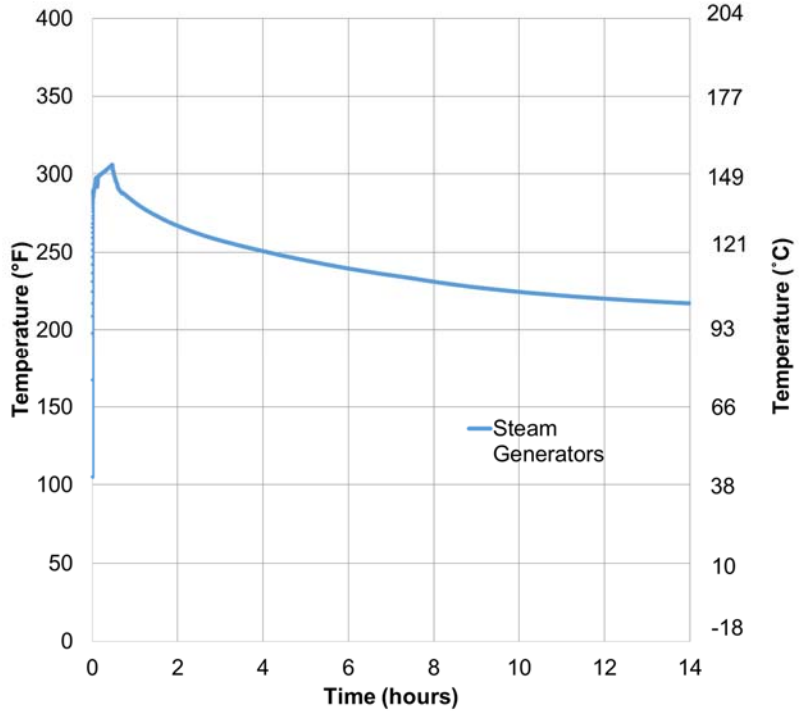
Figure 2.11 Envelope Temperature-time (*T-t*) history for Steam generators (based on [102], [103])
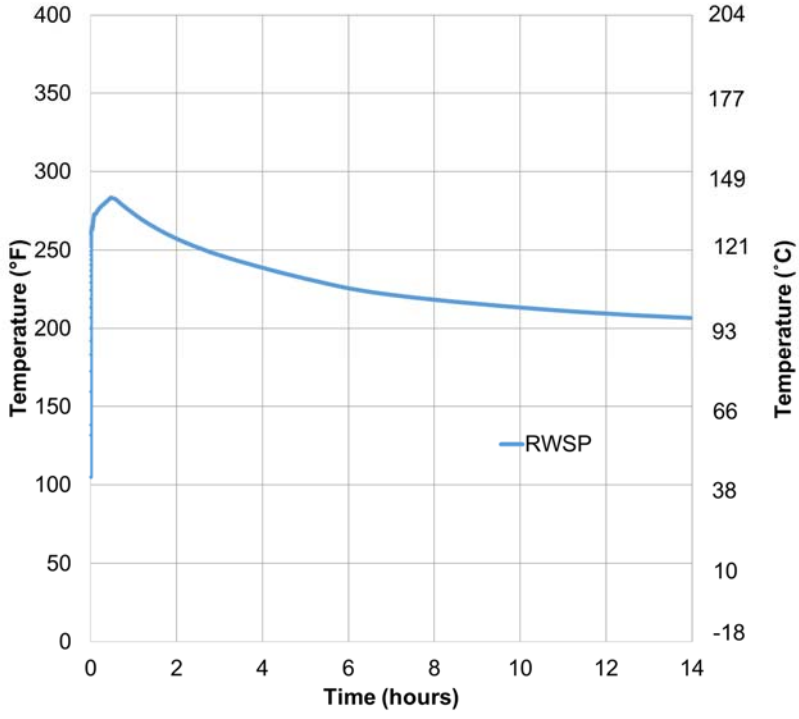
Figure 2.12 Envelope Temperature-time (*T-t*) history for RWSP (based on [102], [103])
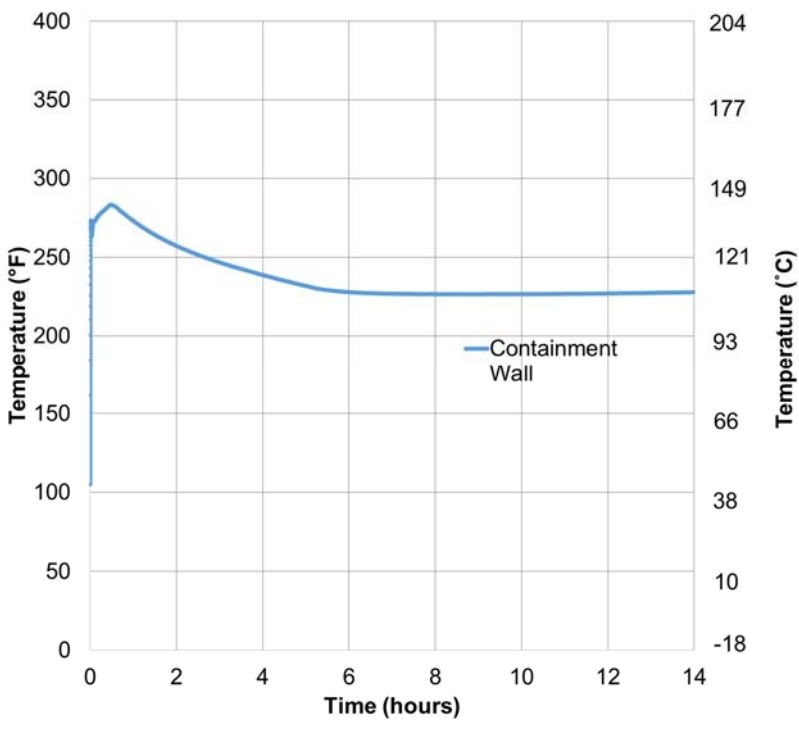
Figure 2.13 Envelope Temperature-time (*T-t*) history for Containment Wall (based on [102], [103])
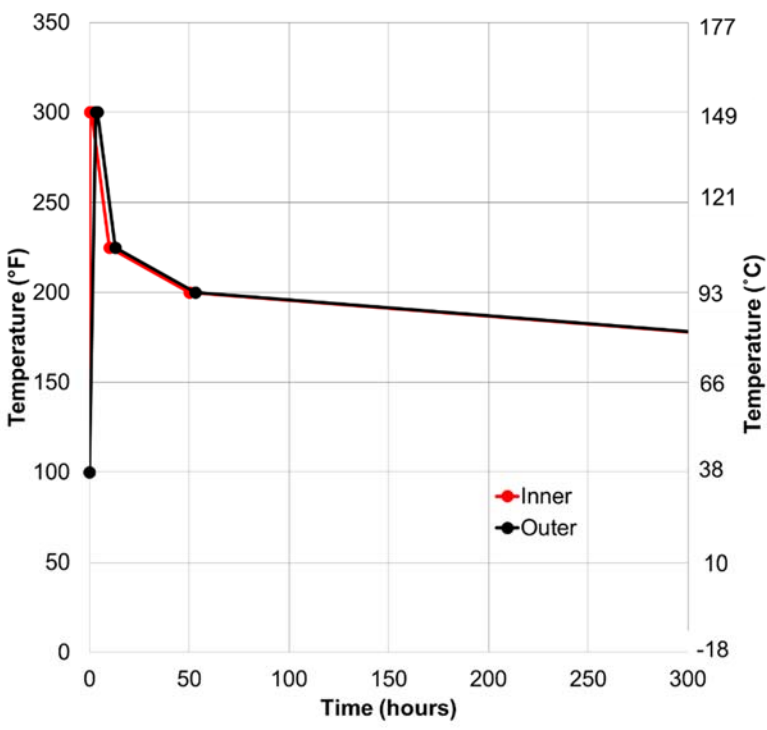
Figure 2.14 Idealized Temperature-time (*T-t*) history for compartment surfaces
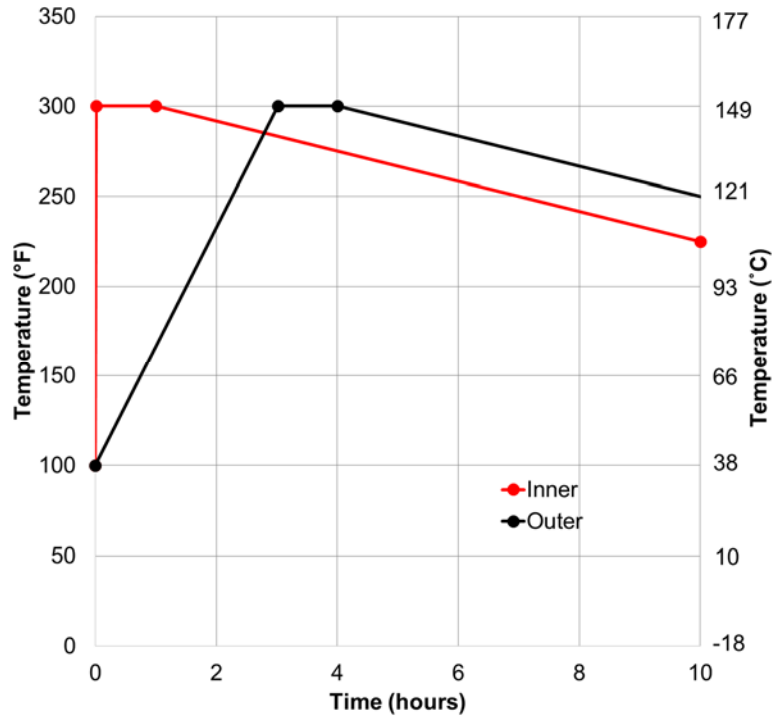
Figure 2.15 Idealized Temperature-time (*T-t*) history for compartment surfaces (zoomed in to first 10 hours)
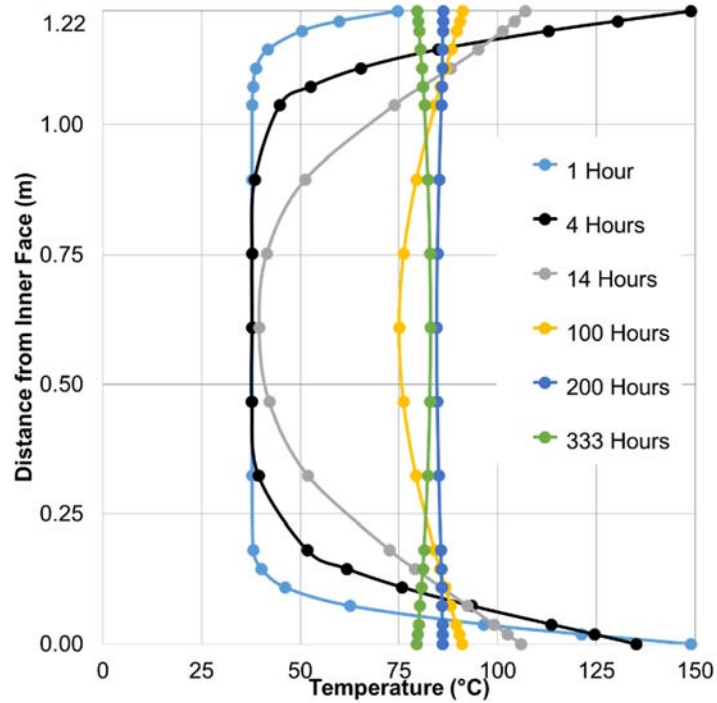
Figure 2.16 Through thickness temperature contours at different time steps
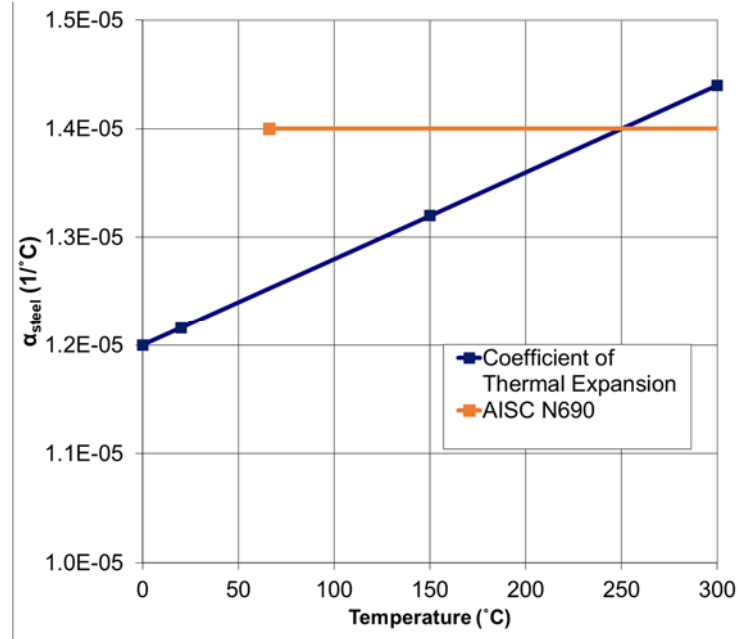
Figure 2.17 Variation of steel coefficient of thermal expansion with temperature (based on [26], [119])
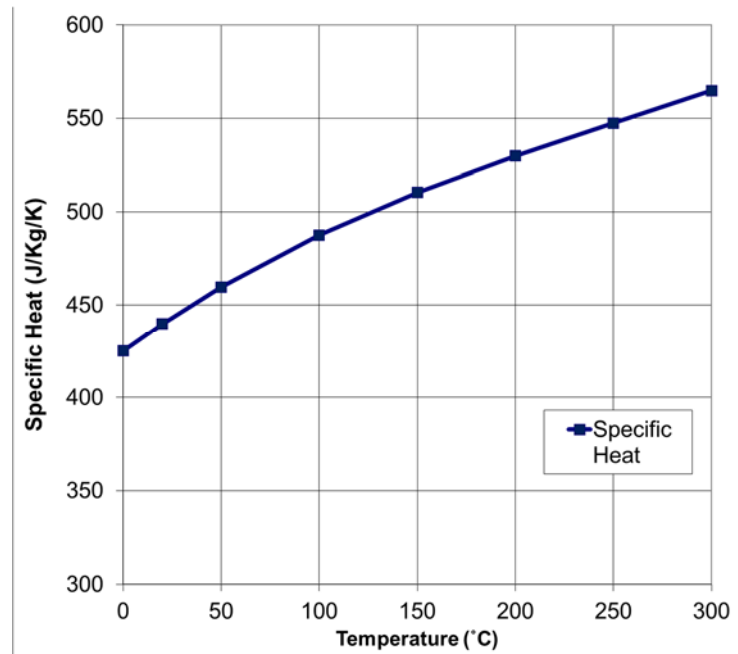
Figure 2.18 Variation of steel specific heat with temperature (based on [119])
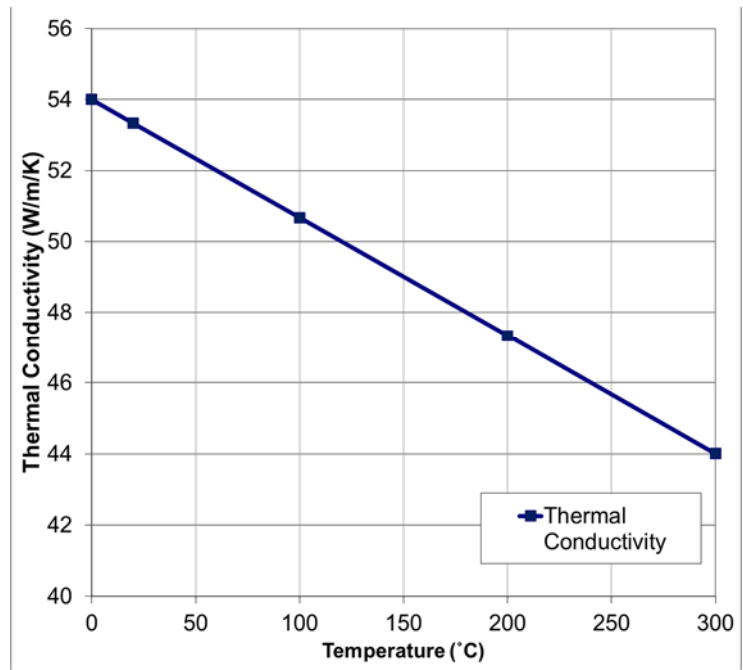
Figure 2.19 Variation of steel thermal conductivity with temperature (based on [119])
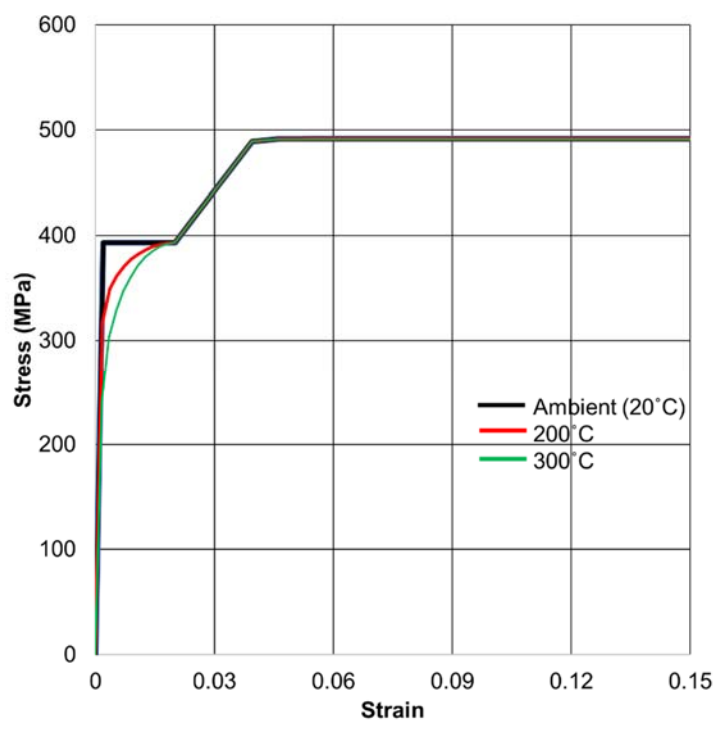
Figure 2.20 Temperature-dependent stress-strain relationship for steel (based on [26], [119]) with measured F_y of 393 MPa
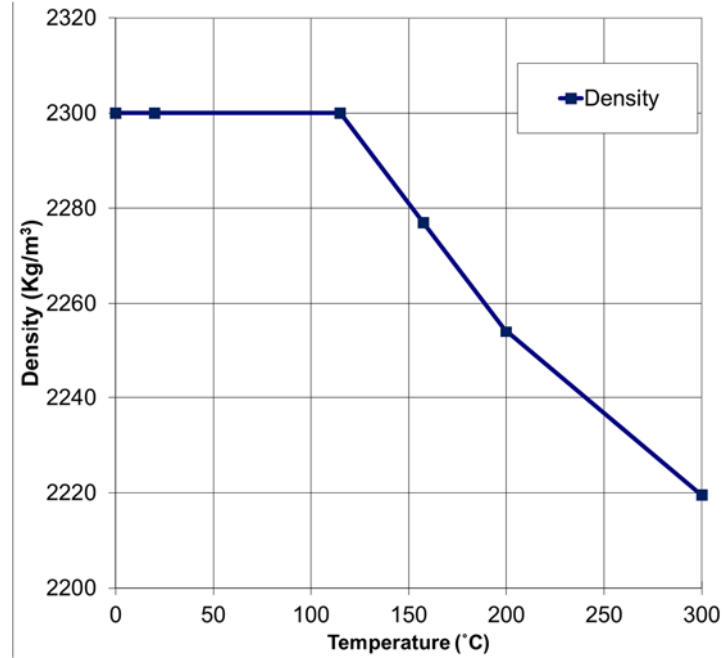
Figure 2.21 Variation of concrete density with temperature (based on [119])
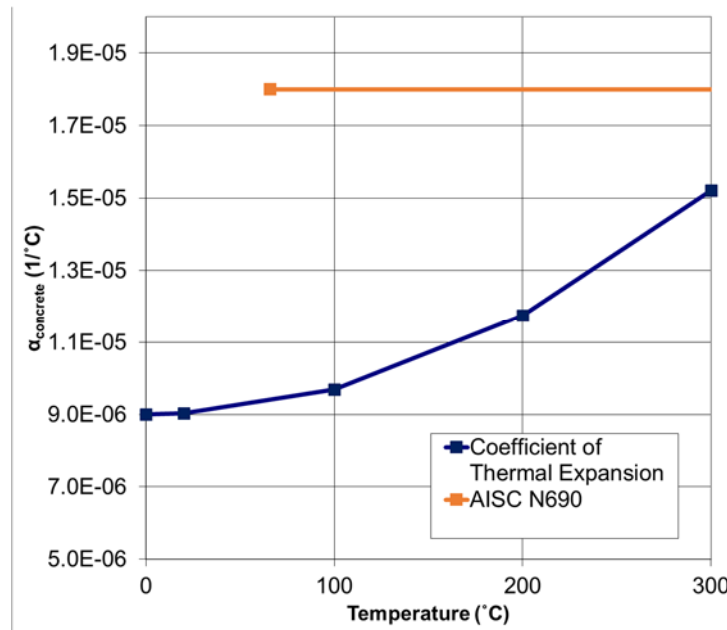
Figure 2.22 Variation of concrete coefficient of thermal expansion with temperature (based on [119], [26])
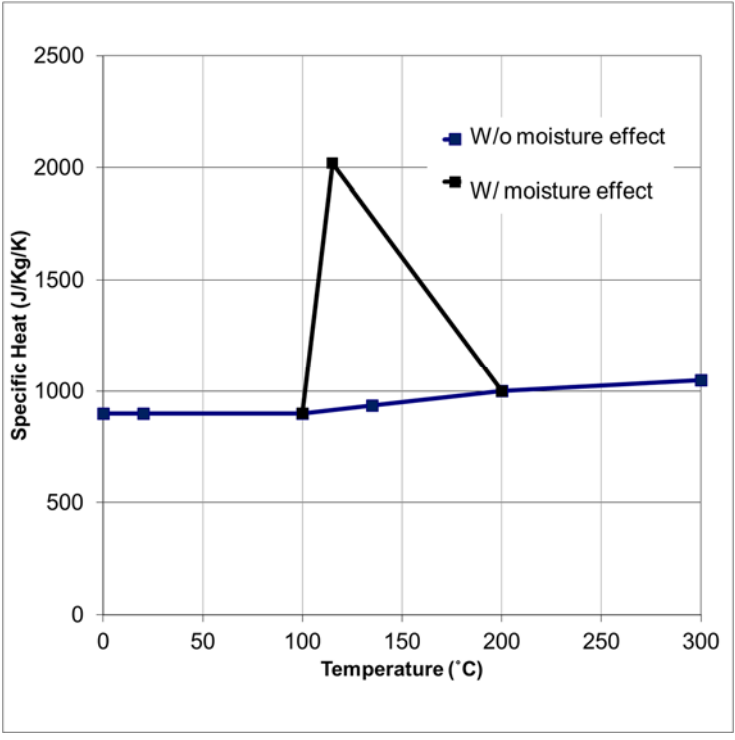
Figure 2.23 Variation of concrete specific heat with temperature (based on [119])
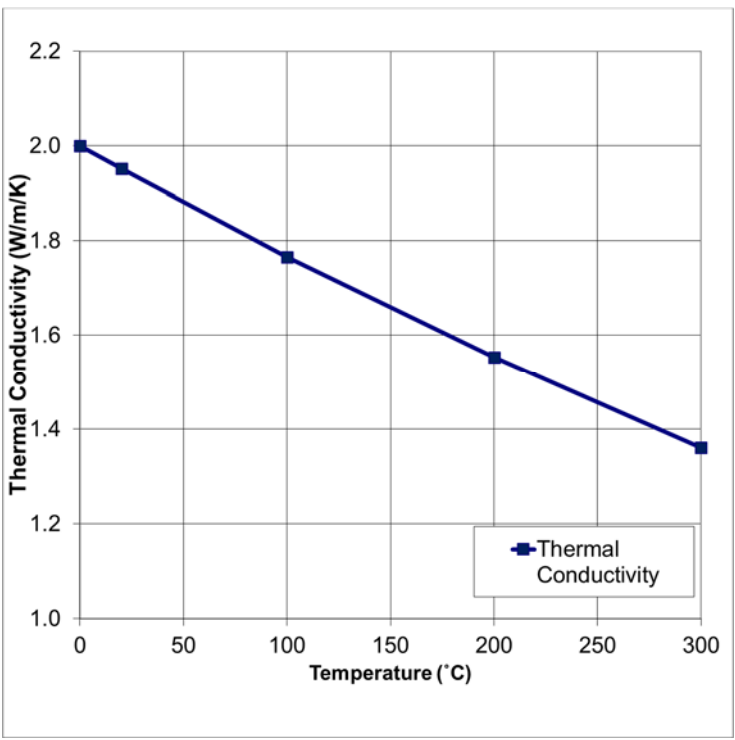
Figure 2.24 Variation of concrete thermal conductivity with temperature (based on [119])
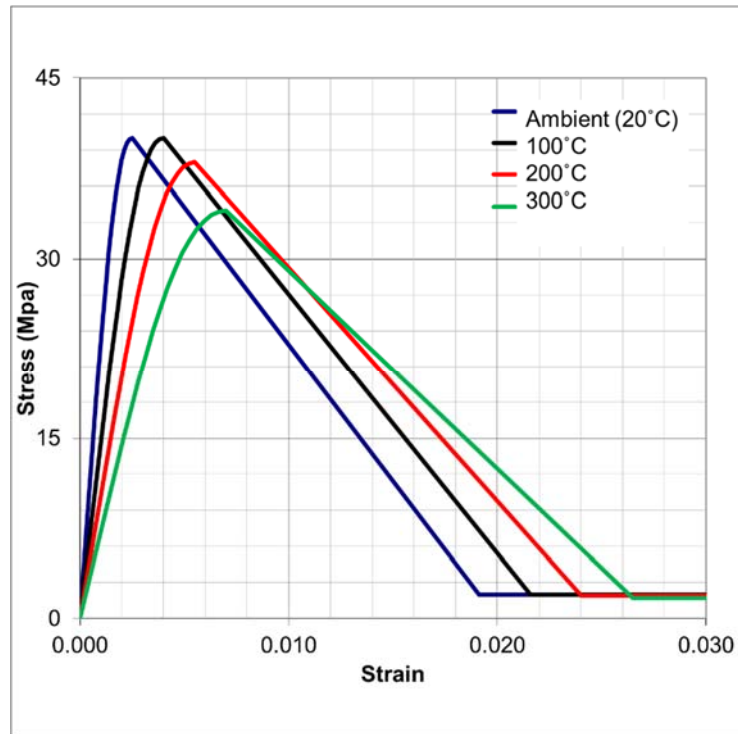
Figure 2.25 Temperature-dependent compression stress-strain relationship for concrete (based on [26], [119]) with measured f'_c of 40 MPa
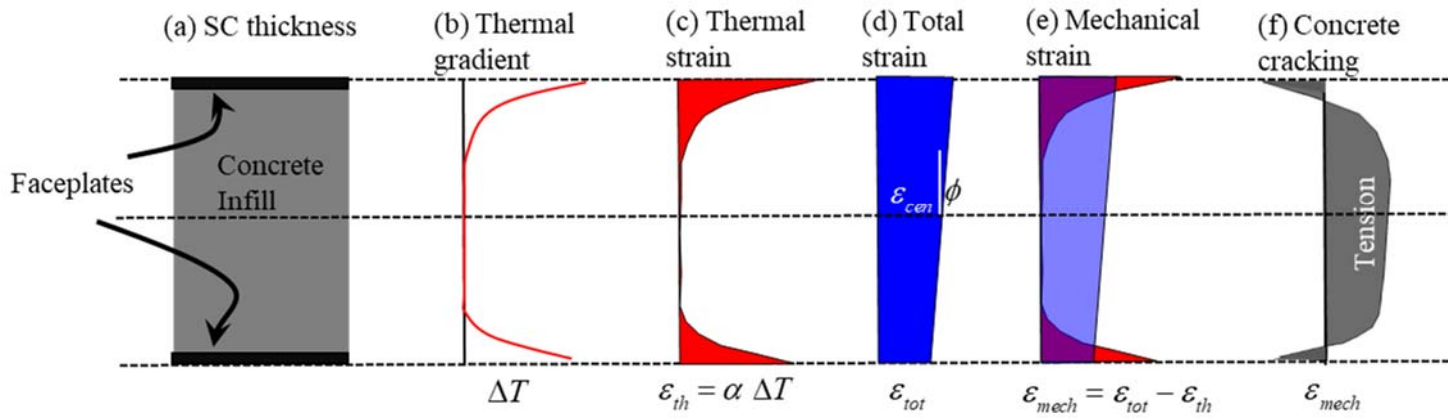
Figure 2.26 Concrete cracking due to through-thickness thermal gradient

3. SC WALL PIERS SUBJECTED TO BIAXIAL LOADING: DESIGN OF EXPERIMENTS

This chapter presents the design of experiments for SC wall piers subjected to biaxial loading (in-plane and out-of-plane forces and moments). Experimental program was developed based on the observed behavior of SC wall piers for individual loadings (discussed in Chapter 2). The specimens were designed to meet the detailing requirements of AISC N690s1 [26].

The chapter is organized into following sections.

- Design of Test Matrix: The specimen details and the basis for selecting the parameters to be varied are discussed in this section.

- Design of Test Setup: This section presents the details of the test setup and the basis of the design.

- Instrumentation of Specimens: The types of instrumentation used, and the measurements recorded for the experiments are discussed in this section.

- Construction Sequence: This section presents the procedure and sequence followed for fabrication and construction of the specimens and the test setup.

- Testing Procedure: Finally, the procedure followed for testing of the specimens is discussed.

3.1 Design of Test Matrix

Specimen details (Table 3.1) and out-of-plane loading details (Table 3.2) were based on the behavior of SC wall piers when subjected to uniaxial loading. The details were finalized based on preliminary numerical analysis presented in Bhardwaj et al. [123]. The effects of variation of parameters and the resulting changes in behavior were studied using benchmarked models

developed in LS-DYNA [91] by Kurt et al. [69]. These analyses indicated that the location of out-of-plane force governs the in-plane capacity of the SC wall piers. As the height of the out-of-plane loading location increases, the corresponding out-of-plane moment becomes large and dominates the overall response. In order to investigate the effects of out-of-plane shear and in-plane shear, the out-of-plane loading location should be kept within a shear span-to-depth ratio of 1 to 2 [123]. Hence, the point of application of out-of-plane loading was kept constant at 457 mm (18 in.) from the base for all specimens, resulting in a shear span-to-depth ratio of 1.5. The parameters varied in the experiments were: i) magnitude of the out-of-plane force applied, and ii) tie spacing.

Table 3.1 shows the specimen details for the experimental investigations. The table presents the specimen height (h), length (l_w), thickness (T), faceplate thickness (t_p), tie diameter (d_{tie}), aspect ratio (h/l_w), reinforcement ratio ($2t_p/T$), stud spacing (s/T), faceplate slenderness ratio (s/t_p), tie spacing (S/T), and day-of-test yield strengths for ties (F_{yt}) and faceplates (F_y), and compressive strength for concrete (f'_c). The specimen height-to-length ratio was kept equal to 0.6 in order to maximize the shear contribution of the wall pier as recommended by Kurt et al. [69]. The specimens were 305 mm (12 in.) thick (1/3 to 1/4 scale of typical SC walls in nuclear facilities), made with 4.8 mm (3/16 in.) steel faceplates, resulting in a plate reinforcement ratio of 0.031. Steel faceplate thickness was set at 4.8 mm because it is the smallest plate thickness in the structural plate category. Smaller thicknesses result in sheet metal properties and associated waviness imperfections which are not representative of the actual structure. Faceplate slenderness ratio was designed to meet the limit recommended by AISC N690s1 [26] to develop faceplate yielding in compression before local buckling, based on Zhang et al. [1]. Figure 3.1 presents the stud and tie layout for specimens SC-T-Vn, SC-T-2.5Vn, and SC-0.5T-Vn. Control specimen (SC-T-C), specimen SC-T-Vn and specimen SC-T-2.5Vn had tie spacing (S) equal to the wall pier thickness

(*T*), which is representative of containment internal structures. Specimen SC-0.5T-Vn had tie

spacing equal to half the wall pier thickness, 0.5*T*.

Table 3.2 presents the out-of-plane loading details of the specimens. The table shows the ACI 349

[25] based out-of-plane shear strength (V_n^{ACI}), AISC N690s1 [26] based out-of-plane flexural

strength (M_n^{AISC}), the ratio of applied out-of-plane shear (V_{oop}) with V_n^{ACI}, and the ratio of resulting

out-of-plane moment at base (M_{oop}) with M_n^{AISC}. For specimens with ties spaced at *T*, V_n^{ACI} will be

equal to concrete contribution, V_c [$2\sqrt{f'_c}\,A_c$ (in psi units), where A_c is the concrete cross-sectional

area]. For specimens with ties spaced at 0.5*T*, V_n^{ACI} will be equal to the sum of concrete

contribution, V_c, and steel contribution, V_s [$A_{st}f_{yt}T/S$, where A_{st} is the area of ties within spacing *S*].

Control specimen (SC-T-C) was not subjected to any out-of-plane (OOP) loading. Specimens SC-

T-Vn and SC-0.5T-Vn were subjected to out-of-plane load (V_{oop}) of magnitude approximately

equal to the out-of-plane shear strength, V_n^{ACI}. For SC-T-Vn, V_{oop} resulted in a base out-of-plane

moment (M_{oop}) equal to 0.37 times the out-of-plane moment capacity (M_n^{AISC}) per AISC N690s1.

For SC-0.5T-Vn the resulting M_{oop} was equal to $0.74M_n^{AISC}$. Specimen SC-T-2.5Vn was subjected

to an out-of-plane force of magnitude about $2.5V_n^{ACI}$ (to force the specimen to fail in vector shear).

Comparison of results from specimens SC-T-C and SC-T-Vn, SC-0.5T-Vn and SC-T-2.5Vn will

present the effect of out-of-plane loading and tie spacing on the in-plane capacity of the wall pier.

The results from specimens SC-T-Vn and SC-T-2.5Vn will be compared to evaluate the influence

of the magnitude of the out-of-plane shear force on the in-plane behavior of the wall pier.

3.2   Design of Test Setup

Setup for the experiments was designed based on the specimen details, design in-plane capacity of

the specimens, and the magnitude of out-of-plane load to be applied. Figure 3.2 presents the 3D

rendering of the test setup with all the components of the test setup. The test assembly with the specimen installed is presented in Figure 3.3. The setup can be categorized as follows.

In-Plane Loading: Cyclic in-plane loading was applied by two double acting hydraulic rams (Enerpac RR50012). The hydraulic rams were each capable of exerting a force of magnitude 565 ton (1130 kips) in push and 314 ton (628 kips) in pull. South end of the rams was connected to an in-plane built-up section through a set of clevises (South Clevis Part North and South Clevis Part South). The in-plane built-up section was post-tensioned to the strong wall using dywidag bars. North end of the in-plane rams was connected to in-plane loading beams through another set of the clevises (North Clevis Part North and North Clevis Part South). The in-plane loading beam applied the load through end bearing and bearing at the holes in the specimens. Since the specimens were to be subjected to combined in-plane and out-of-plane loading, the clevises needed to accommodate deformations in orthogonal directions to prevent any bending stresses in the rams. The clevises were designed and fabricated to accommodate this orthogonal displacement by press-fitting spherical bearings into the clevis holes. Fabrication of the clevises is shown in Figure 3.4. Figure 3.4d shows the clevis with press-fit spherical plain bearings. The spherical plain bearing permits the rotation of the pin that connects two parts of the clevis arrangement, thus enabling orthogonal deformation of the specimens without stressing the rams.

Out-of-plane Loading: Out-of-plane loading was applied by one double acting hydraulic ram (Enerpac RR50012). West end of the ram was connected to an HSS shape through a set of clevises (OOP Clevis West). The HSS shape was braced to the strong floor and bolted to the out-of-plane built-up section. The out-of-plane built-up section was post-tensioned to the strong wall. East end

of the actuator was connected to out-of-plane loading beams through a set of clevises (OOP Clevis East). Stiffness of the out-of-plane loading beams was designed to apply the out-of-plane load uniformly across the length of the specimen. The out-of-plane beams had half-round shapes at the end in contact with the specimens to accommodate the out-of-plane rotation of the specimens. The beams were post-tensioned together to keep them in contact with the specimen. Figure 3.5 shows the fabricated out-of-plane loading beams and the out-of-plane wall box.

Foundation Block and Specimen Connection: The specimens (faceplates without concrete infill) were welded to a re-usable base plate that was centered on top of the foundation block. The faceplate to baseplate connection was designed to be stronger than the wall pier, and limited inelastic action to the wall pier. Details for faceplate-to-baseplate weld are presented in Figure 3.6. The faceplates were prefabricated with a transfer bar welded at the base. The transfer bar was 25.4 mm wide, 38 mm deep (with a 45-degree bevel), and 1524 mm long. The baseplate was 1524 mm long, 543 mm wide, and 25 mm thick. The baseplate had three rows of 9.5 mm diameter shear studs on the top surface to transfer the forces from concrete infill to the baseplate. The baseplate was anchored to the foundation using 85 A706 19 mm dia. (#6) rebars that were 1195 mm long. The rebars were attached to the baseplate using Lenton C3J couplers. The foundation block was post-tensioned to the strong floor. Figure 3.7 presents the plan view of the foundation and baseplate.

3.3 Instrumentation of Specimens

Table 3.3 and Table 3.4 present the measurements taken for in-plane and out-of-plane direction respectively. The basis of the measurements and the instrumentation used to take the measurements are discussed in the tables. Instrumentation layout for the specimens is presented in Figure 3.8, Figure 3.9, and Figure 3.10. Displacement sensors (SPs in Figure 3.8 and Figure 3.9)

were used to measure the in-plane and out-of-plane displacement of the top and bottom of the wall pier. The displacement measurements were used to obtain the in-plane force-displacement response of the specimen, in-plane base slip corrections, and out-of-plane drift and twisting of the specimens. Rotation meters were installed at the base of the wall pier in the in-plane (CM1) and out-of-plane (CM3) direction. Another rotation meter was installed at mid-height of the specimen to observe the out-of-plane rotation at mid-height (CM2). The out-of-plane rotations were used to obtain curvature in the out-of-plane direction. The in-plane rotation data was used to apply base rotation corrections to in-plane displacement. Strain gauges were installed on the faceplates to observe the behavior of faceplates (flexural or shear strains, buckling, yielding) for out-of-plane and in-plane loading. Strain gauge layout for East faceplate is shown in Figure 3.10. The same strain gauge layout was used for West faceplate. Strain gauges were also installed on the corner ties to measure the tensile stresses in ties. Concrete cracks were monitored visually.

3.4   Construction Sequence

Faceplates were fabricated with holes for tie locations, and for threaded bars that connect the in-plane loading beam to the SC wall. These locations are presented in Figure 3.1. The fabricated faceplates also had the beveled transfer bar welded to the bottom (details shown in Figure 3.6). Shear studs were then welded to the faceplates. Figure 3.11 shows the faceplate after the studs had been welded, and before assembling the two steel faceplates to form the empty steel assembly. The beveled transfer bar welded to the bottom of the faceplate, and the holes at tie locations are also visible in the figure. The faceplates (with studs welded) were then assembled together using ties. Figure 3.12 presents the steel assembly before welding the faceplates to the baseplate. Steel pipes were tack-welded to faceplates to leave slots for the threaded bars that connect the in-plane loading beam to the SC specimen. The figure also shows the backup bar tack-welded to the transfer bar at

the bottom of the faceplates. The faceplates had some initial imperfection (out-bow), which was reduced using the arrangement shown in the figure. The arrangement was removed after the steel assembly was tack-welded to the baseplate. Figure 3.13 shows the steel assembly after the faceplates were welded to the baseplates, using flux-cored gas-shielded (Ar-CO2 gas) arc welding technique with 483 MPa (70-ksi) electrode wire. The welding was done in multiple passes, with each new pass beginning at the center of the wall. Figure 3.14 shows the steel assembly before concrete casting. Side plates were tack-welded to the faceplates to serve as formwork for the concrete pour. The side plates were also used during the welding of the baseplate to the faceplates, to limit the out-of-plane expansion of the faceplates due to weld-heat. The side plates were removed after the concrete had cured and gained sufficient strength (approximately 5 days after concrete casting).

3.5   Testing Procedure and Loading Protocol

Figure 3.15 presents the loading protocol for specimens subjected to biaxial loading. Control specimen was subjected to just the in-plane loading protocol. The out-of-plane loading was applied in force control with five incremental cycles until the desired out-of-plane force (V_{oop}) was achieved (with exception of Specimen SC-T-Vn, where two incremental cycles were applied). Out-of-plane loading was then maintained constant and the specimen was subjected to incremental cyclic loading in the in-plane direction. The in-plane load was applied in load control for elastic cycles, and in displacement control for post-yield cycles. The in-plane cyclic loading history is similar to the ATC-24 [124] guidelines for cyclic testing of components of steel structures. Two elastic cycles were conducted under load control at each lateral load level of $0.25P_y$, $0.50P_y$, and $0.75P_y$, where P_y is the expected in-plane load corresponding to compression yield moment (V_{Myc}, based on [69]). For specimens SC-0.5T-Vn and SC-T-2.5Vn, P_y was scaled to account for the

effect of out-of-plane loading, based on Bhardwaj et al. [123]. Secant flexural stiffness (K_{sec}) of the specimen during the first $0.75P_y$ cycle was used to calculate the yield level lateral displacement (Δ_y). K_{sec} was calculated using the average of the recorded lateral displacements at the top of the specimen during the first $0.75P_y$ North and South half-cycles. The yield level lateral displacement (Δ_y) was estimated as P_y divided by K_{sec}. The inelastic cycles were conducted under displacement control at lateral displacement levels of $1.0\Delta_y$, $1.5\Delta_y$, $2.0\Delta_y$, $3.0\Delta_y$. Testing was continued until the specimen failed due to concrete crushing or fracture of the faceplates, or until the lateral load resistance reduced to 50% of the lateral load capacity.

3.6 Chapter Summary

This chapter discussed the design of experiments for SC wall piers subjected to combined in-plane and out-of-plane loading. The test matrix was designed to evaluate the effect of magnitude of out-of-plane loading, and tie spacing on the in-plane response of wall piers. Four SC wall pier specimens were tested. One control specimen (with no out-of-plane loading) and three biaxially loaded specimen were tested. Test setup was designed based on the magnitude of out-of-plane force and expected in-plane strength of the specimens. Clevises with press-fit spherical plain bearings were designed and fabricated to enable orthogonal deformations of the specimens without resulting in stresses in the loading rams. The test measurements recorded, the basis, purpose, and type of instrumentation employed for the measurements are discussed. The fabrication and construction sequence of the test setup and specimens is described. Finally, the chapter presents the loading protocol followed for the experiments. Biaxially loaded specimens were subjected to incremental cyclic out-of-plane loading till the desired out-of-plane force magnitude was achieved. The out-of-plane force magnitude was then maintained, and incremental in-plane cyclic loading was applied up to failure.
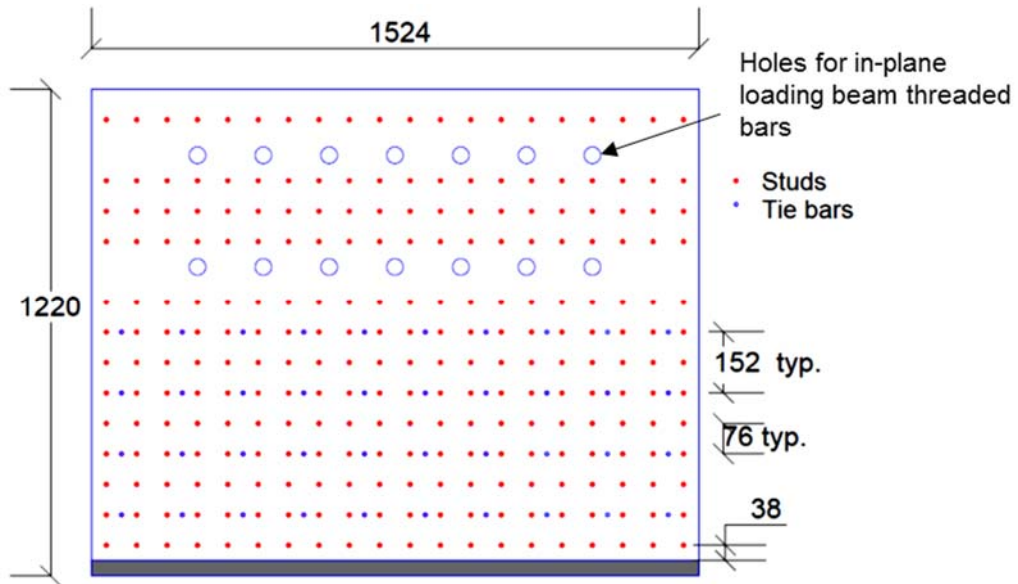
a) Specimen SC-0.5T-Vn (in mm units)
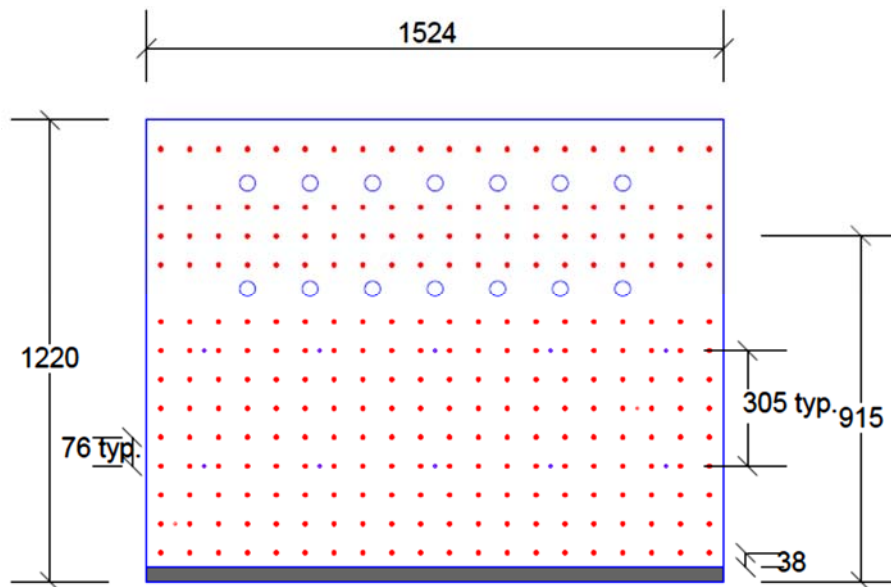
b) Specimens SC-T-Vn and SC-T-2.5Vn (in mm units)

Figure 3.1 Stud and tie layout details
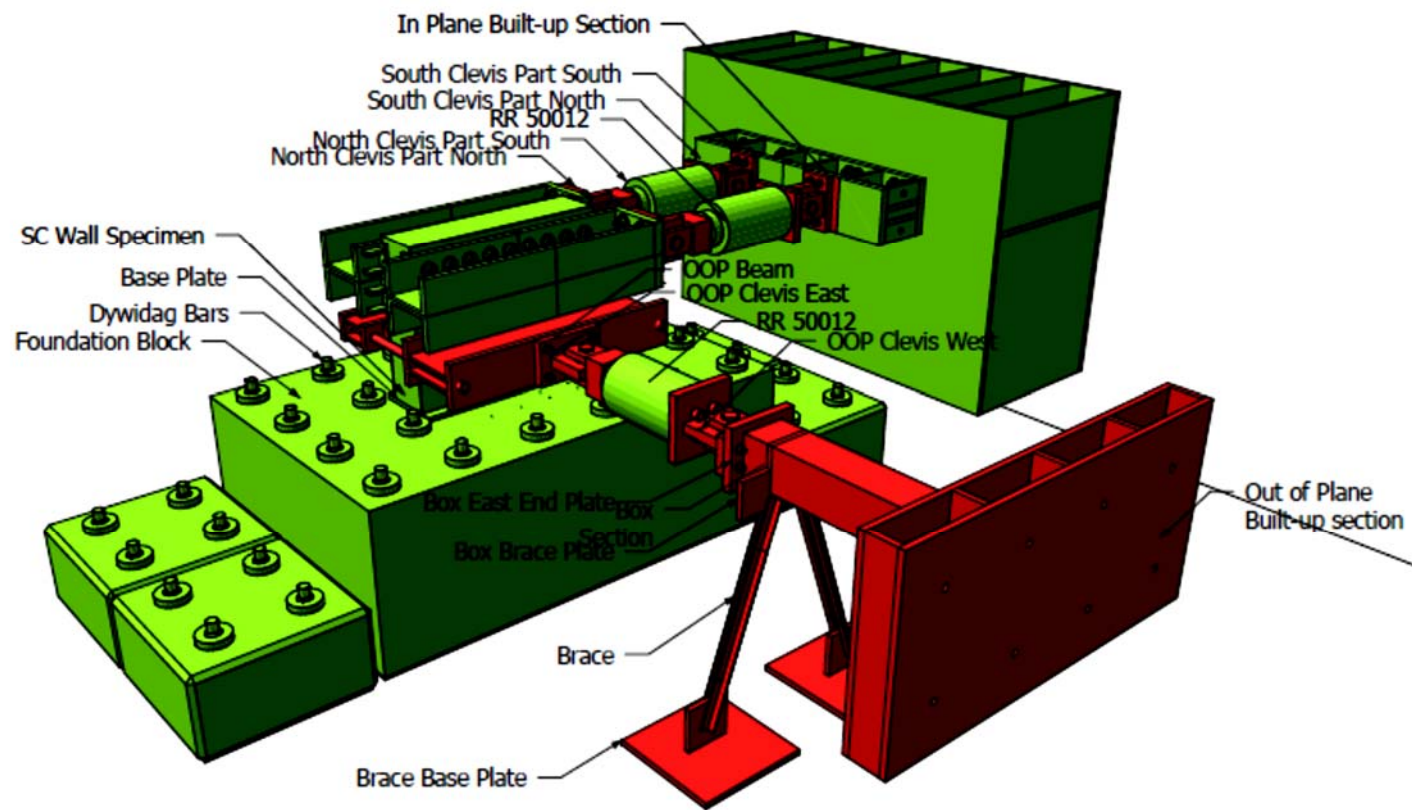
Figure 3.2 3D rendering of the test setup

Figure 3.3 Physical test setup

a) Clevis before welding   b) Pre-heating of clevis for welding

c) Clevis after welding   d) Clevis with press-fitted bearing
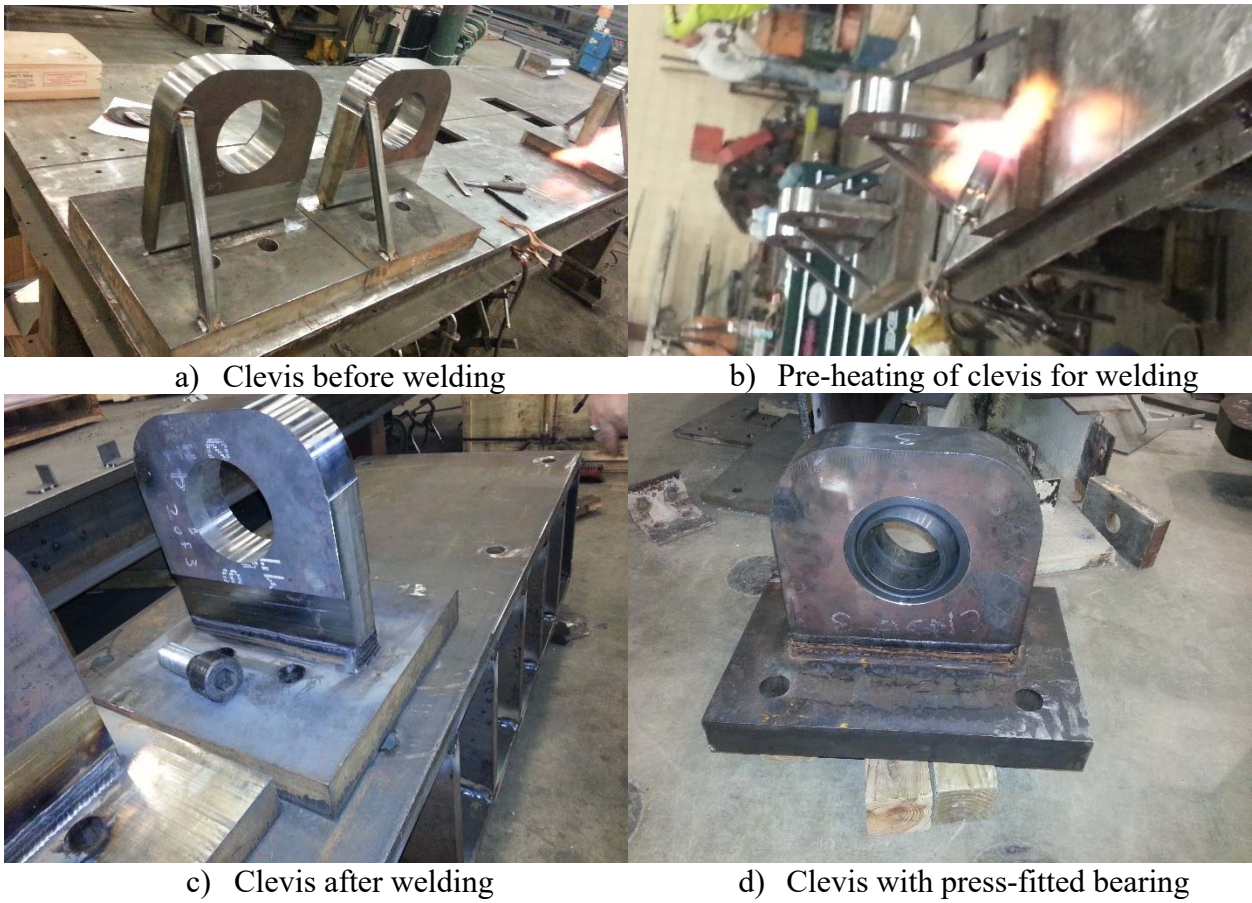
Figure 3.4 Fabrication of clevises

a) Fabricated out-of-plane loading beams

b) Fabricated out-of-plane wall box

Figure 3.5 Components of out-of-plane loading setup
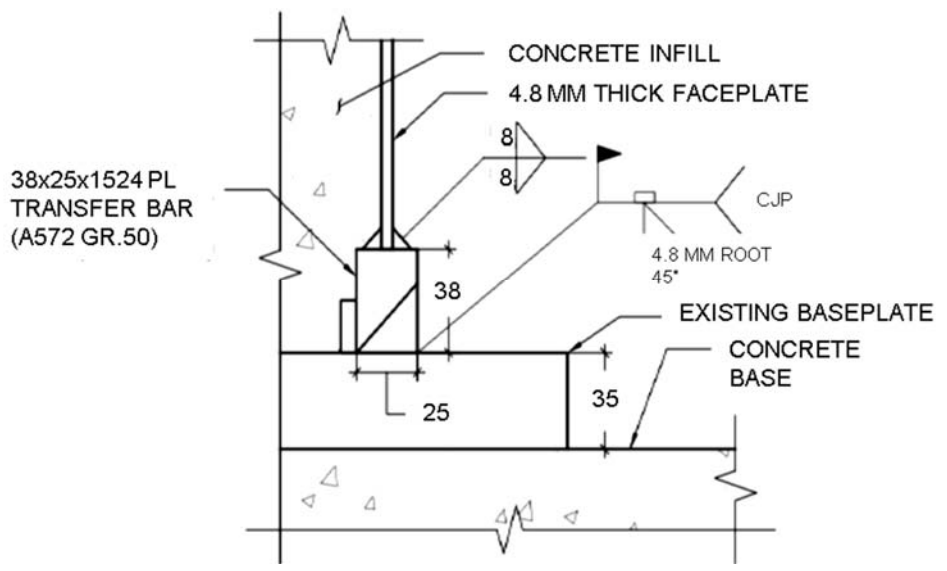
Figure 3.6 Faceplate-to-baseplate weld details (from [33])
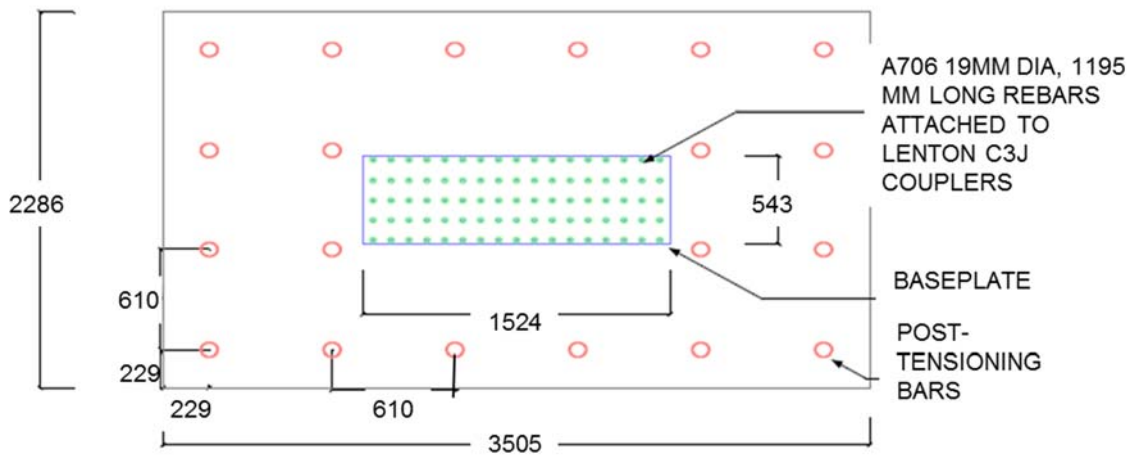
Figure 3.7 Plan view of the foundation and the baseplate (from [33])
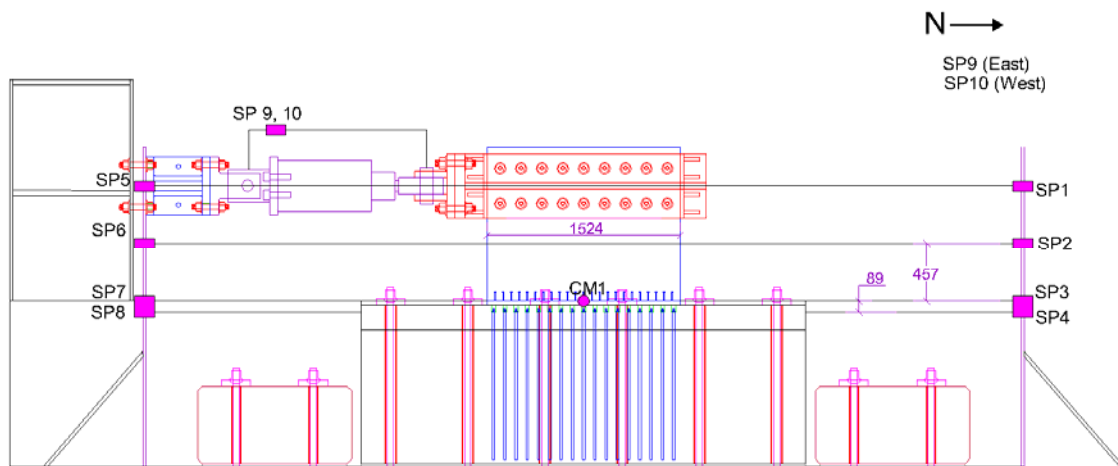
Figure 3.8 In-plane sensors
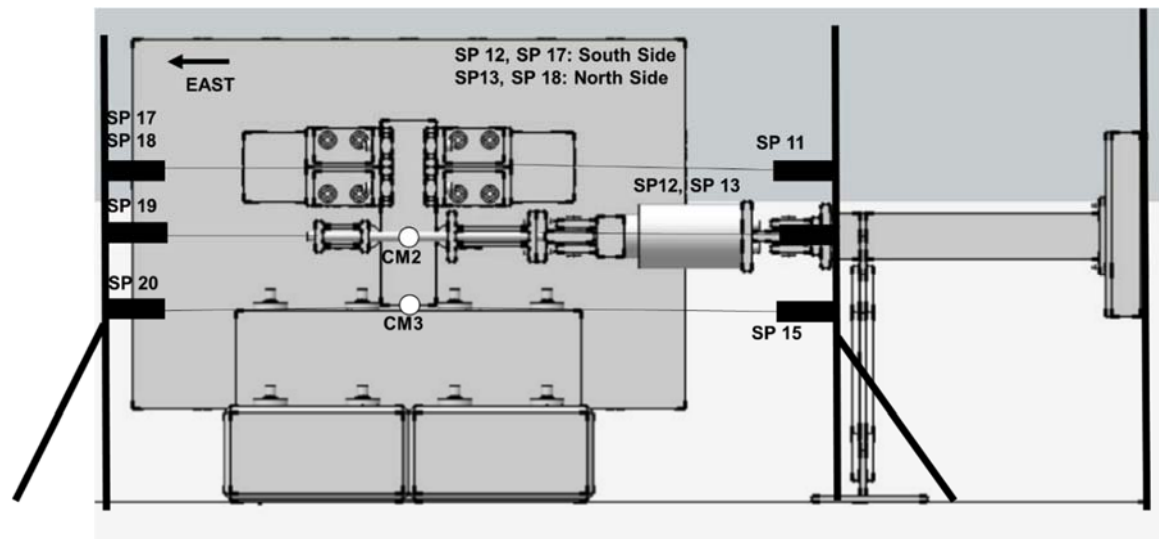
Figure 3.9 Out-of-plane sensors
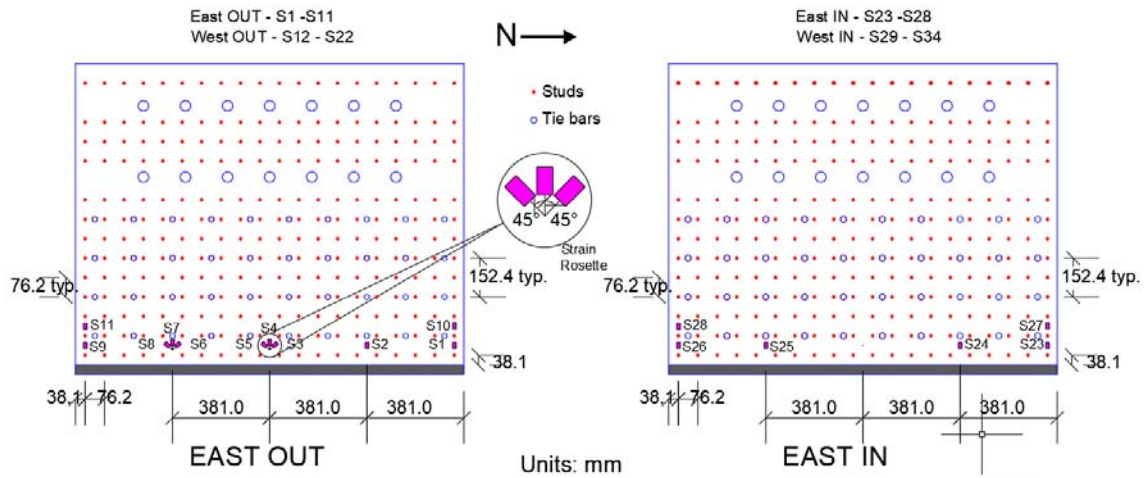
Figure 3.10 Strain gauge layout
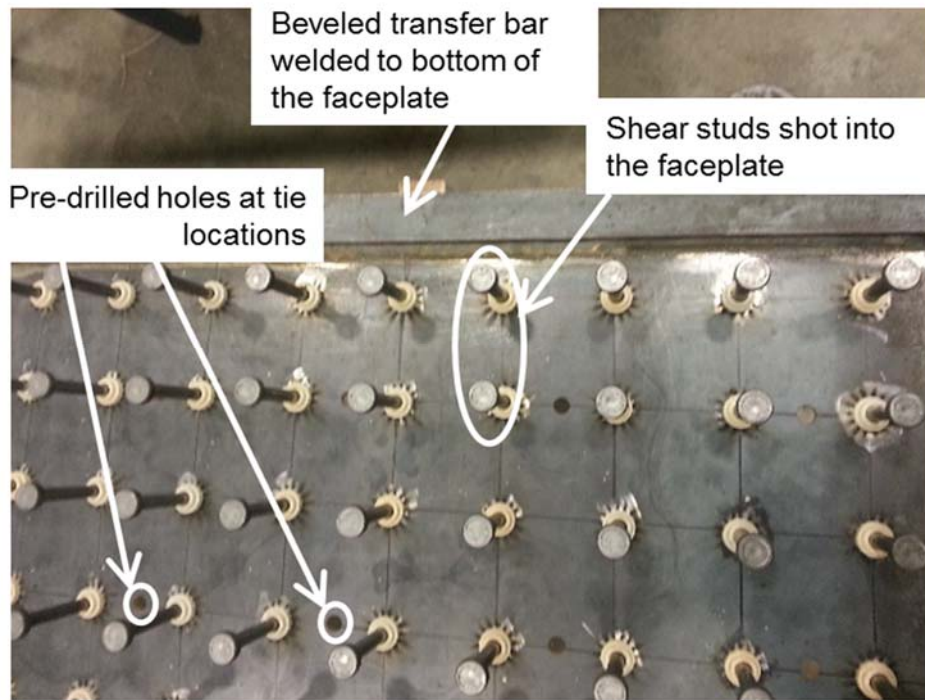
Figure 3.11 Faceplate before assembling the steel
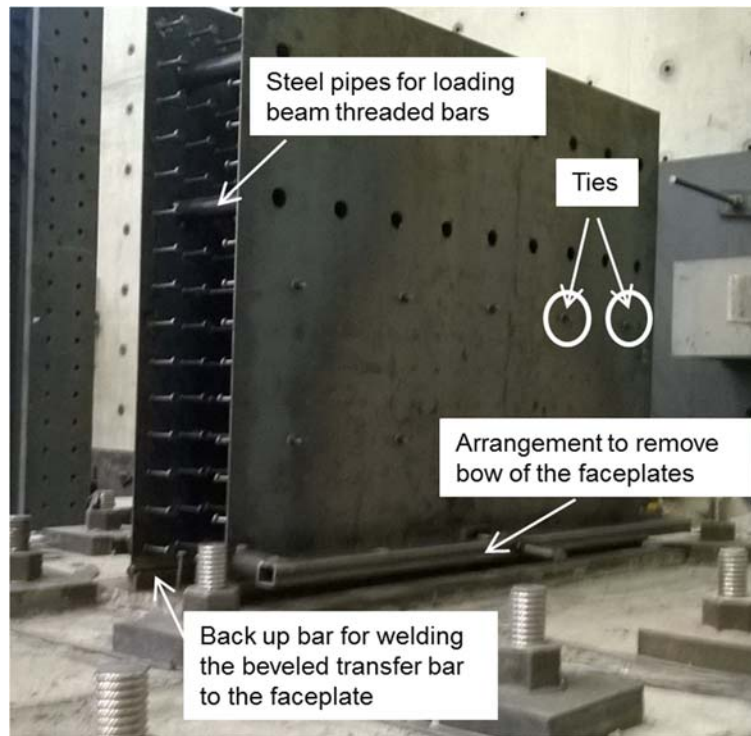
Figure 3.12 Steel assembly before welding

Figure 3.13 Steel assembly after welding

Figure 3.14 Steel assembly before pouring concrete
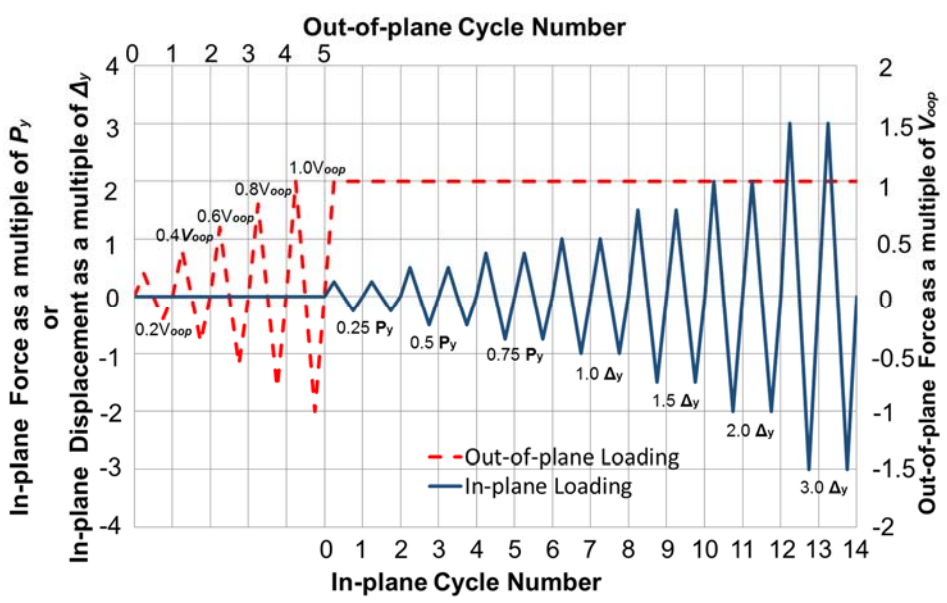
Figure 3.15 In-plane and out-of-plane loading protocol

Table 3.1 Specimen details

Specimen	h (mm)	l_w (mm)	T (mm)	t_p (mm)	d_{tie} (mm)	h/l_w	ρ	$/T$	s/t_p	S/T	Tie F_{yt}, (MPa)	Faceplate F_y (MPa)	Concrete f'_c (MPa)
SC-T-C	914	1524	305	4.8	9.5	0.6	s 0.031	0.33	21	1.0	496	393	40
SC-T-Vn	914	1524	305	4.8	9.5	0.6	0.031	0.25	16	1.0	496	331	53
SC-0.5T-Vn	914	1524	305	4.8	9.5	0.6	0.031	0.25	16	0.5	496	331	36
SC-T-2.5Vn	914	1524	305	4.8	9.5	0.6	0.031	0.25	16	1.0	496	331	36

Table 3.2 Specimen out-of-plane loading details

Specimen	$V_n{}^{ACI}$ (kN)	$M_n{}^{AISC}$ (kN.mm)	$V_{oop}/ V_n{}^{ACI}$	$M_{oop}/ M_n{}^{AISC}$
SC-T-C	473	7.8×10^5	N.A.	N.A.
SC-T-Vn	545	6.6×10^5	0.98	0.37
SC-0.5T-Vn	1041 (1160)*	6.6×10^5	1.03 (0.92)*	0.74
SC-T-2.5Vn	452	6.6×10^5	2.46	0.78

*ACI 349 limits the shear reinforcement yield strength to 414 MPa (60 ksi). The values mentioned are considering the ACI limit. Values mentioned in parenthesis are calculated using the measured yield strength of shear reinforcement, f_{yt} [496 MPa (72 ksi)].

Table 3.3 In-plane measurements

Measurement	Need for the measurement	Instrumentation used
In-plane force	To obtain the in-plane force-displacement response of the specimen	Pressure transducers were mounted on the hydraulic rams to measure the push and pull pressure, which was multiplied by calibration factor for the ram to obtain the push and pull force
Displacement @ a) Top of the foundation block b) Baseplate c) Out-of-plane loading Location d) Top of the specimen	a) To obtain the in-plane force-displacement response of the specimen b) To obtain base slip data	String pots (SP, displacement sensors) employed.
Rotation @ Base of the wall	a) To obtain the in-plane base rotation data b) To correct the in-plane displacements for base rotation	Clinometer (CM, rotation-meter) at the base of the wall
Strains: a) Longitudinal Strain (vertical) at the base of the wall b) Shear strain at the base of the wall	a) To obtain the in-plane neutral axis location b) To observe the yielding and buckling of the faceplates c) To determine the shear strains at the center of the wall	a) Stain gauges (S) installed at the base of the faceplates, inside and outside. b) At the center of the wall, rectangular strain gauge rosettes installed to determine the shear strains

Table 3.4 Out-of-plane measurements

Measurement	Need for the measurement	Instrumentation used
Out-of-plane force	To obtain the out-of-plane force-displacement response of the specimen	Pressure transducers were mounted on the hydraulic rams to measure the push and pull pressure, which was multiplied by calibration factor for the ram to obtain the push and pull force
Displacement @ a) Top of the foundation block b) Baseplate c) Out-of-plane loading Location d) Top of the specimen	a) To obtain the out-of-plane force-displacement response of the specimen b) To obtain base slip data c) To verify the out-of-plane rotation and curvature data for the wall (obtained from clinometers) d) To assess the out-of-plane twisting of the wall	String pots (SP, displacement sensors) employed.
Rotation@ a)Out-of-plane loading location b) Base of the wall	a) To obtain the out-of-plane moment-curvature response, and stiffness of the wall	Clinometers (CM, rotation-meter) installed at the base of the wall, and at the out-of-plane loading location
Strains: a) Longitudinal Strain (vertical) at the base of the wall b) Longitudinal strain in the ties	a) To obtain the out-of-plane neutral axis location b) To observe the yielding and buckling of the faceplates and the twisting behavior of the wall c) To measure force in tie bars due to out-of-plane loading	a) Stain gauges (S) installed at the base of the faceplates, inside and outside. b) Strain gauges installed on the corner tie bars
Concrete cracking: a) Observe cracking of the concrete	To determine the out-of-plane load at which concrete develops diagonal shear cracks	Visual inspection and marking of the cracks

4. SC STRUCTURES SUBJECTED TO BIAXIAL LOADING: EXPERIMENTAL RESULTS

Experimental studies were conducted to evaluate the effect of out-of-plane forces on the in-plane response of SC wall piers. Four SC wall pier specimens were tested. One specimen (control specimen) was subjected to cyclic in-plane loading (no out-of-plane loading). The experimental results for control specimen were discussed in detail by Kurt [33] (Specimen SC 8). The experimental observations for control specimen are summarized in this chapter. The remaining specimens were subjected to different magnitudes of out-of-plane loading in combination with cyclic in-plane loading.

This chapter presents the experimentally observed behavior of the specimens (for in-plane and out-of-plane loading). The measured day-of-test properties of the specimens are summarized in Table 3.1. Concrete uniaxial compressive strength was obtained from cylinders cast at the same time as the specimen. The cylinders were 100 mm in diameter and 200 mm in height and were tested in accordance with ASTM C39 [125]. Concrete strengths presented in the table are the average strengths obtained from cylinders on the day of testing. Faceplate strength was obtained from tension coupons prepared from samples taken, and tested. The average of faceplate strengths obtained from the tests are mentioned in the table. To evaluate the effect of out-of-plane loading and tie spacing, the response of control specimen (not subjected to out-of-plane loading) is briefly discussed. The specimens with biaxial loading are then discussed. The results are employed to evaluate the effect of out-of-plane forces on the in-plane behavior of SC wall piers.

The chapter is organized into following sections.

- SC-T-C: In-plane response of control specimen (with no out-of-plane loading) is summarized.

- SC-0.5T-Vn: Out-of-plane and in-plane response of specimen with ties spaced at half the section thickness, and subjected to an out-of-plane loading of magnitude equal to its nominal out-of-plane shear strength are presented.

- SC-T-Vn: Out-of-plane and in-plane response of specimen with ties spaced at section thickness, and subjected to an out-of-plane loading of magnitude equal to its nominal out-of-plane shear strength are presented.

- SC-T-2.5Vn: Out-of-plane and in-plane response of specimen with ties spaced at section thickness, and subjected to an out-of-plane loading of magnitude equal to 2.5 times its nominal out-of-plane shear strength are presented.

- Evaluation of wall pier behavior: The out-of-plane and in-plane behavior of wall pier specimens are evaluated and compared to each other.

4.1 SC-T-C

Specimen SC-T-C was subjected to cyclic in-plane loading. In-plane force-top displacement response of the specimen is presented in Figure 4.1. Detailed experimental evaluation of the specimen is presented in Kurt et al. [69] and Kurt [33] (specimen SC 8). Failure load for the specimen was measured as 3200-kN (720 kips) on North-direction (+). Measured peak load value in the South direction (-) was 3030-kN (680 kips), giving an average failure load for in-plane shear as 3115-kN. The peak in-plane force was approximately equal to the force corresponding to compression yield moment for the specimen (V_{Myc}). Figure 4.1 also presents the progression of damage in the specimen. Flexural failure of the specimen was initiated by crushing and spalling of the concrete in compression, accompanied by local buckling of the steel plates in compression, and base metal (faceplate) weld rupture. The specimen did not reach its plastic moment capacity due to the weld rupture.

4.2   SC-0.5T-Vn

Specimen SC-0.5T-Vn (with ties spaced at 0.5T) was subjected to an incremental cyclic out-of-plane load of magnitude 1070-kN (240 kips) [approximately equal to V_n^{ACI}]. The out-of-plane loading was then maintained constant, and the specimen was subjected to incremental in-plane load cycles. The out-of-plane and in-plane behavior of the specimen is discussed in this section.

4.2.1   Out-of-plane Behavior

Specimen SC-0.5T-Vn was subjected to incremental out-of-plane loading cycles (133, 267, 400, 534, 1070-kN). The out-of-plane load was then maintained constant at 1070-kN. Figure 4.2 shows the moment-faceplate vertical normal strain relationship for the 1070-kN load cycles [moment is calculated at the strain gauge location (76 mm from the base) corresponding to the applied out-of-plane force]. Faceplate strains exceed the concrete cracking strain [130 µε, considering concrete modulus of rupture to be $7.5\sqrt{f_c'}$, in psi units]. Concrete cracking is also apparent from the difference in faceplate tension and compression strains for the same magnitude of out-of-plane moment. However, the faceplate strains do not exceed the yield strain (1650 µε). Diagonal shear cracks were observed in the specimen during the 1070-kN load cycle [at a load magnitude of about 980-kN (220 kips)]. Diagonal shear cracking of the concrete (as shown in Figure 4.3) is expected to engage the out-of-plane shear reinforcement (ties). The behavior is confirmed by ties (Figure 4.4), as the ties start experiencing tensile strains at an out-of-plane force of about 890-kN (200 kips).

Cracking of concrete under out-of-plane loading (as observed in Figure 4.2 and Figure 4.3) will reduce the out-of-plane flexural stiffness of the SC specimen. Out-of-plane moment-curvature response of specimen SC-0.5T-Vn is presented in Figure 4.5 (for the load cycle of 1070-kN). The out-of-plane curvature is obtained from clinometer rotation data (CM2 and CM3 in Figure 3.9).

Curvature is calculated from measured rotations using the central difference method. Out-of-plane moment is calculated at 229 mm (9 in.) from the base (the location where the curvature is obtained from the central difference method). The out-of-plane cracking moment corresponding to a concrete cracking strain of 130 $\mu\varepsilon$ [$M_{cr\text{-}oop}$, 14x10^4 kN-mm (1240 kip-in.)], and the moment corresponding to out-of-plane shear strength per ACI 349 [25] [$M_{Vn\text{-}oop}$, 24.4x10^4 kN-mm (2160 kip-in)] are also plotted in the figure. The moment-curvature response can be separated into two regions, Region 1 with stiffness close to uncracked stiffness [$E_sI_s+E_cI_c$, 1.6x10^{11} kN-mm^2 (5.54x10^7 kip-in^2)], and Region 2 with stiffness close to cracked-transformed stiffness [$E_sI_s+c_2E_cI_c$, 0.85x10^{11} kN-mm^2 (2.94x10^7 kip-in^2), per AISC N690s1 [26] Equation A-N9-8]. It is observed that the stiffness changes from Region 1 to Region 2 for moment values approximately equal to $M_{cr\text{-}oop}$. Ratio of the stiffness observed experimentally, with the calculated cracked (for Region 2) and uncracked (for Region 1) stiffnesses is also presented in Figure 4.5. The stiffness for Push Region 1 matches the uncracked stiffness. A higher magnitude of shear force (1070-kN) results in additional damage to the specimen, i.e. formation of diagonal shear cracks, which results in the stiffness for Region 2 being even lower than the calculated cracked transformed stiffness. The higher magnitude of pull force (-1070 kN) results in cross-diagonal shear cracks, which further reduces the stiffnesses for the pull cycle that follows.

4.2.2 In-plane Behavior

With the out-of-plane loading maintained constant at 1070-kN, the specimen was subjected to incremental cyclic in-plane loading per the loading protocol discussed previously. Figure 4.6 shows the in-plane force-top displacement response of SC-0.5T-Vn. Average strength of SC-0.5T-Vn was 2738-kN [+2760/-2715 kN (+620/-610 kips)]. Response of the specimen is compared with that of SC-T-C (Control specimen) in Figure 4.7. Applied in-plane force (V_{app}) is normalized with

force corresponding to compression yield moment (V_{Myc}) for the specimens. While the average strength of SC-0.5T-Vn (2738-kN) was about 15% lower than the peak strength of specimen SC-T-C (3115-kN), the normalized strengths of the two specimens were similar (approximately equal to V_{Myc}). Therefore, the out-of-plane force (corresponding to M_{oop} equal to $0.74M_n^{AISC}$) did not result in a significant reduction in the in-plane moment capacity (the specimen reached its compression yield moment capacity). The failure drift for both the specimens was similar (about 1.12%).

Figure 4.8 to Figure 4.16 show the progression of damage for yield and post-yield cycles. The diagonal cracks (formed during the 1070-kN out-of-plane loading cycle) widened with increased in-plane loading, and additional diagonal cracks were observed for elastic cycles (as marked in Figure 4.8). Widening of diagonal cracks and initiation of faceplate buckling (on north end of west faceplate) was observed during the $1.5\Delta_y$ cycles (Figure 4.9). The specimen also started to drift in the out-of-plane direction, with large residual out-of-plane deformations. Buckling was observed for both the faceplates, along with extensive widening of shear cracks, and large out-of-plane deformations, during the $2\Delta_y$ cycles (Figure 4.10 to Figure 4.13). Concrete spalling was observed at the end of the $2\Delta_y$ cycles (Figure 4.13). The specimen failed during the $3\Delta_y$ cycle due to extensive buckling, concrete spalling, and significant out-of-plane deformations (Figure 4.14). Unlike the control specimen (which had symmetric behavior), specimen SC-0.5T-Vn experienced extensive twisting, large residual out-of-plane drifts, and the behavior was asymmetric. The ties experienced additional tensile stresses due to the asymmetric behavior, and this was confirmed by the rupture of a corner tie at the end of the test (as seen in Figure 4.15 and Figure 4.16).

Sustained out-of-plane loading resulted in tensile strains on the West side faceplate (around 1000 $\mu\epsilon$, as observed in S12 and S20 from Figure 4.2) and compressive strains on the East side faceplate.

Figure 4.17 and Figure 4.18 show the faceplate strain plots for $0.25P_y$ and Δ_y loading cycles. The asymmetric strain distribution due to the combination of in-plane and out-of-plane loading is apparent in the figures. The West plate strain gauges (S12 and S20) had an initial strain (with no in-plane force) of about 1000 $\mu\varepsilon$ (shown as ε_{oop} in Figure 4.17). The in-plane loading resulted in strains of opposing nature (tensile vs compressive) on the North and South ends of the wall pier [e.g., S12 and S20 are both on the West plate, but S12 is at South end and S20 is at North end, so they both had similar initial strain (ε_{oop}) due to out-of-plane loading, but experienced opposing strains due to in-plane loading]. The additional strain due to out-of-plane loading, coupled with asymmetric behavior for combined loading, lead to initiation of yielding at south-west corner of faceplate (S12 in Figure 4.17) for an in-plane force of about 670-kN (150 kips). In control specimen, initiation of faceplate yielding was observed around 2970-kN (550 kips). Figure 4.18 shows that the faceplate strains for the Δ_y cycle were well beyond yielding strains. However, the asymmetric behavior was still maintained (West plate strains were higher than East plate strains). Damage to the wall pier at the end of the test (Figure 4.14) highlights the asymmetric behavior and large residual out-of-plane drifts for incremental in-plane loading. The behavior was verified using the experimental measurements. Figure 4.19 shows the twisting of the specimen (at mid-height and top) when incremental in-plane loads (only push (+) half-cycles are plotted) were applied (with out-of-plane force maintained constant). The figure shows the plan view of the wall pier cross-section, with the wall pier thickness (305 mm) along the horizontal axis, and wall pier length (1524 mm) along the vertical axis. For clarity, the out-of-plane deformations are amplified ten times. The out-of-plane deformations were obtained from string pots installed at the top and mid-height of the specimens (SP 12, 13, 17, 18 in Figure 3.9). It is observed that the specimen underwent twisting out-of-plane when incremental in-plane loads were applied. The direction of twist reversed when

the direction of loading was reversed. Additionally, the twist (and resulting residual out-of-plane drifts) increased drastically in the post-yield cycles, and the peak out-of-plane drift of magnitude 25 mm (1 in.) was observed during the $2\Delta_y$ cycle. The residual out-of-plane drift at failure ($3\Delta_y$ push cycle) was 61mm (2.4 in.). Figure 4.20 shows the evolution of neutral axis of the wall pier cross-section (at 76 mm from the base, the strain gauge location) for incremental in-plane loading (only push (+) cycles are plotted in combination with sustained out-of-plane loading). The neutral axis location was determined based on the faceplate strain gauge data. It is observed that the neutral axis rotated counter-clockwise and moved towards the North corner of the wall pier as incremental push (+) in-plane loading subjected South end to tensile strains and North end to compressive strains. Similar twisting and evolution of neutral axis behavior was observed for the pull (-) half cycles of in-plane loading.

4.3   SC-T-Vn

The specimen (with ties spaced at section thickness, T), was subjected to incremental cycles of out-of-plane loading (267, 534-kN). Out-of-plane load was then maintained constant at 534-kN, and the specimen was subjected to in-plane loading cycles.

4.3.1   Out-of-plane Behavior

No diagonal shear cracks were observed in the specimen for the out-of-plane loading cycles. This is because, for a shear span to depth ratio of 1.5, the concrete contribution to out-of-plane strength is expected to be greater than $2\sqrt{f_c'}\,A_c$ (in psi units), and the magnitude of out-of-plane load [534-kN, corresponding to $2\sqrt{f_c'}$ (in psi units)] does not exceed the concrete contribution. Figure 4.21 shows the East (S1 and S9) and West (S12 and S20) faceplate strains during to the out-of-plane force cycle of 534-kN. It is observed that the faceplate strains exceed the concrete cracking strain

(130 με) for both the push and pull directions. However, the magnitude of strains is significantly lower than the faceplate strains for SC-0.5T-Vn (around 1000 με for constant out-of-plane loading of 1070-kN). Since no diagonal shear cracks were observed (and the ties are spaced at section thickness), the out-of-plane loading is not expected to engage the ties. This is confirmed in Figure 4.22, where the S35 (strain gauge at tie on North side) and S37 (strain gauge at tie on South edge) show no tensile strains as the specimen is subjected to 534-kN out-of-plane loading cycle.

No diagonal shear cracks are observed in SC-T-Vn. However, flexural cracking (as seen in Figure 4.21) will reduce the out-of-plane flexural stiffness of the SC specimen. Out-of-plane moment-curvature response of specimen SC-T-Vn is presented in Figure 4.23 (for the load cycle of 534-kN). The out-of-plane curvature is obtained from clinometer rotation data (CM2 and CM3 in Figure 3.9). Curvature is calculated from the measured rotations using central difference method. Out-of-plane moment is calculated at 254 mm (10 in.) from the base (the location where the curvature is obtained from central difference method). Lines with slopes corresponding to uncracked stiffness, EI_{uncr}, [Region 1, $E_sI_s+E_cI_c$, 1.8×10^{11} kN-mm^2 (6.2×10^7 kip-in^2)], and cracked-transformed stiffness, EI_{eff}, [Region 2, $E_sI_s+c_2E_cI_c$, 0.86×10^{11} kN-mm^2 (3.0×10^7 kip-in^2), per AISC N690s1 [26] Equation A-N9-8] are also plotted in the figure. Since the out-of-plane moment [11×10^4 kN-mm (975 kip-in)] is less than the out-of-plane cracking moment corresponding to concrete cracking strain of 130 με [$M_{cr\text{-}oop}$, 16×10^4 kN-mm (1388 kip-in.)], the flexural stiffness of the specimen is close to uncracked stiffness (Region 1). Ratio of the stiffness observed experimentally, with the calculated uncracked (for Region 1) stiffness is also presented in Figure 4.23. Stiffness for Push Region 1 is 0.8 times the uncracked stiffness. Additional flexural cracking in the 534-kN push cycle reduces the Pull region 1 stiffness further to 0.64 times the uncracked stiffness.

4.3.2 In-plane Behavior

With the out-of-plane loading maintained constant at 534-kN, the specimen was subjected to incremental cyclic in-plane loading per the loading protocol discussed previously. Figure 4.24 shows the in-plane force-top displacement response of SC-T-Vn. Average peak strength of SC-T-Vn is 3180 kN [+3200/3160 kN (+720 kips/-710 kips)]. Response of the specimen is compared with SC-T-C (Control specimen) in Figure 4.25. While the average strength of SC-T-Vn (3180-kN) is approximately same as that of specimen SC-T-C (3115-kN), the normalized strength of SC-T-Vn (about $1.10V_{Myc}$, or $0.98V_{Mp}$) is higher [SC-T-C failed due to base metal (faceplate) weld failure and could not reach its plastic moment capacity]. Therefore, the out-of-plane force (corresponding to M_{oop} equal to $0.37M_n^{AISC}$) did not result in a significant reduction in in-plane moment capacity (SC-T-Vn reached its plastic moment capacity). Post-peak response of the specimen is also similar to the control specimen. The specimen failed at a drift ratio of (+/-) 1.5%.

The specimen behavior was similar to SC-T-C. Figure 4.26 to Figure 4.32 show the progression of damage in the specimen for the yield and post-yield cycles. For the Δ_y cycle (Figure 4.26), there was no significant damage in the specimen. There was flexural cracking at the base of the specimen and beneath the out-of-plane loading location. Vertical crack along the stud line was observed on the North face of the specimen for $1.5\Delta_y$ cycle (as seen in Figure 4.27a), and the flexural cracks at the base started widening. Additional diagonal shear cracking was observed on the South face of the specimen (Figure 4.27b). Faceplate buckling was observed during the $2\Delta_y$ cycles (Figure 4.28a, Figure 4.29b, and Figure 4.30a). Extensive opening of the concrete cracks occurred (Figure 4.28b, Figure 4.29a, and Figure 4.30b). Out-of-plane deformation of the specimen was apparent. Concrete spalling was observed in the second $2\Delta_y$ cycle (Figure 4.30). The specimen failed in $3\Delta_y$ cycle due to extensive faceplate buckling and concrete spalling (no weld rupture in the specimen). Specimen state at failure is shown in Figure 4.31 and Figure 4.32.

Lower magnitude of sustained out-of-plane loading (in comparison to SC-0.5T-Vn) resulted in lower tensile strains on the West side faceplate (around 300 $\mu\varepsilon$, as observed in S12 and S20 from Figure 4.21, in comparison to 1000 $\mu\varepsilon$ observed for SC-0.5T-Vn). Figure 4.33 and Figure 4.34 show the faceplate strain plots for $0.75P_y$ and $1.5\Delta_y$ loading cycles. Figure 4.33 shows that the initial faceplate strain due to sustained out-of-plane loading does not affect the faceplate yielding significantly. All the strain gauges reach yield strain around 1870-kN (400-kip) force. This is considerably higher than the force corresponding to initiation of faceplate yielding in SC-0.5T-Vn [around 670-kN (150 kips)]. However, the force is lower than that observed in the control specimen [around 2450-kN (550 kips)]. Therefore, the magnitude of out-of-plane moment (resulting from the out-of-plane force) affects the initiation of yielding of faceplates, as the out-of-plane loading results in additional strains in the faceplates. Figure 4.34 shows the faceplate strains for $1.5\Delta_y$ cycle. Strain gauge S29 was located on the inner face of the faceplate (S12 was placed at the same location on the outer face). Compression buckling of the faceplates is apparent in the figure. S9 and S12 reverse directions (strain increments change from compressive to tensile) when the faceplates buckle (faceplate buckling was observed visually during the $2\Delta_y$ cycle, as seen in Figure 4.28a, Figure 4.29b, and Figure 4.30a). It is observed that West faceplate (S12) buckles before East faceplate (S9) (also seen in Figure 4.28a). The initiation of buckling is around -1335 kN (-300 kips) and -2670 kN (-600 kips) for West and East faceplates respectively. This is counter-intuitive as the sustained out-of-plane loading subjects the West and East plates to additional tensile and compressive stresses respectively. This phenomenon was also observed for SC-0.5T-Vn. The delay in buckling of East plate may be due to the out-of-plane curvature (the East plate is curved in), which may provide additional resistance to buckling.

The extent of twisting and asymmetric behavior observed for SC-T-Vn was lower than SC-0.5T-Vn. Ties did not experience high tension demands (and there was no tie rupture). The asymmetric behavior (including the out-of-plane twisting) of SC-T-C was verified using the experimental measurements. Figure 4.35 shows the twisting of the specimen (at mid-height and top of the wall) when incremental in-plane loads (only push (+) half-cycles are plotted) were applied (with out-of-plane force maintained constant). The figure shows the plan view of the wall pier cross-section, with the wall pier thickness (305 mm) along the horizontal axis, and wall pier length (1524 mm) along the vertical axis. For clarity, the out-of-plane deformations are amplified ten times. The out-of-plane deformations were obtained from the string pots installed at mid-height and top of the specimens (SP 12, 13, 17, 18 in Figure 3.9). It is observed that the specimen underwent twisting out-of-plane when incremental in-plane loads were applied. The direction of twist reversed when the direction of loading was reversed. Additionally, the twist (and resulting residual out-of-plane drifts) increased drastically in the post-yield cycles, and peak out-of-plane drift of magnitude 11 mm (0.4 in) [in comparison to 25 mm (1 in.) for SC-0.5T-Vn] was observed during the $2\Delta_y$ cycle. Residual out-of-plane drift at failure ($3\Delta_y$ push cycle) was 23 mm (0.9 in) [in comparison to 60 mm (2.4 in) for SC-0.5T-Vn]. Figure 4.36 shows the evolution of neutral axis of the wall pier cross-section (at 76 mm from the base, strain gauge location) for incremental in-plane loading (only push (+) cycles are plotted) in combination with sustained out-of-plane loading. The neutral axis location was determined based on the faceplate strain gauge data. It is observed that the neutral axis rotated counter-clockwise and moved towards the North corner of the wall pier as incremental push (+) in-plane loading subjected the South end to tensile strains and North end to compressive strains. Neutral axis locations for Δ_y cycles are similar for SC-T-Vn and SC-0.5T-Vn. Similar

twisting and evolution of neutral axis behavior were observed for the pull (-) half cycles of in-plane loading.

4.4 SC-T-2.5Vn

The specimen (with ties spaced at section thickness, *T*) was subjected to incremental cycles of out-of-plane loading (222, 445, 667, 890, 1113-kN). The out-of-plane load was then maintained constant at 1113-kN (250 kips) and the specimen was subjected to in-plane loading cycles.

4.4.1 Out-of-plane Behavior

The specimen had diagonal pre-cracking in one direction before the application of out-of-plane loading (marked as 0^k in Figure 4.37). These cracks were formed during the post-tensioning of out-of-plane loading beam to the specimen. The specimen was subjected to incremental out-of-plane loading cycles (222-kN increments) till it developed diagonal shear cracks in the push (+) and pull (-) direction, with an intent to force the specimen to fail in vector shear (combination of in-plane and out-of-plane shear). Diagonal shear cracks in both the directions were observed in the 1113-kN loading cycle. This force corresponds to 2.5 times the expected out-of-plane shear strength of the specimen [$2.5 \times 2 \sqrt{f_c'} A_c$ (in psi units)]. The specimen cracking at the end of 1113-kN cycle is shown in Figure 4.38. SC-T-2.5Vn had cross-diagonal cracks and significantly more damage than SC-0.5T-Vn (Figure 4.3) before the application of in-plane loading. Figure 4.39 shows the East (S1 and S9) and West (S12 and S32) faceplate strains during the out-of-plane force cycle of 1113-kN. It is observed that the faceplate strains exceed the concrete cracking strain (130 με) for both the push and pull directions. The tensile strain in push (+) cycle is lower than the pull (-) cycle. This is because of the pre-existing diagonal crack corresponding to the pull direction. The magnitude of strains is lower than the faceplate strains for SC-0.5T-Vn (around 1000 με for

constant out-of-plane loading of 1070 kN). This can be attributed to observation of shear cracks in SP-T-2.5Vn at a lower magnitude out-of-plane force in comparison to SC-0.5T-Vn. As the specimen undergoes diagonal shear cracking between the base and the out-of-plane loading location, the row of ties in the region is expected to undergo tensile stresses. This is confirmed in Figure 4.40, where S35 (strain gauge installed at tie on North side) and S36 (strain gauge installed at tie on South side) show high tensile strains for out-of-plane loading. It is also observed that for pull (-) direction, the ties pick up tensile strains from the beginning of the loading. This is because the specimen was cracked in shear corresponding to pull direction before out-of-plane loading was applied (Figure 4.37). In push (+) direction, the ties pick up tensile strains after diagonal cracks are observed corresponding to the loading (at about +1070-kN load).

Cracking of concrete under out-of-plane loading (as observed in Figure 4.39 and Figure 4.40) will reduce the out-of-plane flexural stiffness of the SC specimen. Out-of-plane moment-curvature response of specimen SC-T-2.5Vn is presented in Figure 4.41 (for the load cycle of 1113-kN). The out-of-plane curvature was obtained from clinometer rotation data (CM2 and CM3 in Figure 3.9). The curvature was calculated from the measured rotations using central difference method. Out-of-plane moment was calculated at 254 mm (10 in.) from the base (the location where the curvature is obtained from central difference method). The out-of-plane cracking moment corresponding to a concrete cracking strain of 130 με [M_{cr-oop}, 14x10^4 kN-mm (1230 kip-in.)] corresponds to an out-of-plane force of 685-kN (154 kips). Since the specimen was subjected to 890-kN cycle before the 1113-kN cycle, the specimen is expected to exhibit cracked-transformed (Region 2) stiffness, EI_{eff}, [$E_sI_s+c_2E_cI_c$, 0.84x10^{11} kN-mm^2 (2.94x10^7 kip-in^2), per AISC N690s1 [26] Equation A-N9-8]. The push stiffness and the pull stiffness of the specimen are close to EI_{eff}, with the stiffness ratios being 0.89 and 0.91 respectively (Figure 4.41).

4.4.2   In-plane Behavior

With the out-of-plane loading maintained constant at 1113-kN, the specimen was subjected to incremental cyclic in-plane loading per the loading protocol discussed previously. Figure 4.42 shows the in-plane force-top displacement response of SC-T-2.5Vn. Average peak strength of SC-T-2.5Vn is 2180 kN [+2225/-2136 kN (+500 kips/-480 kips)], in comparison to 3115-kN for SC-T-C. Normalized response of the specimen is compared with SC-T-C (Control specimen) in Figure 4.43. The normalized peak strength of SC-T-2.5Vn (equal to $0.83V_{Myc}$) is significantly lower than SC-T-C. SC-T-2.5Vn did not reach its compression yield moment capacity. This is because of high in-plane shear force for SC-T-2.5Vn [while M_{oop} was $0.78M_n^{AISC}$ (similar to SC-0.5T-Vn), the corresponding V_{oop} was $2.5V_n^{ACI}$ (compared to $1.0V_n^{ACI}$ for SC-0.5T-Vn)]. The specimen underwent a vector shear (combination of in-plane and out-of-plane shear) failure in the cycle following the peak load cycle. The specimen failed at a drift ratio of (+/-) 0.6%.

Figure 4.44 to Figure 4.48 show the progression of damage for the specimen. The diagonal shear cracks (formed due to out-of-plane loading) widened due to vector shear demands and additional shear cracks formed for in-plane loading cycles (Figure 4.44). There was some initiation of faceplate buckling on North end of the East faceplate for the first Δ_y push (+) cycle (Figure 4.45). The diagonal shear cracks widened and the out-of-plane deformation of the specimen increased during the first Δ_y cycle (Figure 4.45 and Figure 4.46). During the second Δ_y push cycle, North end of the East faceplate buckled, and the diagonal shear crack in concrete extended to the buckled faceplate (Figure 4.47). The specimen had extensive shear cracking, and there was initiation of concrete spalling due to the cracking. The specimen failed during second Δ_y pull cycle, as the faceplate buckling resulted in the inability of the concrete compression strut to be anchored in to the faceplate. This led to the specimen sliding on the diagonal shear crack plane. The specimen

failed due to extensive shear cracking, concrete crushing at the out-of-plane loading location, and sliding on the diagonal crack plane (Figure 4.48). There was no extensive faceplate buckling or yielding, or concrete spalling (these limit states were observed for other specimens).

Magnitude of sustained out-of-plane loading for SC-T-2.5Vn (1113-kN) was similar to that for specimen SC-0.5T-Vn (1070-kN). However, the resulting tensile strains (ε_{oop}) on the West faceplate for SC-T-2.5Vn (around 600 µε, as observed in S12 and S32 from Figure 4.39 and Figure 4.49) were lower than the corresponding strains for SC-0.5T-Vn (1000 µε as shown in Figure 4.17). The lower faceplate strains in SC-T-2.5Vn indicate higher out-of-plane shear distress in the specimen (as confirmed by diagonal shear cracking in the specimen). Figure 4.50 shows the faceplate strain plots for $0.75P_y$ loading cycles. Since S12 was not functioning, the strain gauge at the same location on the inner face of the faceplate (S29) has been used. The West faceplate tensile strains exceeded the yield strains at +1780/-1160 kN (+400/-260 kips). The East faceplate had not yielded yet. The yield force is considerably higher than the force corresponding to initiation of faceplate yielding in SC-0.5T-Vn (around 670-kN as shown in Figure 4.17). The faceplate strain comparison for SC-T-2.5Vn and SC-0.5T-Vn corroborates the fact that the response of SC-T-2.5Vn was shear dominated, which delayed the initiation of faceplate yielding. Figure 4.50 also shows that the behavior of specimen was highly asymmetric, with West faceplate witnessing extensive yielding, while there was no yielding in East faceplate.

Since the specimen failed at low in-plane drift ratio, with poor post-peak response, extent of twisting and asymmetric behavior observed for SC-T-2.5Vn was lower than that for SC-0.5T-Vn. There was no tie rupture. The asymmetric behavior (including the out-of-plane twisting) of SC-T-C was verified using the experimental measurements. Figure 4.51 shows the twisting of the specimen (at mid-height and top of the specimen) when incremental in-plane loads (only push (+)

half-cycles are plotted) were applied (with out-of-plane force maintained constant). The figure shows the plan view of the wall pier cross-section, with the wall pier thickness (305 mm) along the horizontal axis, and wall pier length (1524 mm) along the vertical axis. For clarity, the out-of-plane deformations are amplified ten times. The out-of-plane deformations were obtained from the string pots installed at the mid-height and the top of the specimen (SP 12, 13, 17, 18 in Figure 3.9). It is observed that the specimen underwent twisting out-of-plane when incremental in-plane loads were applied. The direction of twist reversed when the direction of loading was reversed. At failure, out-of-plane drift of magnitude 16 mm (0.6 in) [in comparison to 26 mm (1 in.) for SC-0.5T-Vn] was observed. Figure 4.52 shows the evolution of neutral axis of the wall pier cross-section (at 76 mm from the base, corresponding to strain gauge location) for incremental in-plane loading (only push (+) cycles are plotted in combination with sustained out-of-plane loading). Neutral axis location was determined based on the faceplate strain gauge data. The faceplates underwent extensive tension yielding in the 0.75 P_y and Δ_y cycles, therefore the strain gauge data could not be used to get the neutral axis location for these cycles. It is observed that the neutral axis rotated counter-clockwise and moved towards the North corner of the wall pier as incremental push (+) in-plane loading subjected South end to tensile strains and North end to compressive strains. Neutral axis locations for $0.5\Delta_y$ cycles are similar for SC-T-Vn and SC-0.5T-Vn. Similar twisting and evolution of neutral axis behavior were observed for the pull (-) half cycles of in-plane loading.

4.5 Evaluation of Wall Pier Behavior

4.5.1 Out-of-plane Behavior

Specimens SC-T-Vn, SC-0.5T-Vn, and SC-T-2.5Vn were subjected to cyclic out-of-plane loading. The out-of-plane loading was applied at a distance of 457 mm from the base (resulting in a shear span to depth ratio, a/h, of 1.5). The low a/h was intended to minimize the resulting out-of-plane

flexure demands (and have high shear demands). However, the low shear span to depth ratio was also expected to increase the concrete contribution to out-of-plane shear strength [higher than $2\sqrt{f_c'}$ (in psi units) per ACI 349]. It was observed that the out-of-plane response of the specimens was flexure controlled, with concrete cracking in flexure. SC-T-2.5Vn, subjected to an out-of-plane shear force of magnitude 2.5 times the expected strength per ACI 349, was forced to have a shear dominated response. High magnitude out-of-plane force resulted in cross-diagonal shear cracks in the specimen. As discussed previously (Figure 4.5, Figure 4.23 and Figure 4.41), measured out-of-plane flexural stiffness of the specimens can be compared with calculated cracked or uncracked stiffness. Table 4.1 presents the normalized flexural stiffnesses for the specimens for loading cycles of 534-kN (556-kN for SC-T-2.5Vn) and 1070-kN (1113-kN for SC-T-2.5Vn). The cracking moment at the cross-section where curvature is calculated corresponds to a force of about 680-kN [considering concrete modulus of rupture to be $7.5\sqrt{f_c'}$ (in psi units)]. Therefore, the measured stiffness of the specimens is normalized with the uncracked stiffness (EI_{uncr}) for 534 (or 556) kN cycles, and with cracked stiffness (EI_{eff}) for 1070 (or 1113) kN cycle. As observed in Figure 4.5, both cracked (Region 2) and uncracked (Region 1) stiffnesses were manifest during the 1070-kN cycle for SC-0.5T-Vn. SC-T-Vn exhibited stiffness that is lower than the uncracked stiffness (but greater than cracked stiffness). The reduction in stiffness may be due to cyclic damage. When the cracked stiffnesses for SC-0.5T-Vn (1070-kN, Region 2) and SC-T-2.5Vn (1113-kN) are compared, it is observed that SC-0.5T-Vn witnessed a higher reduction in stiffness. The lower reduction in flexural stiffness for SC-T-2.5Vn is consistent with the observation that the specimen behavior was shear dominated, with the specimen forming cross-diagonal shear cracks.

4.5.2　In-plane Behavior

The in-plane response of specimens SC-T-Vn and SC-0.5T-Vn was flexure controlled, with specimens failing due to faceplate buckling and concrete spalling. Response of SC-T-Vn and SC-0.5T-Vn was similar to that of SC-T-C. However, SC-T-C failed due to base metal (faceplate) weld rupture, and did not reach its in-plane plastic moment capacity. Specimen SC-T-2.5Vn failed in vector shear, by sliding on the diagonal shear crack plane. Biaxial loading resulted in asymmetric response of the specimens, with residual out-of-plane drifts, twisting of the specimens, and asymmetric yielding and buckling of the specimens. Magnitude of out-of-plane loading (in comparison to the out-of-plane strength) affected the in-plane response of the specimen.

In-plane stiffness of the specimens can be determined using the displacement (in Figure 3.8, SP1 and SP5 at top, SP3 and SP7 at base) and force measurements. The top displacement (uncorrected) measurement also includes the effect of base slip and base rotation. Base slip (measurements from SP3 and SP7) and base rotation (measurement from CM1, shown in Figure 3.8) corrections can be applied to obtain the corrected displacement measurements for the specimens. Table 4.2 presents the measured stiffness values for the specimens. The table presents the corrected (for base slip and rotation) and uncorrected stiffness (presented in parenthesis) values for the specimens. Initial stiffness is calculated as secant stiffness between force levels of 222-kN to 445-kN (50 kips to 100 kips) for the first $0.25P_y$ in-plane cycle of the specimen. Secant stiffness for the specimen is the stiffness for the first $0.75P_y$ in-plane cycle of the specimen calculated using the peak force and the corresponding displacement values. Reduction in in-plane stiffness due to out-of-plane loading depends on the magnitude of out-of-plane flexural and shear loads.

Figure 4.53 presents the comparison of normalized in-plane backbone curves for SC wall pier specimens. The in-plane displacement (drift ratio) has been corrected for base slip and base rotation. SC-T-C (no out-of-plane loading) reached an in-plane peak load corresponding $1.01V_{Myc}$

(and $0.87V_{Mp}$). Since the specimen failed due to basemetal (faceplate) weld rupture, it could not reach V_{Mp}. SC-T-Vn (subjected to V_{oop} equal to V_n^{ACI}, and corresponding M_{oop} equal to $0.37M_n^{AISC}$) reached an in-plane peak load corresponding to $0.98V_{Mp}$ (and $1.10V_{Myc}$). SC-0.5T-Vn (subjected to V_{oop} equal to V_n^{ACI}, and corresponding M_{oop} equal to $0.74M_n^{AISC}$) reached an in-plane peak load corresponding to $1.04V_{Myc}$ (and $0.90V_{Mp}$). SC-T-2.5Vn (subjected to V_{oop} equal to $2.5V_n^{ACI}$, and corresponding M_{oop} equal to $0.78M_n^{AISC}$) reached an in-plane peak load corresponding to $0.83V_{Myc}$ (and $0.71V_{Mp}$). A comparison of SC-T-Vn and SC-0.5T-Vn in-plane response indicates that the magnitude of out-of-plane moment affects the in-plane strength and stiffness of the specimen. This is because the behavior of the wall piers is flexure controlled, and higher magnitude of out-of-plane moment results in higher faceplate flexural stresses (and strains) due to the out-of-plane loading, thus reducing the magnitude of additional in-plane load the specimen can carry. The higher out-of-plane loading also leads to diagonal shear cracking (and additional flexural cracking) in the specimen, which reduces the in-plane stiffness of the specimen. A comparison of SC-T-Vn and SC-T-2.5Vn indicates that if the specimen is subjected to an out-of-plane force significantly higher than the expected out-of-plane shear capacity (forcing the specimen to have vector shear failure), the in-plane response of the specimen is significantly hindered. SC-T-2.5Vn had no post-peak performance and failed in vector shear. SC-T-C and SC-0.5T-Vn reached an average drift of about 1%. SC-T-Vn reached an average drift of 1.3%. Since SC-T-2.5Vn had almost no post-peak response, average drift for the specimen was about 0.5%.

Progression of damage for the biaxially loaded specimens is presented in Figure 4.54. Since the damage states for SC-T-C have been presented previously (Figure 4.1), the specimen has not been included in Figure 4.54. SC-0.5T-Vn and SC-T-2.5Vn were cracked (due to the out-of-plane loading) before the application of in-plane loading. Initiation of faceplate yielding in SC-0.5T-Vn

was at a lower load (about $0.2V_{Myc}$, 670-kN) in comparison to SC-T-Vn and SC-T-2.5Vn (about $0.5V_{Myc}$, 1780-kN). This was due to the higher flexural stresses in SC-0.5T-Vn caused by the out-of-plane loading (flexural stresses in SC-T-2.5Vn were lower as specimen had shear dominated behavior). In comparison to SC-T-Vn, SC-0.5T-Vn experienced faceplate buckling and concrete spalling at higher drifts. SC-0.5T-Vn witnessed tie rupture towards the end of the test, due to the asymmetric behavior of the specimen.

Summary of the in-plane response of the specimens is presented in Table 4.3. The table presents normalized out-of-plane force (V_{oop}/V_n^{ACI}), corresponding normalized out-of-plane moment at base (M_{oop}/M_n^{AISC}), experimental in-plane capacity (V_{n-ip}), ratio of in-plane capacity to lateral force corresponding to compression yielding moment capacity (V_{n-ip}/V_{Myc}) and plastic moment capacity (V_{n-ip}/V_{Mp}). In-plane response of flexure-controlled specimens was not significantly affected by out-of-plane loads. Both SC-T-Vn and SC-0.5T-Vn reached the compression yield moment capacity. However, when SC-T-2.5Vn was forced to undergo vector shear failure, the in-plane response of the specimen was significantly affected. The specimen failed at about 20% below the compression yield capacity. Experimentally-observed corrected initial stiffness for the first cycle (K_{in}) is normalized with the theoretical uncracked stiffness of the specimens, K_{uncr} (considering EI_{uncr} and GA_{uncr}). Uncracked stiffness was not manifest in the wall pier specimens. Flexural cracking due to out-of-plane loading further reduced in the initial stiffness of the specimens. However, shear cracking due to out-of-plane loading does not seem to reduce the in-plane initial stiffness of the specimens. Corrected average secant stiffness of the specimens (for the first $0.75P_y$ cycle), K_{sec}, is normalized with theoretical cracked stiffness (K_{cr}). K_{cr} was calculated considering the cracked flexural stiffness (EI_{cr}) and cracked shear stiffness (GA_{cr}). EI_{cr} was calculated corresponding to the neutral axis location for compression yield moment (M_{yc}). GA_{cr} was

calculated as the sum of steel shear stiffness (G_sA_s) and the shear stiffness of the uncracked region of concrete (in compression). The uncracked concrete area corresponds to neutral axis location for M_{yc}. Additionally, a reduction factor of 0.25 is applied to the concrete uncracked area contribution. The reduction factor accounts for the fact that there are no flange boundary elements for concrete compression strut to anchor at, and fully develop. Therefore, the concrete shear stiffness was considered as $0.25G_cA_c{}^{uncr}$. Out-of-plane loading significantly reduced the in-plane secant stiffness of the specimens (the reduction was up to 40%). The corrected maximum drift ratio ($\Delta_{u\text{-}ip}{}^{corr}$) for the specimens is also presented in the table. Squat SC wall pier specimens (aspect ratio of 0.6) reached peak drifts greater than 1%. For SC-T-2.5Vn, the peak drift was significantly lower (0.5%) as the specimen failed in vector shear before reaching in-plane compression yield moment capacity.

4.6   Chapter Summary

This chapter presents the results for SC wall pier specimens subjected to combined in-plane and out-of-plane loadings. Four SC wall pier specimens were tested. The control specimen was subjected to in-plane loading (no out-of-plane loading). Three SC wall pier specimens were subjected to different magnitudes of out-of-plane loadings, in combination with in-plane loading. In-plane response of wall piers with aspect ratios greater than or equal to 0.6 was flexure dominated, with specimens failing due to excessive faceplate yielding, compression buckling, and concrete spalling. Introducing an out-of-plane force resulted in out-of-plane shear and moment in the wall piers. The out-of-plane response of wall pier specimens was flexure controlled with concrete cracking. Out-of-plane flexural stiffness can be reasonably estimated using the provisions of AISC N690s1. Diagonal shear cracking of the wall piers depended on the magnitude of out-of-plane force in comparison to concrete contribution to shear strength (V_c). SC wall pier with ties spaced at half the section thickness developed diagonal shear cracks when subjected to out-of-plane shear

equal to the nominal shear strength. No diagonal shear cracking was observed for wall pier specimen with ties spaced at section thickness and subjected to out-of-plane shear equal to nominal shear strength. Wall piers subjected to out-of-plane shear equal to their nominal shear strength (per US codes) develop flexural yielding and failure due to interaction between the in-plane and out-of-plane moments. Shear failure does not occur for these wall piers. In-plane flexural strength of the specimens was influenced by the magnitude of out-of-plane moments. The wall pier specimen subjected to out-of-plane shear force that is 2.5 times the nominal shear strength (per US codes) was forced into a shear failure mode by the interaction of in-plane shear and out-of-plane shear. Specimens subjected to biaxial loading exhibited asymmetric response with twisting of the specimens, and tie rupture for SC-0.5T-Vn.
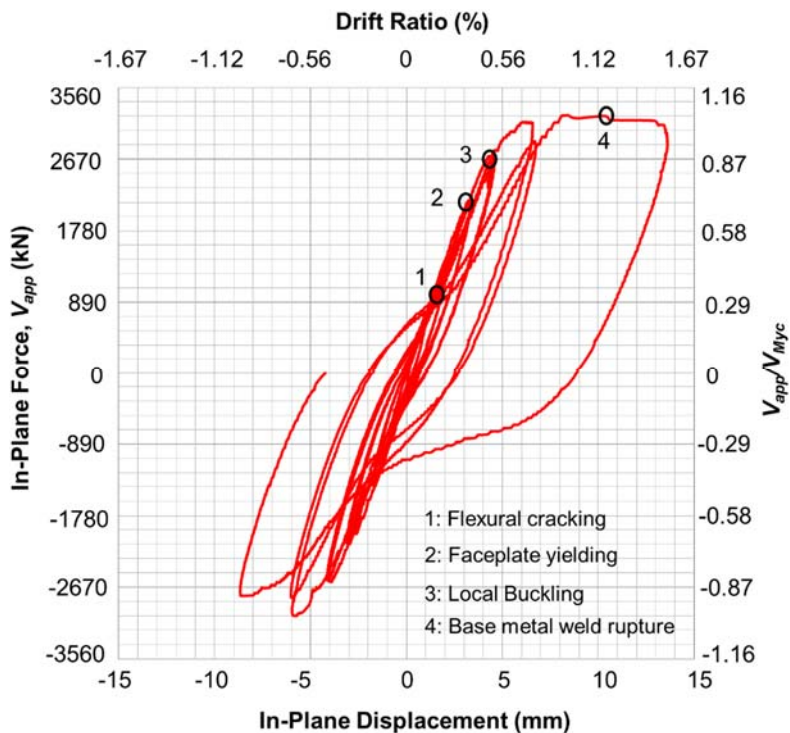
Figure 4.1 In-plane force-top displacement response of SC-T-C
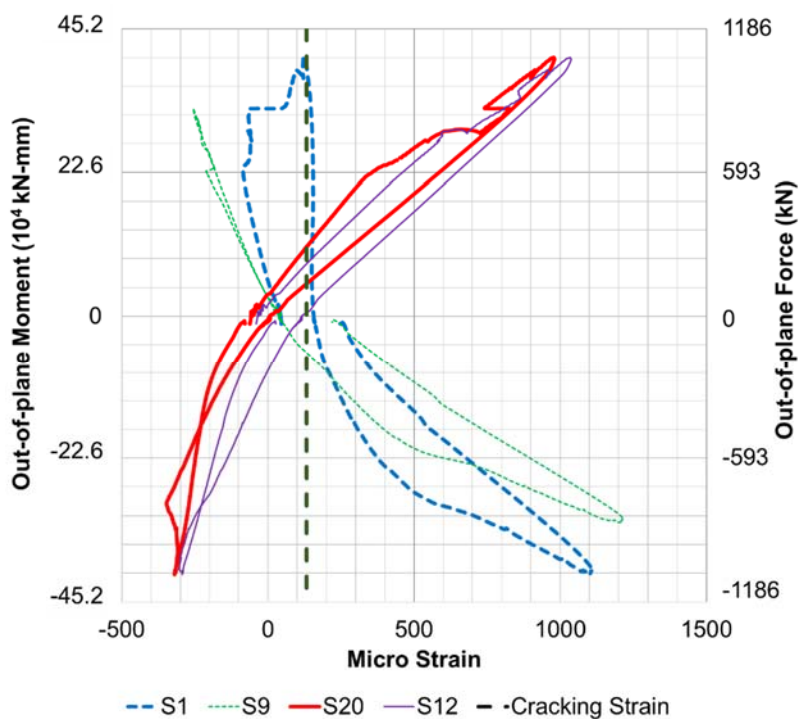
Figure 4.2 SC-0.5T-Vn: Faceplate moment-strain plots (for 1070-kN out-of-plane loading cycle)
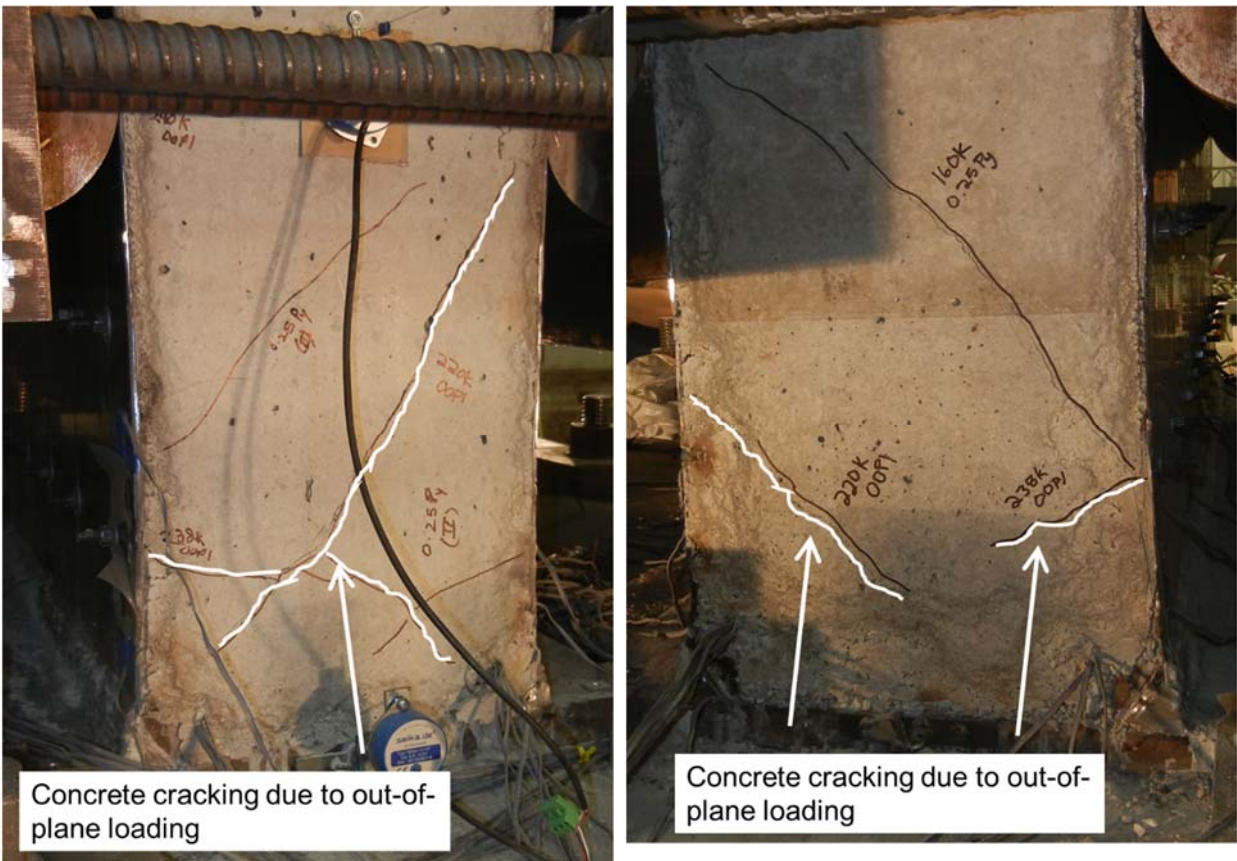
a) North face b) South face

Figure 4.3 SC-0.5T-Vn: Diagonal shear cracking (after $0.25P_y$ in-plane cycles)
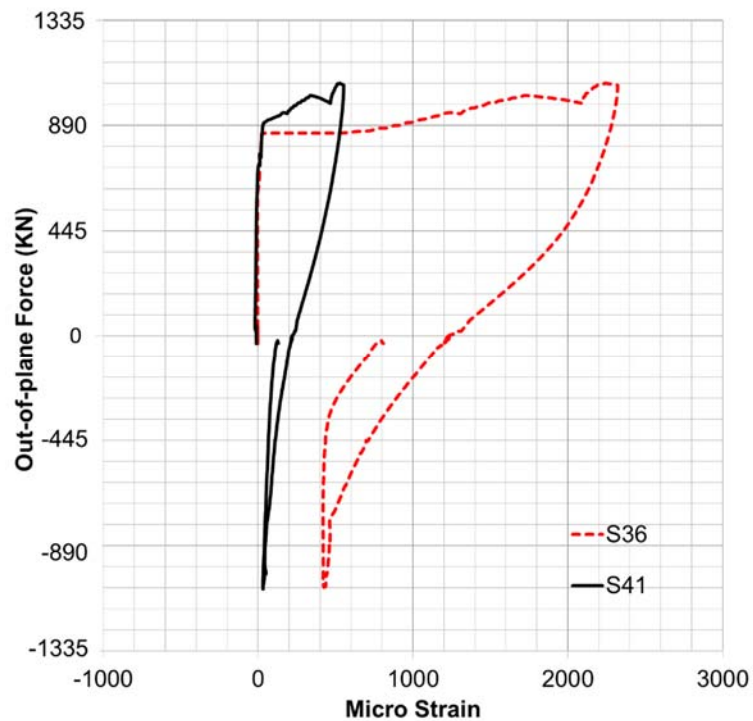
Figure 4.4 SC-0.5T-Vn: Tie strains (for 1070-kN out-of-plane loading cycle)
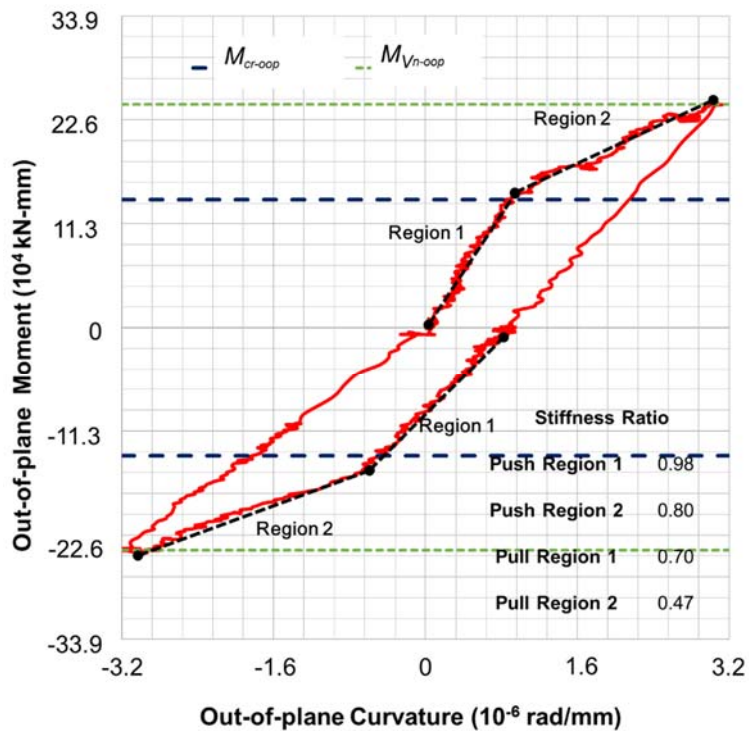
Figure 4.5 SC-0.5T-Vn: Out-of-plane moment-curvature relationship (for 1070-kN cycle)
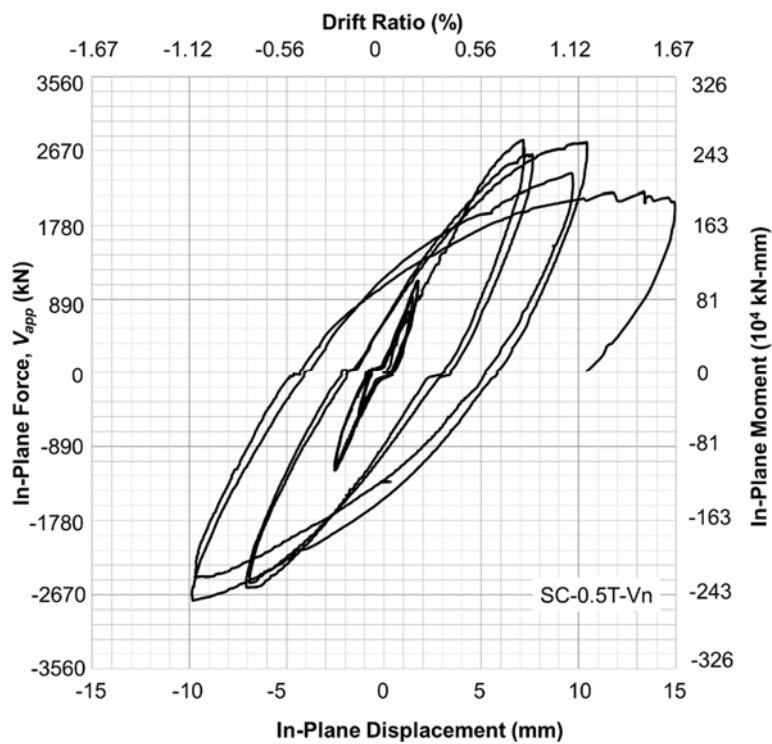
Figure 4.6 In-plane force-top displacement response of SC-0.5T-Vn
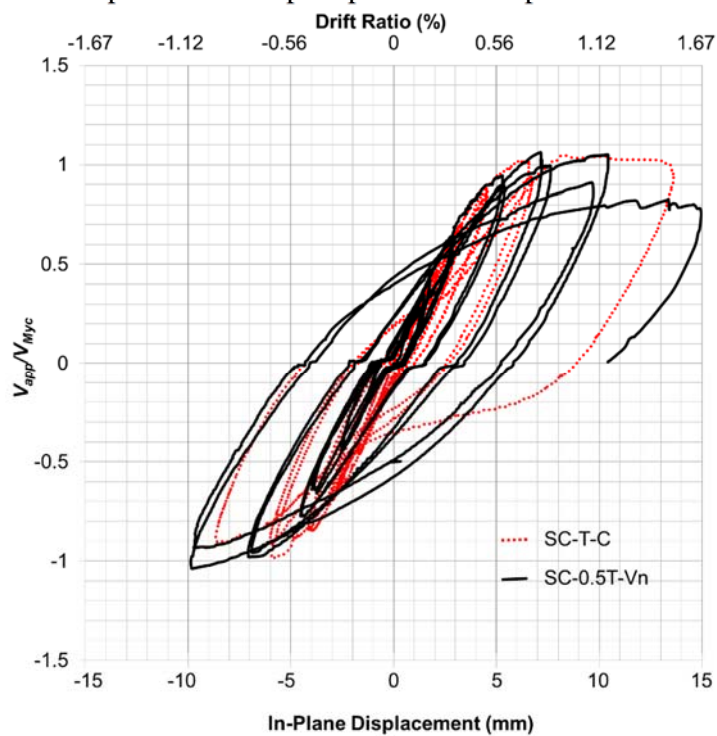
Figure 4.7 Comparison of in-plane force-top displacement response (SC-0.5T-Vn and SC-T-C)
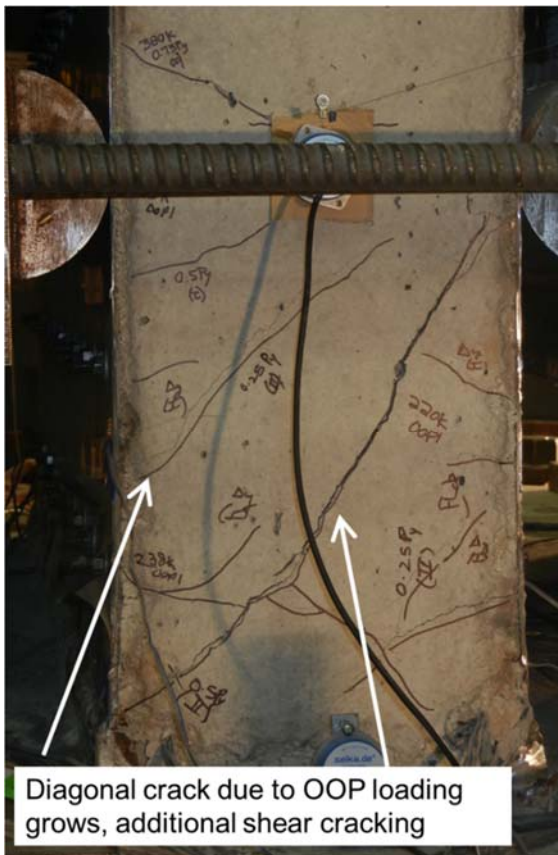
a) North face

b) South face

Figure 4.8 SC-0.5T-Vn: Specimen state at Δ_y cycle

a) North face   b) South face

Figure 4.9 SC-0.5T-Vn: Specimen state at 1.5Δ_y cycle

| a) North face | b) South face |

Figure 4.10 SC-0.5T-Vn: Specimen state at 2Δ*y* push cycle 1

a) North face   b) South face

Figure 4.11 SC-0.5T-Vn: Specimen state at $2\Delta_y$ pull cycle 1
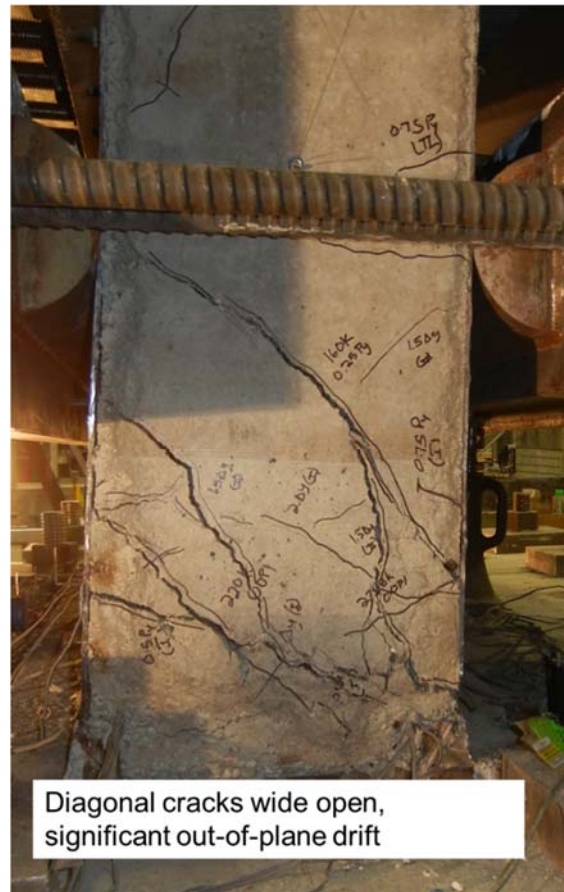
a) North face   b) South face

Figure 4.12 SC-0.5T-Vn: Specimen state at $2\Delta_y$ push cycle 2

a) North face   b) South face

Figure 4.13 SC-0.5T-Vn: Specimen state at 2Δ$_y$ pull cycle 2

a) North face   b) South face

Figure 4.14 SC-0.5T-Vn: Specimen state at failure ($3\Delta_y$ push cycle 1)

Figure 4.15 SC-0.5T-Vn: Tie bar rupture at failure
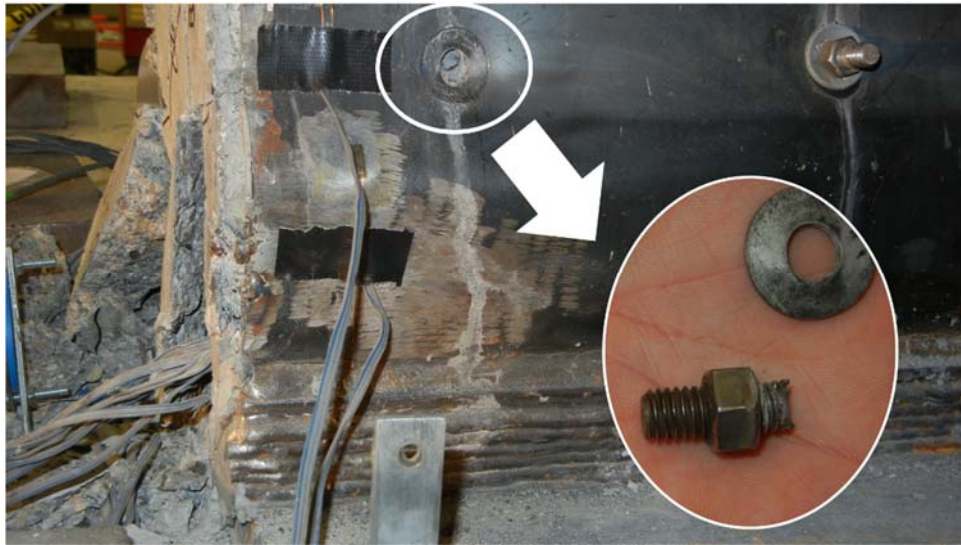
Figure 4.16 SC-0.5T-Vn: Tie bar rupture (zoomed in)
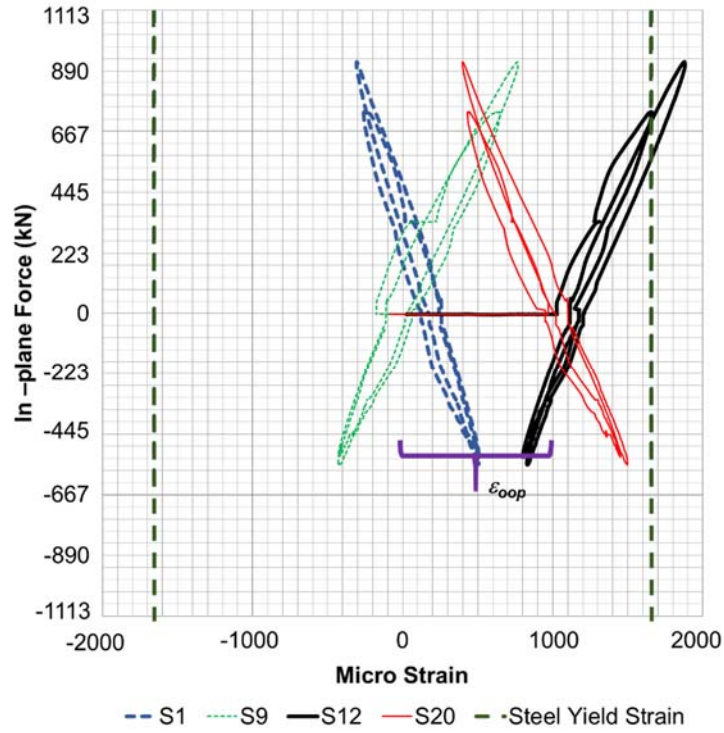
Figure 4.17 SC-0.5T-Vn: Faceplate strains for $0.25P_y$ cycles
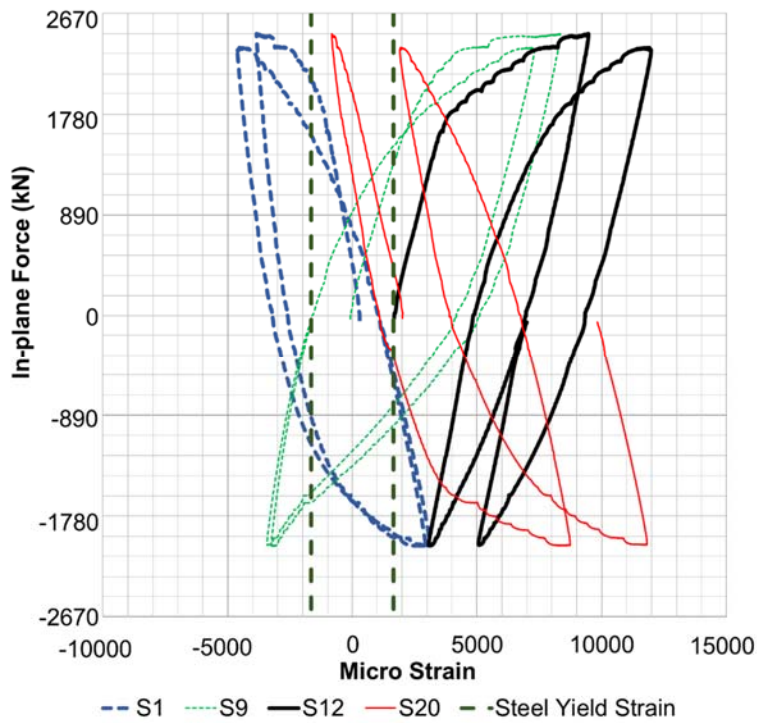
Figure 4.18 SC-0.5T-Vn: Faceplate strains for Δ_y cycle
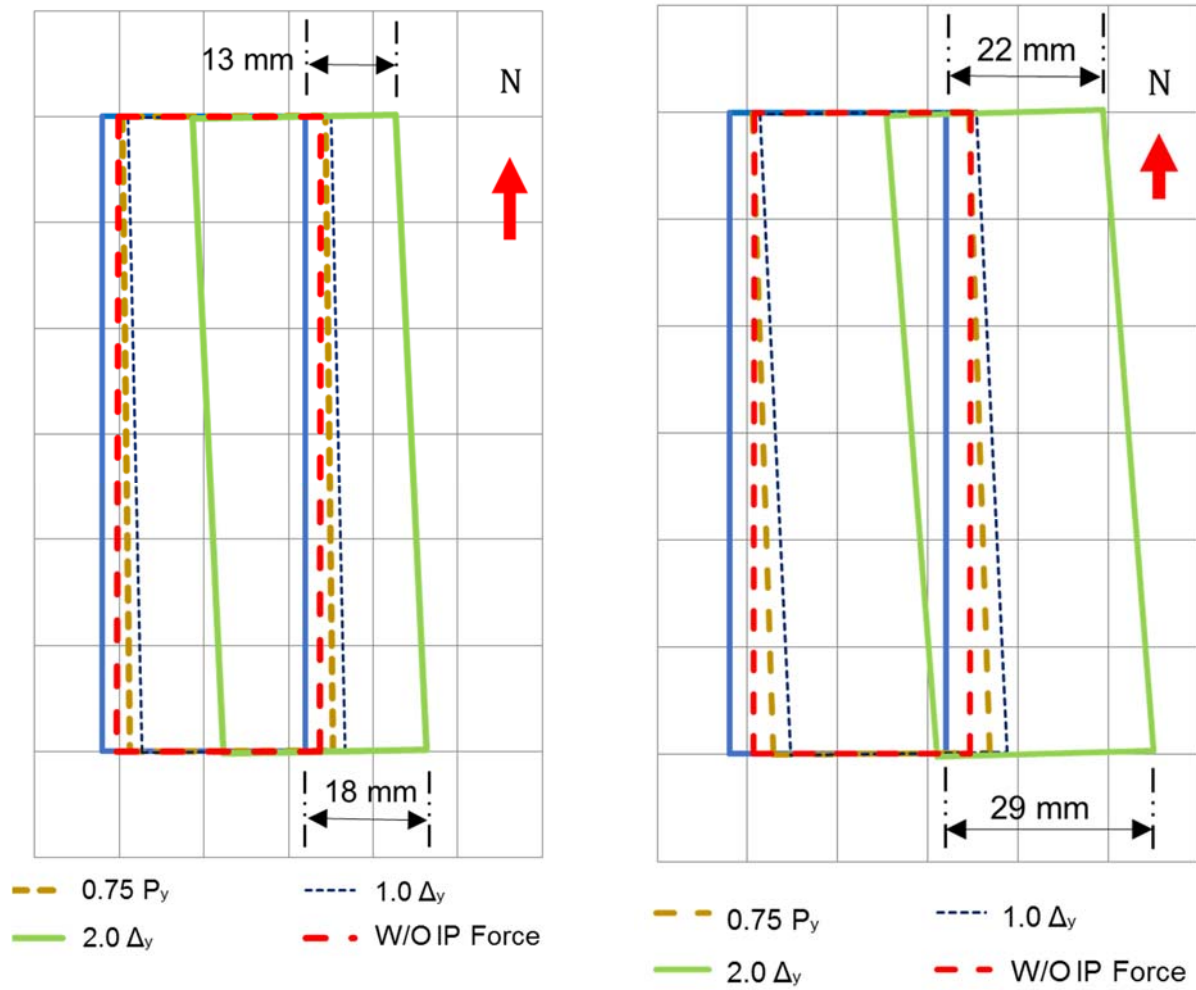
a) At mid-height (457 mm)   b) At top of the wall (915 mm)

Figure 4.19 SC-0.5T-Vn: Out-of-plane twisting (in-plane push (+) half cycles)
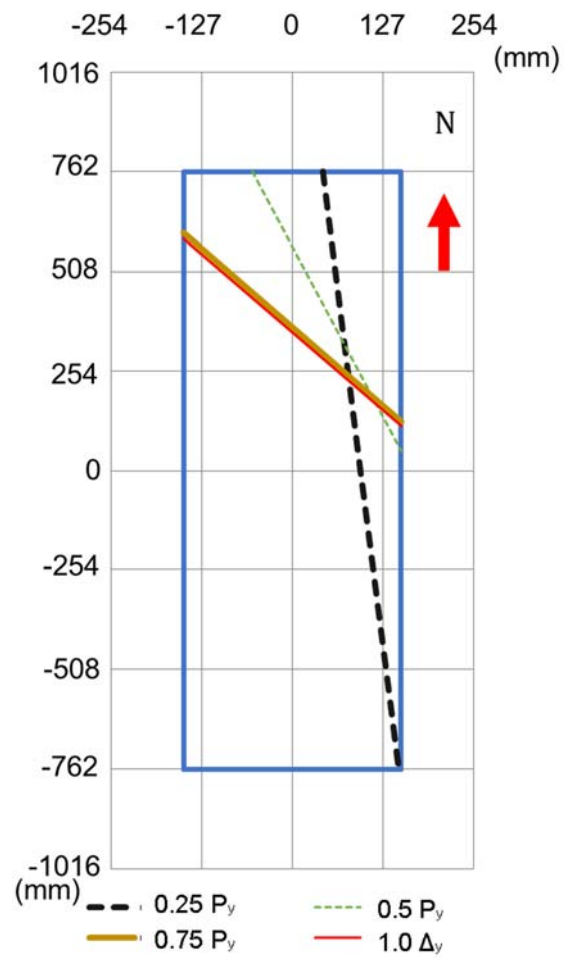
Figure 4.20 SC-0.5T-Vn: Evolution of Neutral axis (in-plane push (+) half cycles)
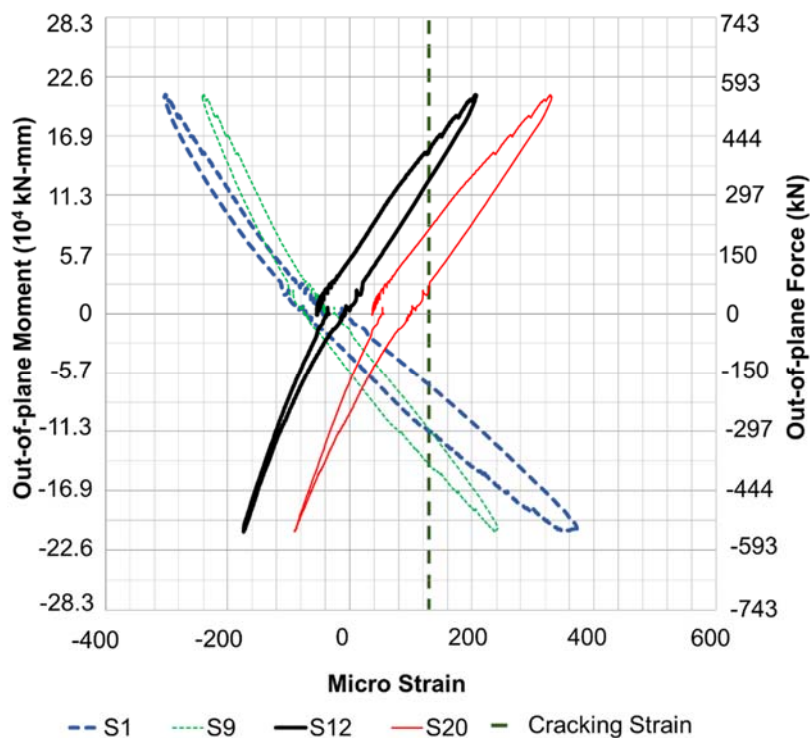
Figure 4.21 SC-T-Vn: Vertical strains for 534-kN out-of-plane loading cycle
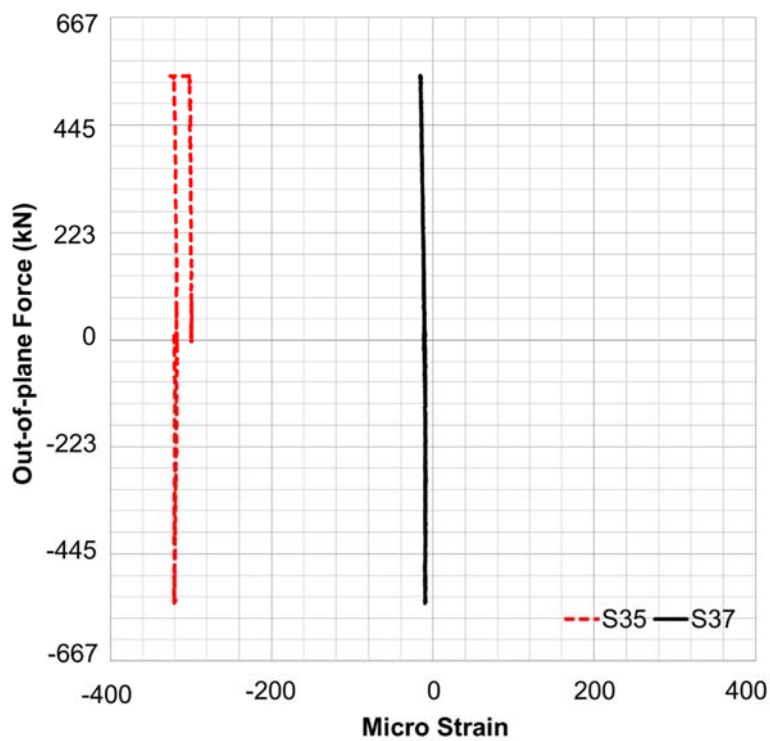
Figure 4.22 SC-T-Vn: Tie strains for 534-kN out-of-plane loading cycle
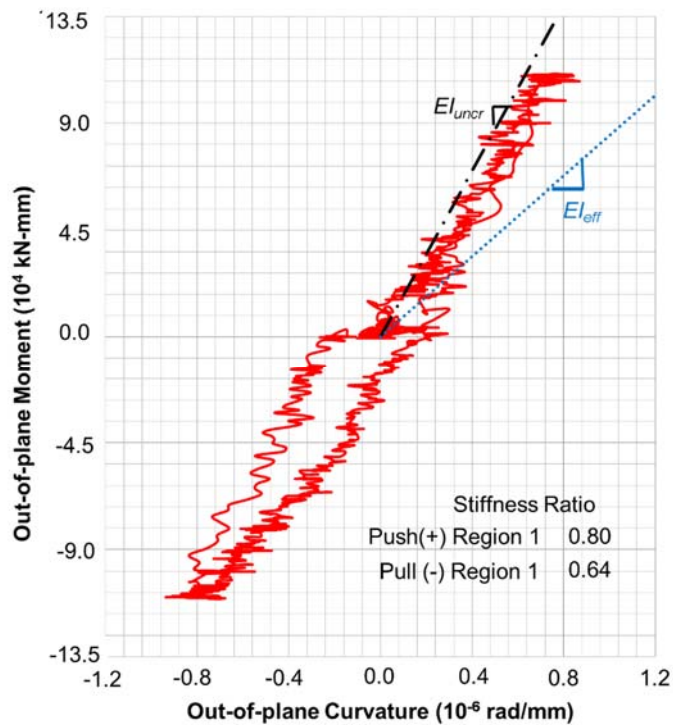
Figure 4.23 SC-T-Vn: Out-of-plane moment-curvature relationship (for 534-kN loading cycle)
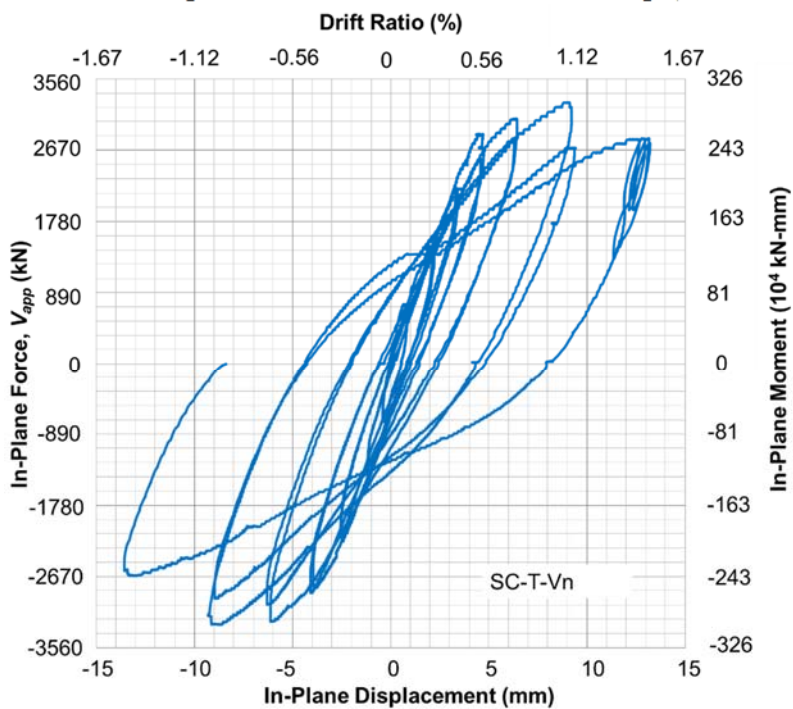
Figure 4.24 In-plane force-top displacement response of SC-T-Vn
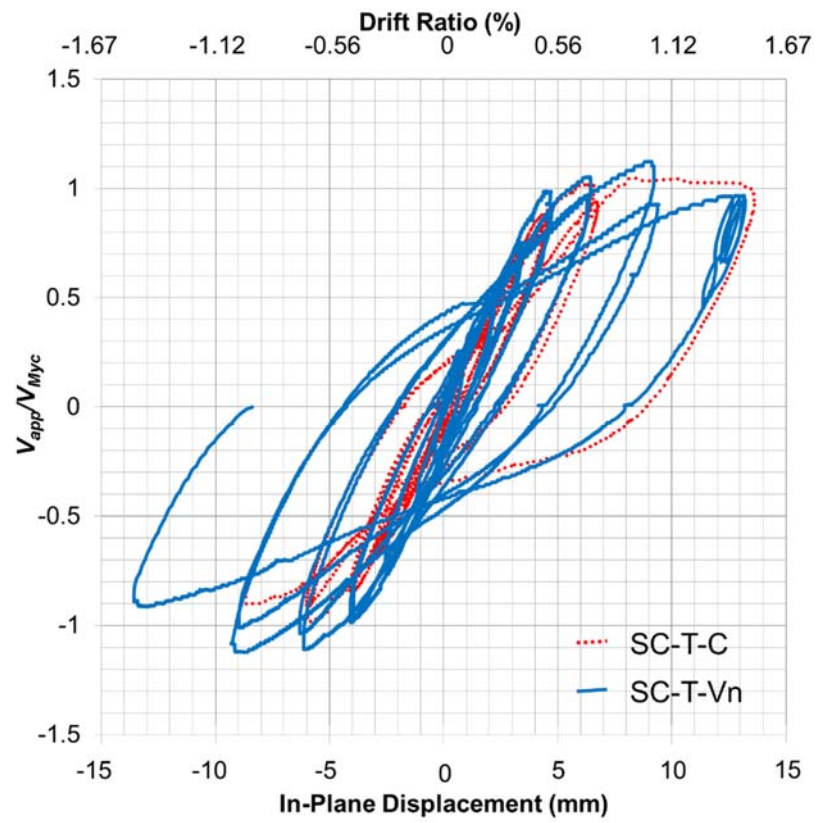
Figure 4.25 Comparison of in-plane force-top displacement response (SC-T-Vn and SC-T-C)
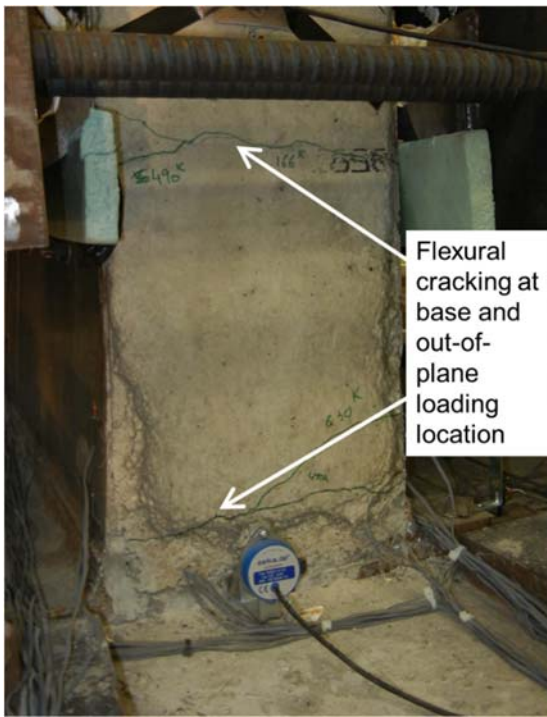
a) North face   b) South face

Figure 4.26 SC-T-Vn: Specimen state at Δ_y cycle
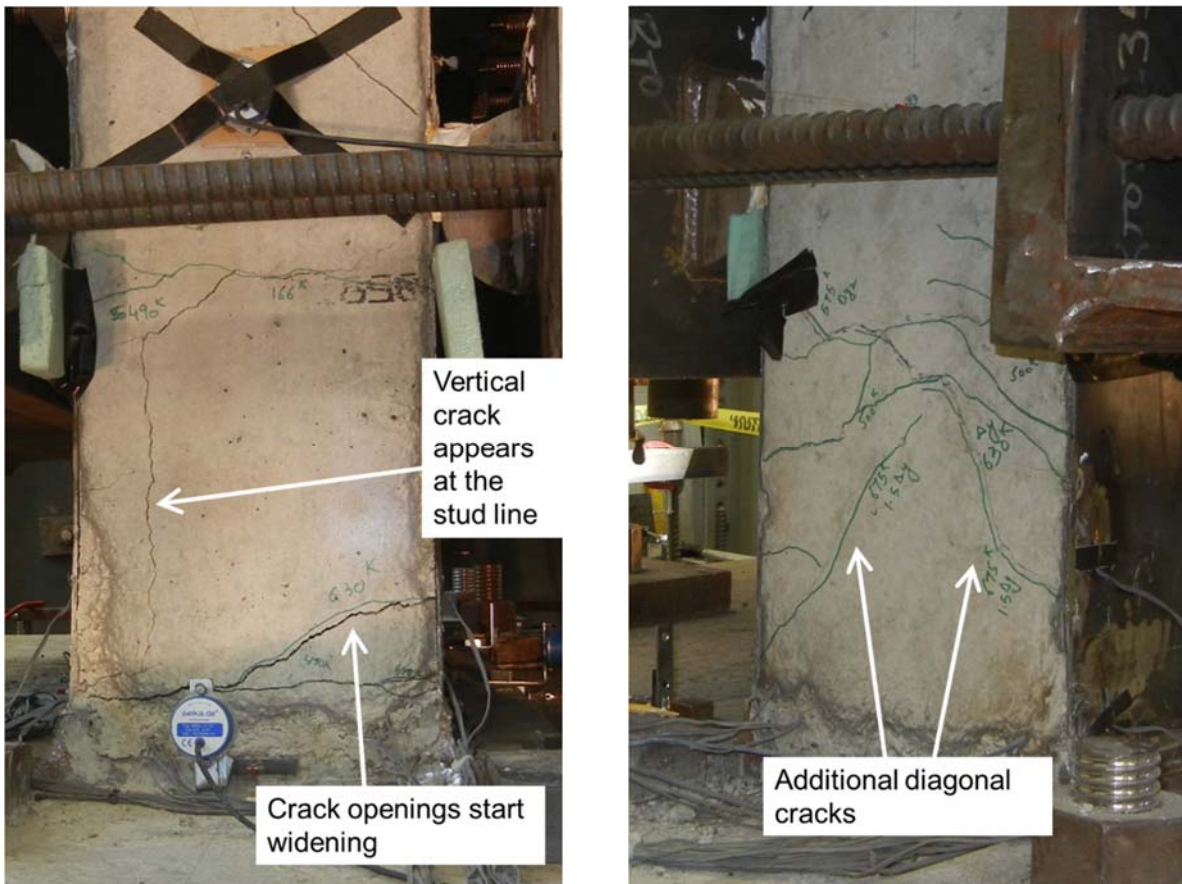
a) North face   b) South face

Figure 4.27 SC-T-Vn: Specimen state at $1.5\Delta_y$ cycle

a) North face   b) South face

Figure 4.28 SC-T-Vn: Specimen state at $2\Delta_y$, push cycle 1
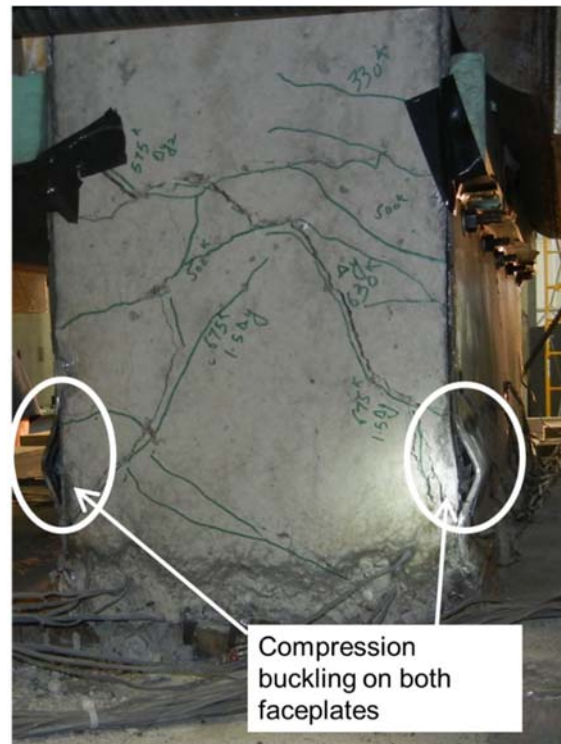
a) North face   b) South face

Figure 4.29 SC-T-Vn: Specimen state at 2Δ_y, pull cycle 1

a) North face   b) South face

Figure 4.30 SC-T-Vn: Specimen state at 2Δ$_y$, push cycle 2

a) North face   b) South face

Figure 4.31 SC-T-Vn: Specimen state at 3Δ$_y$, push cycle

a) North face   b) South face

Figure 4.32 SC-T-Vn: Specimen state at $3\Delta_y$, pull cycle
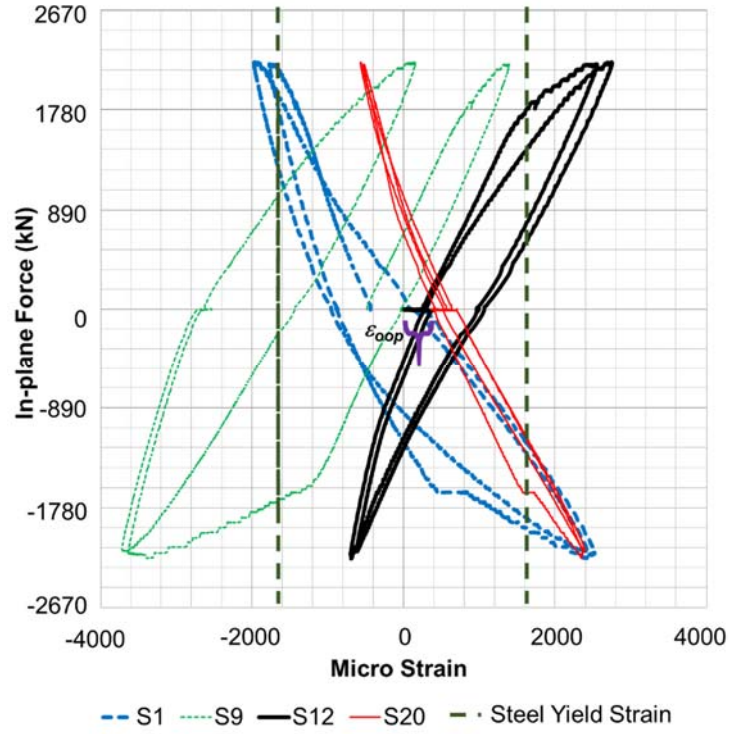
Figure 4.33 SC-T-Vn: Faceplate strains for $0.75P_y$ cycles
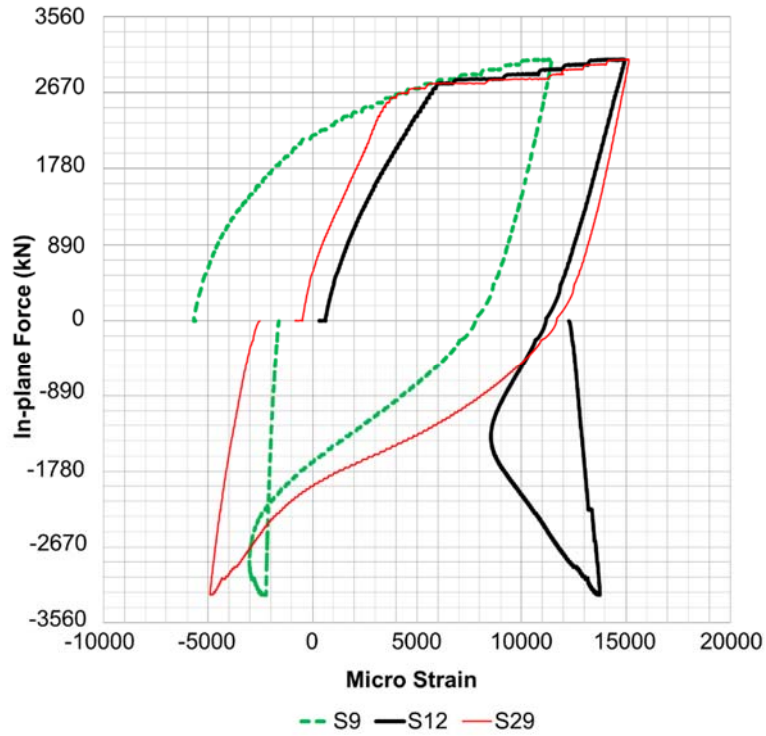
Figure 4.34 SC-T-Vn: Faceplate strains for $1.5\Delta_y$ cycle

a) At mid-height (457 mm)   b) At top of the wall (915 mm)
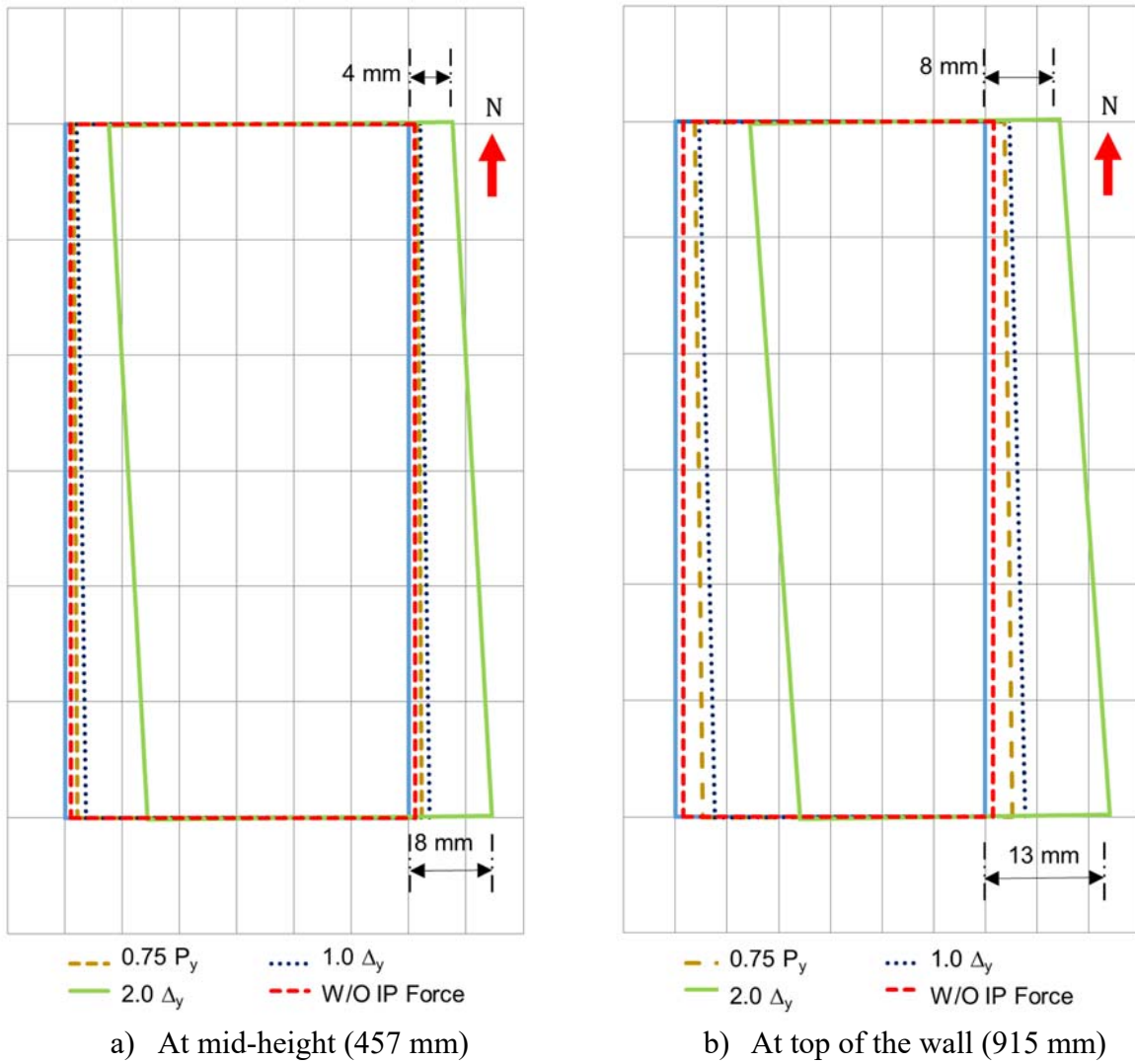
Figure 4.35 SC-T-Vn: Out-of-plane twisting (in-plane push (+) half cycles)
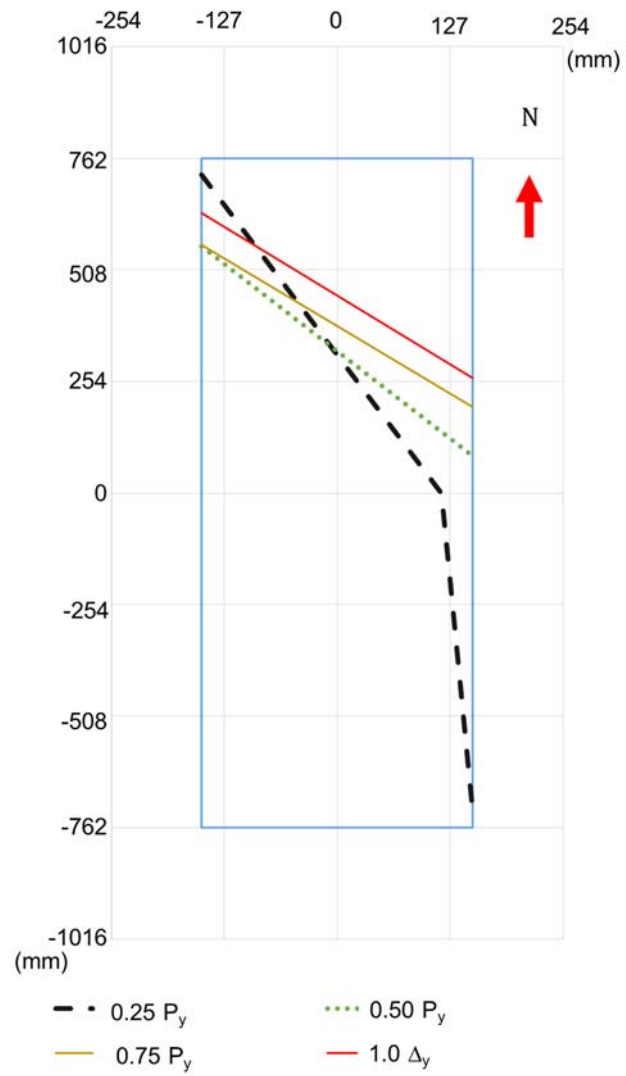
Figure 4.36 SC-T-Vn: Evolution of neutral-axis (in-plane push (+) half cycles)

a) North face   b) South face

Figure 4.37 SC-T-2.5Vn: Pre-cracking in the specimen before loading

a) North face   b) South face

Figure 4.38 SC-T-2.5Vn: Specimen state before in-plane loading cycles
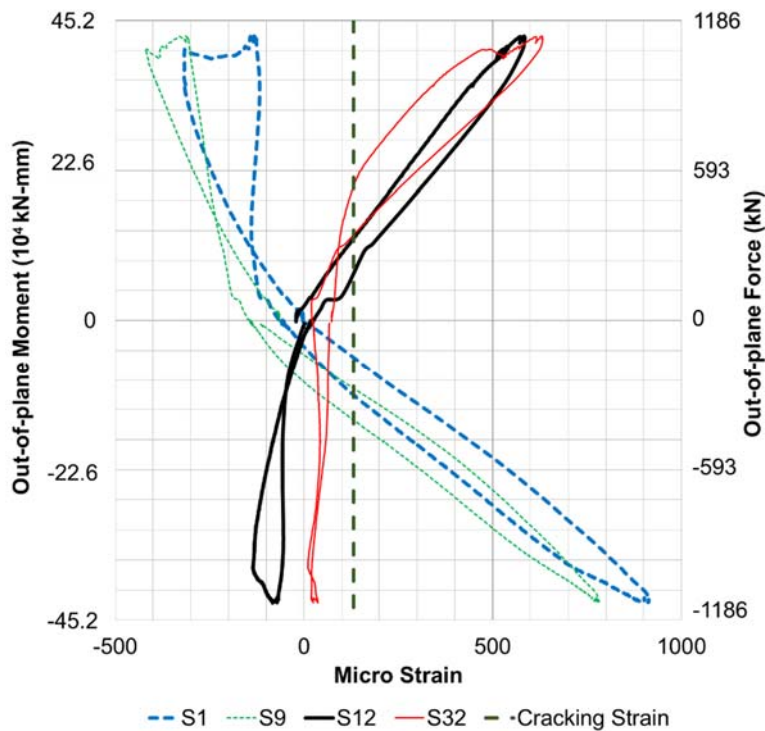
Figure 4.39 SC-T-2.5Vn: Faceplate vertical strains for 1113-kN out-of-plane loading cycle
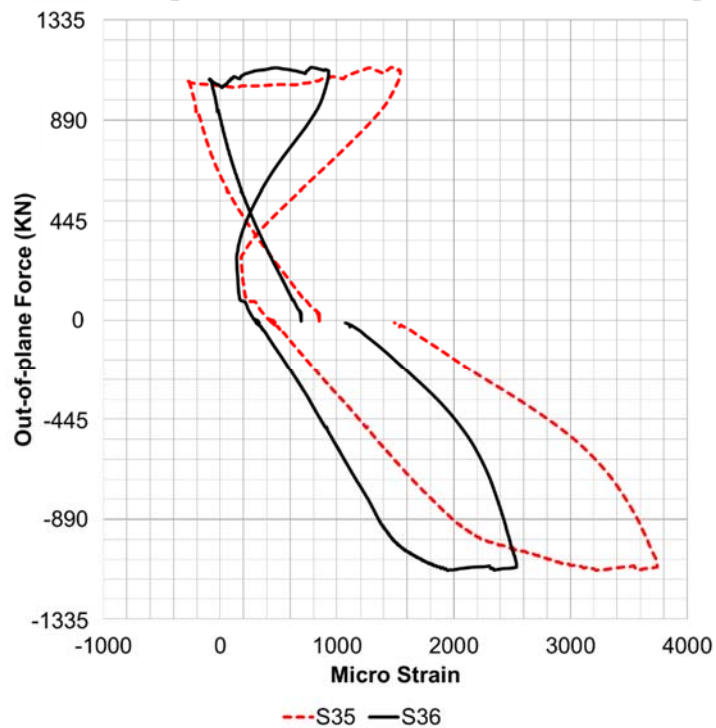
Figure 4.40 SC-T-2.5Vn: Tie strains for 1113-kN out-of-plane loading cycle
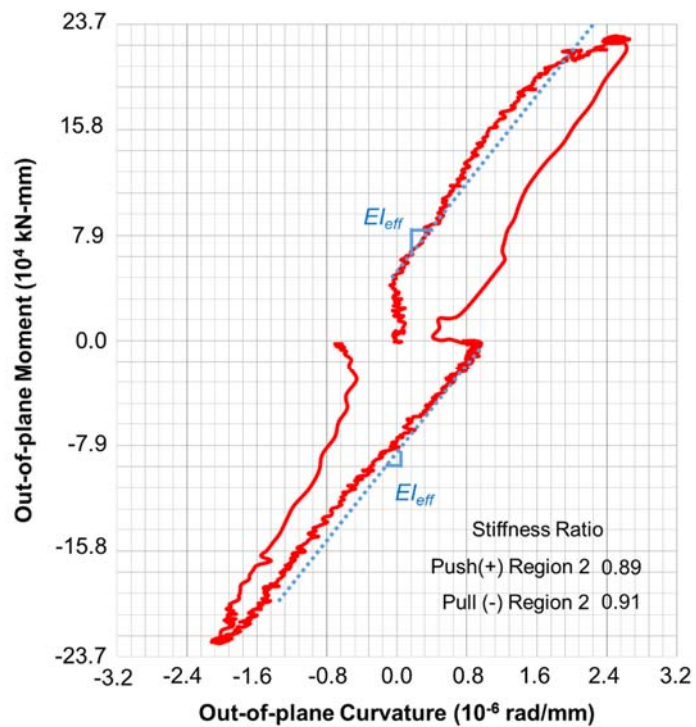
Figure 4.41 SC-T-2.5Vn: Out-of-plane moment-curvature response (for 1113-kN cycle)
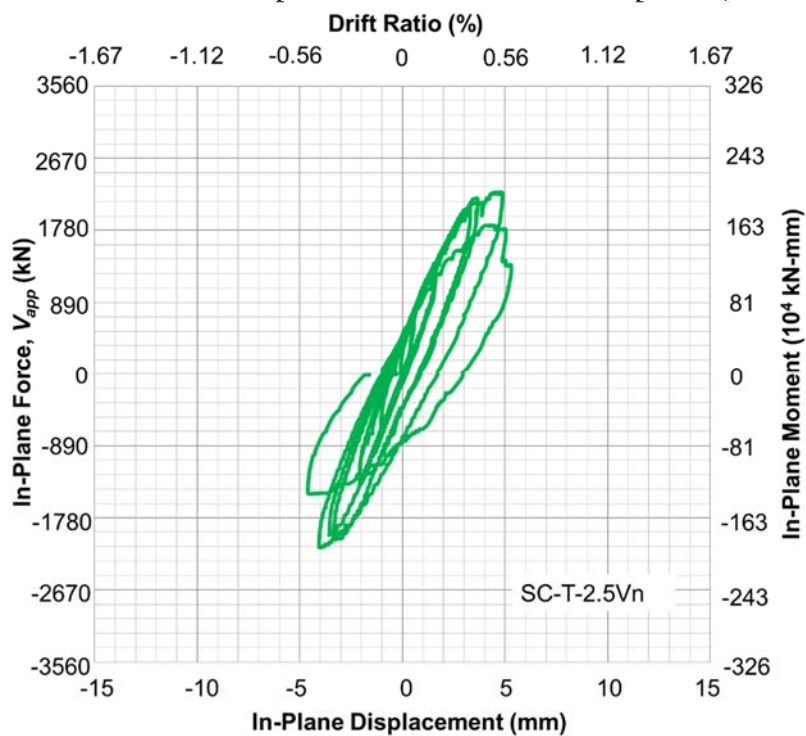
Figure 4.42 In-plane force-top displacement response of SC-T-2.5Vn
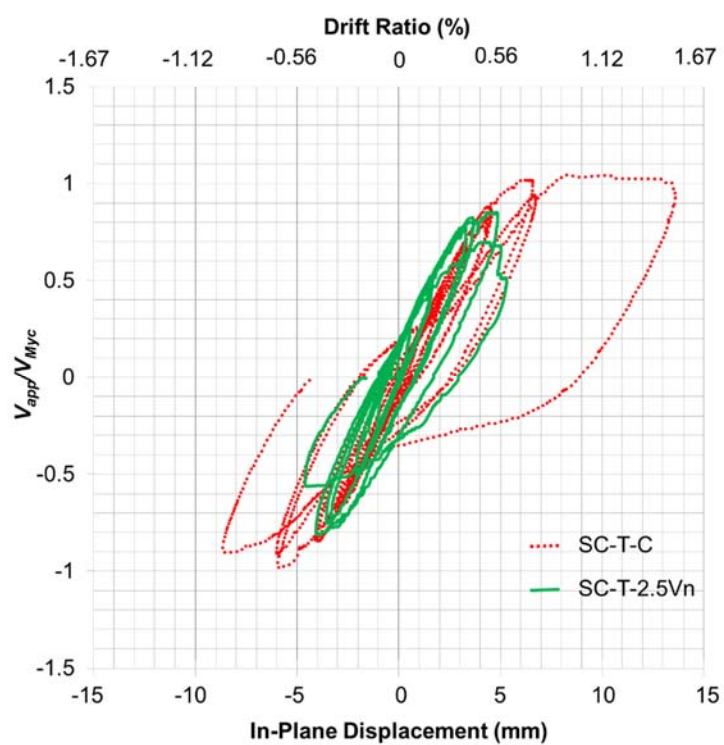
Figure 4.43 Comparison of in-plane force-top displacement response (SC-T-2.5Vn and SC-T-C)
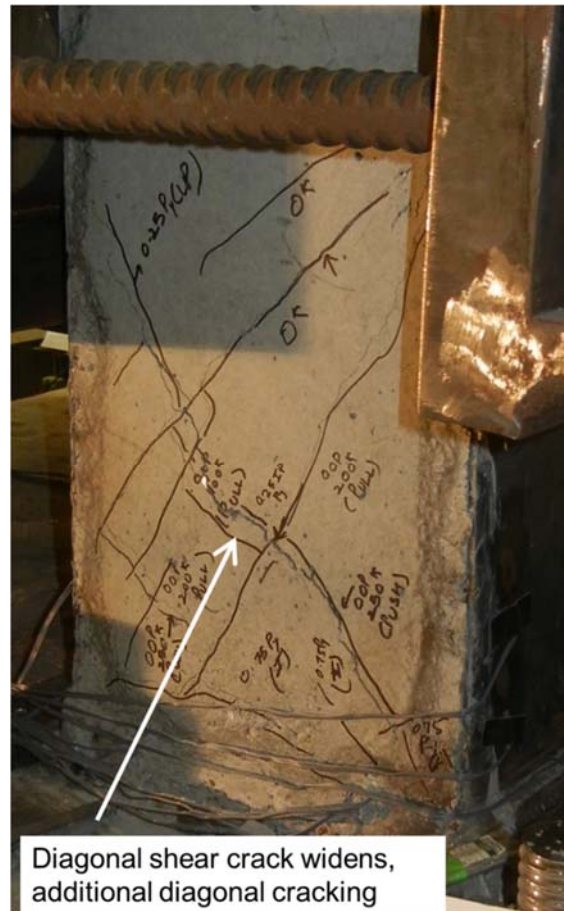
a) North face   b) South face

Figure 4.44 SC-T-2.5Vn: Specimen state at $0.75P_y$ cycles

Initiation of faceplate buckling

Diagonal shear crack widens, out-of-plane deformation increases
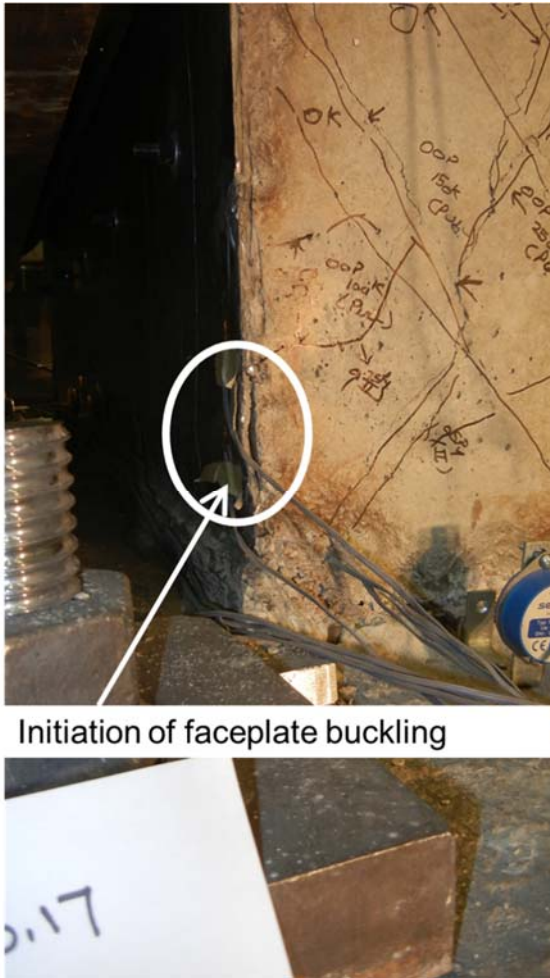
a) North face   b) South face

Figure 4.45 SC-T-2.5Vn: Specimen state at Δ_y, push cycle 1

Figure 4.46 SC-T-2.5Vn: Specimen state (North face) at Δ*y*, pull cycle 1
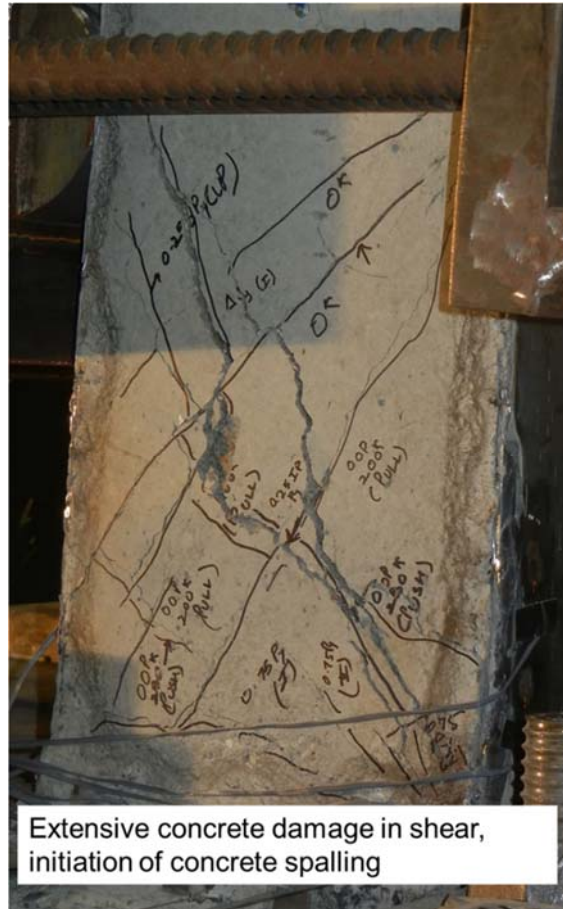
a) North face   b) South face

Figure 4.47 SC-T-2.5Vn: Specimen state at Δ_y, push cycle 2

Concrete crushing at out-of-plane loading location

Concrete crushing at out-of-plane loading location

Specimen slides on the shear crack, as the compression strut can't be anchored on to the buckled faceplates

Faceplate buckling, specimen slides on the shear crack, as the compression strut can't be anchored on to the buckled faceplates

a) North face   b) South face

Figure 4.48 SC-T-2.5Vn: Specimen state at failure (Δ_y, pull cycle 2)
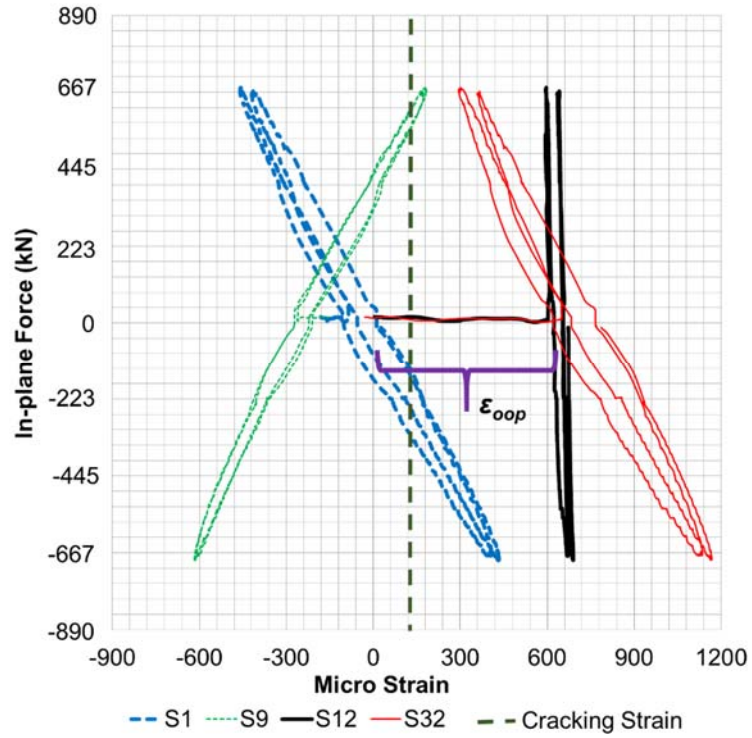
Figure 4.49 SC-T-2.5Vn: Faceplate strains for 0.25P_y cycles
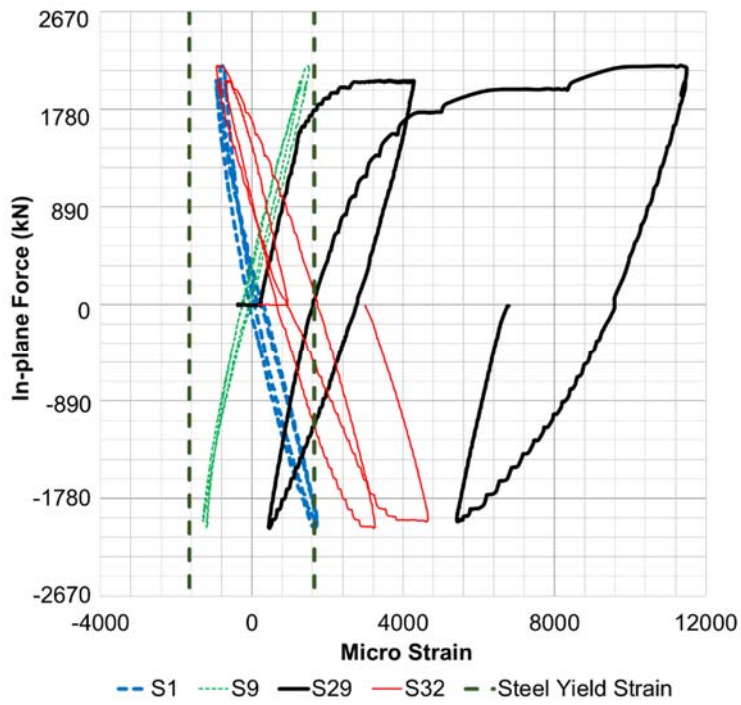
Figure 4.50 SC-T-2.5Vn: Faceplate strains for 0.75P_y cycles

a) At mid-height   b) At top of the specimen
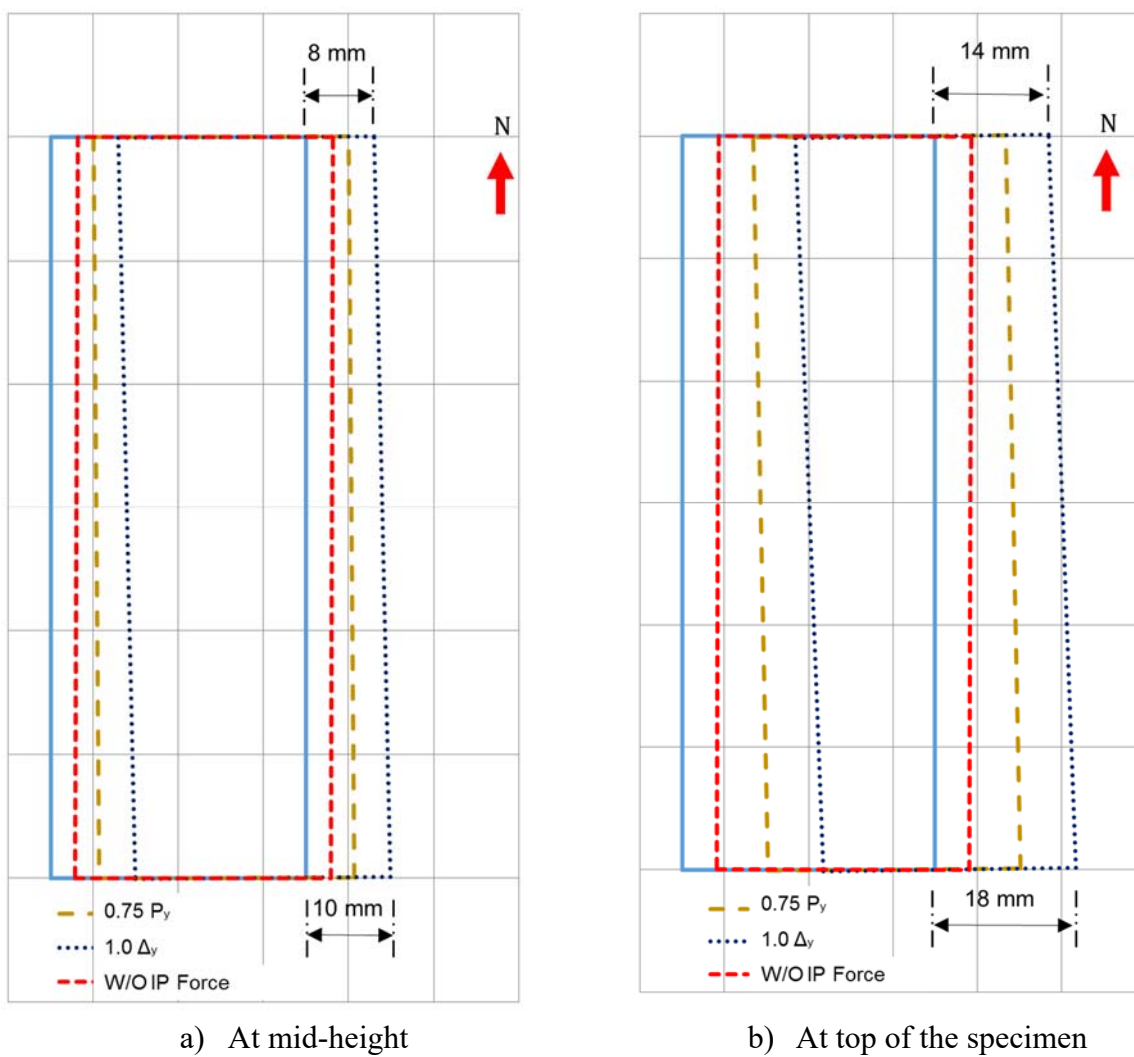
Figure 4.51 SC-T-2.5Vn: Out-of-plane twisting (in-plane push (+) half cycles)
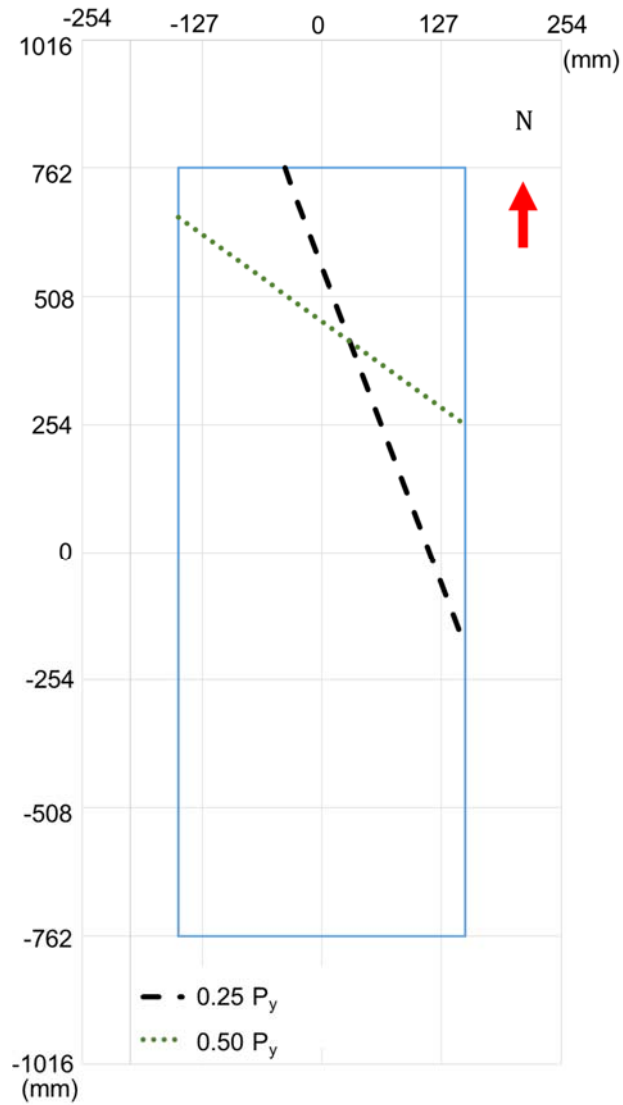
Figure 4.52 SC-T-2.5Vn: Evolution of neutral-axis (in-plane push (+) half cycles)
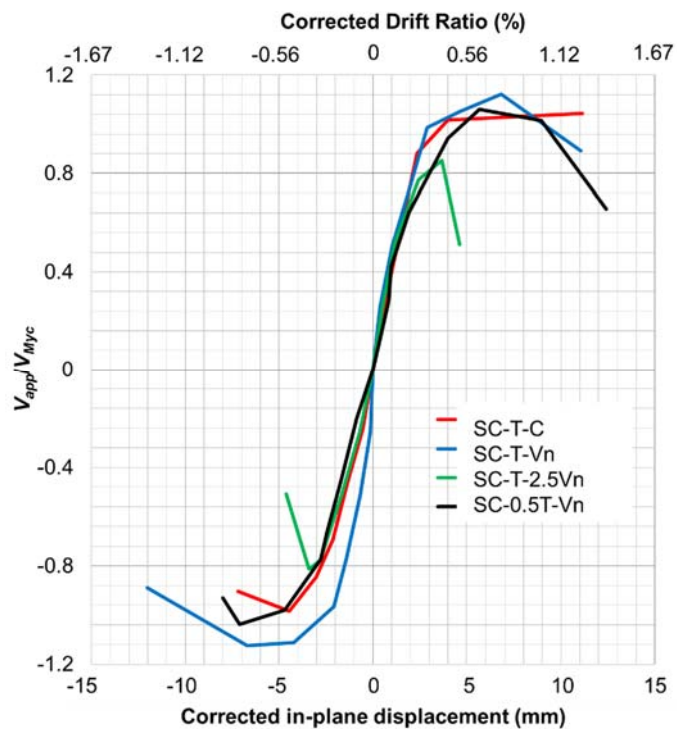
Figure 4.53 Normalized in-plane backbone curves for SC wall pier specimens (with corrected drift)
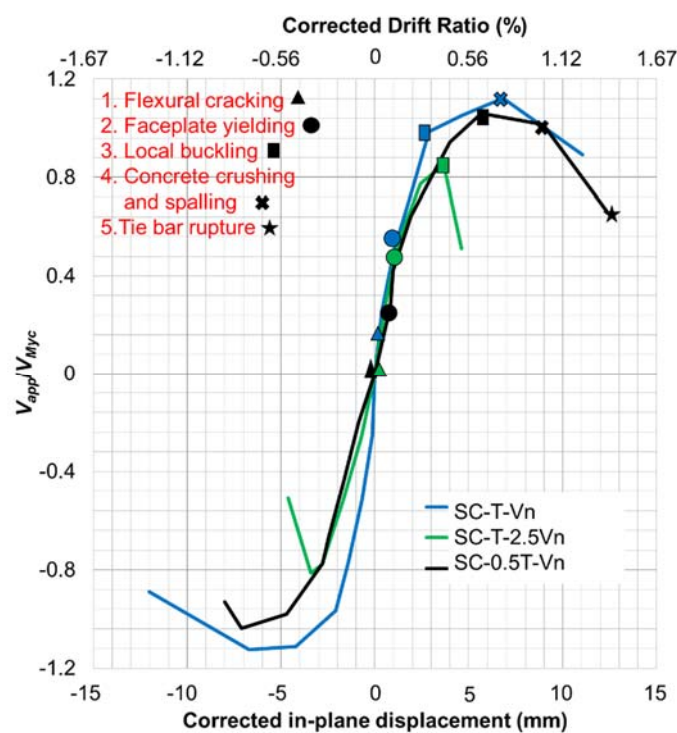
Figure 4.54 Damage states for specimens with biaxial loading (with corrected drift)

Table 4.1 Normalized out-of-plane stiffnesses

Specimen	SC-T-Vn	SC-0.5T-Vn		SC-T-2.5Vn	
Out-of-plane force cycle (kN)	534	534	1070	556	1113
Stiffness Ratio* (Push)	**0.80**	**0.96**	**0.98** (0.80)	**0.64**	0.89
Stiffness Ratio* (Pull)	**0.64**	**1.12**	**0.70** (0.47)	**0.60**	0.91

*Values in bold are the ratio of Region 1 (corresponding to out-of-plane moment less than the cracking moment) stiffness with EI_{uncr}. The remaining values are the ratio of Region 2 (corresponding to out-of-plane moment greater than the cracking moment) stiffness with EI_{eff}.

Table 4.2 Measured in-plane stiffnesses of the specimens

Specimen	Initial Stiffness* (kN/mm)		Secant Stiffness* (kN/mm)	
	Push	Pull	Push	Pull
SC-T-C	1765 (980)	1400 (890)	980 (635)	925 (570)
SC-T-Vn	1625 (810)	1390 (760)	1115 (690)	1015 (635)
SC-0.5T-Vn	915 (615)	720 (450)	640 (440)	570 (395)
SC-T-2.5Vn	1840 (1055)	1030 (740)	655 (580)	630 (500)

*Stiffness values in parenthesis are the uncorrected stiffnesses corresponding to measured top displacement (not accounting for the slip at the base and rotation at base).

Table 4.3 Summary of experimental results (in-plane)

Specimen	V_{oop}/V_n^{ACI}	M_{oop}/M_n^{AISC}	$V_{n\text{-}ip}$ (kN)	$V_{n\text{-}ip}/V_{Myc}$	$V_{n\text{-}ip}/V_{Mp}$	K_{in}/K_{uncr}	$_{sec}/K_{cr}$	$\Delta_{u\text{-}ip}^{corr}$ (%)
SC-T-C	N.A.	N.A.	3115	1.01	0.87	0.38 K	0.88	1.02
SC-T-Vn	0.98	0.37	3180	1.10	0.98	0.32	0.98	1.29
SC-0.5T-Vn	0.92*	0.74	2738	1.04	0.90	0.21	0.57	0.95[#]
SC-T-2.5Vn	2.46	0.78	2180	0.83	0.71	0.36	0.60	0.51

* V_n^{ACI} is calculated using measured properties for rebars.

[#]Value is for the last full-cycle completed ($2\Delta_y$ cycle)

5. SC STRUCTURES SUBJECTED TO SEISMIC AND THERMAL LOADS: DESIGN OF EXPERIMENTS

This chapter presents the design of experiments for SC walls and wall piers subjected to combined seismic (in-plane) and accident thermal loads. The experimental program was developed based on the observed behavior of SC walls and wall piers for in-plane loading, typical accident durations and magnitudes, and structural response to accident thermal loading. The specimens were designed to meet the detailing requirements of AISC N690s1 [26]. The program focused on evaluating the effect of different durations and magnitudes of accident temperature loads on the in-plane response of SC walls and wall piers.

The chapter is organized into following sections.

- Design of Test Matrix: Specimen details and the basis of selecting the parameters to be varied are discussed in this section.

- Loading and Heating Protocol: Rationale behind the loading and heating protocol designed for the specimens is discussed in this section.

- Design of Test Setup: This section presents the details of the test setup and the basis of the design. The heater assembly design and details are described.

- Instrumentation of Specimens: The types of instrumentation used, and the measurements recorded for the experiments are described in this section.

- Construction Sequence: This section presents the procedure and sequence followed for fabrication and construction of the specimens and the test setup.

5.1 Design of Test Matrix

For SC wall piers (SC-WP), SC-T-C (discussed in Chapters 3 and 4) was used as control specimen (called as SC-WP-C). SC-WP-C was subjected to in-plane loading (no heating). One heated (SC-WP-H) specimen were tested. One heated SC wall (SC-W-H) specimen was tested. The heated specimens were also subjected to cyclic in-plane loading.

Table 5.1 presents the specimen details for the experiments. The table presents the specimen height (h), length (l_w), thickness (T), faceplate thickness (t_p), flangeplate thickness (t_f), aspect ratio (h/l_w), reinforcement ratio ($\rho = 2t_p / T$), faceplate stud spacing (s/T), faceplate slenderness ratio (s/t_p), flangeplate slenderness ratio (s_f/t_f), and tie spacing (S/T). Measured faceplate (f_{yp}) and flangeplate (f_{yf}) yield strength, day-of-test concrete compressive strength (f'_c), and maximum surface temperature for the specimens is also provided in the table.

For SC wall piers (SC-WP), the specimen aspect ratio was kept equal to 0.6 in order to maximize the shear contribution of the wall pier as recommended by Kurt et al. [69]. The specimens were 305 mm (12 in.) thick (1/3-1/4 scale of typical SC walls in nuclear facilities). Steel faceplate thickness was 4.8 mm (3/16-in.), resulting in a faceplate plate reinforcement ratio of 0.031. Steel faceplate thickness was set at 4.8 mm because it is the smallest plate thickness in the structural plate category. Smaller thicknesses result in sheet metal properties and associated waviness imperfections, which are not representative of the actual structure. The faceplate slenderness ratio was designed to meet the limit recommended by AISC N690s1 [26] to develop faceplate yielding in compression before local buckling, based on Zhang et al. [1].The stud and tie layout for SC-WP-H is presented in Figure 5.1. The specimen had ties spaced at half the section thickness. SC-WP-C had ties spaced at section thickness.

Typical SC walls in safety-related nuclear facilities have cross-walls connected to them. Therefore, the lateral load response of these walls is typically shear dominated. Additionally, shear failure is a more onerous limit state in comparison to flexural failure, and should preferably not be the governing limit state. Therefore, for SC wall (aspect ratio of 0.75) specimen, flange plate thickness, faceplate thickness, and the specimen dimensions were designed to ensure that the wall fails in in-plane shear mode without premature buckling of the faceplates. Specimens tested by Kitajima et al. [122] were modeled and analyzed to develop benchmark models that were later used for predicting the ambient behavior and response of SC-W-H. The monotonically loaded specimen tested by Kitajima et al. [122] in ambient condition (Specimen No. 2) was modeled using the finite element method for developing benchmark models. In-plane force-top displacement response of Specimen No. 2 is compared with the numerical analysis results in Figure 5.2. The figure also includes horizontal lines corresponding to shear (V_n^{AISC}) and flexural strength (M_{ny}) of the wall. The shear strength was calculated using the in-plane shear strength equations in AISC N690s1 [26]. The flexural strength was calculated based on section analysis assuming yielding in the end-plates, faceplates in the elastic range and rectangular block for concrete in compression. The benchmarked models were then used to predict the behavior and response of the designed SC wall specimens. The end plate thickness was used as a parameter to design the specimen to have flexural strength larger than shear strength and to have in-plane shear as the governing failure mode. As shown in Figure 5.3, three different thicknesses for end plates were used in the models [12.7, 19.0, 25.4 mm (0.50, 0.75 and 1.00 in.)]. The response comparisons indicate that the 19-mm endplate thickness provided sufficient flexural capacity that the specimen fails in shear. Flangeplate stud details and flangeplate-to-baseplate weld details are presented in Figure 5.4. Studs were welded on flangeplates to ensure composite action between flangeplates and concrete infill. Faceplate

thickness was kept at 2.64 mm (0.104 in) to ensure that the specimen has a shear controlled response. Figure 5.5 presents the stud and tie layout, and dimensions for the faceplates. SC-W-H had ties spaced at half the section thickness.

5.2 Loading and Heating Protocol

Loading and heating protocol for the heated specimens is summarized in Table 5.2. The heated specimens were subjected to two surface temperature amplitudes [149°C (300°F) and 232°C (450°F)] and subjected to force cycles at heating durations of 1 hour and 3 hours. The temperature amplitudes are based on idealized typical surface time-temperature histories for containment internal structures (CIS) for postulated pipe break scenarios as obtained from public domain documents [101] (discussed previously in Section 2.6). Based on the discussion in Bhardwaj et al. [104], 1-hour heating duration was chosen to obtain a non-linear thermal gradient (resulting in extensive concrete cracking) through the cross-section. The 3-hour heating duration will result in more uniform temperatures through the cross-section (reducing the crack widths). The heating durations were scaled down for the specimens (1/3 to 1/4 scaled specimens) to result in through thickness temperature profiles similar to those observed in physical wall structures (Figure 2.16), as discussed in Sener et al. [101]. The specimens were cooled to ambient condition after completing the load cycle at 3 hours of heating, and heated/loaded to the next temperature/load level.

The first three load cycles were performed at ambient temperature and the load levels corresponded to 25, 50 and 75% of the estimated specimen strength, F_n (Cycles 1, 2, 3). For SC-WP-H, F_n is the force corresponding to the compression yield moment (M_{yc}) [69]. For SC-W-H, F_n is the force corresponding to the nominal shear strength of the specimen, based on AISC N690s1 [26] Equation A-N9-19. The initial cycles were performed to investigate the ambient response of the wall pre-

and post-concrete cracking and before faceplate yielding, and to compare the ambient response with response under accident thermal loads. The ambient cycles were followed with heated load cycles by subjecting the faceplate to surface temperature of 149°C for 1 and 3 hours (Cycles 4, 5). Similar load cycles were conducted for surface temperature of 232°C (Cycles 6 and 7). The test was switched to displacement controlled loading in the remaining load cycles. The yield displacement (Δ_y) was estimated as the displacement corresponding to the expected strength (F_n) of the specimen, based on the secant stiffness observed in Cycles 6 and 7. The test continued with displacement cycles at $1.0\Delta_y$ (Cycles 8, 9), $1.5\Delta_y$ (Cycles 10, 11). For specimen SC-W-H, additional ambient loading cycles (9b and 11b) were performed after the heated cycles at target displacement levels of $1.0\Delta_y$ and $1.5\Delta_y$ to verify if there is an increase in the specimen stiffness post-cooling. The ambient specimen (SC-WP-C) was subjected to two loading cycles at each target force or displacement level. The loading and heating cycles following the cycles mentioned in Table 5.2 were decided based on the post-peak response of the specimens. Figure 5.6 presents the loading and heating time history for specimen SC-WP-H. The history is consistent with the loading and heating protocol presented in Table 5.2. Post $1.5\Delta_y$ displacement cycles, the specimen was subjected to $2.0\Delta_y$ displacement with the surface temperatures maintained at 232°C for a duration of 4 hours. Figure 5.7 presents the loading and heating time history for specimen SC-W-H. Post $1.5\Delta_y$ displacement cycles, the specimen was subjected to $2.0\Delta_y$ displacement cycles with surface temperatures maintained at 232°C for heating durations of 1 hour and 3 hours.

5.3 Design of Test Setup

Setup for the experiments was designed based on the specimen details, design in-plane capacity of the specimens, and the magnitude and duration of thermal loading to be applied. Figure 5.8 presents the 3D rendering of the test setup (for SC wall pier specimens) with all the components

of the test setup (ceramic heaters for applying the thermal loading not shown). Test assembly with the SC wall pier specimen installed is presented in Figure 5.9a. The heaters were installed on the faceplates as shown in Figure 5.9b. The same test assembly was used for SC-W-H specimen. For SC-W-H, heaters were installed on the faceplates (webplates) and the flangeplates. The setup can be categorized as follows.

In-Plane Loading: Cyclic in-plane loading was applied by two double acting hydraulic rams (Enerpac RR50012). The hydraulic rams were each capable of exerting a force of magnitude 565 ton (1130 kips) in push and 314 ton (628 kips) in pull. The actuators were post-tensioned to a reaction wall through clevises and a built-up wall box. The actuators applied load to the specimens through a loading beam, in end bearing and bearing at holes in the specimens.

Foundation Block and Specimen Connection: The SC-WP steel assembly (faceplates without concrete infill) were welded to a re-usable base plate that was centered on top of the foundation block. Baseplate and foundation block details have been discussed previously in Section 3.2. For SC-W specimen (with flangeplates), the steel assembly (with flangeplates, faceplates, studs, and ties) was fabricated, and then welded to the re-usable baseplate. The faceplate (and flangeplate) to baseplate connection was designed to be stronger than the wall and limited the inelastic action to the wall. Weld details for SC wall pier and faceplates of SC wall specimen are shown in Figure 3.6. Weld details for flangeplate-to-baseplate connection are shown in Figure 5.4b. Concrete was poured into the assembly after the assembly had been welded to the baseplate.

Thermal Loading: Heating equipment employed for these experiments has previously been successfully used for conducting fire testing of structural elements (CFT columns, beam-columns, slabs, and connections) at Purdue University ([27]–[31]). Accident thermal loading was applied using high-temperature ceramic-fiber radiant heating panels. The heaters were manufactured by Watlow Electric Manufacturing Company. Each heater panel consisted of a flat heating element, ceramic fiber insulation, and a custom built outer metal casing. The metal casing could be used for mounting different configurations and numbers of panels on the test setup, allowing for flexibility in the implementation of heating. Heaters were placed close to the specimen surface using springs that held the heaters together (as shown in Figure 5.9b). White fiberglass insulation was used to reduce heat losses during the experiments. The insulation was placed between the edges of the heaters and the specimens. Each heater was controlled individually and operated on a feedback control loop that referenced a thermocouple attached to the heated surface of the specimens. The heating was controlled using the PID-Controller of the heaters and software package SpecView [126]. SpecView provides a graphical user interface for controlling and monitoring the heaters based on the surface temperature and the specified temperature. The software controls the amount of power input to the heaters based on the difference in surface temperature and the specified temperature.

5.4   Instrumentation of Specimens

Figure 5.10 to Figure 5.14 present the instrumentation and heater layout for SC-WP-H specimen. High-temperature strain gauges (ZF series manufactured by TML Ltd.) were employed to measure the strains. Since the response of the wall piers was expected to be flexure controlled, strain gauges were installed in the bottom region of the faceplates (as shown in Figure 5.10). Strain gauge rosettes were installed to obtain shear strain values for the wall pier. Displacement sensors (SPs in

Figure 5.11) were used to measure the in-plane displacement of the top, mid-height, and bottom of the wall. The displacement measurements were employed to obtain in-plane force-displacement response of the specimen, and in-plane base slip corrections. Rotation meter (clinometer) was installed at the base of the wall in the in-plane direction (CM1 in Figure 5.11). For SC-WP-C, another clinometer was installed in the in-plane direction 51 mm (2 in.) above the baseplate. The clinometer data was used to obtain base rotation correction values for specimen displacement. For redundancy, two sets of displacement measurements were recorded at each location.

Figure 5.12 presents the heater assembly layout and the details of thermocouples installed on the surface of the specimen. Region of the faceplates between the base and the loading beam [610 mm (24 in.)] was heated. The heater assembly for each faceplate consisted of four heaters. Sets of two thermocouples (STs in the figure) was installed on the faceplates at locations corresponding to the center of each heater. One of the thermocouples (e.g., ST1) was connected to the control program to monitor and control the heaters and the surface temperatures. The second thermocouple (e.g., ST2) was connected to the data acquisition system to record the surface temperature data. Type-K thermocouples capable of measuring temperatures up to 1250˚C were used for the experiments. The thermocouples were spot-welded to the faceplates using a portable strain-gauge welder, and the thermocouple junctions were protected and insulated with the Omega high-temperature cement. Dimensions of heaters for the heater assembly and the locations of surface thermocouples for East and West Faceplates are shown in Figure 5.13. An important objective of the experiments was to obtain the evolution of non-linear thermal gradients through the thickness of the specimens as the surface was subjected to accident temperature histories. Figure 5.14 shows the thermocouple tree layout for SC-WP-H specimen. A thermocouple tree consisted of five thermocouples welded on a steel rod. The steel rod was then either left hanging in the steel assembly before concrete was

poured (CTs), or the thermocouples were installed on a tie bar (TTs). Multiple thermocouple trees were embedded in concrete to obtain redundant temperature data.

Instrumentation details for SC-W-H specimen are presented in Figure 5.15 to Figure 5.20. High-temperature strain gauges were installed on the inner and outer faces of the flangeplates to obtain flexural strain values and to check for any buckling the flangeplates (Figure 5.15). Since the response of SC-W-H was expected to be shear dominated, numerous strain gauge rosettes were installed on the faceplates to enable measurement of shear strain data (Figure 5.16 and Figure 5.17). Figure 5.18 shows the details of the displacement sensor layout for the specimen. The displacement measurements were used to obtain the in-plane force-displacement response of the specimen, and in-plane base slip corrections (and to back-calculate the flexural deformation of SC wall). Rotation meters (clinometers) were installed at the base of the wall in the in-plane (CM1 and CM2) and out-of-plane (CM3) direction. The in-plane rotation data was used to apply base rotation corrections to in-plane force-displacement plots. Layout of the heater assembly and surface thermocouples is also presented in the figure. Details of the heater assembly and surface thermocouple locations are presented in Figure 5.19. Details of the thermocouple trees, with heaters overlaid, are presented in Figure 5.20.

5.5 Construction Sequence

Construction sequence of SC wall pier specimen was similar to that for biaxially loaded specimens (discussed in Section 3.4). Figure 5.21 shows the faceplate after installation of shear studs and strain gauges. The ties were placed to receive the other faceplate, and assemble the steel. After the faceplates were assembled, the empty wall pier was placed on the re-usable baseplate, and faceplates were welded to the baseplate. Figure 5.22 shows the welding in progress. The interior region of faceplate was welded to the baseplate in multiple passes using a semi-automated welding

process. The corners were then welded manually. Concrete was poured after the weld cooled down. Since the specimens were scaled, pea-gravel concrete mix was used. Figure 5.23 presents the slump measurements performed before concrete pouring. Once the concrete hardened, instrumentation was installed. Figure 5.24 shows the specimen post installation of surface thermocouples and external strain gauges. Wires for the sensors were insulated using sheathing and insulating fiberglass wool. Figure 5.25 shows the specimen after the heater assembly (as discussed in Section 5.3) was installed, and instrumentation completed.

For SC wall specimen, the studs were shot into the faceplates and flangeplates, and strain gauges were installed on the interior surface. The steel assembly was then fabricated, by welding the faceplates and flangeplates. Figure 5.26 and Figure 5.27 show the welded steel assembly. Faceplates had transfer bars welded at base to enable welding to the baseplate. Flangeplates were also beveled for the same purpose. Hollow steel pipes, that enable the threaded bars for in-plane loading beam to pass through the specimen, were also welded to the faceplates. The steel assembly was then welded to the baseplate. Figure 5.28 shows the welding of faceplate to baseplate in progress. The flangeplate-to-baseplate weld was done manually. The weld was run out of the faceplate to baseplate weld around the corner. Concrete was then poured. Pea-gravel concrete mix was used. Figure 5.29 shows the slump measurements before concrete was poured.

5.6   Chapter Summary

This chapter discussed the design of experiments for SC wall and wall pier specimens subjected to combined in-plane and accident thermal loading. The test matrix was designed to evaluate the effect of different magnitudes and durations of accident temperatures on the in-plane response of wall piers. One SC wall pier and one SC wall specimen were tested for combined in-plane and thermal loading. Wall pier specimen was designed to have a flexure-controlled response (aspect

ratio of 0.6). The wall specimen was designed to undergo in-plane shear failure. Two temperature magnitudes (149˚C and 232˚C) and two heating durations (1-hour and 3 hours) were selected. The specimens were subjected to heating and loading cycles. SC wall pier specimen was subjected to heating on the faceplates. SC wall specimen was subjected to heating on the faceplates (webplate) and flangeplates. The test setup was designed based on the expected in-plane capacity of the specimens. Clevis with press-fit spherical plain bearings was designed and fabricated to enable orthogonal deformations of the specimens without resulting in stresses in the loading rams. The test measurements recorded, the basis, purpose, and type of instrumentation employed for the measurements are discussed. Heating setup and instrumentation employed for tests is discussed in detail. The fabrication and construction sequence of the test setup and specimens is described.
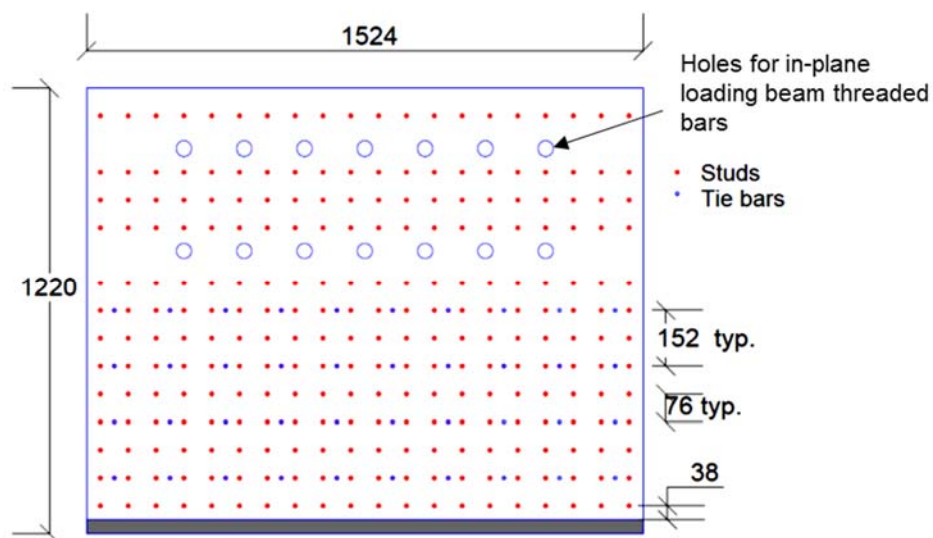
Figure 5.1 SC-WP-H: Stud and tie layout details (in mm units)
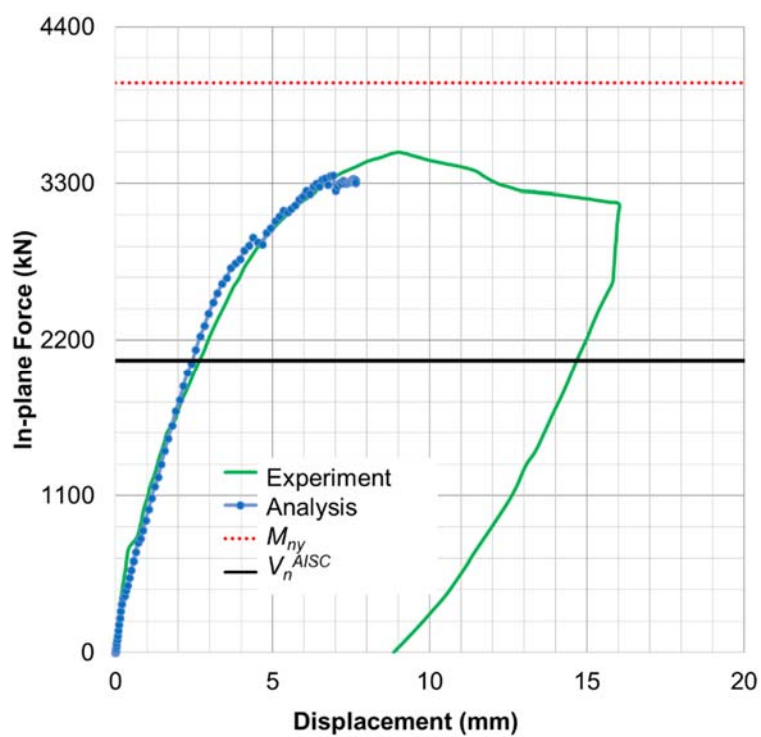
Figure 5.2 Lateral load-deformation response of Specimen No. 2 from Kitajima et al. [122]
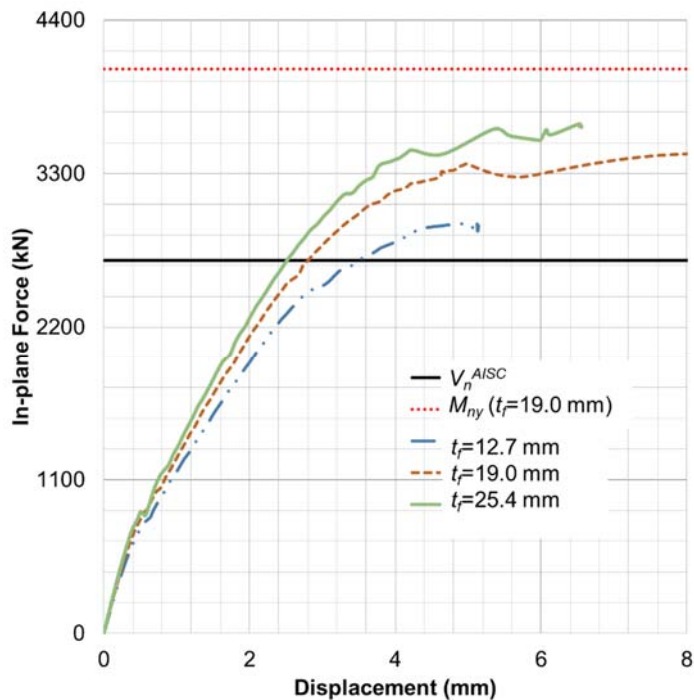
Figure 5.3 Lateral load-deformation response of proposed SC wall specimen (SC-W)
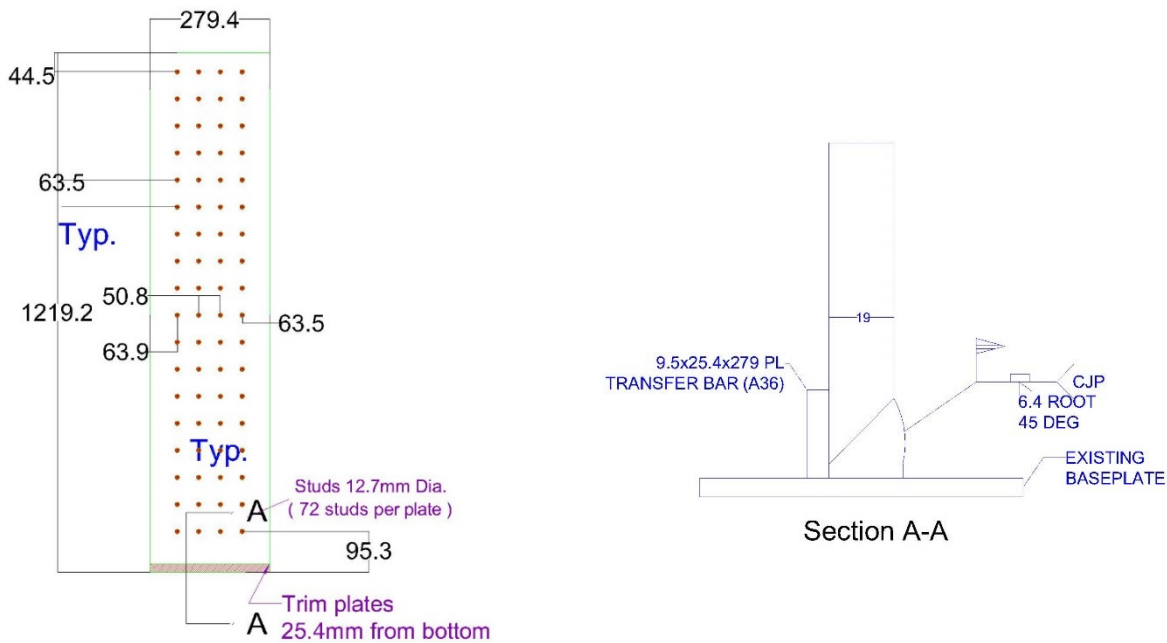
a) Stud and tie layout details   b) Flangeplate-to-baseplate weld details

Figure 5.4 SC-W-H: Flangeplate details
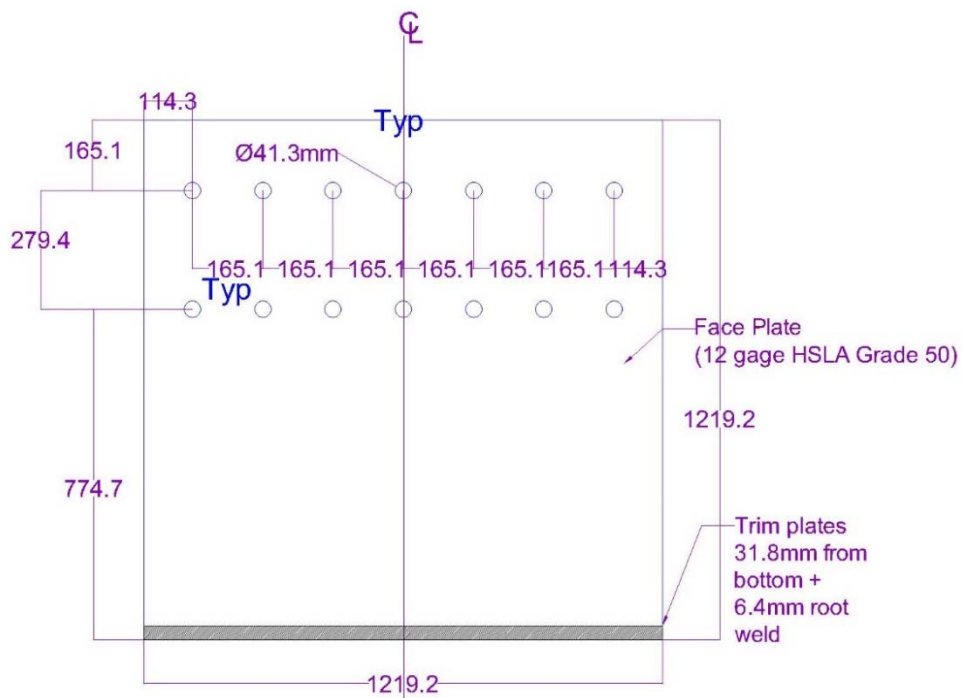
a) Faceplate dimensions

b) Faceplate stud and tie details

Figure 5.5 SC-W-H: Faceplate details (in mm units)
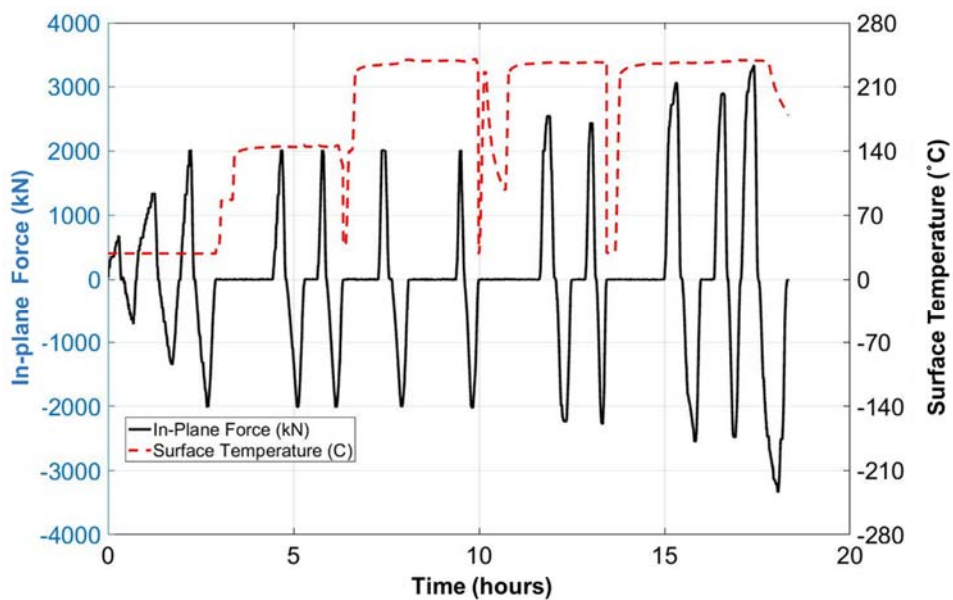
Figure 5.6 SC-WP-H: Load and temperature time history
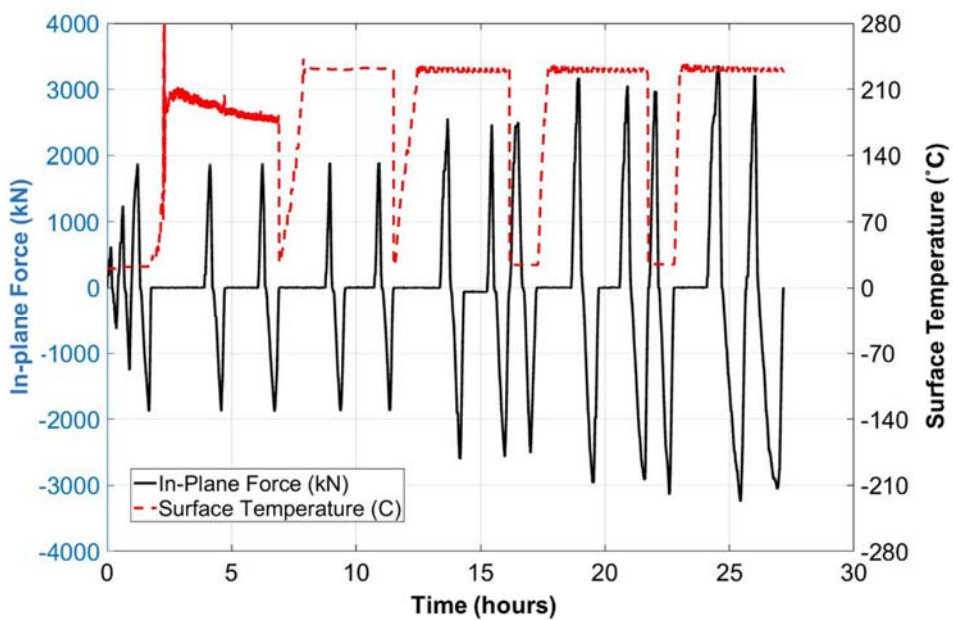
Figure 5.7 SC-W-H: Load and temperature time history
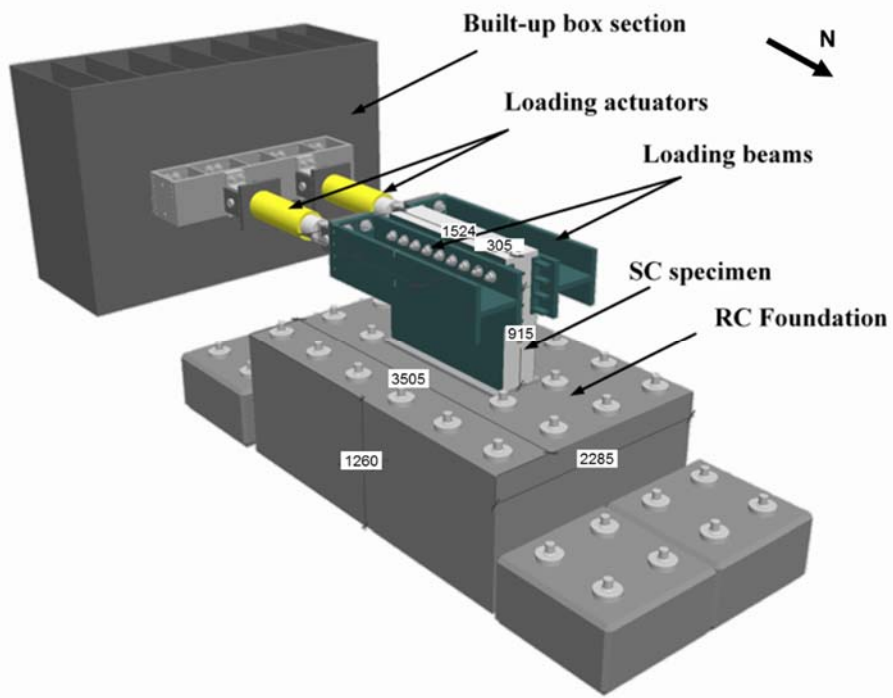
Figure 5.8 SC-WP-H: 3D rendering of the test setup without heaters (from [33])
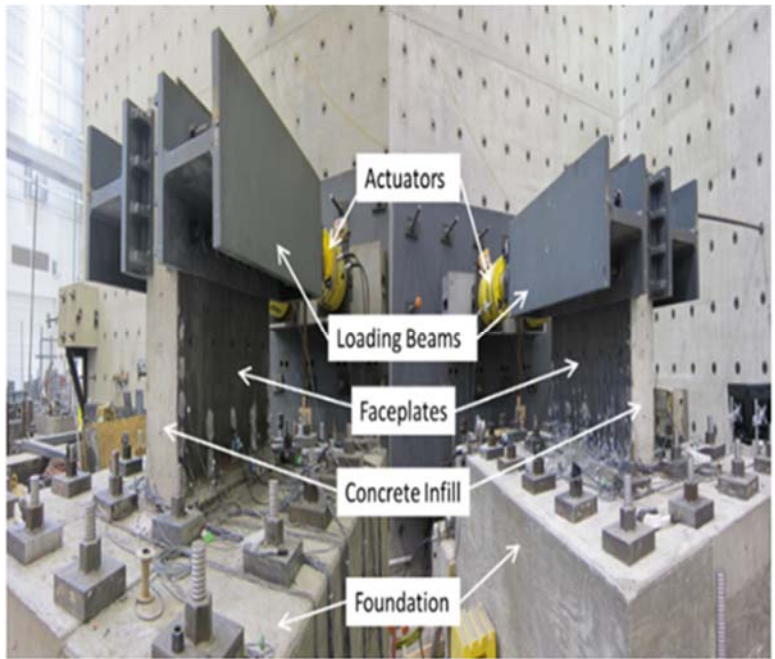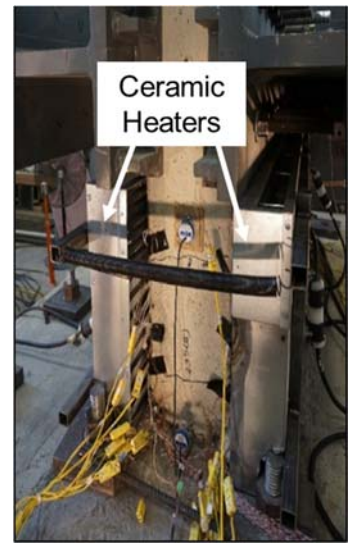
a) Without heaters   b) Heaters installed

Figure 5.9 SC-WP-H: Physical test setup
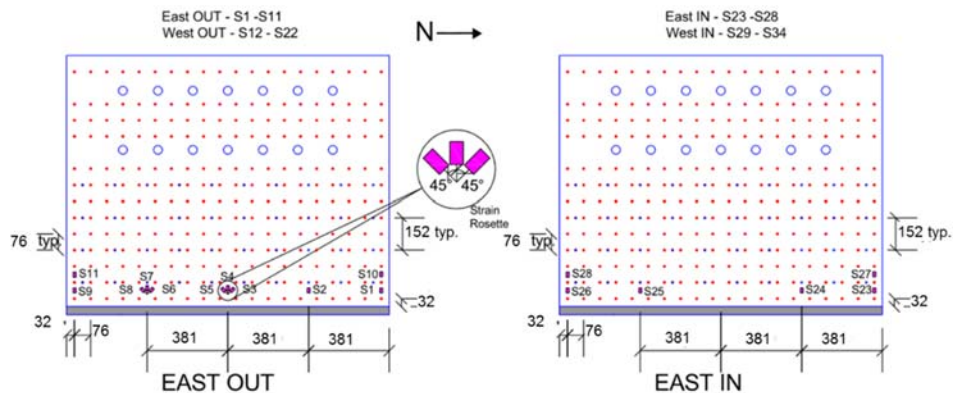
Figure 5.10 SC-WP-H: Strain gauge layout
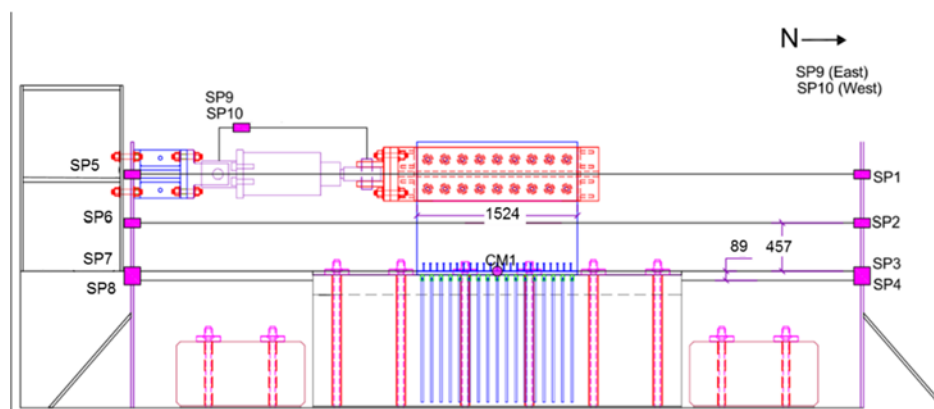
Figure 5.11 SC-WP-H: Displacement sensors (string pots and clinometers)
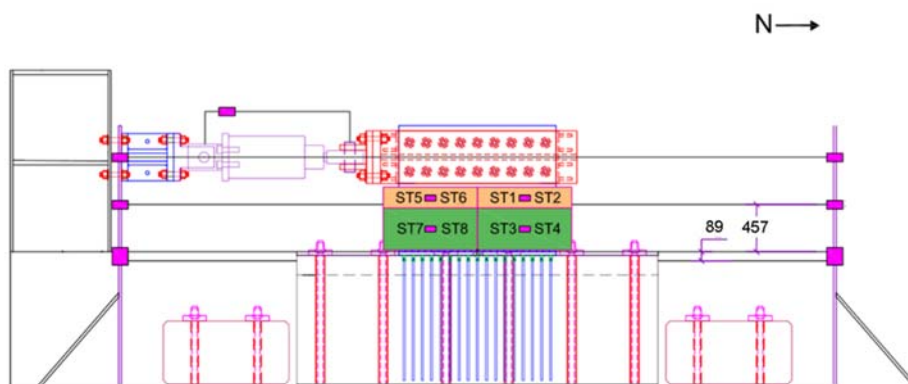
Figure 5.12 SC-WP-H: Heater layout and surface thermocouples
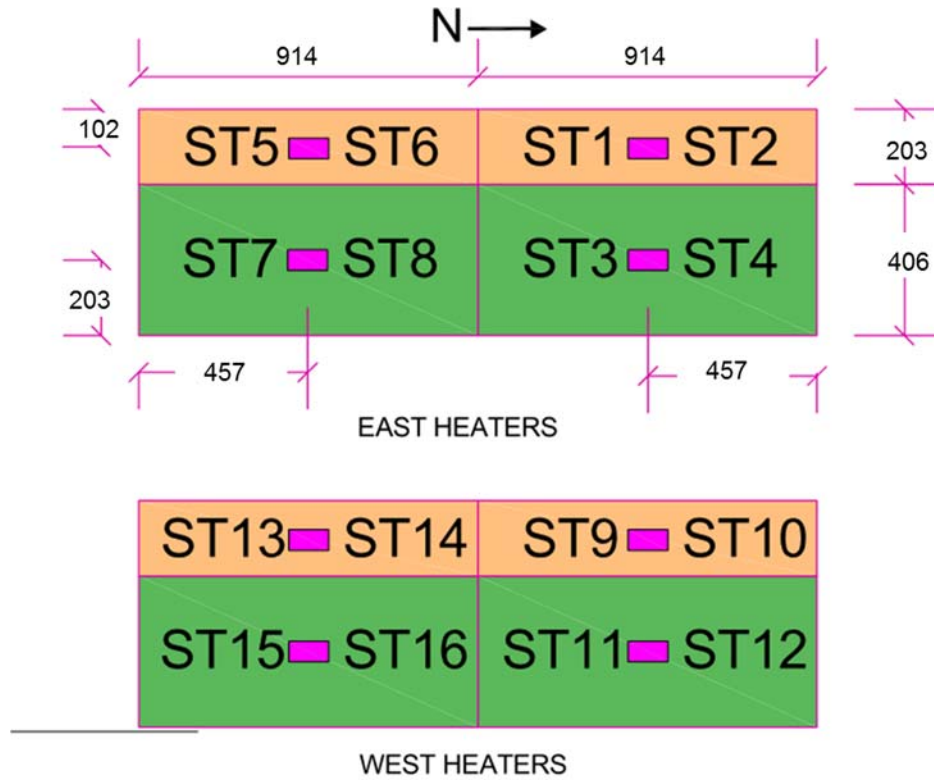
Figure 5.13 SC-WP-H: Heater and surface thermocouple details
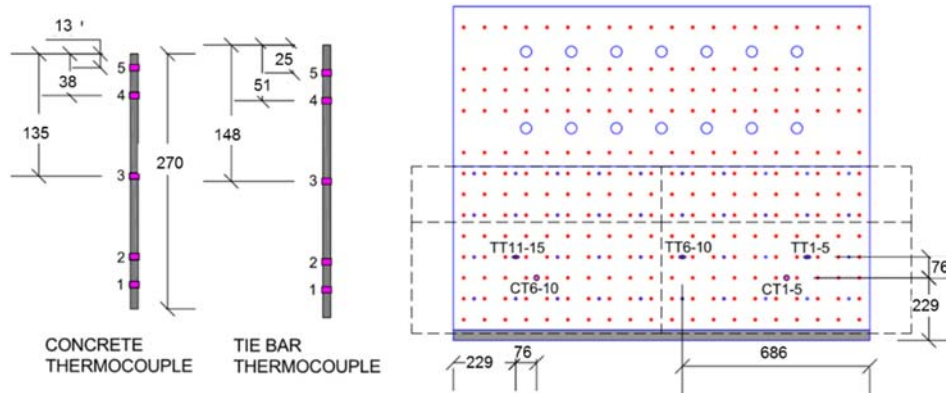
Figure 5.14 SC-WP-H: Thermocouple tree layout (with heaters overlaid)
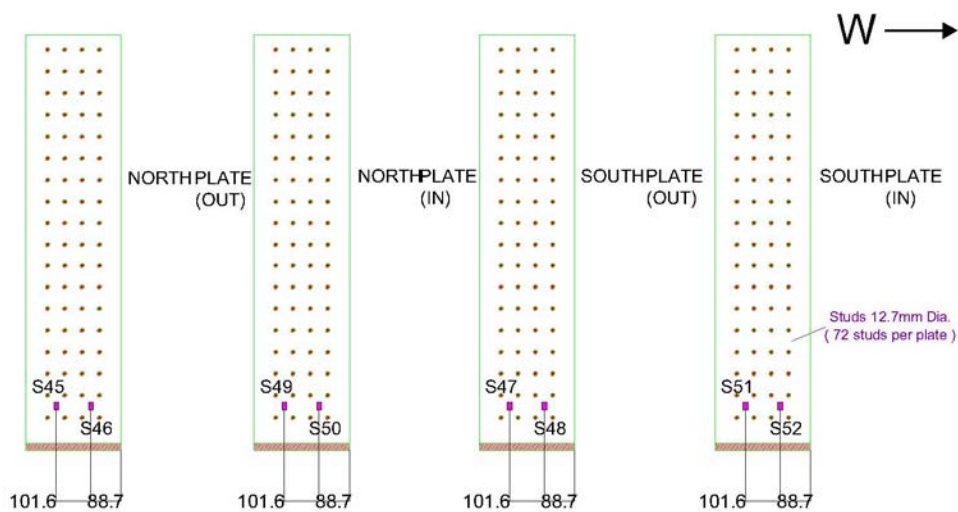
Figure 5.15 SC-W-H: Flangeplate strain gauge layout
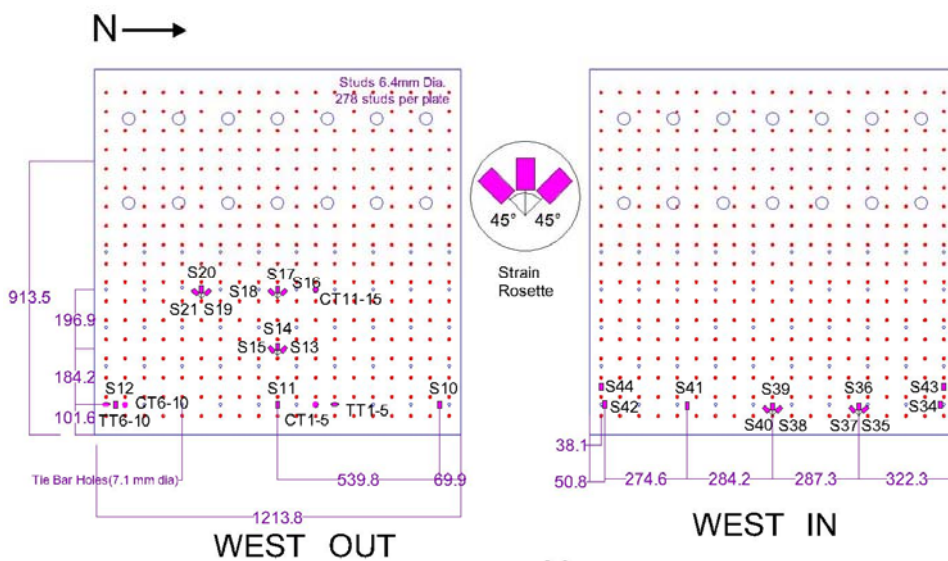
Figure 5.16 SC-W-H: West faceplate strain gauges, and thermocouple tree layout
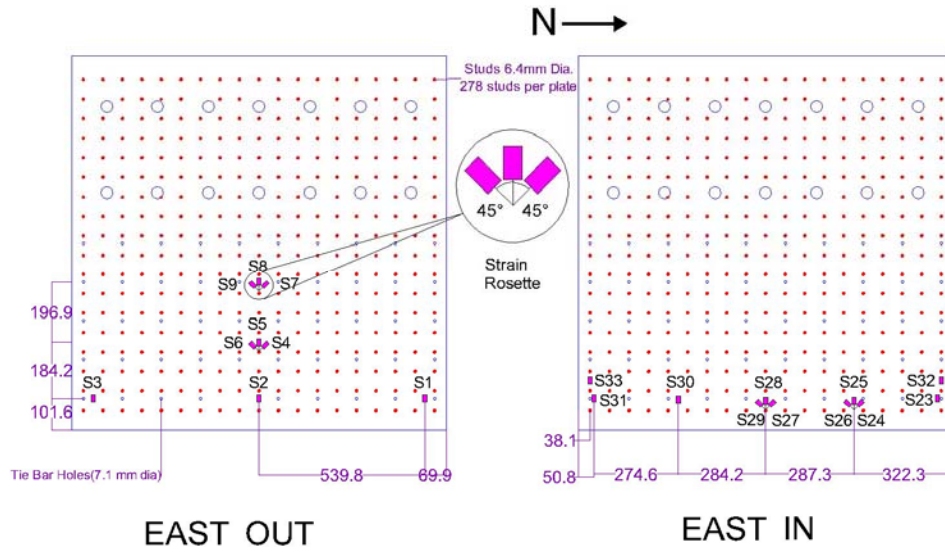
Figure 5.17 SC-W-H: East faceplate strain gauge layout
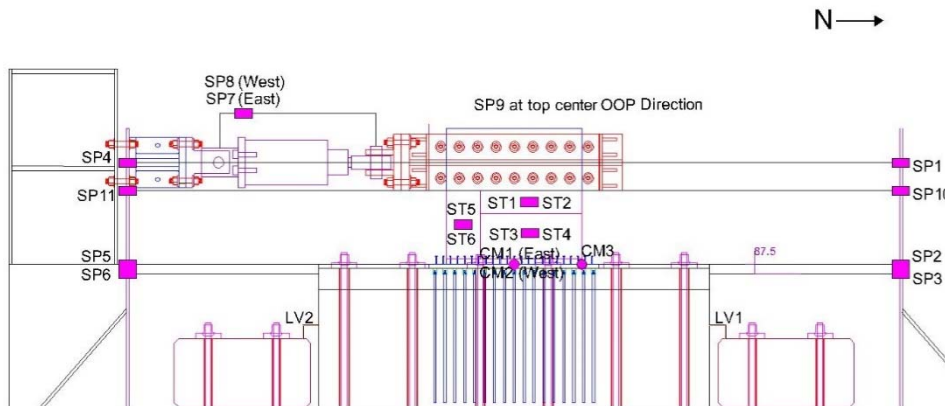
Figure 5.18 SC-W-H: Displacement sensors (string pots and clinometers) and heater layout
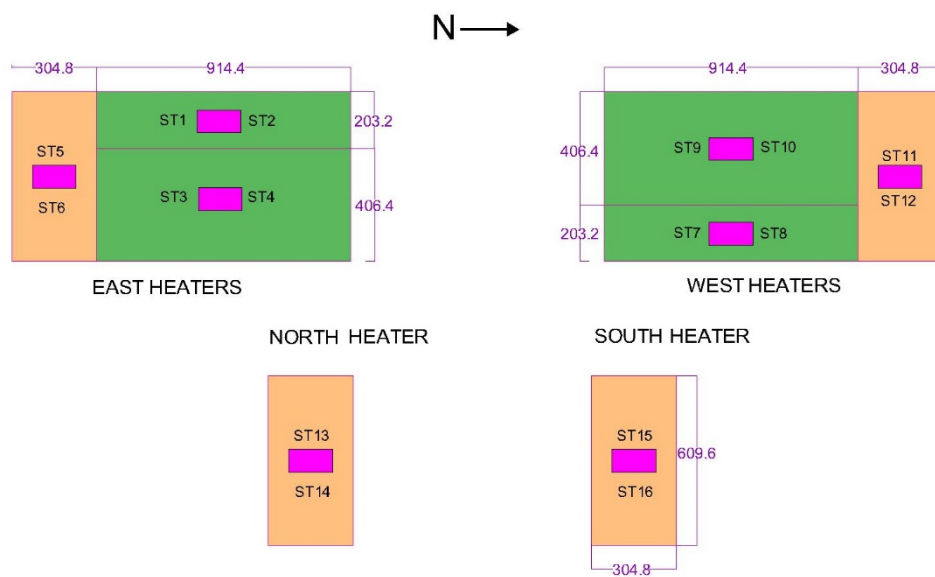
Figure 5.19 SC-W-H: Heater and surface thermocouple details
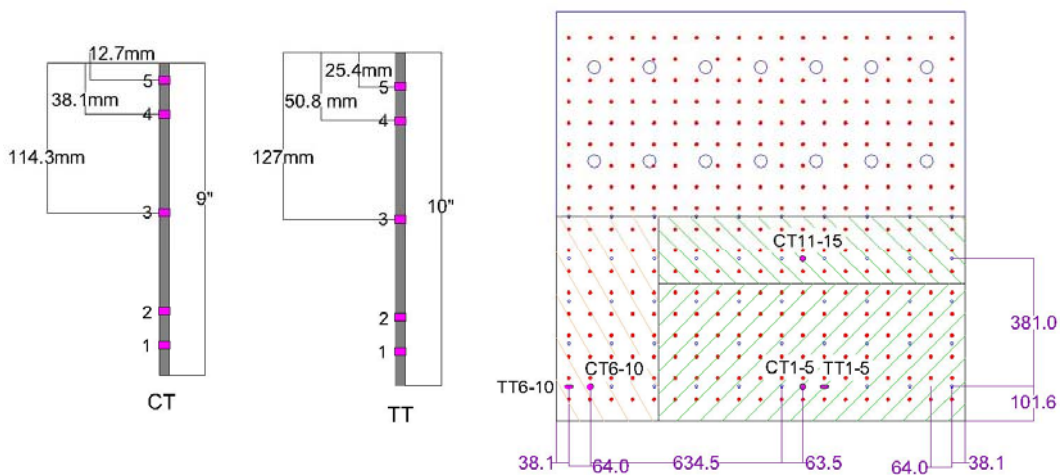
Figure 5.20 SC-W-H: Thermocouple tree details (with heaters overlaid)

Figure 5.21 SC-WP-H: Faceplate with studs and strain gauges installed
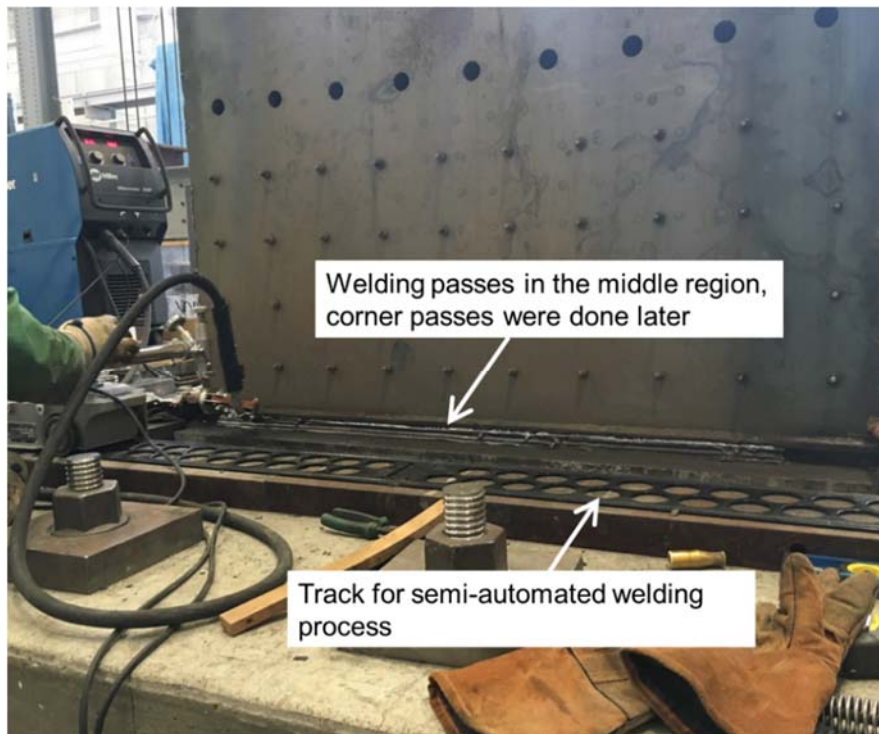
Figure 5.22 SC-WP-H: Faceplate-to-baseplate welding in progress

Figure 5.23 SC-WP-H: Measurement of slump before concrete casting
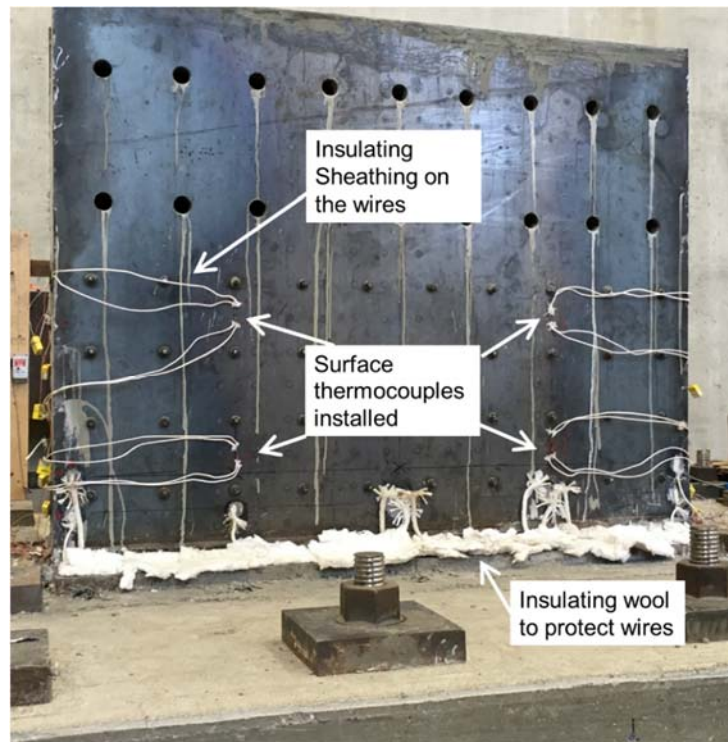
Figure 5.24 SC-WP-H: Installation of instrumentation post concrete curing

Figure 5.25 SC-WP-H: Heater assembly installed
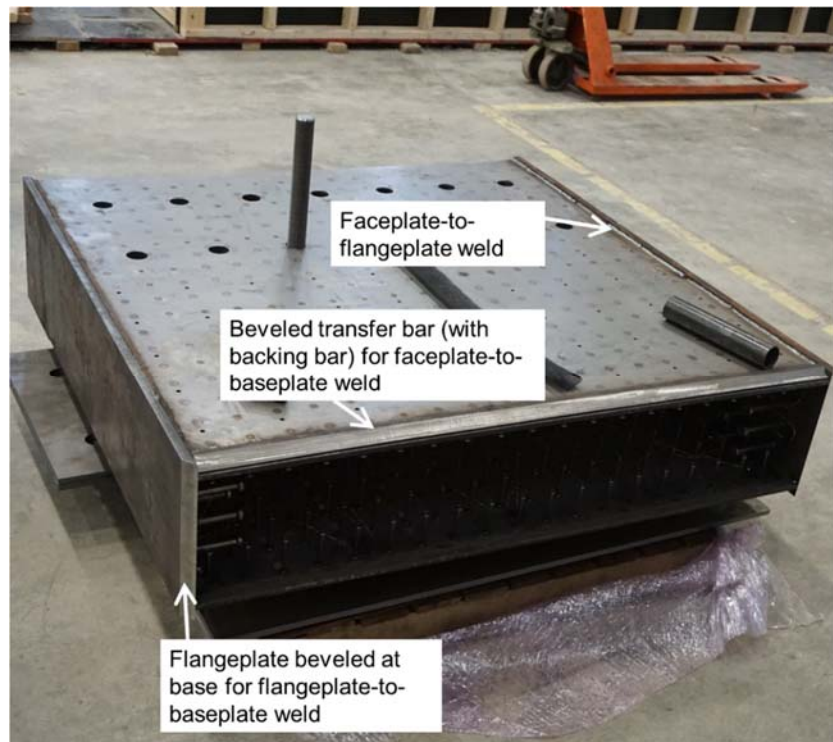
Figure 5.26 SC-W-H: Welded steel assembly
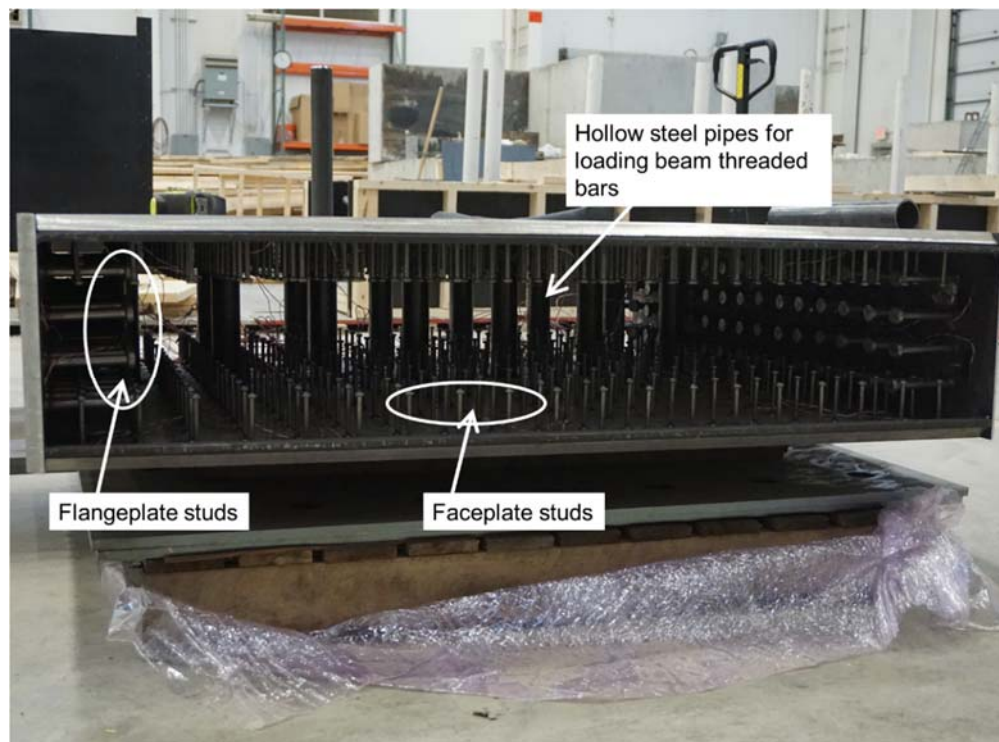
Figure 5.27 SC-W-H: Welded steel assembly (another view)
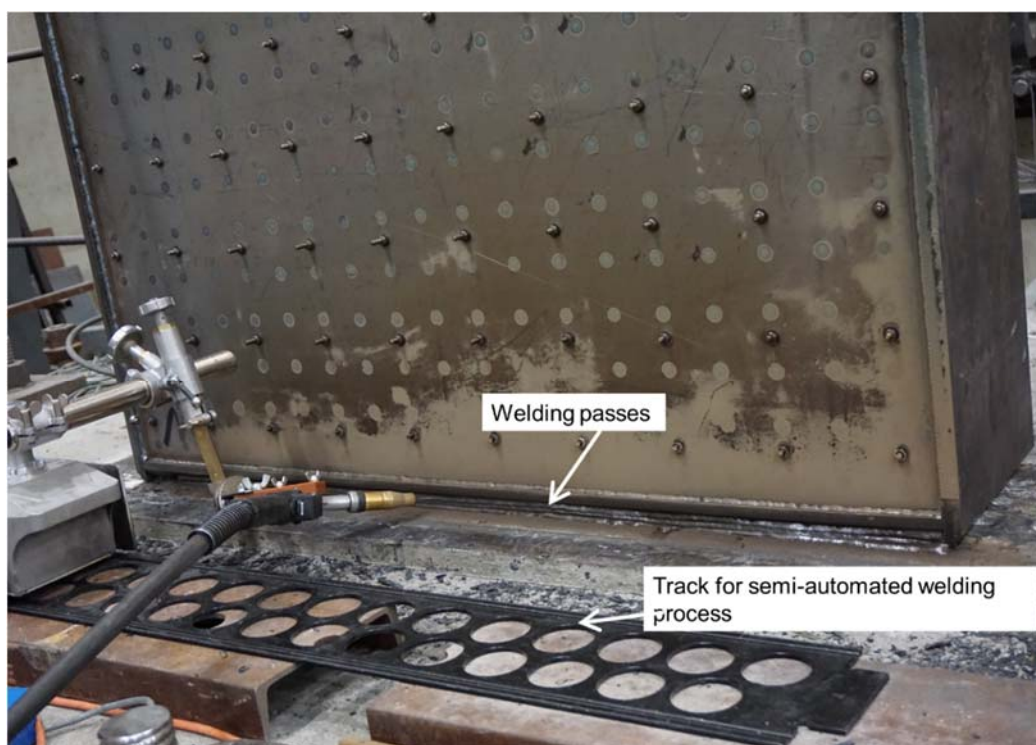
Figure 5.28 SC-W-H: Faceplate-to-baseplate welding in progress

Figure 5.29 SC-W-H: Concrete slump test before casting

Table 5.1 Specimen details

Specimen	h (mm)	l_w (mm)	T (mm)	t_p (mm)	t_f (mm)	h/l_w	ρ_s	$/T$	s/t_p	s_f/t_f	S/T	F_{yw} (MPa)	F_{yf} (MPa)	f'_c (MPa)	T_{max} (°C)
SC-WP-C	914	1524	305	4.8	-NA-	0.6	0.031	0.33	21	-N.A.-	1.0	393	-NA-	40	-NA-
SC-WP-H	914	1524	305	4.8	-NA-	0.6	0.031	0.25	16	-N.A.-	0.5	331	-NA-	38	232
SC-W-H	914	1219	254	2.64	19	0.75	0.021	0.25	24	3.33	0.5	396	413	44	232

Table 5.2 Loading and heating protocol for heated specimens

Cycle No.	Surface Temperature (˚C)	Heating Duration (hours)	Target Force/ Displacement Level
1	Ambient	-NA-	$0.25F_n$
2	Ambient	-NA-	$0.5F_n$
3	Ambient	-NA-	$0.75F_n$
4	149	1	$0.75F_n$
5	149	3	$0.75F_n$
6	232	1	$0.75F_n$
7	232	3	$0.75F_n$
8	232	1	$1.0\Delta_y$
9	232	3	$1.0\Delta_y$
9b*	Ambient	-NA-	$1.0\Delta_y$
10	232	1	$1.5\Delta_y$
11	232	3	$1.5\Delta_y$
11b*	Ambient	-NA-	$1.5\Delta_y$

*Cycles conducted only for SC-W specimen

6. SC STRUCTURES SUBJECTED TO SEISMIC AND THERMAL LOADS: EXPERIMENTAL RESULTS

Experimental studies were conducted to evaluate the in-plane (seismic) response of SC walls and wall piers subjected to accident thermal loadings. Two SC wall pier specimens were tested. One specimen (control specimen) was subjected to cyclic in-plane loading (no accident thermal loading). Control specimen for first series of experiments (SC-T-C, as discussed in Chapter 3 and Chapter 4) was also considered as the control specimen for SC wall piers subjected to seismic and thermal loads. Design and experimental results for control specimen were discussed in detail by Kurt [33] (Specimen SC 8). The second SC wall pier specimen was subjected to a combination of seismic and accident thermal loading. One SC wall specimen was tested. The SC wall specimen was subjected to a combination of seismic and accident thermal loading.

This chapter presents the experimentally observed behavior of the specimens. The measured day-of-test properties for the specimens are summarized in Table 5.1. Concrete uniaxial compressive strength was obtained from cylinders cast along with the specimen. The cylinders were 100 mm in diameter and 200 mm in height and were tested in accordance with ASTM C39 [125]. Concrete strengths presented in the table are the average strengths obtained from cylinders on the day of testing. For SC wall piers, faceplate strength was obtained from tension coupons prepared from samples taken, and tested. The average of faceplate strengths obtained from the tests are mentioned in the table. For SC wall specimen, certified mill test reports (CMTRs) were obtained for the faceplates, and the values mentioned in the table are based on the CMTRs. The behavior of SC wall pier control (SC-WP-C) and heated (SC-WP-H) specimens is discussed, followed by the behavior of SC wall (SC-W-H) specimen.

The chapter is organized into following sections.

- SC-WP-C: In-plane response of control wall pier specimen (with no thermal loading) is summarized. A discussion is provided on the uncorrected and corrected secant stiffness of the specimen.

- SC-WP-H: In-plane response of wall pier specimen subjected to two temperature magnitudes and durations is presented. Strength and stiffness response of the specimen is compared with that for SC-WP-C.

- SC-W-H: In-plane response of wall specimen subjected to two temperature magnitudes and durations is presented. A discussion on shear and secant stiffness of the specimen is provided.

- Evaluation of SC wall and wall pier behavior: The effect of thermal loads on the in-plane response of wall and wall pier specimens is evaluated.

6.1 Specimen SC-WP-C

Specimen SC-WP-C was subjected to cyclic in-plane loading (no heating). Lateral force-top displacement response of the specimen is presented in Figure 6.1 (the figure is same as Figure 4.1). Detailed experimental evaluation of the specimen is presented in Kurt et al [69] and Kurt [33] (specimen SC 8). Failure load for the specimen was measured as 3200-kN (720 kips) on North-direction (+). The measured value in the South direction (-) was 3030-kN (680 kips), giving an average failure load for in-plane shear as 3115-kN. The peak in-plane force was approximately equal to the force corresponding to compression yield moment for the specimen (V_{Myc}). The figure also presents the progression of damage to the specimen. The flexural failure of the specimen was initiated by crushing and spalling of the concrete in compression, accompanied by local buckling of the steel plates in compression, and base metal (faceplate) weld rupture. The specimen did not reach its plastic moment capacity as it failed due to the weld rupture.

Figure 6.2 presents the reduction in secant stiffness (K_{sec}) of the specimen with load cycles. The stiffness presented is the average of push (+) and pull (-) cycle secant stiffnesses. Secant stiffness is calculated using the peak loads and the corresponding displacement values for a cycle. Uncorrected stiffness is obtained from the displacement measured at the top of the wall (914 mm from base). Displacement at the top will include the displacement due to slip at base, and base rotation. 'Corrected1' stiffness includes the corrections due to base slip and base rotation. Since the wall piers have a flexure-controlled response, lateral loading will result in cracking at the base. 'Corrected2' stiffness includes the correction in displacement due to slip at base and rotation 51 mm above the base (with an intent to evaluate the reduction in stiffness due to concrete cracking at the base of the wall). Figure 6.3 presents the uncorrected and corrected force-displacement response of the specimen for first Δ_y cycle. It is observed that the stiffness of the specimen is significantly higher when the base corrections are applied. Theoretical cracked stiffness (K_{cr}) is also plotted in Figure 6.2. K_{cr} is calculated considering the cracked flexural stiffness (EI_{cr}) and cracked shear stiffness (GA_{cr}). EI_{cr} is obtained corresponding to the neutral axis location for compression yield moment (M_{yc}). GA_{cr} is calculated as discussed in Section 4.5.2 (considered as the sum of steel shear stiffness, G_sA_s, and effective concrete shear stiffness, $0.25G_cA_c^{uncr}$). It is observed that uncracked stiffness is not manifest in the wall. A comparison of Corrected1 and Corrected2 stiffnesses indicates that bulk of the reduction in stiffness of the wall piers was due to the cracking at base (up to 50% reduction). However, since the flexure-controlled wall piers will be subjected to cracking at the base, Corrected2 stiffness can only be considered for analysis or design when the wall-to-base connection is modeled using flexural stiffness springs. The magnitude of base slip and base rotation will depend on the foundation and anchorage connection design, and will typically be negligible for physical structures. Therefore, Corrected1 stiffness is

a realistic measure of the wall stiffness. It is observed that the stiffness for first cycle (Corrected1) is equal to 1.2K_{cr}. The stiffness of the specimen corresponding to 0.75F_n cycles is 88% of the cracked stiffness.

6.2 Specimen SC-WP-H

SC-WP-H was subjected to the heating and loading protocol presented in Table 5.2. Figure 6.4 and Figure 6.5 present the evolution of through-thickness temperature profiles for surface temperatures of 149$°$C and 232$°$C respectively. The temperature profiles are obtained from the surface thermocouples (STs in Figure 5.12 and Figure 5.13) and the thermocouple trees (CTs and TTs in Figure 5.14) embedded in concrete. For a surface temperature of 149$°$C, the non-linear thermal gradients are lower in comparison to the case with surface at 232$°$C, and reduce significantly as the duration of heating continues (at 3 hours of heating, center of the wall is at about 110$°$C). A significant thermal gradient exists through the wall when the surface is at 232$°$C (at 3 hours of heating, center of the wall is at about 125$°$C). Higher non-linear thermal gradients are expected to result in more concrete cracking and reduction in the stiffness. Considering a parabolic thermal gradient, the average concrete temperatures are 130$°$C and 160$°$C for surface temperatures of 149$°$C and 232$°$C respectively.

Figure 6.6 presents the in-plane force-top displacement response of SC-WP-H. The ambient and heated cycles have been shown in different colors. Average peak strength of SC-WP-H was 3300-kN (+3265kN/-3341kN), as compared to 3115-kN (+3200kN/-3030kN) observed for SC-WP-C. SC-WP-C failed due to faceplate rupture during the 2Δ_y cycle (upon reaching V_{Myc}). SC-WP-H reached a peak load of 1.25V_{Myc}, and then failed due to faceplate rupture during the next cycle (the failure cycle is not shown in the figure). SC-WP-H failed at a drift ratio of 1.3% compared to 1.2%

for SC-WP-C. A comparison of $0.75F_n$ ambient and heated cycles (about 1800-kN force) indicates that there is a reduction in specimen stiffness due to thermal loading. To look closely into the stiffness reduction, $0.75F_n$ cycles are plotted separately in Figure 6.7. The heated cycles had lower stiffness than the ambient cycle. Reduction in the stiffness was higher for surface temperature of 232˚C. Additionally, the 3-hour duration heated cycles were marginally stiffer than the corresponding 1-hour duration heated cycles. For typical accident thermal temperatures, reduction in steel [5% reduction for 149˚C and 13% reduction for 232˚C, per AISC 360 [116]] and concrete modulus of elasticity [12% reduction for 130˚C and 18% reduction for 160˚C, per AISC 360 [116]] will contribute to reduction in experimental stiffness. Thus, for heated cycles, the stiffness reduction is due to combination of thermally-induced concrete cracking and reduction in flexural and shear moduli at elevated temperatures.

Figure 6.8 presents the lateral force-vertical normal strain plot for $0.5F_n$ and $0.75F_n$ ambient cycles. For SC-WP-H, strain gauges S1 and S9 were installed on the North and South corners of the East faceplate (Figure 5.10). S20 was installed on the West faceplate at the location corresponding to S9 on the East side. The yield strain for the faceplates (1655 µε) is also plotted in the figure. The faceplates did not undergo any yielding for the $0.5F_n$ cycle. For $0.75F_n$ cycle, the faceplates started yielding in tension. However, there was still no compression yielding in the faceplates.

Figure 6.9 to Figure 6.17 show the progression of damage in the specimen. In-plane loading (at ambient temperature) resulted in flexural cracking in the wall. Figure 6.9 shows the flexural cracking observed in the specimen at the end of $0.5F_n$ cycle. Application of thermal loading resulted in loss of moisture from the specimen during the initial heating. Moisture oozing out of the cracks can be observed in Figure 6.10 and Figure 6.11. Thermal loading resulted in increased crack-widths and additional cracking in the specimen. Some of the cracks observed were vertical

or diagonal cracks (Figure 6.12). Compression faceplate yielding was observed in Δ_y cycle. Additionally, the specimen did not lose any additional moisture in post-yield cycles, and the flexural cracks started widening (Figure 6.13). Compression buckling of faceplates was first observed in $2\Delta_y$ cycle, and was accompanied by further widening of concrete cracks in tension (Figure 6.14). The flexural failure of SC-WP-H was initiated by extensive spalling of the concrete, accompanied by local buckling of the faceplates in compression, and faceplate rupture in tension. Faceplate rupture and concrete spalling, and faceplate compression buckling at failure can be seen in Figure 6.15. The test was stopped after the faceplate ruptured all through the length of the specimen (Figure 6.16). Top and bottom portions of the ruptured specimen are shown in Figure 6.17. Faceplate rupture plane, and the damage to concrete due to cyclic-in-plane loading can be seen in the figure.

Since the concrete and steel strengths were different for SC-WP-C and SC-WP-H specimens (Table 5.1), response of the specimens needs to be normalized in order to be compared. Normalized in-plane force-top displacement response of SC-WP-H is compared with that of SC-WP-C in Figure 6.18. The applied lateral force (V_{app}) is normalized with force corresponding to compression yield moment (V_{Myc}, based on [69]). SC-WP-C failed due to faceplate rupture during the $2\Delta_y$ cycle (upon reaching V_{Myc}). SC-WP-H reached a peak load of $1.25V_{Myc}$ and then failed due to faceplate rupture. SC-WP-H failed at a drift ratio of 1.3%, compared to 1.2% for SC-WP-C. A comparison of experimental response of SC-WP-C and SC-WP-H indicates that typical accident temperatures do not significantly affect the strength and post-peak behavior of SC wall piers. SC-WP-H reached a peak load 25% greater than the compression yield moment capacity. However, post-heating stiffness of SC-WP-H was lower than SC-WP-C stiffness, and SC-WP-H ambient stiffness. The reduction in stiffness is apparent from the comparison of SC-WP-H cycles at similar displacement

or force levels (Figure 6.7). Post-yield stiffnesses of SC-WP-H and SC-WP-C specimens are compared in Figure 6.19. The figure compares $1.5\Delta_y$ cycles for the two specimens. SC-WP-H specimen has lower stiffness than SC-WP-C due to additional cracking caused by accident thermal loads.

Due to differences in steel and concrete strengths for SC-WP-C and SC-WP-H specimens, the stiffness comparisons need to be made using normalized values. Figure 6.20 shows the comparison of normalized wall stiffness degradation in SC-WP specimens. The secant stiffness (K_{sec}) is the average of stiffness values for push (+) and pull (-) cycles. Stiffness for a cycle is calculated from the peak forces and corresponding displacement values for the cycle. The secant stiffness is normalized with wall cracked stiffness (K_{cr}, calculated as discussed for SC-WP-C, in Section 6.1 and Section 4.5.2). The displacement is corrected for base slip and base rotation (similar to Corrected1 stiffness in Figure 6.2). For SC-WP-C, stiffness for the first cycle at a force/displacement level is plotted. For SC-WP-H, stiffnesses for all load cycles are plotted. Uncracked stiffness is not manifest in the specimens. Normalized stiffness for ambient $0.25F_n$ cycle for SC-WP-H is higher than the corresponding stiffness for SC-WP-C. This may be due to more cracking at the base for SC-WP-C. Stiffnesses for both the specimens are close to K_{cr} for $0.5F_n$ cycles (1.1 K_{cr} for SC-WP-C and 0.9 K_{cr} for SC-WP-H), as flexural cracks develop in the specimens. The stiffnesses for $0.75F_n$ ambient cycles are similar for both specimens (about $0.8K_{cr}$). However, stiffness for SC-WP-H drops significantly as thermal loads are applied. There is 20% reduction for 149°C and 40% reduction for 232°C, in comparison to normalized ambient $0.75F_n$ cycle stiffness. A higher magnitude of temperature results in more reduction in stiffness. The reduction in normalized stiffness can also be obtained considering temperature-dependent elastic and shear moduli for steel and concrete (percentage reduction for typical accident temperatures

has been discussed previously in Section 2.6.1). The normalized stiffness (considering temperature

dependent properties) would provide an estimate of stiffness reduction due to thermally-induced

cracking. Considering temperature dependent properties, there is 11% reduction for 149°C and 23%

reduction for 232°C, in comparison to normalized ambient $0.75F_n$ cycle stiffness Thus for typical

accident temperatures, the contribution of reduced elastic and shear moduli to stiffness reduction

is about 50% of the overall stiffness reduction. For $0.75F_n$ load level, stiffness for 3-hour duration

heating cycles is marginally higher than stiffness for 1-hour duration heating cycles. The stiffness

increases marginally as the non-linear thermal gradient reduces with increase in duration of heating,

leading to some crack closure. SC-WP-H stiffness for post-yield cycles remains lower than that

for SC-WP-C. For the $2\Delta_y$ cycle, the normalized stiffnesses for both the specimens are similar, as

SC-WP-C witnessed faceplate rupture in the cycle, leading to a reduction in its stiffness.

6.3   Specimen SC-W-H

Specimen SC-W-H was subjected to the loading and heating protocol presented in Table 5.2. The

loading and heating history for the specimen is presented in Figure 5.7. Since the specimen was

heated on all sides (flanges and web both were heated), there was no outlet for heat. This led to a

sharp rise in the surface temperatures for the first heated cycle (cycle 4, also seen in Figure 5.7).

However, the temperature was controlled by lowering the surface control temperature for some

heaters, and the same process was followed for remaining heated cycles. Evolution of through-

thickness temperature profiles (in the central region of the wall) for surface temperatures of 149°C

and 232°C was similar to that observed for SC-WP-H. Figure 6.21 presents the evolution of thermal

gradient for surface temperature of 232°C (obtained for CT 6-10 in Figure 5.20). A significant

thermal gradient exists through the wall thickness, with the center of wall at 124°C for 3-hour

heating duration (corresponding temperature was 125˚C for SC-WP-H). Thermal gradient through the wall thickness is expected to result in thermally-induced concrete cracking in the wall.

Figure 6.22 presents the lateral force-top displacement response of SC-W-H. Ambient and heated cycles for the specimen are shown in different colors. The nominal in-plane shear strength (V_n^{AISC}, using measured properties) of the specimen, based on AISC N690s1 [26] provisions, is also plotted in the figure. SC-W-H reached an average peak load of 3300-kN (+3360kN/-3240kN). Peak load for the specimen was 30% higher than V_n^{AISC} (2550-kN). The experimental strength was higher than V_n^{AISC}, as AISC conservatively limits the in-plane strength to Von-Mises yielding of the faceplates, and does not account for additional strength provided by concrete compression strut (discussed previously in Section 2.5, based on [100]).

Therefore, the strength of SC walls subjected to typical accident temperatures can be conservatively estimated using current US code provisions. However, accident thermal loads do reduce the stiffness of the specimen. Heated cycles (shown with solid red lines) are softer than the corresponding ambient cycles (shown with black dotted lines). To look closely at the stiffness reduction due to accident thermal loads, ambient and heated (3-hour duration) $0.75F_n$ cycles are plotted in Figure 6.23. The heated cycles were less stiff than the ambient cycle, and the reduction in stiffness was higher for surface temperature of 232˚C. Stiffness reduction in SC-W-H due to thermally-induced concrete cracking was consistent with that for SC-WP-H (stiffness reduction for SC-WP-H was presented in Figure 6.7) and is discussed in detail later. SC-W-H exhibited pinched force-displacement response post-application of thermal loads (as seen in Figure 6.22). The extent of pinching was higher than would be typically observed, as the concrete cracks took longer to close in compression due to thermal gradients. This resulted in a low stiffness initially, and the stiffness increased as the compression force led to closure of thermally-induced cracks.

Incremental lateral (in-plane) loading resulted in concrete flexural and shear cracking, followed by faceplate yielding in tension. Figure 6.24 presents the lateral force-vertical normal strain response of the faceplates for ambient and heated (232˚C-1 hour) $0.75F_n$ and Δ_y cycles (cycle no. 3, 6, 8 and 9b in Table 5.2). Strain gauges S3 and S10 were located at the base of the wall, between the first and second row of studs (shown in Figure 5.16 and Figure 5.17). Faceplates started yielding in tension for ambient $0.75F_n$ cycle. S3 and S10 strains reached peak tensile strains of around 2000 με (incremental tensile strains in S10 and S3 were 2300 and 1750 με respectively, compared to yield strain of 1980 με). For $0.75F_n$-232˚C-1 hour heated cycle, the incremental tensile strains were similar. There was no compression yielding in the faceplates for $0.75F_n$ cycles. For Δ_y heated and ambient cycles, the faceplate tensile strains exceeded the yield strain. However, there was no compression yielding in the faceplates. Since the specimen was designed to have a shear failure, the flangeplates were not expected to yield till after the Δ_y cycles.

Figure 6.25 presents the lateral force-vertical normal strain response of the flangeplates for ambient $0.75F_n$, Δ_y and $1.5\Delta_y$ cycles (Cycle No. 3, 9b, 11b in Table 5.2). Since the incremental faceplate strains for ambient and heated cycles were similar (Figure 6.24), only the ambient cycle strains have been plotted in Figure 6.25. Strain gauges S45 (East flangeplate) and S47 (West flangeplate) were installed between the first two rows of studs on flangeplates, at 125 mm from the base (shown in Figure 5.15). Flangeplates did not undergo yielding for the cycles shown in the figure (tensile and compressive strains were lower than yield strain, 2070με). However, a reversal of strains was observed for $1.5\Delta_y$ cycle (encircled in the figure). Since the flange plate studs were detailed to ensure that slenderness criterion of AISC N690s1 [26] was satisfied, the flangeplates were not expected to undergo buckling before compression yielding. However, as the lateral load increased and faceplates yielded in compression, the magnitude of concrete compression strut

force (anchoring in at the faceplate-flangeplate-baseplate joint) increased. This compression strut, coupled with the flangeplate compressive force, forced the flangeplate (and faceplates near corners) to bulge out between the bottom two rows of studs. The flangeplate bulging out resulted in a reversal of strains on the exterior face of flangeplates.

The concrete compression strut also produced additional stresses in the faceplate-flangeplate-baseplate weld. The weld (detail shown in Figure 6.26) was a highly constrained weld with discontinuity. Additional stresses at the weld location resulted in the initiation of weld fracture at the faceplate-flangeplate-baseplate joint during the second $2\Delta_y$ cycle (cycle 13). Weld fracture at South-West corner of the specimen is shown in Figure 6.27. The fracture progressed upwards into the faceplate-flangeplate weld, and downwards into the flangeplate-baseplate weld (as seen in Figure 6.27 and Figure 6.28). Similar initiation of fracture was observed at other corners of the specimens (Figure 6.29). This fracture resulted in faceplate and flangeplate rupture, and failure of the specimen in the next cycle. Steel rupture of the specimen is shown in Figure 6.30 and Figure 6.31. The weld fracture propagated to fracture the flangeplate weld, and then ruptured the faceplates. The bulging of the faceplate near corners due to the concrete compression strut (as discussed previously) is also visible in Figure 6.31. Flangeplate weld fracture surface is shown in Figure 6.32. The weld failed in brittle Type 1 fracture. Post the failure of the specimen, one of the faceplates was cut off to inspect the concrete infill. Figure 6.33 shows the concrete cracking and damage in the specimen at failure. Concrete infill cracked predominantly in shear (the cracking angle varied between 35 and 45 degrees). Rupture of the faceplates and flangeplate at the base during the failure cycle resulted in the concrete infill being pulled in tension (due to bond with faceplates and flangeplates) and resulted in tension 'tearing' damage to the concrete. Since the

specimen failed due to rupture, there was no concrete compression crushing or faceplate shear buckling in the specimen.

Lateral force-top displacement response of the specimen (Figure 6.22 and Figure 6.23) indicated a reduction in wall stiffness due to thermal loading. Figure 6.34 shows the response of the specimen for Δ_y ambient and heated cycles. The ambient cycle was performed after the heated cycles to observe any increase in specimen stiffness due to crack closure post-cooling. Consistent with observations for pre-yield cycles, the ambient cycle was marginally stiffer than the heated cycle. Since the specimen was shear controlled, the effect of thermal loads on the shear stiffness on the specimen is of particular interest. Shear stiffness of the wall can be compared with stiffness provisions for analysis provided in AISC N690s1 [26]. Per AISC N690s1, shear stiffness of the SC wall depends on the magnitude of lateral loading. For lateral loads lower than a cracking threshold (S_{cr}^{AISC}), uncracked shear stiffness (GA_{uncr}^{AISC}) is considered. For lateral loads greater than $2S_{cr}$, the stiffness is considered to reduce to cracked secant stiffness (GA_{cr}^{AISC}, considering orthotropic cracked concrete and plane stress steel properties). The stiffness can be linearly interpolated between uncracked and cracked stiffness for lateral loads between S_{cr}^{AISC} and $2S_{cr}^{AISC}$. For accident thermal load combinations, the shear stiffness is considered to be cracked (GA_{cr}^{AISC}). Figure 6.35 presents in-plane (lateral) force-shear strain response of the specimen (for $0.25F_n$ and $0.5F_n$ cycles). Slope of the response is the experimentally observed shear stiffness and is compared with AISC stiffness provisions (force-shear strain plots with slopes corresponding to AISC stiffnesses). Force-shear strain plot with slope corresponding to tangent cracked shear stiffness (GA_{cr}^{TAN}) for SC walls is also plotted in the figure (based on [5], [8]). Shear strain for the specimen was calculated from strain gauge rosettes (S4-6, S7-9, S13-15, S16-18). Location of strain gauges S13-18 is shown in Figure 5.16 and Figure 5.17. Strain values from rosettes were used to obtain

principal strains and directions. Shear strain (γ_{xy}) was calculated using the principal strains and direction. Average shear strain for the four strain gauge rosettes was plotted in Figure 6.35. It was observed that the uncracked stiffness was not manifest in the specimen. The specimen developed shear cracks at force level approximately equal to S_{cr}, and the stiffness reduced further thereafter. Shear stiffness for the $0.25F_n$ cycle was approximately equal to cracked secant stiffness (GA_{cr}^{AISC}). For $0.5F_n$ cycle, the stiffness dropped below GA_{cr}^{AISC}. However, the shear stiffnesses for both the cycles were higher than the tangent cracked stiffness (GA_{cr}^{TAN}). Therefore, GA_{cr}^{TAN} provides a lower bound estimate of the shear stiffness of the specimen. AISC recommended secant stiffness (GA_{cr}^{AISC}) is higher than experimentally observed stiffness. This is because the uncracked stiffness was not manifest (or the specimen cracked at a low magnitude of lateral force), which makes the tangent stiffness a better predictor of the cracked shear stiffness of the specimen.

Figure 6.36 presents degradation of the experimentally observed shear stiffness of the specimen. Experimentally observed shear stiffness is normalized with the cracked tangent stiffness (GA_{cr}^{TAN}). Shear stiffness was obtained from the strain gauge rosettes (as discussed for Figure 6.35). Shear stiffness was also obtained from the displacement measurements of the specimen (to cross-check the values obtained from strain gauge rosettes, and to obtain stiffness for cycles where strain gauges were damaged due to heating). Corrected top displacement (corrected for base slip and base rotation) consists of shear and flexural deflection. The flexural deflection can be calculated using EI_{cr} (cracked flexural stiffness). For calculation of EI_{cr}, the location of neutral axis is considered as one-third of the length of the specimen (consistent with that observed from strain gauge data, and cross-section moment-curvature relationship). For heated cycles, the flexural stiffness is considered to linearly reduce from EI_{cr} to EI_{steel} for surface temperature increase (ΔT) from 0˚C to 150˚C (based on the observations and recommendations discussed later). The shear

deflection (and the shear strain) was then calculated by subtracting the flexural deflection from the total deflection. The shear stiffnesses obtained from the strain gauges and wall displacement agree reasonably for pre-yield cycles. Displacement data stiffness for $0.5F_n$ is higher than the corresponding shear strain stiffness. For $0.75F_n$-149˚C cycles, some of the rosettes were damaged due to heating, and the average shear strain consists of only the functioning rosettes. For Δ_y cycles, displacement data stiffnesses are higher as the specimen was undergoing shear yielding, which was not considered in displacement data stiffnesses. Based on the comparisons, stiffness obtained from the displacement data can be considered (with reasonable accuracy). As observed in Figure 6.36 and Figure 6.35, shear stiffness for $0.25F_n$ and $0.5F_n$ ambient cycles was higher than the cracked tangent shear stiffness ($GA_{cr}{}^{TAN}$). $0.75F_n$ ambient shear stiffness was approximately equal to $GA_{cr}{}^{TAN}$. However, the normalized stiffness for $0.75F_n$ cycles drops considerably as thermal loading is applied. The normalized stiffness reduction was 21% for 149˚C and 38% for 232˚C. The reduction in normalized stiffness can also be obtained considering temperature-dependent elastic and shear moduli for steel and concrete (percentage reduction for typical accident temperatures has been discussed previously). The normalized stiffness (considering temperature dependent properties) would provide an estimate of stiffness reduction due to thermally-induced cracking. Considering temperature dependent properties, the stiffness reduction is 16% for 149˚C and 26% for 232˚C, in comparison to normalized ambient $0.75F_n$ cycle stiffness. Therefore, the shear stiffness reduction (below cracked stiffness) due to thermal loading needs to be considered for seismic and thermal loading combinations. Based on Figure 6.36, the shear stiffness can be considered to linearly reduce from $GA_{cr}{}^{TAN}$ to GA_{steel} for surface temperature increase (ΔT) from 0˚C to 150˚C. This would provide a lower-bound estimate of the shear stiffness, and also negate the need for using temperature-dependent properties for typical accident temperatures.

Overall stiffness response of the SC wall is a combination of its flexural and shear stiffnesses. As for SC-WP specimens, the stiffness degradation of SC-W-H specimen can be compared with calculated wall cracked stiffness (K_{cr}). Figure 6.37 presents the secant stiffness degradation of the specimen over the loading and heating cycles. Secant stiffness (K_{sec}) was calculated as the average of push (+) and pull (-) stiffnesses. The push and pull stiffnesses were calculated from the peak force and corresponding displacement values (corrected for base slip and base rotation) for a cycle. K_{sec} is normalized with calculated wall cracked stiffness (K_{cr}). K_{cr} was calculated considering EI_{cr} and GA_{cr}^{TAN}. EI_{cr} was calculated considering the neutral axis at one-third of the specimen length (as discussed previously). GA_{cr}^{TAN} is the tangent shear stiffness for the SC wall and includes plane stress steel and orthotropic cracked concrete contributions. It is observed that uncracked stiffness was not manifest in the wall. Stiffness of the wall for $0.25F_n$ cycle was about 1.9 times K_{cr} (0.52 times the uncracked stiffness). Stiffness of the wall reduced for higher lateral loads as the concrete developed shear and flexural cracks. Ambient stiffness of the specimen corresponding to $0.75F_n$ cycle was approximately equal to $0.9K_{cr}$. Accident thermal loading reduced the normalized stiffness significantly. The reduction in normalized stiffness was 25% for 149°C and 40% for 232°C, in comparison to normalized ambient $0.75F_n$ cycle stiffness (20% reduction for 149°C and 28% reduction for 232°C, when temperature dependent properties are considered). Contrary to observations for SC-WP specimen, the $0.75F_n$-3 hour stiffness is lower than stiffness for corresponding 1-hour duration heating cycles. This may be because, for some of the push cycles, string pot showed no movement for loads up to 250-kN (can also be seen in Figure 6.34). To evaluate the stiffnesses further, the pull (-) stiffness degradation was plotted, and is shown in Figure 6.38. It is observed that the stiffness degradation trend for pull cycles is consistent with SC-WP specimens, i.e., the 3-hour stiffnesses were marginally higher than 1-hour stiffnesses. The

stiffness increased marginally as the non-linear thermal gradient reduced with an increase in duration of heating, leading to some crack closure. The effect of temperature magnitudes and heating duration on stiffness degradation of SC-W-H is consistent with that observed for SC-WP-H. For Δ_y and 1.5Δ_y displacement levels, ambient cycles were performed after the heated cycles (the specimen was allowed to cool down) to evaluate the change in stiffness upon closure of thermal cracks. The normalized ambient stiffness for Δ_y cycle is higher (both in Figure 6.37 and Figure 6.38) than normalized heated stiffness (ambient stiffness is 20% higher than the heated stiffness). Similarly, for 1.5Δ_y cycle, the ambient stiffness is marginally higher than heated stiffness.

6.4   Evaluation of Wall and Wall Pier Behavior and Recommendations

Test matrix for SC specimens subjected to a combination of accident thermal and seismic loads consisted of two SC wall pier (without boundary elements) specimens [one control (SC-WP-C) and one heated specimen (SC-WP-H)], and one SC wall (with flange walls) specimen (heated specimen, SC-W-H). The SC wall pier specimens (aspect ratio of 0.6) were flexure controlled. The SC wall specimen was designed to have a shear dominated response. The specimens were subjected to cyclic lateral loading in combination with accident thermal loading. Two surface temperature magnitudes (149°C and 232°C) and two heating durations (1 hour and 3 hours) were selected for application of thermal loads. A non-linear thermal gradient developed through the wall thickness due to thermal loads. The extent of non-linearity reduced as the duration of heating increased. The thermal gradient was higher for surface temperature of 232°C. Centre of the specimens was at about 125°C corresponding to a surface temperature of 232°C, and a heating

duration of 3 hours. The non-linear thermal gradient results in concrete-cracking due to self-restraint and external restraints, which reduces the stiffness of the specimens.

Table 6.1 presents the measured initial (K_{in}) and secant (K_{sec}) stiffnesses of the specimens. The table presents the corrected (for base slip and rotation) and uncorrected stiffness (presented in parenthesis) for the push (+) and pull (-) cycles. K_{in} is calculated for the force (and corresponding displacement) levels of 224 kN to 445 kN (50 kips to 100 kips) for the first $0.25F_n$ cycle. K_{sec} is the secant stiffness for the $0.75F_n$ cycle, calculated from the peak force and corresponding displacements. The secant stiffness of the specimens reduced upon application of thermal loads.

Summary of the experimental results is presented in Table 6.2. The table presents the maximum surface temperature (T_{max}), measured lateral strength (V_{n-ip}) and the ratio of measured strength with nominal strength (using measured properties). For SC wall piers, measured strength (V_{n-ip}) is normalized with a lateral force corresponding to compression yielding (of faceplates) moment (V_{Myc}). For SC walls, the measured strength (V_{n-ip}) is normalized with in-plane shear strength per AISC N690s1 [26] (V_n^{AISC}). Measured strength for SC-WP-H was $1.25V_{Myc}$. Similarly, the peak strength for SC-W-H was about $1.29V_n^{AISC}$. Based on the experimental results, the strength of specimens subjected to typical accident thermal temperatures and durations can be conservatively estimated using existing strength equations (per US codes) for ambient conditions.

Table 6.2 also presents the normalized initial (K_{in}) and secant stiffnesses (K_{sec}), and the failure drift ratio for the specimens. The initial and secant stiffness values considered are average of push (+) and pull (-) cycle values. Initial stiffness of the specimens is normalized with theoretical uncracked stiffness (K_{uncr}) for the specimens. K_{uncr} is calculated considering uncracked shear and flexural stiffnesses of the specimens. Experimental results indicate that uncracked stiffness was not manifest in SC wall and wall pier specimens. This may be due to shrinkage cracking in the

specimens, and the cracking of specimens at low magnitude of lateral loads. Secant stiffness of the specimens is normalized with theoretical cracked stiffness (K_{cr}) of the specimens. As discussed previously (Sections 4.5.2, 6.1 and 6.2), for SC wall piers K_{cr} can be calculated considering EI_{cr} (for neutral axis location corresponding to compression faceplate yielding moment, M_{yc}), and GA_{cr} (sum of steel shear stiffness and effective concrete shear stiffness). For SC walls, K_{cr} can be calculated considering EI_{cr} [the neutral axis location can be calculated from moment-curvature relationship, e.g., for SC-W-H specimen the neutral axis was considered at one-third the length of the wall (consistent with strain gauge readings)], and GA_{cr}^{TAN} (considering plane stress steel, and orthotropically cracked concrete, as discussed previously). Cracked tangent shear stiffness was used because it provided a better estimate of the shear stiffness of the SC wall specimen (in comparison to GA_{cr}^{AISC}). Ambient secant stiffness of SC walls and wall piers can be reasonably estimated as K_{cr}. Accident thermal loads significantly reduce the stiffness of the SC wall and wall piers. The extent of reduction in stiffness depends on the temperature magnitude and duration of the thermal accident. The heated secant (and shear) stiffness for the SC wall reduces by about 25% for 149˚C and 40% for 232˚C, in comparison to ambient secant (and shear) stiffness for the SC wall. For SC wall piers, the reduction is about 20% for 149˚C and 40% for 232˚C. The stiffness of the specimens increases marginally as the thermal accident duration increases.

Based on the experimental results, the secant stiffness (flexure and shear stiffness) for shear controlled SC walls and flexure controlled SC wall piers can be considered to linearly reduce from cracked stiffness to steel-only stiffness for surface temperature change (ΔT) from 0˚C to 150˚C. The effective in-plane flexural and shear stiffnesses for SC walls and wall piers can be calculated as shown in Equations 6.1 and 6.2.

$$EI_{eff}^{ip} = EI_{cr} - \frac{\left(EI_{cr} - E_s I_s\right)}{150}\Delta T \geq E_s I_s \qquad \text{Equation 6.1}$$

$$GA_{eff} = GA_{cr} - \frac{\left(GA_{cr} - G_s A_s\right)}{150}\Delta T \geq G_s A_s \qquad \text{Equation 6.2}$$

Table 6.3 presents the comparison of secant stiffnesses for the specimens normalized with cracked stiffnesses (K_{sec}/K_{cr}, same as presented in Table 6.2) and recommended effective stiffnesses (K_{sec}/K_{eff}). K_{eff} is calculated considering EI_{eff}^{ip} and GA_{eff} as recommended in Equations 6.1 and 6.2. The secant stiffnesses (ambient and heated) of the specimens can be reasonably estimated using the recommendations. Since the recommended reductions provide lower bound estimates of stiffness, they eliminate the need to consider temperature dependent properties (for typical accident temperatures up to 300˚C).

6.5 Chapter Summary

This chapter presented the results for SC wall and wall pier specimens subjected to combination of accident thermal and in-plane loadings. The specimens were subjected to two magnitudes (149˚C and 232˚C) and durations (1-hour and 3 hours) of heating. Accident thermal loading resulted in non-linear thermal gradients through the thickness of the specimens. The non-linearity of thermal gradients was higher for higher surface temperatures. The gradient reduced as the duration of heating increased. The measured in-plane strength of heated wall pier specimen was 1.25 times the in-plane force corresponding to compression yield moment capacity. Similarly, the measured in-plane strength of heated wall specimen was 1.29 times the nominal in-plane shear strength (using measured properties) per AISC N690s1. Therefore, typical accident thermal temperatures do not significantly reduce the strength of SC walls. The strength can be calculated using current strength equations (per US codes) for ambient temperatures.

However, non-linear thermal gradients lead to concrete cracking due to external and self-restraint. The concrete cracking results in significant reduction in the stiffness of SC walls. The extent of reduction in stiffness depends on the temperature magnitude and duration of the thermal accident. The heated secant (and shear) stiffness for the SC wall reduces by about 25% for 149˚C and 40% for 232˚C, in comparison to ambient secant (and shear) stiffness for the SC wall. For SC wall piers, the reduction is about 20% for 149˚C and 40% for 232˚C. The in-plane shear and flexural stiffnesses of SC walls can be considered to linearly reduce from cracked stiffness to steel only (fully cracked) stiffness for temperature increments (ΔT) of 0˚C to 150˚C. The recommended stiffnesses compare reasonably with experimentally observed stiffness for heated cycles. Since the recommendations provide a lower bound stiffness, they eliminate the need for considering temperature-dependent properties for typical accident temperatures.

Figure 6.1 In-plane force-top displacement response of SC-WP-C (same as SC-T-C)
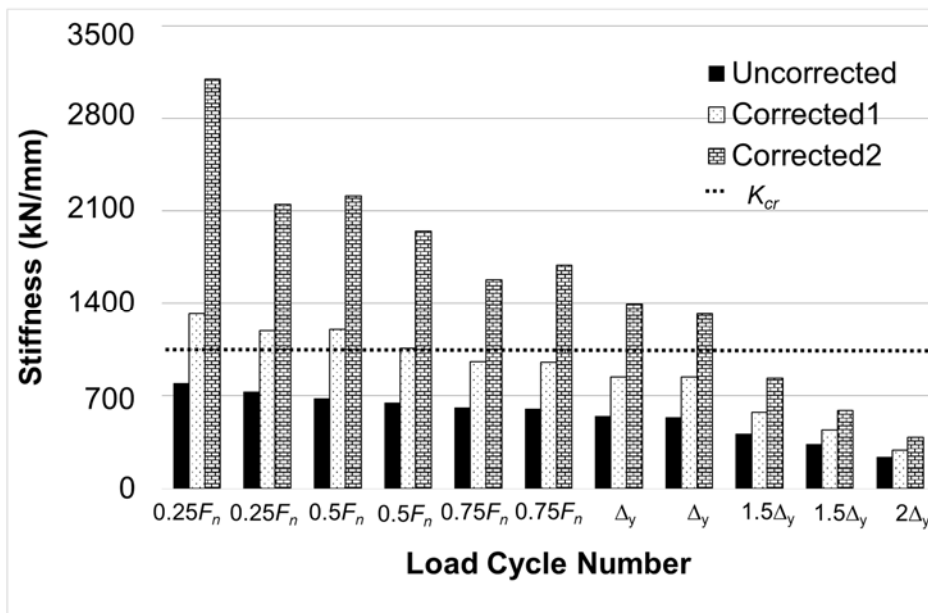
Figure 6.2 SC-WP-C: Degradation of secant stiffness
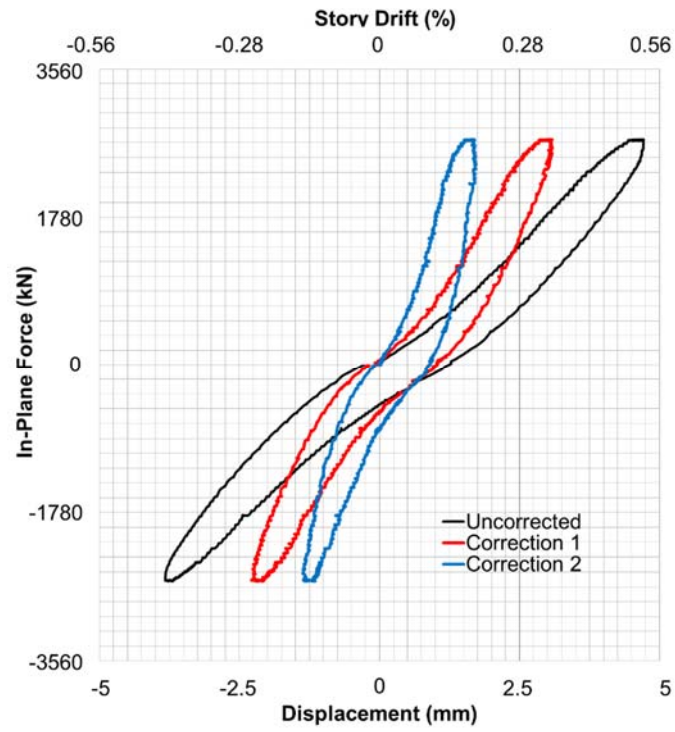
Figure 6.3 SC-WP-C: Base slip and rotation corrections (for Δ_y cycle 1)
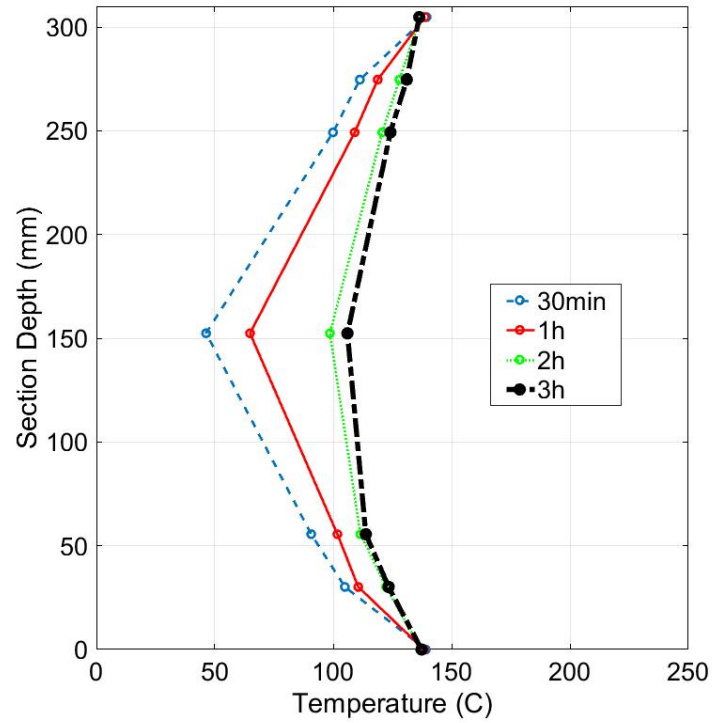
Figure 6.4 SC-WP-H: Evolution of thermal gradient (for surface temperature of 149˚C)
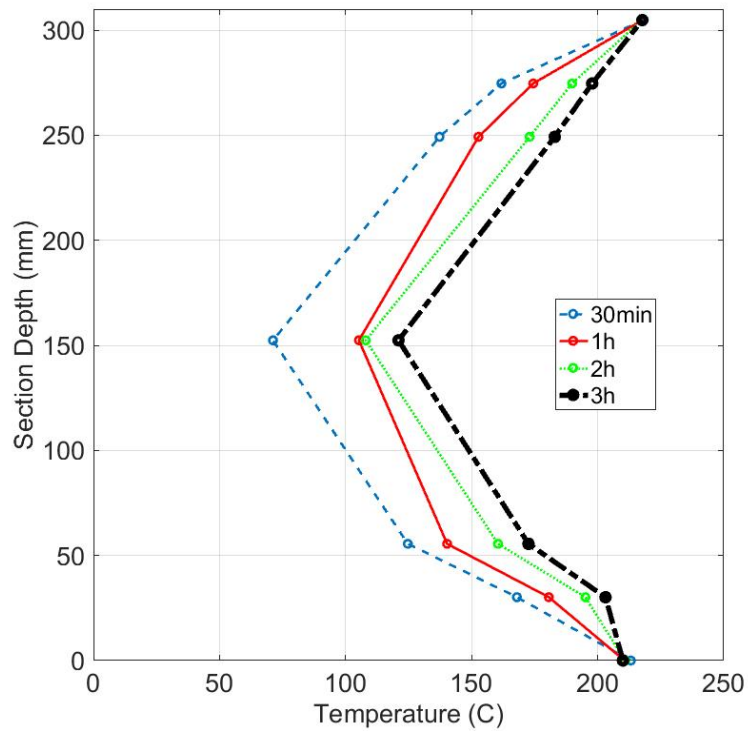
Figure 6.5 SC-WP-H: Evolution of thermal gradient (for surface temperature of 232˚C)
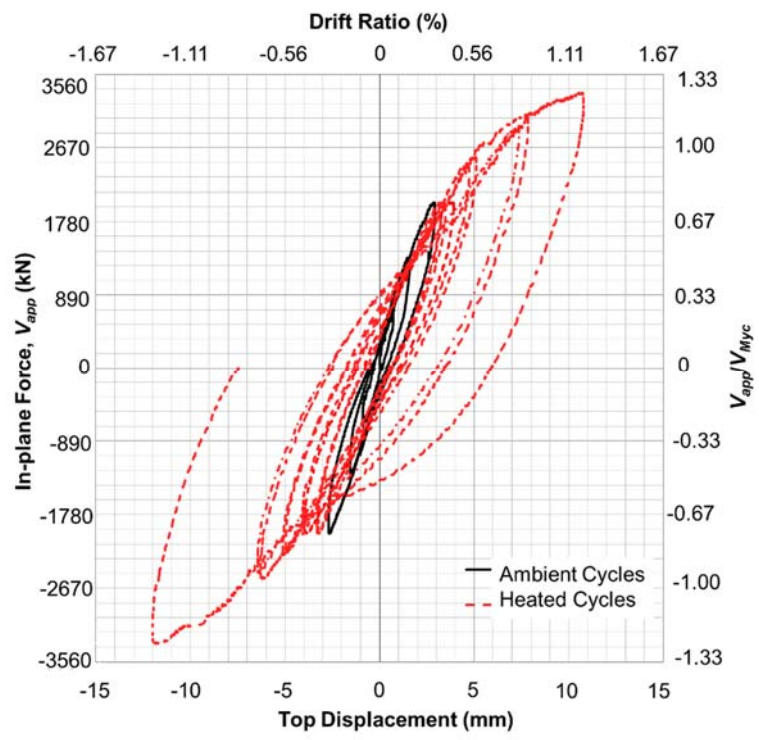
Figure 6.6 SC-WP-H: In-plane force-top displacement response
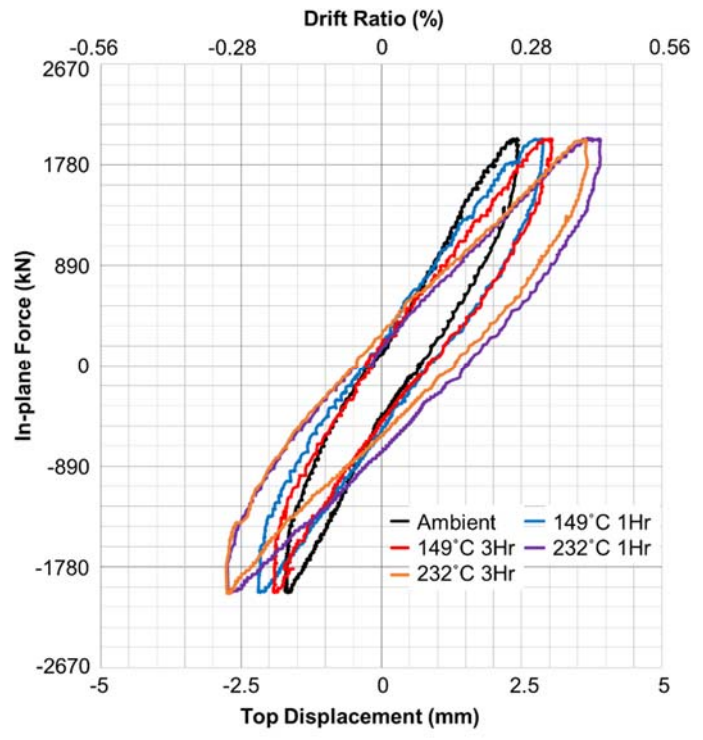
Figure 6.7 SC-WP-H: In-plane force-top displacement response (for $0.75F_n$ cycles)
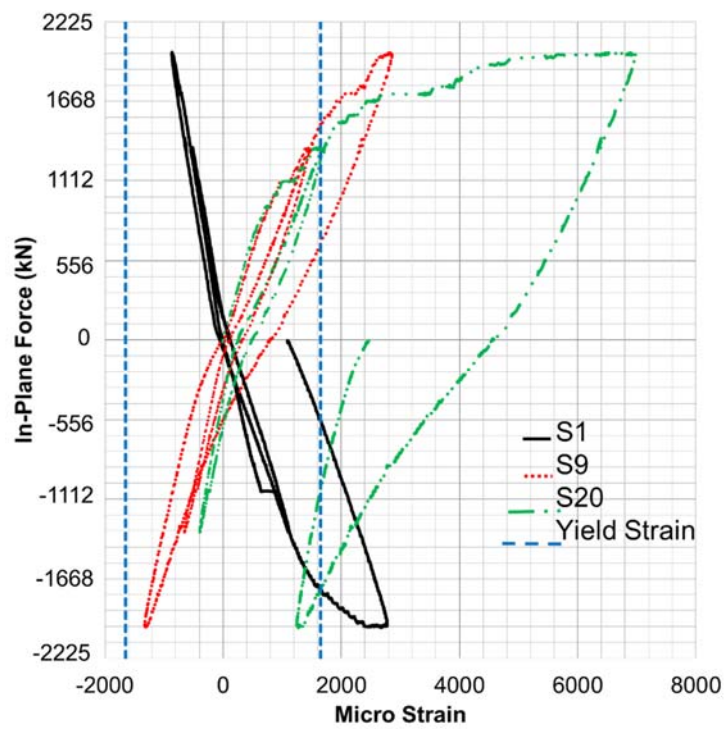
Figure 6.8 SC-WP-H: In-plane force-faceplate strains (F-ε) for $0.5F_n$ and $0.75F_n$ cycles

a) North face   South face

Figure 6.9 SC-WP-H: Specimen state at $0.5F_n$ ambient cycle (cycle no. 2)

a) North face
                                                       b) South face

Figure 6.10 SC-WP-H: Specimen state at $0.75F_n$-149°C-1 hour cycle (cycle no. 4)

a) North face   b) South face

Figure 6.11 SC-WP-H: Specimen state at $0.75F_n$-232˚C-1 hour cycle (cycle no. 6)

Figure 6.12 SC-WP-H: Specimen state (North face) at Δ_y-232°C-1 hour cycle (cycle no. 8)

Concrete dried up, cracks widening

Figure 6.13 SC-WP-H: Specimen state (South face) at 1.5Δ_y-232˚C-1 hour cycle (cycle no. 10)

a) North face   b) South face
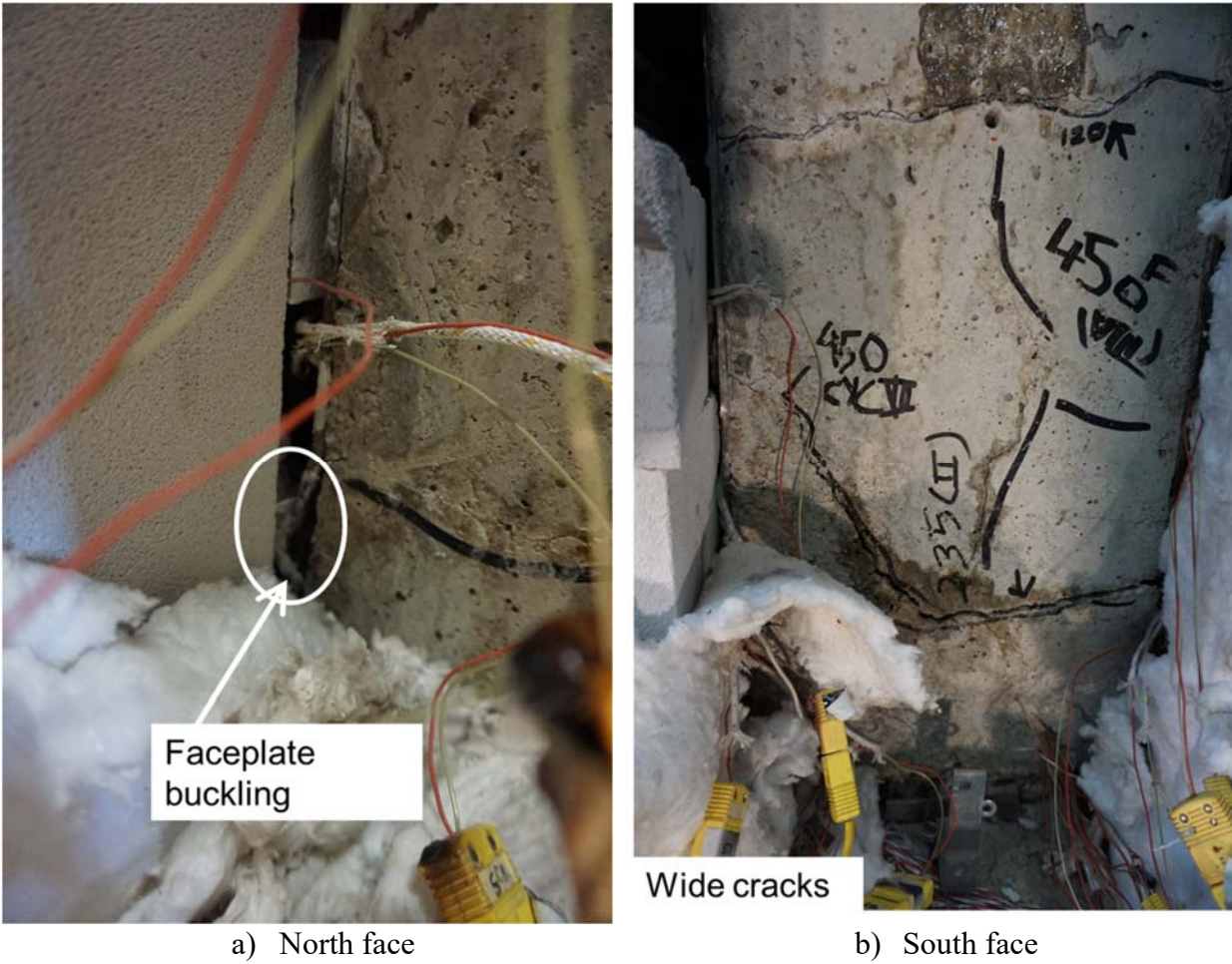
Figure 6.14 SC-WP-H: Specimen state at 2Δ*y*-232˚C-4 hour cycle (cycle no. 12)

a) North face

b) South face

Figure 6.15 SC-WP-H: Specimen state at failure (cycle no. 13)

Figure 6.16 SC-WP-H: Specimen at failure (faceplate rupture)

a) Top portion

b) Bottom portion

Figure 6.17 SC-WP-H: Specimen state at failure (top and bottom portions)
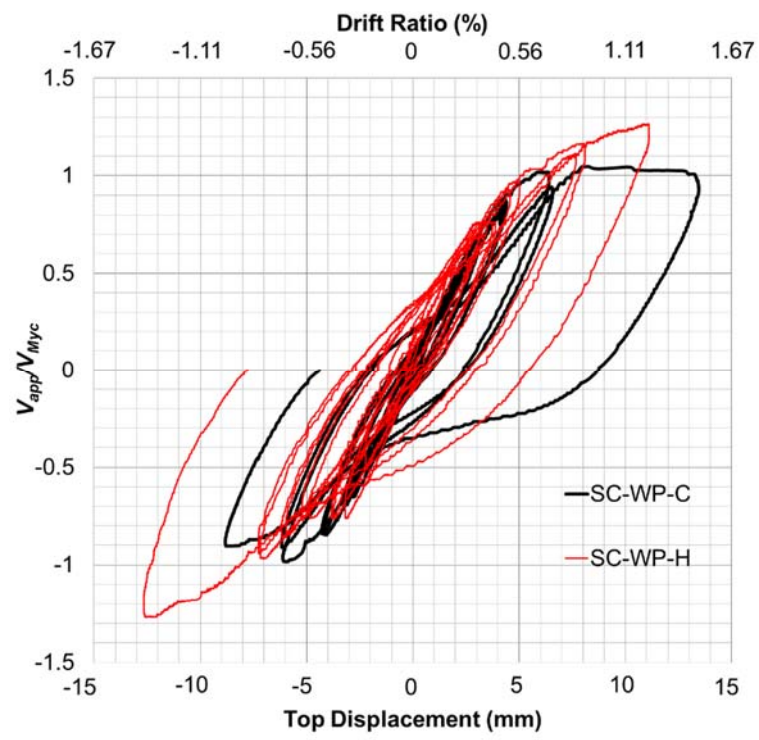
Figure 6.18 Comparison of in-plane force-top displacement response (SC-WP-C and SC-WP-H)
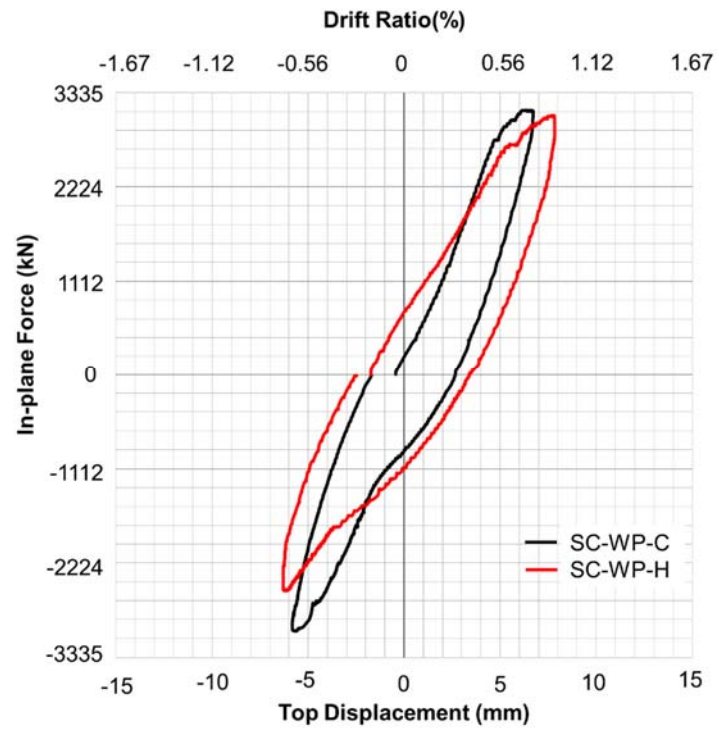
Figure 6.19 Comparison of 1.5Δ*y* cycles (SC-WP-C and SC-WP-H)
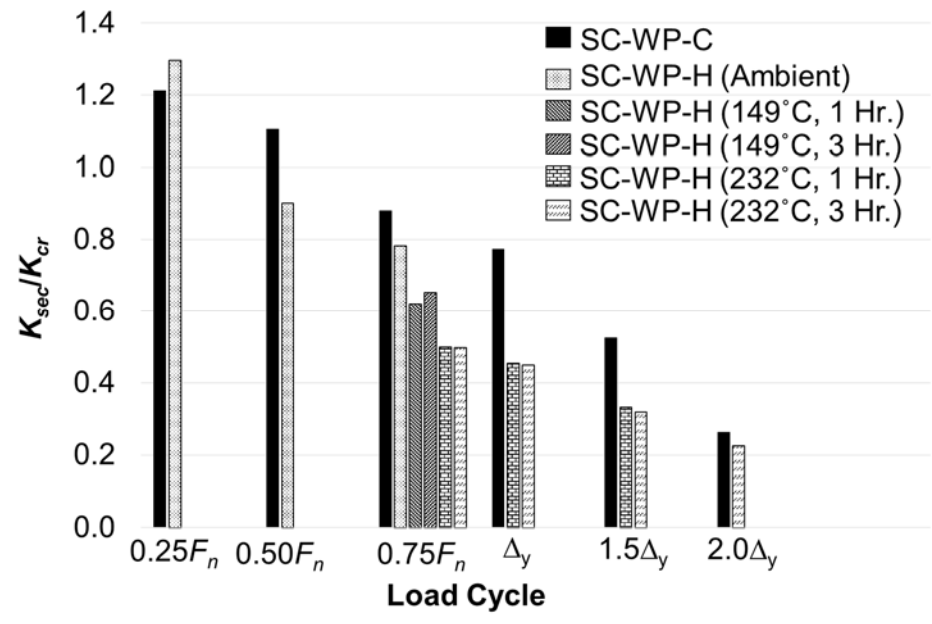
Figure 6.20 Comparison of stiffness degradation (SC-WP-C and SC-WP-H)
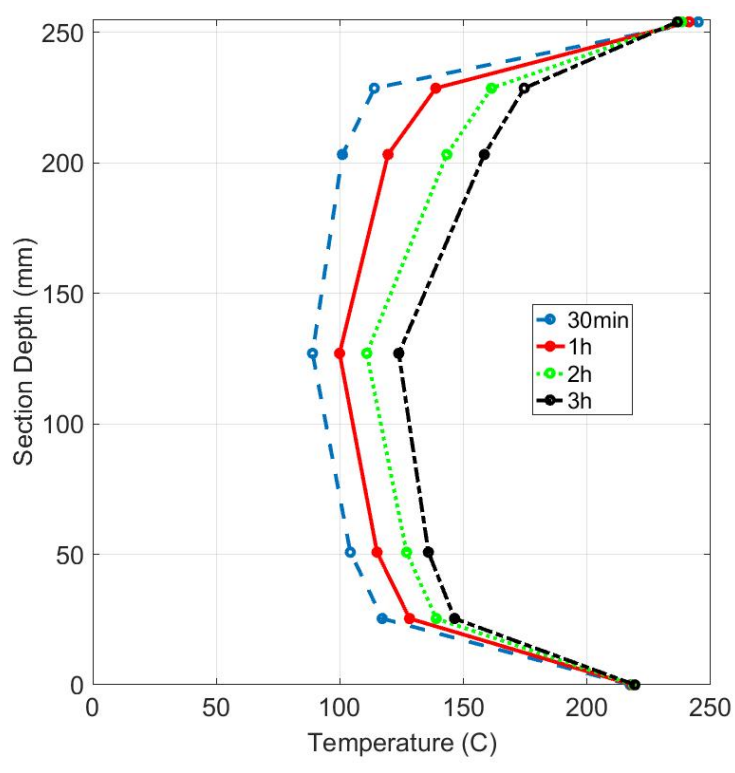
Figure 6.21 SC-W-H: Evolution of thermal gradient (for surface temperature of 232˚C)
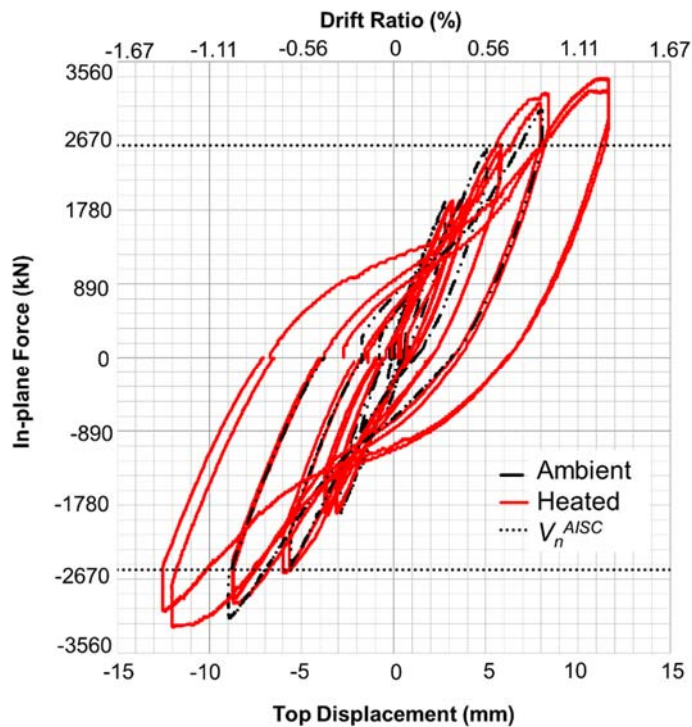
Figure 6.22 SC-W-H: In-plane force-top displacement response
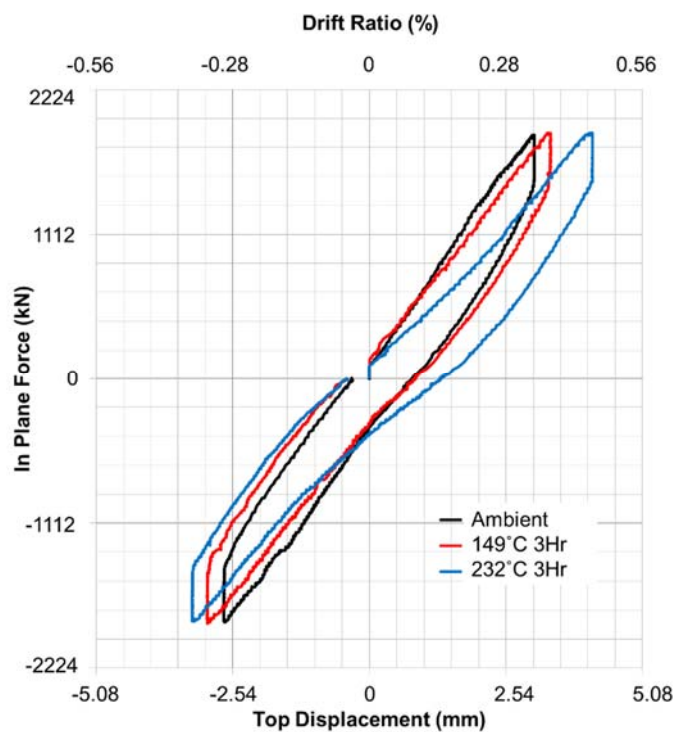
Figure 6.23 SC-W-H: In-plane force-top displacement response (for $0.75F_n$ cycles)
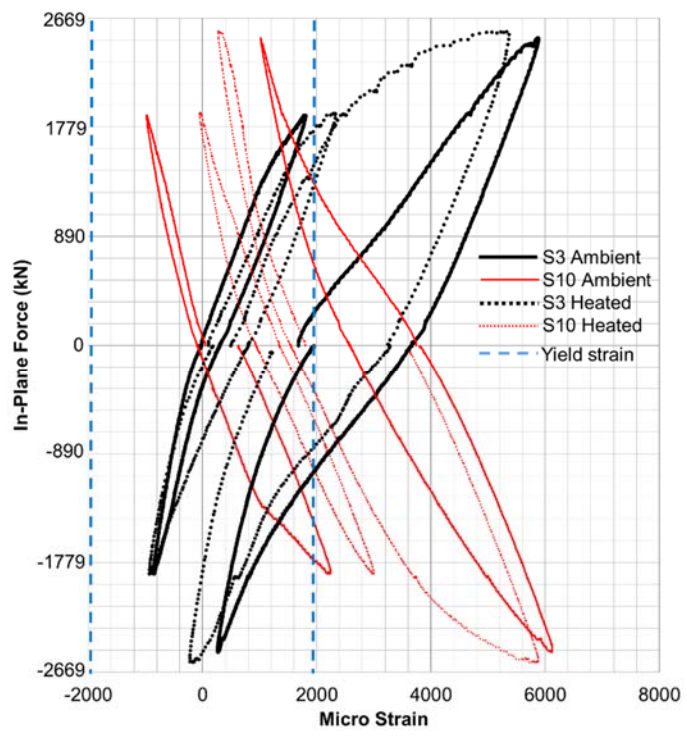
Figure 6.24 SC-W-H: Faceplate strains (for ambient and heated $0.75F_n$ and Δ_y cycles)
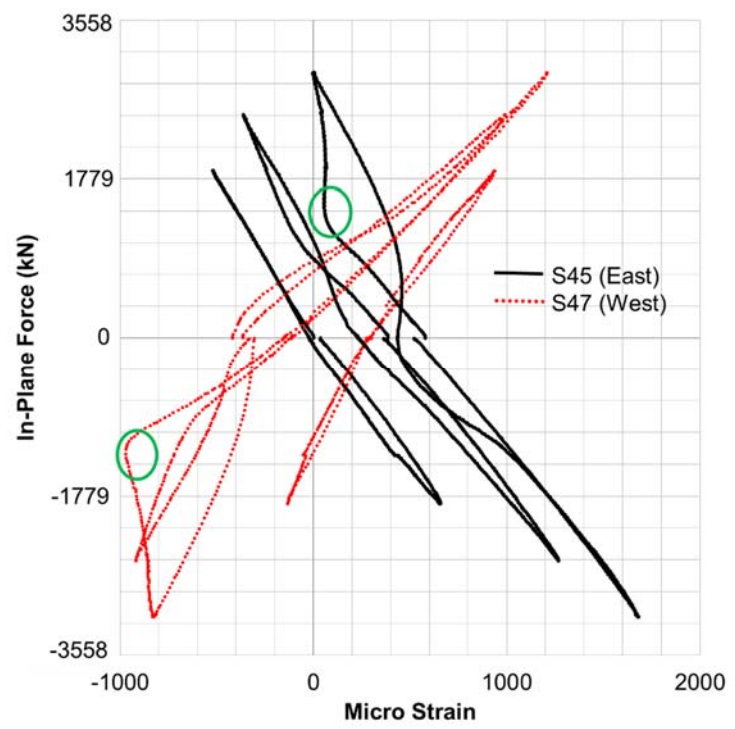
Figure 6.25 SC-W-H: Flangeplate strains (for ambient $0.75F_n$, Δ_y, and $1.5\Delta_y$ cycles)

Figure 6.26. SC-W-H: Faceplate-flangeplate-baseplate weld detail

Figure 6.27 SC-W-H: Weld fracture at detail A (observed after $2\Delta_y$ heated cycles)
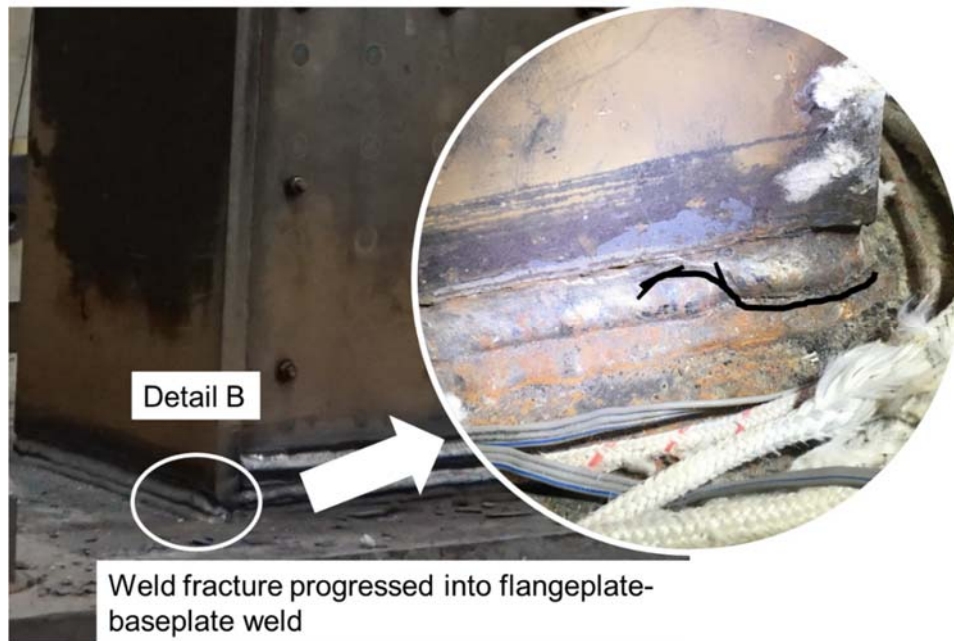
Figure 6.28 SC-W-H: Weld fracture at detail B (observed after $2\Delta_y$ heated cycles)

Figure 6.29 SC-W-H: Weld fracture initiated at other corners of the specimen (observed after $2\Delta_y$ heated cycles)

Figure 6.30 SC-W-H: East view of specimen after failure (failed during $3\Delta_y$ push cycle)

Figure 6.31 SC-W-H: South-West view of specimen after failure (failed during $3\Delta_y$ cycle)
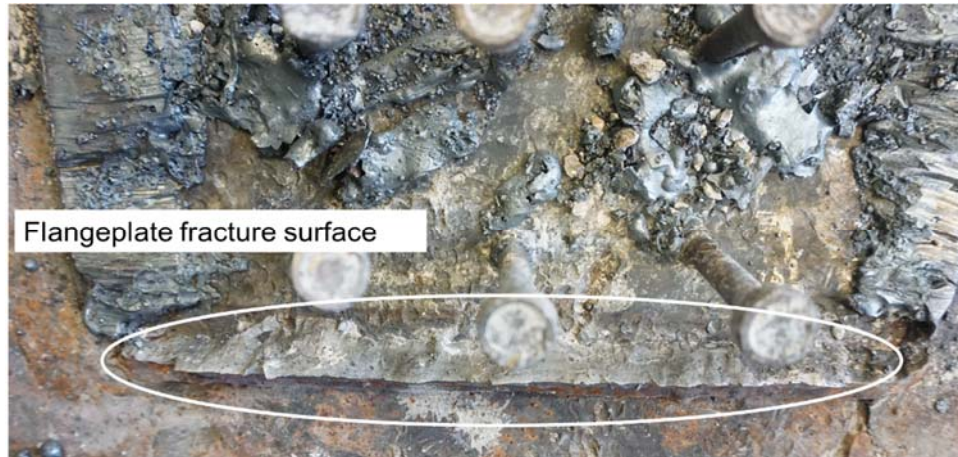
Figure 6.32 SC-W-H: Top view of baseplate (specimen removed)
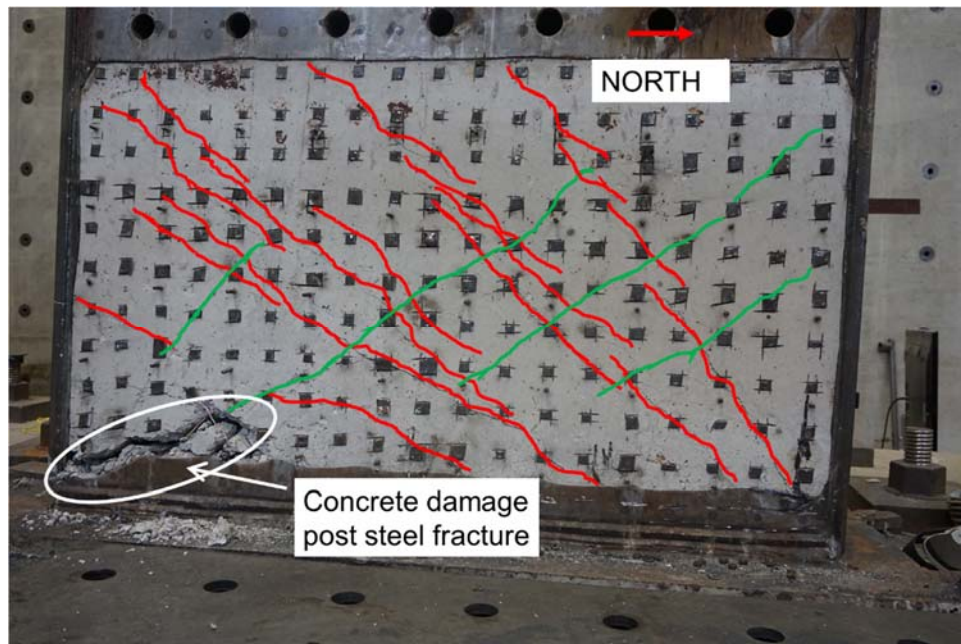
Figure 6.33 SC-W-H: Concrete cracking and damage at failure (faceplate removed)
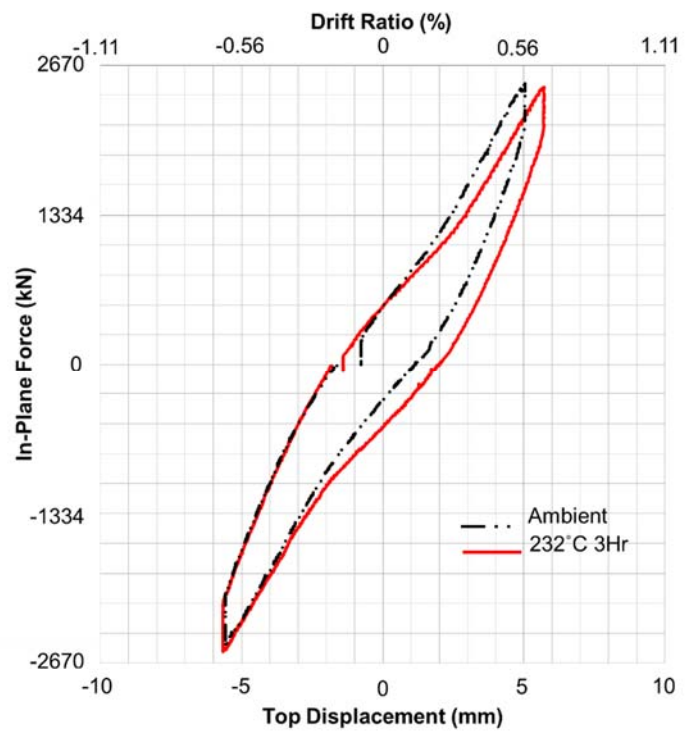
Figure 6.34 SC-W-H: Comparison of Δ_y heated and ambient cycles (ambient cycle conducted after heated cycles)
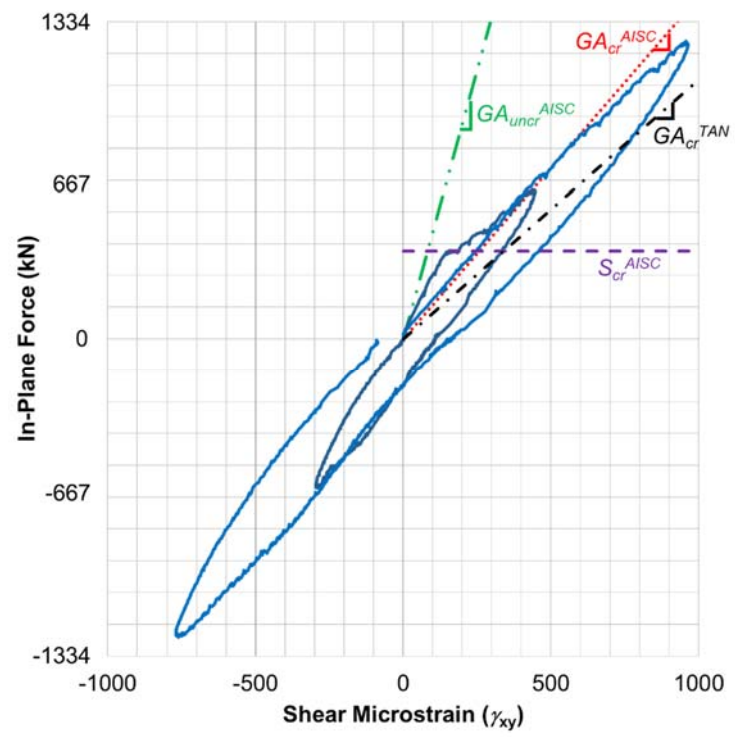
Figure 6.35 SC-W-H: Shear stiffness comparisons ($0.25F_n$ and $0.5F_n$ cycles)
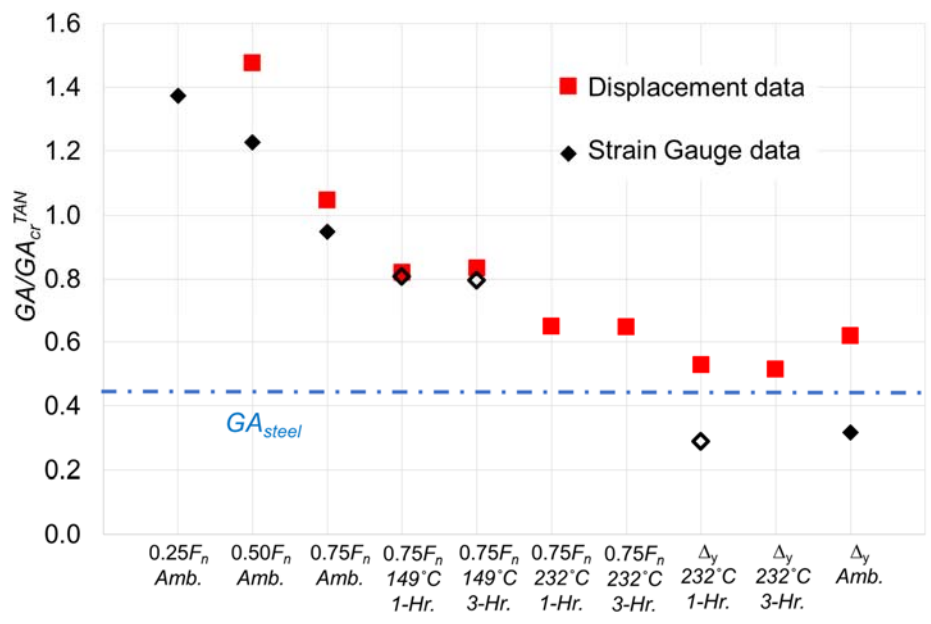
Figure 6.36 SC-W-H: Shear stiffness degradation
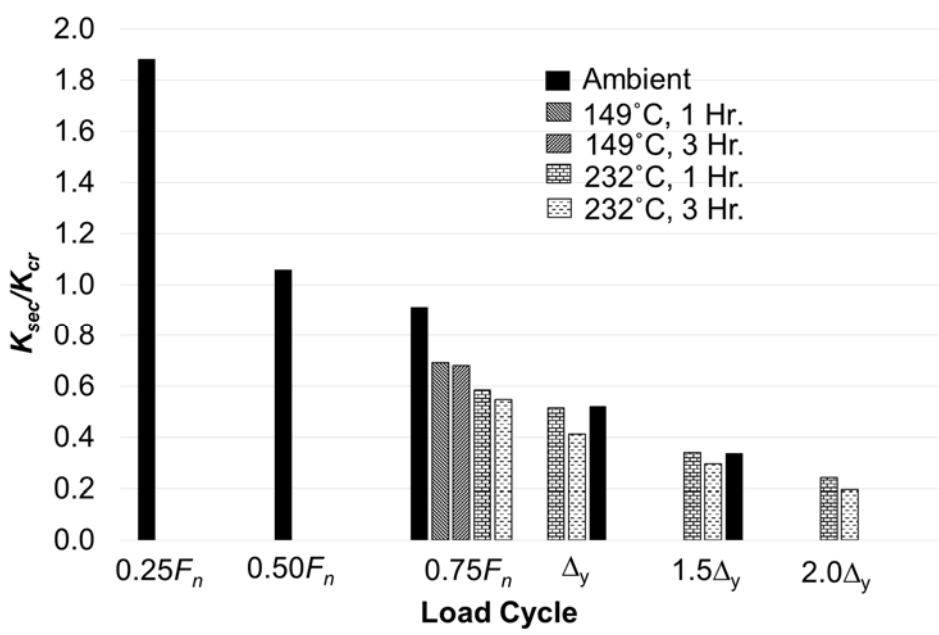
Figure 6.37 SC-W-H: Secant stiffness degradation
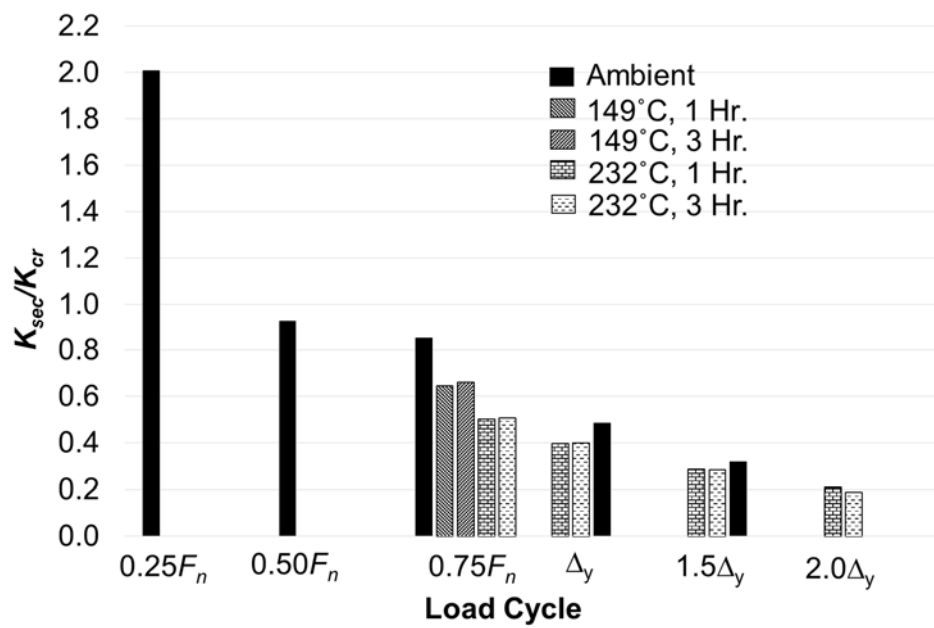
Figure 6.38 SC-W-H: Secant stiffness degradation [pull (-) cycles only]

Table 6.1 In-Plane stiffness of the specimens

Specimen	Initial Stiffness, K_{in}* (kN/mm)		Secant Stiffness, K_{sec}* (kN/mm)					
	Push (+)	Pull (-)	Ambient		149˚C		232˚C	
			Push	Pull	Push	Pull	Push	Pull
SC-WP-C	1765 (980)	1400 (890)	980 (635)	925 (570)	N.A.	N.A.	N.A.	N.A.
SC-WP-H	2325 (1085)	1745 (725)	775 (550)	890 (550)	655 (495)	665 (450)	550 (430)	510 (380)
SC-W-H	1410 (750)	1755 (915)	920 (580)	810 (535)	665 (515)	630 (485)	555 (450)	480 (400)

*Stiffness values in parenthesis are the uncorrected stiffnesses corresponding to measured top displacement (without correcting for the slip at the base and rotation at base).

Table 6.2 Summary of experimental results

Specimen	T_{max} (˚C)	$V_{n\text{-}ip}$ (kN)	$V_{n\text{-}ip}/V_{Myc}$ or $V_{n\text{-}ip}/V_n^{AISC}$	K_{in}/K_{uncr}	K_{sec}/K_{cr}			Drift ratio failure* (%)
					Ambient	149˚C	232˚C	
SC-WP-C	N.A.	3115	1.01	0.38	0.88	N.A.	N.A.	1.02 (1.24)
SC-WP-H	232	3300	1.25	0.50	0.78	0.62	0.50	1.14 (1.32)
SC-W-H	232	3300	1.29	0.52	0.91	0.68	0.55	1.17 (1.35)

*The values in parenthesis correspond to top displacement (without correcting for base slip and base rotation)

Table 6.3 Comparison of measured and calculated secant stiffnesses

Specimen	K_{sec}/K_{cr}			K_{sec}/K_{eff}		
	Ambient	149˚C	232˚C	Ambient	149˚C	232˚C
SC-WP-C	0.88	N.A.	N.A.	0.88	N.A.	N.A.
SC-WP-H	0.78	0.62	0.50	0.78	0.85	0.76
SC-W-H	0.91	0.68	0.55	0.91	1.13	1.10

7. FIBER MODEL FOR AXIAL FORCE-BIAXIAL MOMENT-SHEAR INTERACTION

The behavior of SC wall piers subjected to biaxial (in-plane and out-of-plane) loading was experimentally evaluated in Chapter 4. The response of SC wall piers with an in-plane aspect ratio greater than or equal to 0.6 was flexure controlled. The specimens failed due to interaction of in-plane and out-of-plane moments. Specimen SC-T-2.5Vn was forced to fail in vector shear by subjecting it to out-of-plane force of magnitude 2.5 times its nominal out-of-plane shear strength. Since the response was flexure controlled, an analytical model was developed and employed to obtain biaxial flexure interaction of wall piers [127]. The model was then updated to consider axial force-biaxial moment-shear interaction [128]. This chapter discusses the fiber model in detail. The chapter is organized into following sections:

- Development of the model: The algorithm for the model is presented, and the assumptions and material properties considered are presented.

- Validation of the fiber model: The fiber model is validated using strain gauge data from biaxial experiments discussed in Chapter 4.

- Biaxial Moment Interaction: A biaxial moment interaction surface is developed for SC wall piers. The interaction surface is compared with experimental results and finite element results.

- Axial force-biaxial moment Interaction: The effect of axial force on biaxial moment interaction surface is discussed, and axial force-biaxial moment interaction is defined.

- Biaxial Moment-shear Interaction: The interaction surface for biaxial moments and shears is developed.

7.1 Development of the Model

A finite difference based cross-section fiber model was developed to evaluate the interaction of forces and moments in SC wall piers. Algorithm for the fiber model is presented in Figure 7.1 and Figure 7.2. The part of algorithm presented in Figure 7.1 can be employed to obtain biaxial moment interaction surface. The complete algorithm needs to be employed if the axial force-biaxial moment-shear interaction is desired.

Cross-section of the wall is discretized into a two-dimensional fiber mesh, where the element size can be defined by the user. The model has currently been setup for rectangular cross-sections but can be updated to consider any cross-section. Steel and concrete model properties used for the model, and the algorithms for biaxial moment and biaxial moment-shear interactions are discussed in the following sub-sections.

7.1.1 Material Properties

The uniaxial stress-strain behavior of concrete is shown in Figure 7.3. The concrete contribution in tension was conservatively ignored. The uniaxial compressive stress-strain behavior of concrete was defined using Popovic's model [129]. Concrete is considered to reach peak compressive stress at a compression strain of 0.0035. The compressive stress then degrades, and failure is considered at a strain of 0.005.

The uniaxial stress-strain behavior of steel is shown in Figure 7.4. Steel is considered elastic-perfectly plastic in tension (post-yield hardening of steel is conservatively ignored). For compression, the buckling of faceplates is considered. Since the faceplate slenderness for specimens discussed in Chapter 4 ensures that faceplates yield in compression before local buckling (based on [26]), the steel compression stress is modeled to reach yield stress, and then degrade to consider buckling. Post-buckling, the stress is considered to reduce by 25% (from F_y to

0.75F_y) as the compressive stress increases from ε_y to $2\varepsilon_y$. The stress is then considered to remain constant. Experimental results by Zhang [70] indicate that for SC walls meeting the slenderness requirements of AISC N690s1 [26], plate buckling was observed at strain (ε_{cr}) values greater than 1.3 times the yield strain (ε_y). Therefore, the compression buckling behavior considered is conservative. Additionally, the peak response of the specimens is expected in strain ranges of 1 to 2 times the yield strain. Detailed finite element analysis using benchmarked models can be conducted to obtain the effective stress-strain response of steel plates (as discussed in [72]). The effective stress-strain curves for steel can then be used to define the compression stress-strain curve for steel to be used in the fiber model.

7.1.2 Biaxial Moment Interaction

Figure 7.1 shows the steps for biaxial moment part of the algorithm. Cross-section and material parameters are input into the model, and the cross-section is discretized based on desired fiber element size. The element size was set at 4.8 mm along the thickness (faceplate thickness for biaxially loaded specimens) and 25.4 mm along the length. The axial load value can be specified, or the algorithm can be run for a range of axial force values by setting a loop. The initial trial value of the centroidal strain is calculated based on the axial force and stiffness. A range of out-of-plane curvatures is provided. For each value of out-of-plane curvature, the fiber model iteratively establishes force equilibrium to obtain the in-plane moment-curvature. Error tolerance is set as 1% of the applied force or moment. To optimize the run-time of the fiber model, error correction is set to dynamically change based on the error trends and number of iterations. Peak in-plane moment is recorded for the value of out-of-plane moment corresponding to the out-of-plane curvature. Thus, for a range of out-of-plane moments (from out-of-plane curvature inputs), the in-plane

moment capacity of the cross-section is obtained. These sets of in-plane and out-of-plane moments establish the biaxial moment interaction for the cross-section.

7.1.3   Biaxial Moment-Shear Interaction

For SC wall piers with aspect ratios less than 0.6, or for wall piers having shear dominated response (e.g., Specimen SC-T-2.5Vn in Chapter 4 was forced to have a shear dominated failure by subjecting it to an out-of-plane shear of magnitude 2.5 times its nominal strength), the interaction of biaxial moments with vector shears may need to be considered. The biaxial moment interaction algorithm discussed in the previous section was updated to consider the shear forces. Figure 7.2 presents the procedure to consider vector shear failure into the biaxial moment interactions. Once equilibrium has been established for a set of values of out-of-plane and in-plane curvatures, and the corresponding moments obtained, the in-plane and out-of-plane shear forces are calculated. The shear forces are calculated based on the in-plane and out-of-plane aspect ratios (shear span-to-depth ratios), which are input parameters.

The out-of-plane shear force (V_{oop}) is considered to be uniformly distributed over the concrete area in compression (uncracked concrete). For SC wall piers with ties spaced at greater than half the section thickness, the out-of-plane strength is the greater of steel and concrete contributions (per AISC N690s1 [26]). Typically, the concrete contribution will be higher than the steel contribution. Per ACI 349 [25] just the concrete contribution of concrete is considered to out-of-plane strength for ties spaced at greater than half the section thickness. For ties spaced at less than half the section thickness, the out-of-plane strength is the sum of steel and concrete contributions. Currently, the model conservatively does not consider tie contribution to out-of-plane shear strength. However, the tie contribution can be subtracted from the total shear force, and the net shear to be resisted by concrete can be uniformly distributed to uncracked concrete. The in-plane shear force (V_{ip}) is

distributed between steel plates and concrete in terms of their relative stiffnesses. Steel stiffness is calculated based on the shear modulus of steel and cross-sectional area of the plates. Shear stiffness of the uncracked concrete in considered. Shear force distribution in steel is considered parabolic. For concrete, uniform distribution is considered.

The uncracked concrete fibers will be subjected to a combination of axial and shear stresses due to biaxial moments and vector shears. Shear failure of concrete fibers is checked using Mohr-Coulomb ([130], [131]) interaction surface for axial and shear stresses. Mohr-Coulomb failure surface can be expressed as Equation 7.1, where τ is the shear strength of concrete, σ is the normal stress, ϕ is the angle of internal friction and c is cohesion.

$$\tau = \sigma \tan(\phi) + c \qquad \text{Equation 7.1}$$

The angle of internal friction and cohesion values for concrete can be obtained from the literature. For this model, experimentally determined values by Pul et al.[132] were used. The authors conducted direct shear tests on prismatic concrete specimens with varying shear gaps, concrete strength, and maximum aggregate size. The values corresponding to compression strength (36 MPa) and maximum aggregate size (9.5 mm) for SC-0.5T-Vn specimen were selected. The values of ϕ and c used for the model are 34.5-degrees and 7.1 MPa respectively. Based on the Mohr-Coulomb failure criteria, if the shear stress in a concrete fiber is greater than the shear strength, the fiber is considered to have failed and does not resist any normal or shear stress. Stress in steel fibers is limited by Von-Mises yielding criteria. The normal stress for steel fibers with Von-Mises stress exceeding the yield stress is adjusted to meet the yield criteria. The updated stress states are employed to re-establish equilibrium. This process is repeated for all pairs of in-plane and out-of-plane curvatures to obtain biaxial moment interaction considering shear failure.

7.2   Model Capabilities and Assumptions

The fiber model can be employed to obtain the evolution of normal strains and stresses for various combinations of axial force and biaxial moments. In-plane moment curvature diagrams can be obtained for different values of out-of-plane moments. The evolution of specimen damage can be monitored, e.g., faceplate yielding and buckling, concrete crushing, etc. The model can provide biaxial moment interaction diagrams for flexure controlled walls. Biaxial moment interaction diagrams can also be obtained while accounting for axial force and vector shear.

Since the cross-section fiber model was intended to serve as a simplistic tool to obtain biaxial moment interaction, some simplifications and assumptions have been made. While they have been discussed in the previous section, they are summarized again here.

- Conservatively, hardening is not considered in the steel stress-strain curve. Compression buckling is considered to initiate as soon as yield stress in reached (conservative).

- Conservatively, concrete contribution in tension is not considered. For compression, the effect of confinement is not considered (conservative).

- Out-of-plane shear is considered to be resisted by uncracked portion of concrete infill (concrete in compression). The contribution of out-of-plane shear reinforcement is not considered (conservative).

- Concrete fiber elements are considered to resist no axial or shear stress post shear failure using Mohr-Coulomb criteria (conservative).

7.3   Validation of Fiber Model

The fiber model was verified against experimental results from biaxially loaded specimens discussed previously (Chapter 4). Strain profiles obtained from the fiber model were compared with experimentally observed strains for Specimen SC-0.5T-Vn. Figure 7.5 compares the strains

when an out-of-plane load of magnitude 534-kN (120 kips) was applied (with no in-plane loading). For fiber model, measured steel and concrete properties for SC-0.5T-Vn were used (provided in Table 3.1). Figure 7.5a shows the strain gauge profile for a cross-section at the base of the wall. The out-of-plane moment corresponded to a force of 534-kN applied at 381 mm from the base (to match the strain gauge locations). A linear strain gradient is observed through the thickness of the wall, with peak tensile strains of magnitude 500 $\mu\epsilon$ and peak compressive strain of magnitude (-)200 $\mu\epsilon$. Figure 7.5b shows the experimental force-strain plot for 534-kN out-of-plane loading cycle. Strain gauges shown in the figure are located 76 mm from the base and 38 mm from the edge. Strain gauge location is shown in Figure 3.10. The peak tensile strains vary from 250 to 420 $\mu\epsilon$ (in comparison to 500 $\mu\epsilon$ from fiber model), and peak compressive strains vary from 100 to 250 $\mu\epsilon$ (in comparison to 200 $\mu\epsilon$ from fiber model). The tensile strains from fiber model are higher because the model does not consider the concrete contribution in tension.

Figure 7.6 presents the comparison of strains from fiber model with experimentally observed strains for biaxial loading. Figure 7.6a shows the strain gauge profile for a cross-section at the base of the wall. The out-of-plane moment corresponded to a force of 1070-kN applied at 381 mm from the base (to match the strain gauge locations). The in-plane moment corresponded to a force of 1112-kN applied at 838 mm from the base. Biaxial loading results in an asymmetric strain profile that varies through the length and the thickness of the specimen. Peak tensile strains of magnitude 1700 $\mu\epsilon$ were observed at the corner subjected to tension due to out-of-plane and in-plane loadings. Peak compressive strain of magnitude (-) 1000 $\mu\epsilon$ were observed at the opposite corner (subjected to compression due to in-plane and out-of-plane loadings). Figure 7.6b shows the experimental force-strain plot for 1112-kN in-plane loading cycle (with a constant out-of-plane load of 1070-kN). Peak tensile strain for corner subjected to compression due to biaxial loading is approximately

2100 με. However, the strain gauge data does not indicate any flattening due to yielding. The values are higher than that observed from fiber model (1700 με), which may be due to cyclic damage in the specimen. Peak compressive strain for S9 (subjected to compression due to biaxial loading) is approximately the same as observed from fiber model (1000 με).

The comparisons of strains obtained from fiber model with those observed experimentally indicate that the fiber model reasonably predicts the evolution of through-thickness strain profile for biaxial moments. For further verification, the moment-curvatures and biaxial moment interactions obtained from the fiber model will be compared with experimental results (and finite element results) in the following sections.

7.4   Biaxial Moment Interaction

The fiber model can be employed to obtain in-plane moment-curvature response for different magnitudes of out-of-plane moments (for no axial force, and not considering shear forces). Figure 7.7 presents the in-plane moment curvature corresponding to the out-of-plane loading cases for specimens tested and discussed in Chapter 4. The figure also plots the in-plane plastic (M_p) and compression yield moment (M_{yc}) capacities calculated per Kurt et al. [69]. Measured steel and concrete properties for SC-0.5T-Vn were used for all the cases. Curve 'No OOP' corresponds to no out-of-plane force applied (the case for SC-T-C). SC wall piers (with aspect ratios greater than or equal to 0.6) with no out-of-plane loading are expected to reach M_p (SC-T-C failed due to weld rupture, and did not reach M_p). '$0.37M_n^{AISC}$' corresponds to the out-of-plane moment applied for SC-T-Vn. The peak moment for '$0.37M_n^{AISC}$' case is approximately equal to M_p (consistent with experimental observations for SC-T-Vn). '$0.74M_{n-oop}$' corresponds to the out-of-plane moment applied for SC-0.5T-Vn. While SC-0.5T-Vn reached M_{yc}, peak moment from fiber model is

marginally (7%) lower. This may be because steel stress-strain behavior was considered to be elastic-plastic in the fiber model. Thus, the fiber model can reasonably predict the in-plane moment capacities of biaxially loaded SC wall pier specimens.

The fiber model provides in-plane moment capacity for an applied magnitude of the out-of-plane moment. The sets of values for in-plane and out-of-plane moments can be used to develop the biaxial moment interaction surface for wall piers. Figure 7.8 presents the interaction of normalized in-plane moment with the normalized out-of-plane moment. The in-plane moment is normalized with in-plane plastic moment capacity, M_p. The out-of-plane moment is normalized with nominal out-of-plane moment strength (M_n^{AISC}, using measured properties per AISC N690 [26]). It is observed that a weak interaction exists between the in-plane and out-of-plane moments.

Finite element models were used to validate the interaction obtained from the fiber model. The wall pier was modeled in ABAQUS [92] using layered composite shell (LCS) elements with a fixed base. The wall pier section (with section and material parameters consistent with the fiber model) was subjected to different combinations of in-plane and out-of-plane moments to obtain the data points (FEA data points) plotted in Figure 7.8. Data points for the experiments are also plotted on the interaction surface and it is observed that specimens SC-T-Vn and SC-0.5T-Vn lie outside the interaction surface, indicating the conservatism of the interaction surface. SC-T-2.5Vn lies inside the interaction surface. However, specimen SC-T-2.5Vn was subject to an out-of-plane force magnitude of 2.5 times the out-of-plane shear strength of the specimen, which forced the specimen to develop a vector shear failure mode as discussed previously. The specimen does not have a flexure controlled behavior and the interaction surface is not applicable to the specimen. Biaxial moment-shear interaction needs to be considered for SC wall piers that have shear

dominated response (due to high magnitude of shear loading, or low aspect ratio). Biaxial moment interaction considering shear forces is discussed in Section 7.6.

For design purposes, the quadratic interaction can be simplified to a trilinear interaction surface, anchored at in-plane compression yield moment capacity (0, M_{yc}), nominal out-of-plane moment capacity (M_n^{AISC}, 0), ($0.4M_n^{AISC}$, M_{yc}), and (M_n^{AISC}, $0.4M_p$). The design interaction surface is conservative in comparison to experimental results, the fiber model interaction surface, and the finite element analysis data points, and can be employed to consider biaxial moment interaction for the design of SC wall piers.

7.5   Axial Force-Biaxial Moment Interaction

SC wall piers in nuclear facilities are stocky and may not be subjected to high axial forces (in comparison to the capacity). The axial loads for these walls are expected to be lower than the balance point for axial force-moment interaction diagrams. However, walls in commercial applications may be subjected to considerable axial demands (due to sustained loads or vertical components of seismic demands). Axial force-biaxial moment interaction needs to be evaluated for SC wall piers. The fiber model can be employed to evaluate the axial force-moment (P-M) interaction for SC wall piers.

Figure 7.9 presents the normalized in-plane and out-of-plane P-M interaction for SC wall piers. Consistent with previous sections, material and section parameters for SC-0.5T-Vn were used. The axial compressive force (P) is normalized with nominal axial strength (P_n). The in-plane and out-of-plane moments are normalized with the corresponding moment capacities (for no axial load) obtained from the fiber model ($M_{n\text{-}fiber}$) The nominal axial strength is calculated using Equation 7.2 (Equation A-N9-15 of AISC N690s1 [26]), where A_s and A_c are steel and concrete cross-sectional areas, and F_y and f'_c are steel and concrete strengths.

$$P_n = A_s F_y + 0.85 f_c' A_c \qquad \text{Equation 7.2}$$

The in-plane and out-of-plane *P-M* interaction diagrams are similar with peak normalized moments of 1.5 to 1.6, corresponding to normalized axial loads of 0.3 to 0.4 (balance point). Thus, axial compressive forces up to $0.7P_n$ increase the moment capacity of the wall piers in comparison to capacity at no axial load. For higher magnitude of axial loads, the moment capacity starts reducing.

Figure 7.10 shows the change in the biaxial moment interaction surface as axial compression is applied. The in-plane and out-of-plane moments are normalized with M_p and M_n^{AISC} respectively (without considering *P-M* interaction). It is observed that the interaction surface expands as axial compression increases up to $0.4P_n$. As the compression force increases further, the interaction surface starts shrinking again. For very high axial loads, the interaction surface shrinks below the surface for no axial load.

The biaxial moment interaction can be updated to include *P-M* interaction obtained from the fiber model. Figure 7.11 shows the interaction where in-plane and out-of-plane moments are normalized with moment capacities obtained from the fiber model for different magnitudes of axial forces (as shown in Figure 7.9). It is observed that the interaction curves are reasonably similar. For the purpose of design, *P-M* interactions can be conservatively simplified to bilinear or trilinear curves, which can then be employed to obtain biaxial interactions considering *P-M* interaction. Figure 7.12 and Figure 7.13 show the simplified in-plane and out-of-plane *P-M* interactions respectively. The interactions have been simplified to bilinear or trilinear interactions. Figure 7.14 presents the biaxial interaction for different magnitudes of axial compressive loads. The out-of-plane moments have been normalized with nominal out-of-plane capacity per AISC N690s1 [26], scaled based on simplified *P-M* interaction (Figure 7.13), M_n^{AISC-P}. Similarly, the in-plane moments have been normalized with plastic moment capacity, scaled based on simplified *P-M* interaction (Figure 7.12).

The idealized trilinear design interaction for biaxial moments (as discussed in Figure 7.8) has also been plotted in Figure 7.14. The design interaction is conservative for different magnitudes of axial compressive forces. Biaxial interaction curves for axial loads less than the balance point ($0.4P_n$) are within 20% of the design interaction surface. However, the conservatism of design surface increases for higher magnitude of axial compressive forces (above $0.4P_n$). This is because the simplified *P-M* interactions considered are more conservative for higher axial forces (as seen in Figure 7.12 and Figure 7.13). However, the stocky nuclear walls are not expected to experience axial forces greater than the balance point. The simplified *P-M* interaction curves can be refined to improve the accuracy of the axial force-biaxial moment interaction curves for high magnitudes of axial compressive forces.

7.6   Biaxial Moment-Shear Interaction

The response of structural walls may be shear or flexure controlled depending on the aspect ratio. As observed for specimen SC-T-2.5Vn, walls with aspect ratios corresponding to flexure failure modes may be forced into shear failure by significantly high shear forces. Therefore, it is important to consider the biaxial shear-moment interaction for shear walls. The fiber model was employed to obtain biaxial moment interaction considering shear failure. Figure 7.15 presents the variation in biaxial moment interaction considering shear forces corresponding to the moments. Interaction surface for pure biaxial moments is also presented (also presented in Figure 7.8). The out-of-plane aspect ratio is kept constant at 1.5 (same as the experiments), and the in-plane aspect ratio is varied from 1.0 to 0.5. The interaction surface shrinks as the walls get squatter (in-plane aspect ratios decrease). This is because squatter walls will experience higher vector shear forces for the same magnitude of base moments. Higher shear stresses will result in Von-Mises yielding of steel fibers at lower magnitudes of flexural stresses. Similarly, high vector shear in concrete fibers will result

in shear failure for lower magnitudes of flexural stresses. The in-plane moment capacity reduces by about 15% as the aspect ratio changes from 1.0 to 0.5. Thus, the fiber model provides biaxial moment interaction surfaces for SC wall piers while accounting for vector shear forces.

As seen previously in Figure 7.8, specimen SC-T-2.5Vn lay inside the interaction surface. Since the specimen failed due to vector shear, the biaxial moment interaction surface (without considering shear loads) did not apply to the specimen. Figure 7.16 presents the comparison of experimental results with biaxial moment interaction surface, with and without consideration of shear failure. The biaxial moment interaction surface (while accounting for vector shear loads corresponding to an in-plane aspect ratio of 0.6 and an out-of-plane aspect ratio of 1.5) is conservative in comparison to the experimental results (including SC-T-2.5Vn).

7.7   Chapter Summary

This chapter describes a finite-difference based cross-section fiber analysis model for developing axial force-biaxial moment-shear interaction. Material properties and algorithm for the model are presented. The model iteratively establishes equilibrium for axial forces and biaxial moments. Shear interaction is considered by incorporating Mohr-Coulomb based shear failure for concrete and Von-Mises yielding for steel. Capabilities and assumptions for the model are listed in the chapter. The model is validated using experimental results for wall pier specimens subjected to biaxial loadings. A discussion on the *P-M* interaction for wall piers is provided. The *P-M* interaction can be incorporated in biaxial moment interaction. Idealized biaxial moment interaction surface is developed. The interaction surface compares conservatively with finite element model results and experimental results. For shear controlled SC wall piers, the biaxial interaction surface is updated to consider shear failure. The fiber model can be employed to obtain axial force-biaxial moment-shear interaction for SC wall piers.
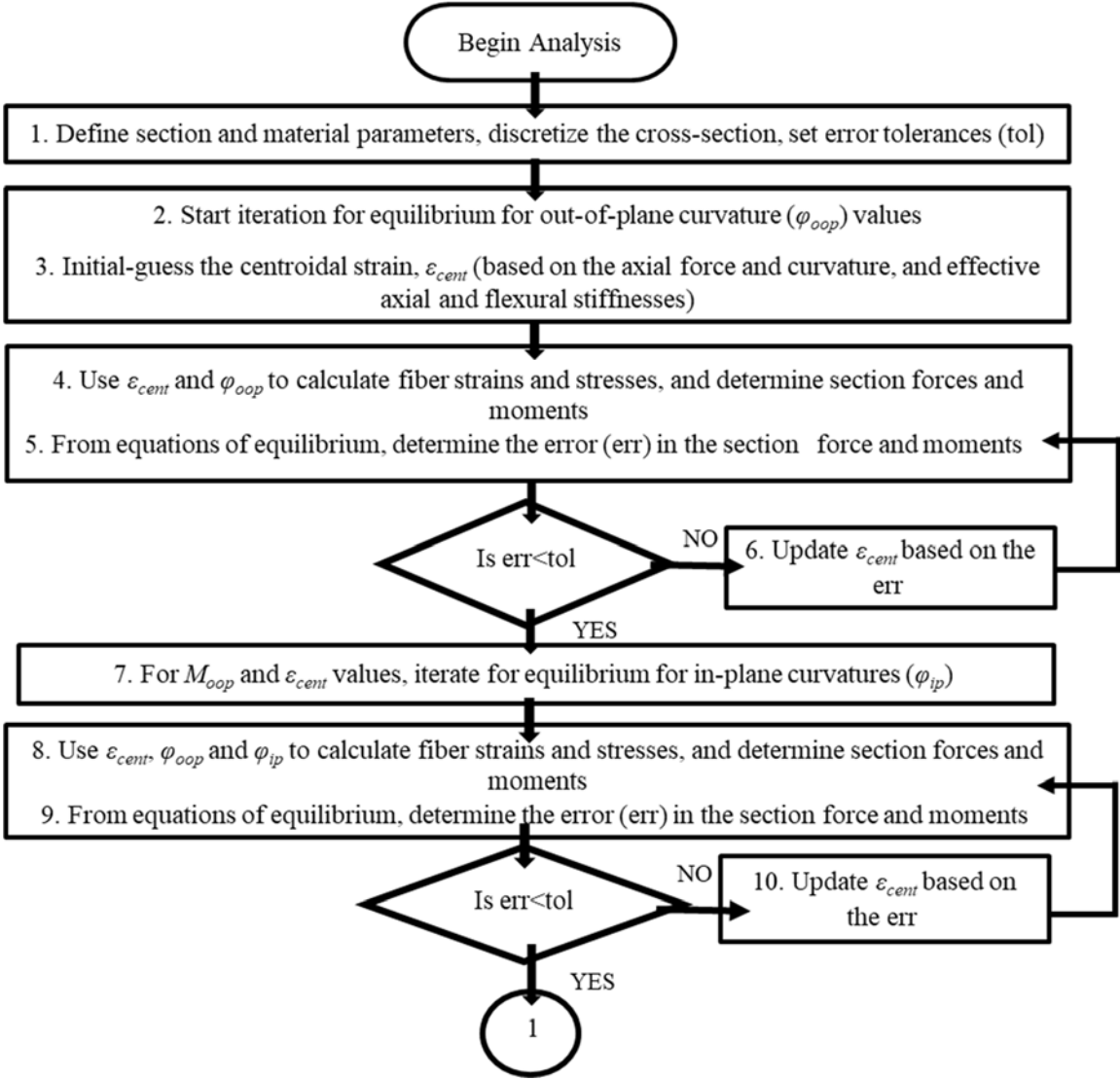
Figure 7.1 Algorithm for axial force-biaxial moment-shear interaction
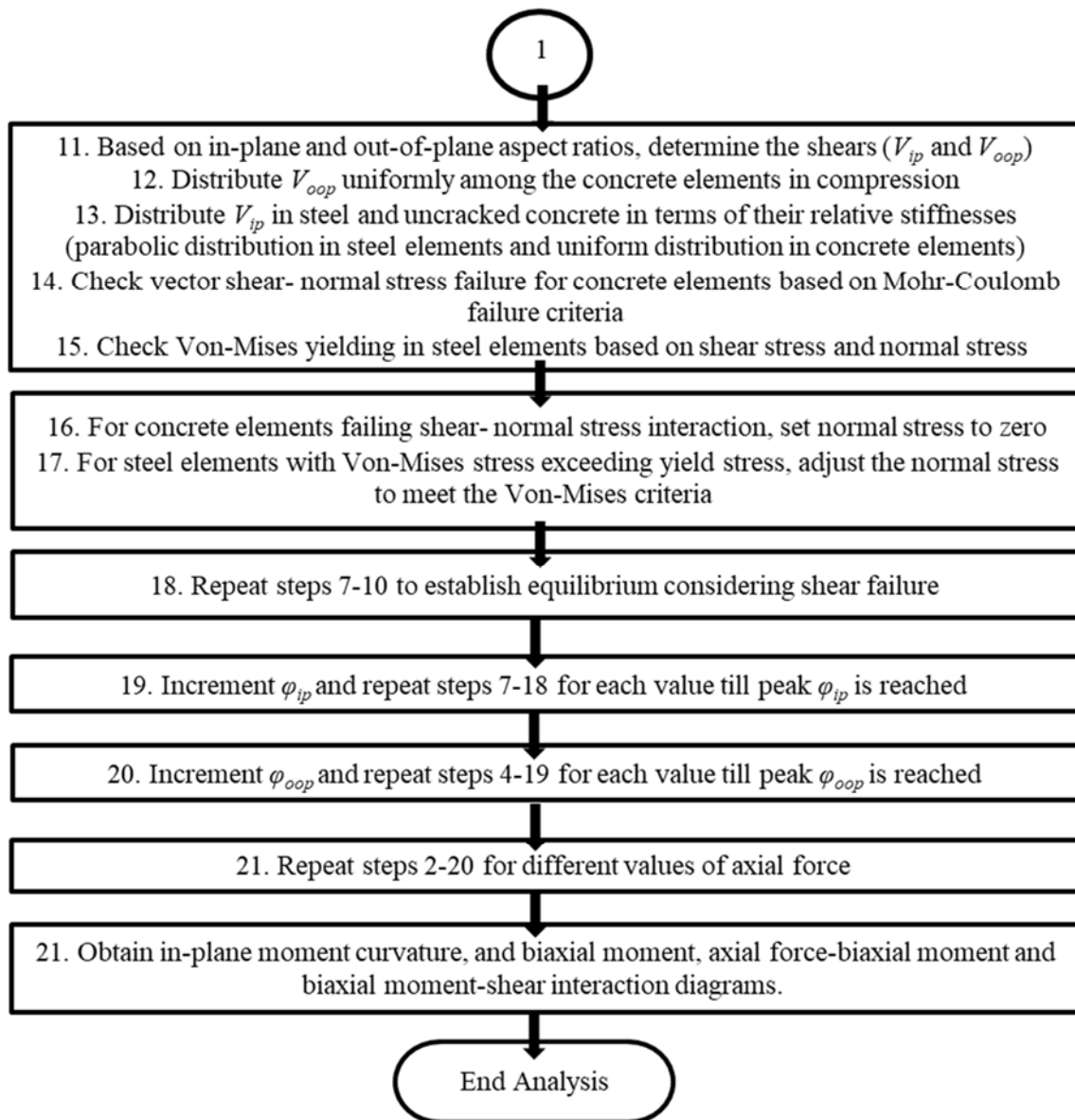
Figure 7.2 Algorithm for axial force-biaxial moment-shear interaction (contd.)
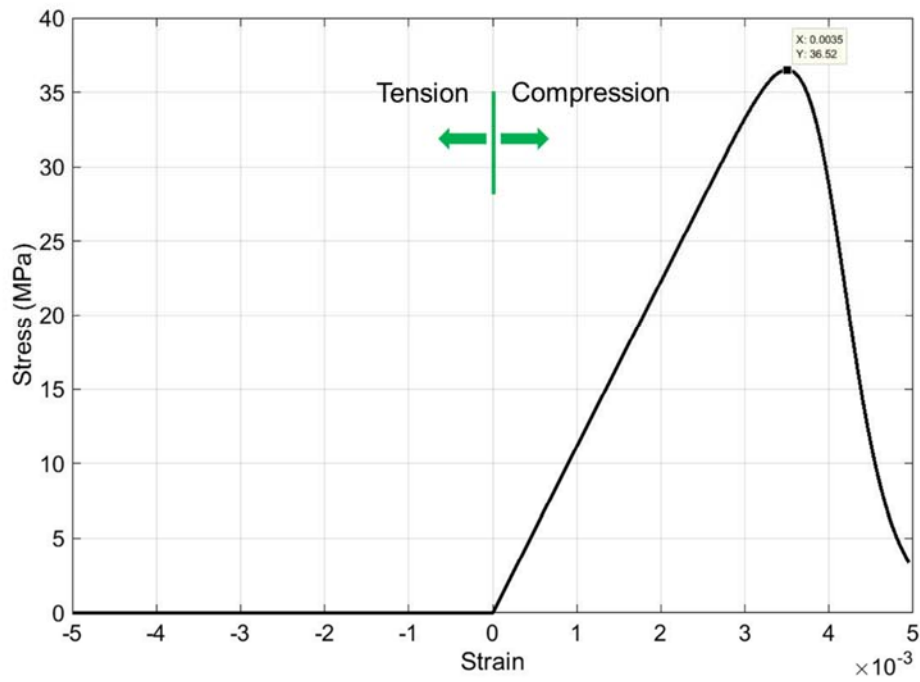
Figure 7.3 Uniaxial stress-strain curve for concrete
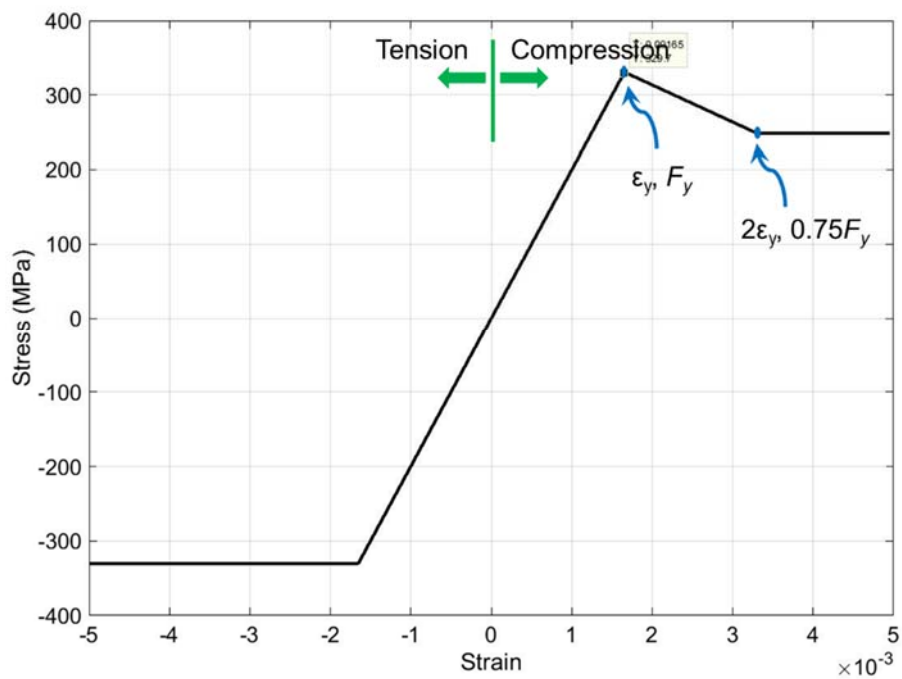
Figure 7.4 Uniaxial stress-strain curve for steel
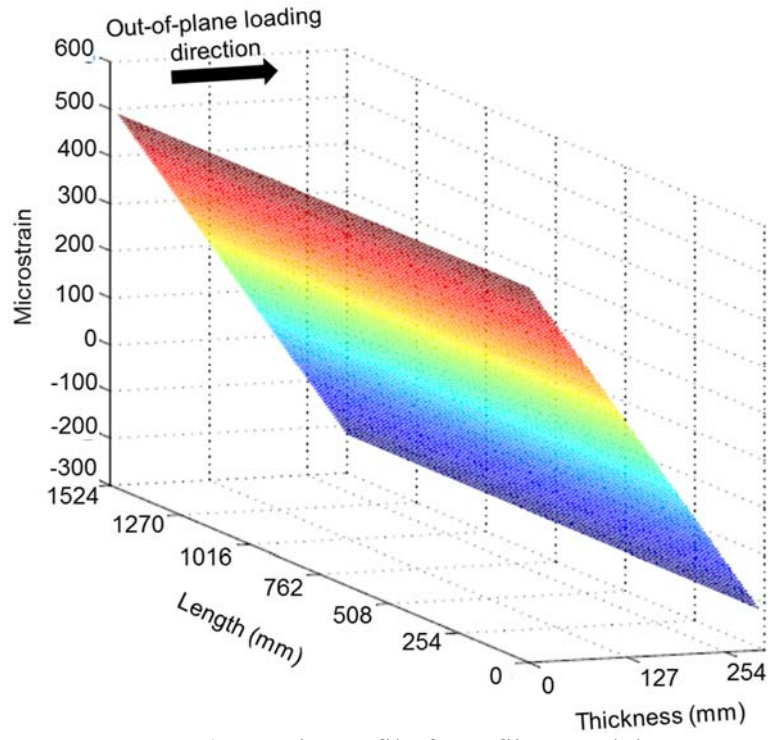
a) Strain profile from fiber model
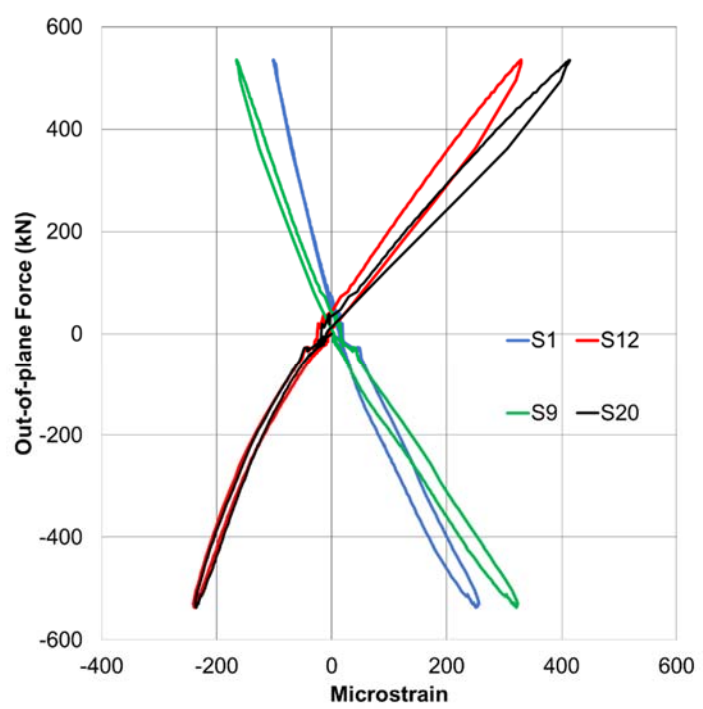
b) Force-strain plot for 534-kN out-of-plane load cycle (Specimen SC-0.5T-Vn)

Figure 7.5 Comparison of strains for out-of-plane moment
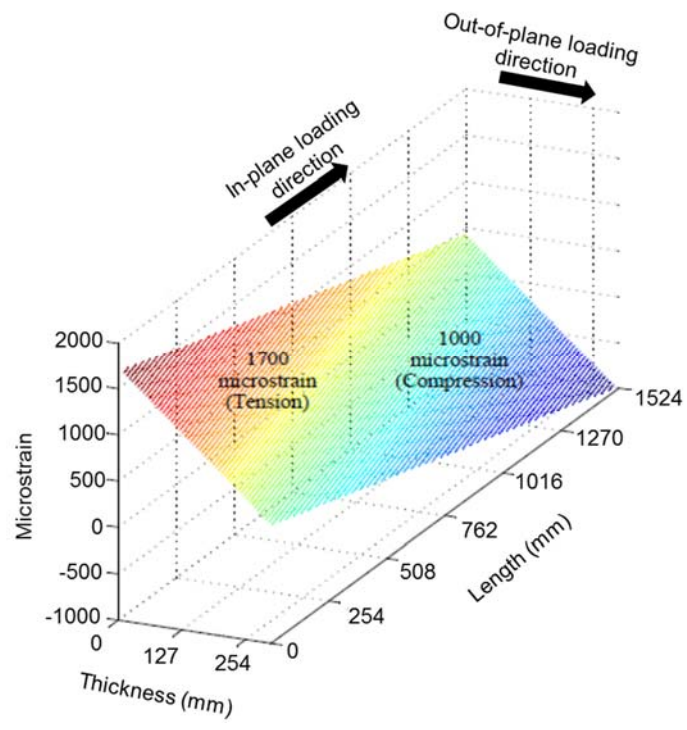
a) Strain profile from fiber model
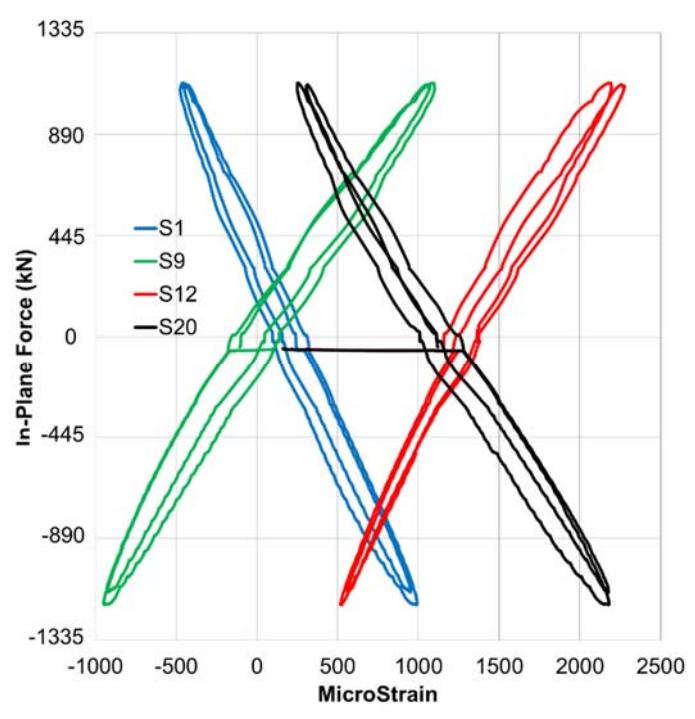
b) Force-strain plot for 0.50F_n in-plane cycle (with 1070-kN out-of-plane load), Specimen SC-0.5T-Vn

Figure 7.6 Comparison of strains for biaxial moments
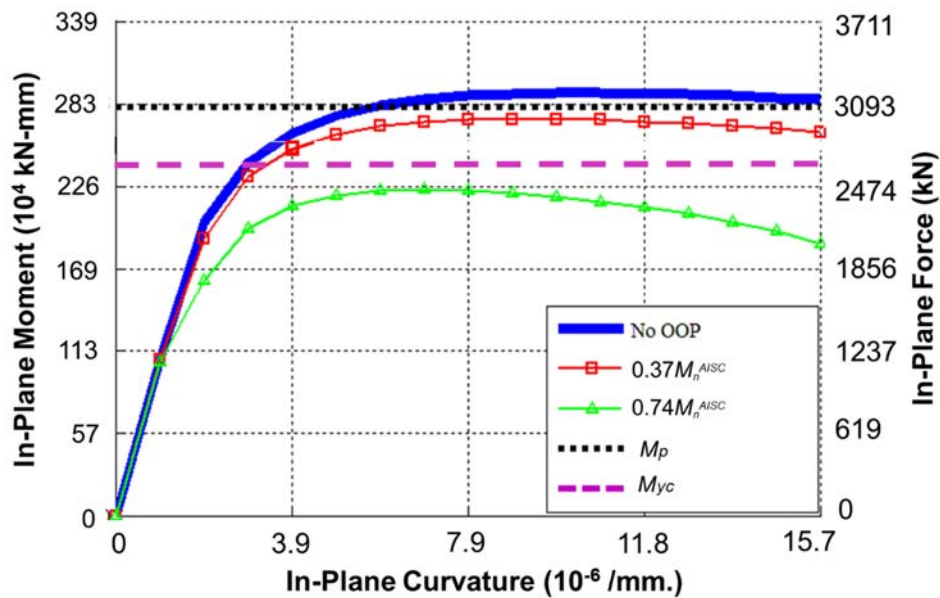
Figure 7.7 In-Plane moment-curvature for different magnitudes of out-of-plane loading
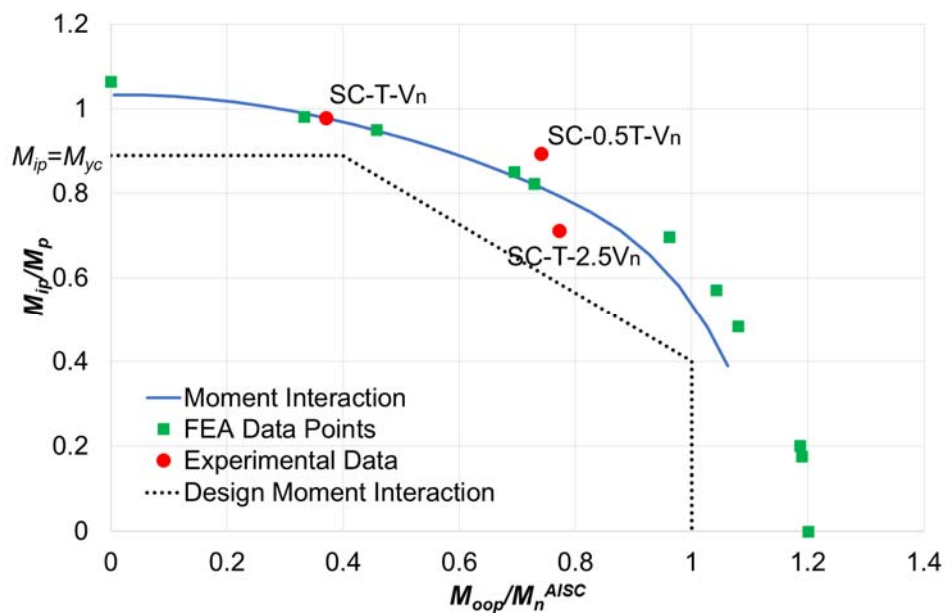
Figure 7.8 Biaxial moment interaction for SC wall pier specimens
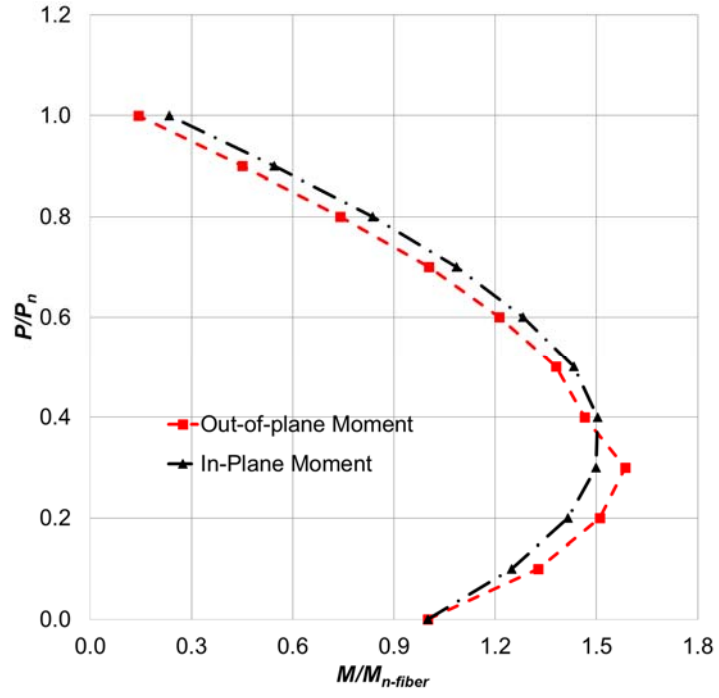
Figure 7.9 In-plane and out-of-plane *P-M* interaction
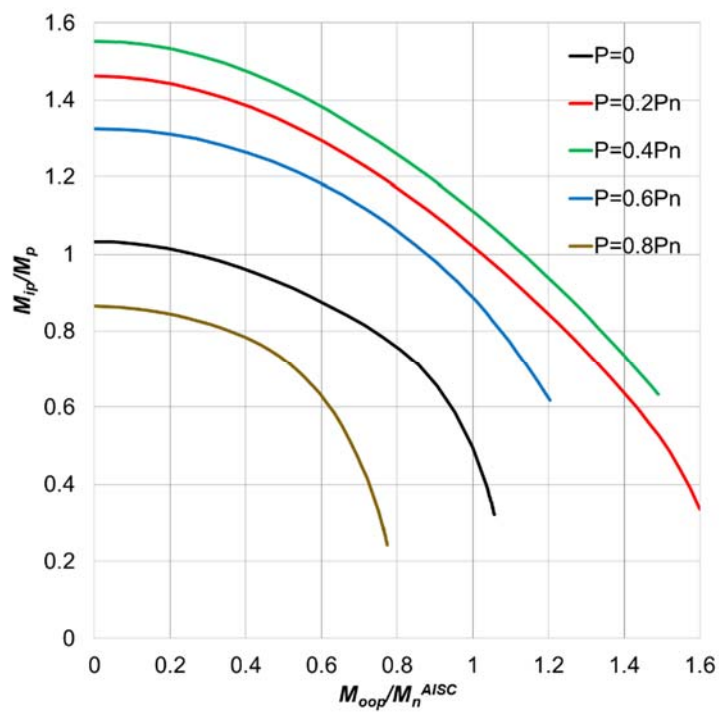
Figure 7.10 Biaxial moment interaction for axial compressive loads (without considering *P-M* interaction)
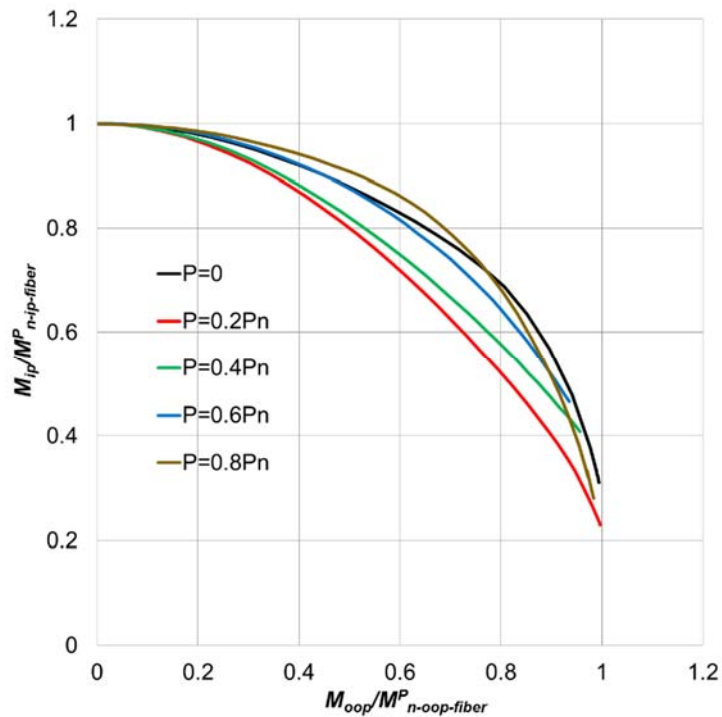
Figure 7.11 Biaxial moment interaction for axial compressive loads (considering *P-M* interaction obtained from fiber model)
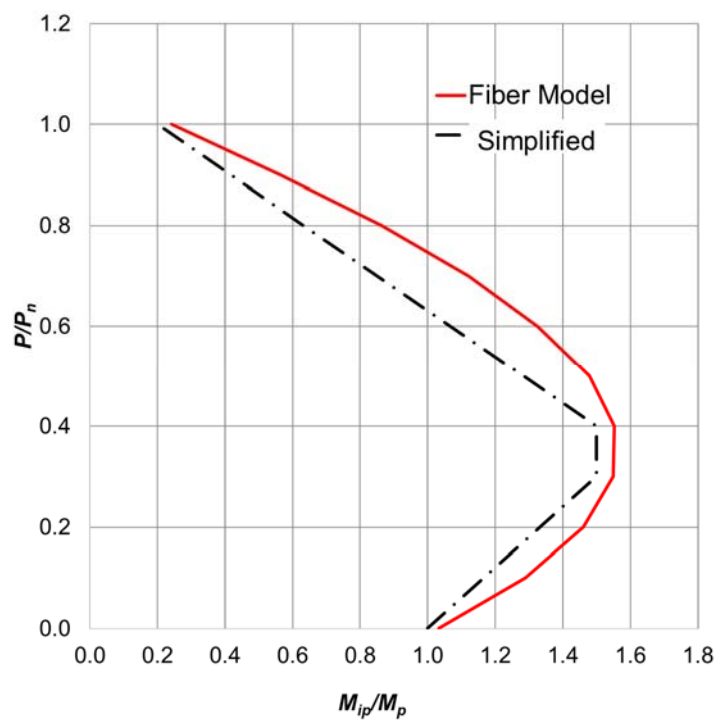
Figure 7.12 Simplified in-plane *P-M* interaction for design
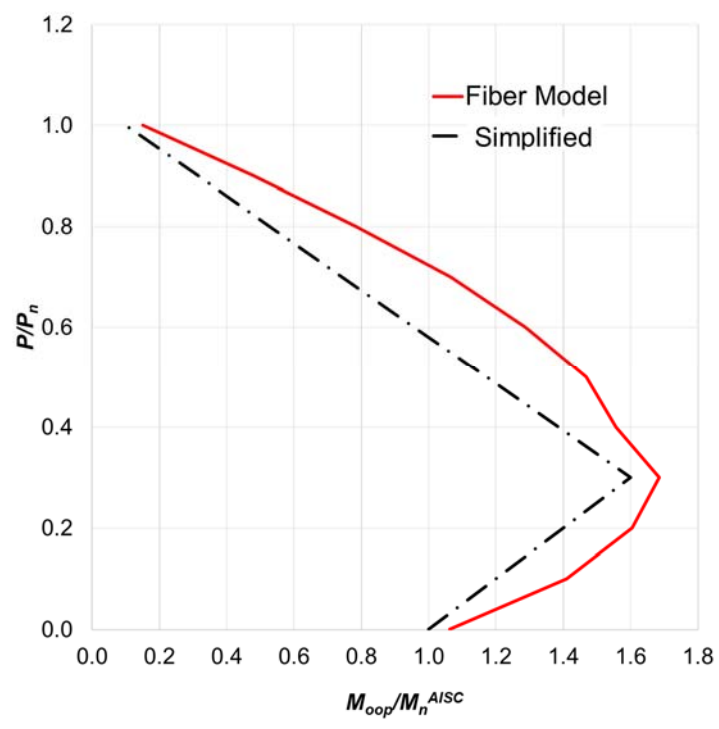
Figure 7.13 Simplified out-of-plane *P-M* interaction for design
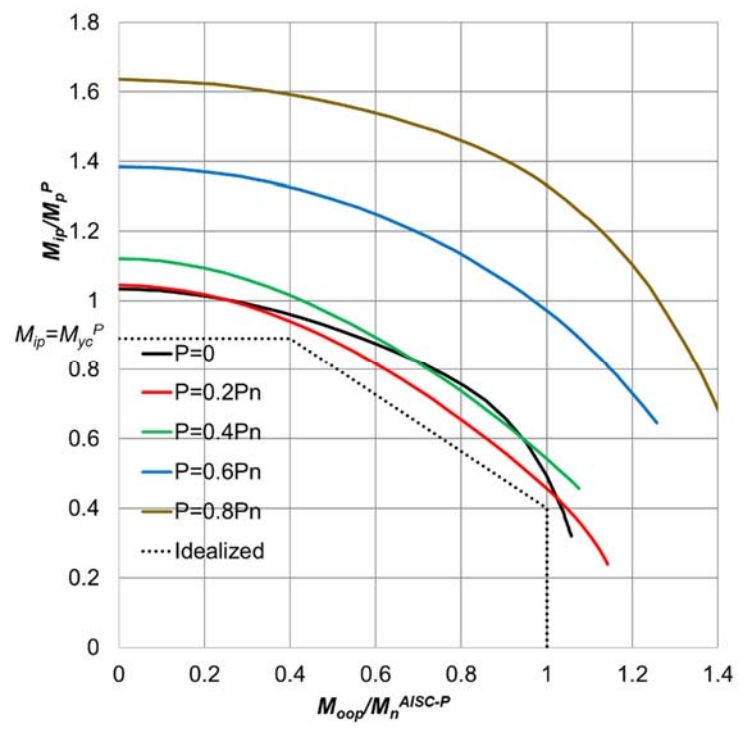
Figure 7.14 Biaxial moment interaction for axial compressive loads (considering simplified *P-M* interaction for design)
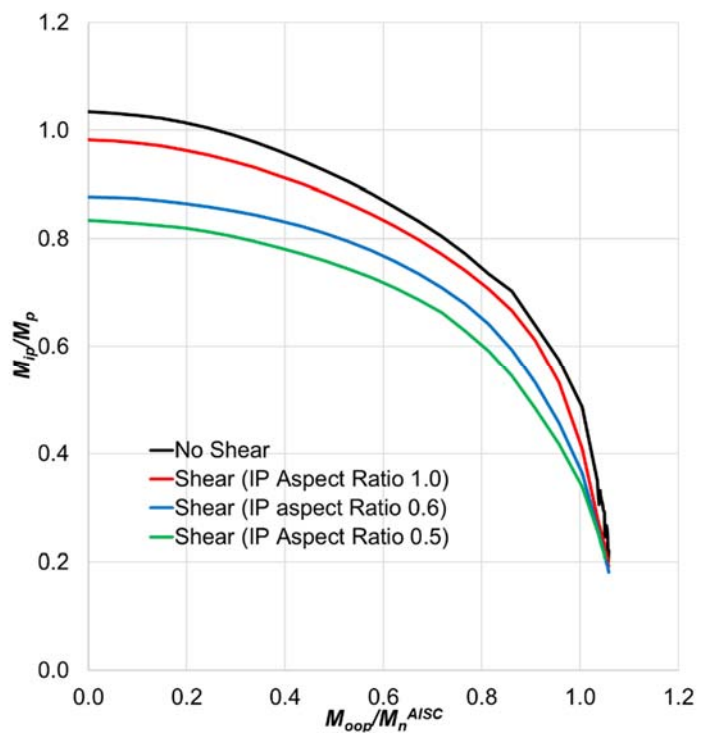
Figure 7.15 Biaxial moment interaction (considering vector shear failure), out-of-plane aspect ratio of 1.5
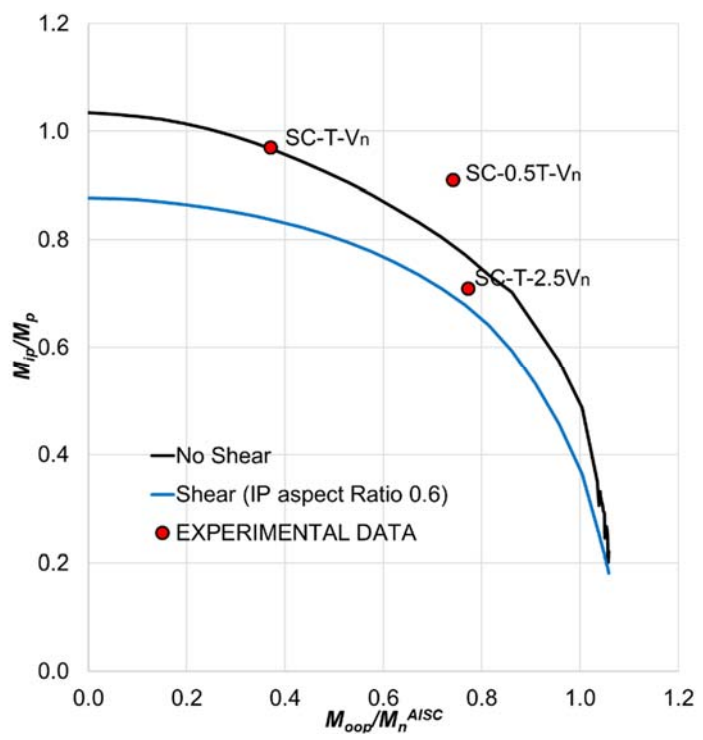
Figure 7.16 Comparison of biaxial moment interaction surfaces with experimental results

8.   BENCHMARKED FINITE ELEMENT MODELS

The in-plane behavior of SC walls and wall piers for out-of-plane and accident thermal loads was evaluated based on experimental studies (discussed in Chapters 3 to 6). However, time and financial constraints limit the number and scale of experiments that can be conducted. Detailed non-linear 3D finite element models can be developed and benchmarked against experimental results. The benchmarked models can be employed to corroborate experimental observations, and evaluate the wall behavior in more detail. The models can also be employed to conduct parametric studies that can validate the analysis and design recommendations based on experimental studies. However, the numerical models may have some inherent limitations, and the user needs to be cognizant of them.

This chapter discusses the development of detailed finite element models, and the benchmarking of those models against the experimental results. The comparison of numerical results with experimental observations, and any limitations of the numerical models thereof are discussed. The chapter is organized into following sections.

- Biaxially loaded SC wall pier specimens: Model geometry and material models for SC wall pier specimens subjected to biaxial loading are presented. Numerical results for all the specimens are compared with experimental observations. Faceplate and concrete infill behavior is evaluated in detail.

- SC wall and wall piers subjected to in-plane and accident thermal loading: Model geometry and material models for SC wall and wall pier specimens subjected to combined in-plane and thermal loading are presented. Numerical results for the specimens are compared with experimental observations. Steel plate and concrete infill behavior are evaluated in detail.

8.1   Biaxially Loaded SC Wall Piers

Chapter 4 presents the experimental evaluation of SC wall pier specimens subjected to biaxial loading. One control specimen (SC-T-C) and three biaxially loaded specimens (SC-T-Vn, SC-T-2.5Vn and SC-0.5T-Vn) were tested. The control specimen was subjected to cyclic in-plane loading. The biaxially loaded specimens were subjected to incremental out-of-plane loading cycles till the desired out-of-plane load was achieved. The out-of-plane loading was then maintained constant and incremental in-plane loading cycles were applied. This section discusses the finite element models for the experiments.

8.1.1   Model Geometry

Detailed 3D finite element models were developed in LS-Dyna [91] to simulate the SC wall pier response to biaxial loading. The models were based on benchmarked models developed by Kurt et al. [69]. Model geometry and details are presented in Figure 8.1 and Figure 8.2. Foundation block for the experiments was not modeled because corrected drift of the specimens (correction for slip and rotation at the base of the wall) was calculated in Chapter 4. Backbone curves of SC wall pier specimens considering corrected drifts were presented in Figure 4.53. Faceplate-to-baseplate connection (detail shown in Figure 3.6) was not modeled and the faceplates were considered directly connected to the baseplate. The height of the modeled specimens was accordingly reduced by 38 mm (transfer bar dimensions). Steel faceplates were modeled using fully integrated four-node shell elements. Belytchko-Tsay shell formulation, which considers the shell elements to be perfectly flat, was used. Concrete infill was modeled using eight-node constant stress solid elements (reduced integration). The baseplate was also modeled using eight-node constant stress solid elements. Shear stud and ties, and base studs were explicitly modeled using two-node beam elements with cross-section integration (Hughes-Liu formulation). Mesh size for

concrete elements was 25 mm. For faceplates, mesh size was 12.5 mm. Shear studs and ties were tied to the faceplates and embedded in concrete using "Lagrange-in-solid" keyword. The keyword couples the acceleration and velocities of stud and tie elements to those of concrete elements. Base studs were tied to the baseplate and embedded in concrete. Contact between faceplates and concrete infill was defined using "Automatic_Surface_To_Surface" keyword. The two-way contact formulation checks the slave and master nodes for penetration. No friction was considered between the faceplates and concrete infill. Contact between concrete infill and baseplate was also defined using "Automatic_Surface_To_Surface" keyword. A static coefficient of friction of 0.2 was considered for the contact. Elements with reduced integration elements may undergo hourglassing. The concern was addressed by using stiffness based hourglass control with a coefficient of 0.05 for all the models (consistent with the value used by [33]).

SC-T-C was subjected to incremental in-plane displacement at 876 mm from the base [location same as for the experiments, deducting the distance corresponding to the faceplate-to-baseplate connection (38 mm)]. For biaxially loaded specimens, monotonic out-of-plane loading was applied at 419 mm from the base. The out-of-plane loading was maintained constant, and then the specimens were subjected to incremental in-plane displacement applied at 876 mm from the base. Benchmarking of the models was limited to monotonic loading due to limitations of the concrete model used. These limitations have been discussed in the following section.

8.1.2   Material Models

Material models for steel and concrete were selected from the available models in LS-DYNA. The material models are discussed in this section.

8.1.2.1 Concrete

Concrete infill was modeled using Winfrith concrete model (MAT 85) in LS-DYNA. The model was previously used for SC walls by Kurt [33] and Bruhl [133] with reasonable success. Winfrith model accounts for tension behavior of concrete by smeared cracking and Hillerborg's fracture energy approach. However, for compression, the model is elastic-perfectly plastic and does not account for post-peak compression softening. The model is unable to capture the crushing and spalling of concrete. Concrete damage can be artificially included by defining the erosion criteria for concrete elements. However, the erosion criteria (failure strain or principal stress) for concrete would need to be calibrated. In the absence of reliable data for calibration, element erosion was not considered. Winfrith model can be used with strain rate effects turned on (MAT 84) or turned off (MAT 85). Since the experiments involved loading the specimens quasi-statically, MAT 85 (strain rate effects turned off) was used. The following input parameters were used for defining Winfrith concrete model.

The tangent modulus and uniaxial compressive strength for concrete were defined (the model does not have an option to input a compression curve). Winfrith model is based on uniaxial cube strength of concrete in compression. Measured day-of-test concrete compressive strength (presented in Table 3.1) for the specimens was multiplied by 1.25 to convert cylinder strength to cube strength [134]. Tangent modulus of concrete (E_{ci}) was calculated using Equation 8.1 per CEB-FIP model code [120], where E_{co} is 2.15x10^4 MPa, f_{cm} is the measured strength of concrete at 28 days, and f_{cmo} is 10MPa.

$$E_{ci} = E_{co} \left[f_{cm} \big/ f_{cmo} \right]^{1/3} \qquad \text{Equation 8.1}$$

Tension properties of concrete were also defined using CEB-FIP model code. Mean tensile strength value (f_{ctm}) was calculated using Equation 8.2, where $f_{ctko,m}$ is 1.40MPa, f_{cko} is 10MPa, and measured strength was used as f_{ck}.

$$f_{ctm} = f_{ctko,m} \left(\frac{f_{ck}}{f_{cko}} \right)^{2/3}$$

Equation 8.2

When strain rate effects are not considered (MAT 85), the crack width for which concrete stress goes to zero needs to be input. The crack width can be calculated using the tensile strength and the fracture energy. Fracture energy will be equal to the area under the tension stress vs. crack width curve. Fracture energy was calculated using Equation 8.3 per CEB.FIP model code, where G_{Fo} depends on the aggregate size and is 0.026 Nmm/mm^2 for pea gravel concrete mix used (maximum aggregate size of 9.5 mm).

$$G_F = G_{Fo} \left(\frac{f_{cm}}{f_{cmo}} \right)^{0.7}$$

Equation 8.3

A linear variation of tensile stress with crack width was considered, and crack width corresponding to zero tensile stress (w_c) was calculated using Equation 8.4.

$$w_c = \frac{2G_F}{f_{ctm}}$$

Equation 8.4

The aggregate size radius (4.75 mm for pea-gravel concrete) was also inputted into the Winfrith model.

Simulations with cyclic axial compression-tension loading protocol (multiple cycles) for concrete cube panels indicate that the Winfrith model unloads elastically from compression envelope, and goes into crack opening in tension. Once the model is cycled in tension and the loading reversed, the cracks close at origin and the model follows elastic-plastic path again in compression. For material points in wall models, the crack closure may occur before origin. This cyclic hysteretic

response of the model is not representative of concrete behavior. Therefore, cyclic simulations of the experiments were not conducted and the benchmarking was limited to monotonic loading.

8.1.2.2 Steel

Steel faceplates were modeled as isotropic elastic, followed by metal plasticity behavior after yielding using "Piecewise_Linear_Plasticity" model. The model is based on Von-Mises yield criteria, associated flow rule, and kinematic yielding. Uniaxial stress-strain curves were obtained from standard tension coupons fabricated from the faceplates (measured yield strengths for the faceplates were presented in Table 3.1). These stress-strain curves were converted to piecewise linear true stress-effective plastic strain curves used to define the post-yield hardening behavior of faceplates. Measured effective stress-strain response of faceplate tension coupons is presented in Figure 8.3. The post-yield effective stress-plastic strain relationship input for LS-DYNA is presented in Figure 8.4. Since the model used for LS-DYNA did not account for post-yield ductile damage or fracture, the failure strain (effective plastic strain) for faceplates was set at 15%. This is consistent with tension coupon results where necking of coupons was observed at strains of 15-20%. The failure criteria would ensure that the analysis results are not unrealistically high. "Piecewise_linear_plasticity" model was also used for ties and shear studs, with model parameters defined based on uniaxial tension tests for ties.

"Plasticity_With_Damage" steel model was also used for steel faceplates in order to compare the results obtained from two steel models. "Plasticity_With_Damage" model enables the modeling of damage by considering plastic strain at the initiation of material softening, and plastic strain at rupture. Damage in the steel material is calculated based on these strain values. Based on the measured stress-strain response from tension coupons (Figure 8.3), the plastic strain at initiation of softening was considered as 15% and strain for rupture was considered as 25%.

8.1.3   Model Results and Comparisons

This section presents the results of models for specimens SC-T-C, SC-T-Vn, SC-0.5T-Vn and SC-T-2.5Vn. The discussion of numerically observed behavior of SC wall pier specimens is also provided. Numerical results are compared with experimental observations presented in Chapter 4.

8.1.3.1   SC-T-C

Specimen SC-T-C was subjected to in-plane loading (no out-of-plane loading). Experimental results for SC-T-C were discussed in Section 4.1. The specimen was modeled in LS-DYNA using the parameters discussed previously and was subjected to monotonically increasing displacement. Figure 8.5 presents the comparison of experimental and numerical (FE) backbone curves. Experimental backbone curve is corrected for base slip and rotation to provide the net drift of the wall. The curve is based on push (+) half-cycles. Finite element results considering "Piecewise_linear_plasticity" (PLP) and "Plasticity_with_damage" (PD) material models for steel faceplates are presented in the figure. Finite element backbone curves for the two steel models are identical. This is because the model reached its peak strength before effective plastic strain (PEEQ) in faceplates reached 15%. The two steel models are identical before a PEEQ strain of 15% is reached. Therefore, the response of the specimen is evaluated using results for FE model with PD model for faceplates.

Initial stiffness of finite element models agrees well with that observed experimentally. Secant stiffness of the FE models is marginally higher than experimental secant stiffness. However, the experimental backbone curve is obtained from cyclic loading history of SC-T-C. Cyclic loading is expected to lead to reduced stiffness (in comparison to monotonic loading) due to additional concrete cracking and faceplate yielding. Peak strength for FE models was higher than experimentally observed strength. Specimen SC-T-C had reached a peak load corresponding to

$1.05M_{yc}$. However, the specimen had failed due to weld (basemetal) rupture and did not reach its plastic moment capacity (M_p). Baseplate-to-faceplate weld was not modeled in the FE models to ensure that the strength is not limited by weld failure. FE models reached a peak strength corresponding to $1.15M_{yc}$ ($0.99M_p$). Thus, the FE models reached peak in-plane load corresponding to the plastic moment capacity of the specimen. This is an expected result based on the experimental observations for specimen SC-T-Vn (discussed in Section 4.3). Specimen SC-T-Vn (subjected to combined in-plane and out-of-plane loading) reached its in-plane plastic moment capacity despite the presence of out-of-plane loading. Response of the FE model can be evaluated in detail by considering the stress and strain states for steel and concrete elements.

Figure 8.6 presents the effective plastic strain (PEEQ) distribution in the faceplates at peak load. The deformations have been amplified 5 times for clarity. At peak load, faceplate buckling was observed on the compression end of both the faceplates. The buckling was observed between the base and first row of studs. The faceplate region near to the base had yielded throughout the length of the specimen (shown in blue color in the figure). Peak plastic strains in the faceplates were less than 5%. The strain values are lower than PEEQ value defined for plasticity damage (15%). This confirms the observation in Figure 8.5, where both FE models (PD and PLP) had an identical response. Von-Mises stress in the faceplates at peak load is shown in Figure 8.7. The stress exceeds yield stress in the region close to the base. Buckling of both the faceplates in compression can also be seen in the figure.

Figure 8.8 presents the concrete principal compression stress distribution at peak load. Compression toe of the concrete experiences very high stresses, which may be unreal. The low aspect ratio of the specimen (0.6) results in the formation of concrete compression struts in the wall. However, the response of the wall is still flexure controlled (as observed experimentally by

Kurt et al. [69]). Figure 8.8 and Figure 8.9 show the concrete cracking at peak load. Concrete cracks in the direction perpendicular to principal tension stress. Extensive flexural cracking is observed at the base of the wall. Flexural-shear cracking is also observed in the wall along the height (parallel to the principal compression strut). Flexural cracking at the base and along the height was also observed in the experiments (from visual inspection of the sides).

Distribution of the in-plane force in faceplates and concrete infill is of interest as it would provide information about the relative stiffnesses of faceplates and concrete. Figure 8.10 shows the distribution of in-plane force in faceplates and concrete infill. Concrete and faceplate contribution is similar initially, as the extent of cracking in concrete is low. As the in-plane loading increases, the extent of cracking in concrete increases resulting in a higher relative contribution of faceplates. At peak load, the concrete contribution is about $2/3^{rd}$ of the faceplate contribution. However, the Winfrith model is elastic-plastic in compression, without any compression softening. Therefore, the relative concrete contribution observed from the FE models may be higher than actual contribution in experiments.

The response of SC wall piers to in-plane loading is symmetric (observed experimentally and in FE models). In-plane loading is not expected to result in significant stresses in ties. Figure 8.11 shows the effective plastic strain (PEEQ) in the ties at failure. There is no significant yielding in the ties. Yielding in the corner tie is observed at failure. However, this may be due to additional stress in the ties post faceplate yielding and buckling.

8.1.3.2 SC-T-Vn

Specimen SC-T-Vn was subjected to incremental cyclic out-of-plane loading till the desired out-of-plane force was reached (535-kN). The out-of-plane load was then maintained and cyclic in-plane loading was applied. Experimental results for SC-T-Vn were discussed in Section 4.3. The

specimen was modeled in LS-DYNA using the parameters discussed previously, and was subjected to monotonically increasing out-of-plane load to the desired load. The out-of-plane load was then maintained constant and monotonically increasing in-plane displacement was applied. Figure 8.12 presents the comparison of experimental and numerical (FE) backbone curves. Experimental backbone curve is corrected for base slip and rotation to obtain the net drift of the wall. The curve is based on push (+) half-cycles. Finite element result considering "plasticity_with_damage" (PD) material model for steel faceplates is presented in the figure (as discussed for SC-T-C, the two material models considered for steel faceplates give identical results, so only the PD model is considered here).

Initial stiffness of finite element models agree well with that observed experimentally. Secant stiffness of the FE model is higher than experimental secant stiffness. However, the experimental backbone curve is obtained from cyclic loading history of SC-T-Vn. Cyclic loading is expected to lead to reduced stiffness (in comparison to monotonic loading) due to additional concrete cracking and faceplate yielding. Additionally, the Winfrith concrete model is elastic-perfectly plastic in compression, with no compression softening. This would also result in a stiffer response. Peak strength for FE model is marginally higher than experimentally observed strength. Specimen SC-T-Vn had reached a peak load corresponding to $1.10M_{yc}$ ($0.98M_p$). FE model reached its plastic moment capacity, M_p. The strength corresponded to $1.15M_{yc}$. Since the concrete model is elastic-perfectly plastic, the FE strength does not drop significantly till after faceplate strains reach softening strains. However, the FE response cannot be used reliably post the faceplates yielding in compression and tension. Response of the FE model is compared to experimentally observed behavior by evaluating the stress and strain states of steel and concrete elements.

Figure 8.13 and Figure 8.14 present the faceplate normal vertical strains for out-of-plane loading. The strain contours are not symmetric as some magnitude of in-plane loading had been applied at the time the data was recorded. The faceplates experienced a compressive strain of 100 $\mu\varepsilon$ and tensile strain of 300 $\mu\varepsilon$. This is consistent with faceplate strains observed experimentally (as shown in Figure 4.21), where the faceplates experienced tensile strains of magnitude 250-400 $\mu\varepsilon$ and compressive strains of magnitude 200-330 $\mu\varepsilon$ for out-of-plane loading cycle of 535-kN. Figure 8.15 shows the concrete cracking and principal compressive stresses due to the out-of-plane loading applied. Consistent with experimental observations, magnitude of the out-of-plane load was not high enough to result in significant concrete cracking. Some flexural cracking at the base of FE model was observed. No shear cracking was observed. Since there was no shear cracking, the tie bars were not engaged in the experiments (as was confirmed by Figure 4.22). This was also confirmed by the FE model, as seen in Figure 8.16. The axial stresses in ties are very low [less than 2ksi (14 MPa)]. Since the out-of-plane loading did not result in high faceplate strains or extensive concrete cracking, the in-plane response of the FE model was not affected by the out-of-plane loading, and the FE model reached its plastic moment capacity (as discussed previously).

Figure 8.17 presents the Von-Mises stresses in the faceplates at peak load. There was significant yielding in the faceplates. Buckling of the faceplates in compression is also visible. Buckling of both the faceplates (Figure 4.29 and Figure 4.30), and extensive faceplate yielding (Figure 4.34) was also observed experimentally in the peak load cycles. The extent of yielding in faceplates is marginally higher than that observed for SC-T-C FE model (Figure 8.7). Additional faceplate strains due to out-of-plane loading and out-of-plane deformation lead to yielding of faceplates at a slightly lower in-plane loading.

Figure 8.18 presents the state of concrete infill at peak in-plane load. The concrete response is consistent with that observed for SC-T-C FE model. Flexural cracking at the base and flexural shear cracking along the height of the specimen is observed. The formation of concrete compression struts can also be seen. Flexural and shear cracking patterns observed in FE model are similar to those observed in experiments (Figure 4.26 to Figure 4.32). However, no concrete crushing or spalling was observed in the FE model (due to elastic-perfectly plastic material model and no erosion criteria used). This results in no significant drop in FE model strength post-peak, until the faceplates rupture. In experiments, concrete crushing and spalling resulted in significant degradation of post-peak response.

Since there was no shear cracking for out-of-plane loading, the asymmetry in the in-plane response of the specimen is low (as seen from comparisons with other specimens in Figure 4.19, Figure 4.35 and Figure 4.51). No significant axial stress or yielding is expected in the ties. Figure 8.19 shows that no yielding was observed in the ties at peak in-plane load. Figure 8.20 shows the specimen state at peak load. The faceplates yielded (Figure 8.17) and buckled in compression. The response of SC-T-Vn FE model was flexure controlled, with flexural cracking in concrete and yielding and buckling of faceplates. However, some shear cracking (in-plane and out-of-plane directions) was observed. The FE model also experienced out-of-plane deformations, which increased when in-plane load was applied.

8.1.3.3   SC-T-2.5Vn

Specimen SC-T-2.5Vn was subjected to incremental cyclic out-of-plane loading till the desired out-of-plane force was reached (1113-kN). This out-of-plane load was 2.5 times the nominal out-of-plane shear strength of the specimen. The out-of-plane load was then maintained constant and cyclic in-plane loading was applied. Experimental results for SC-T-2.5Vn were discussed in

Section 4.4. The specimen was modeled in LS-DYNA using the parameters discussed previously and was subjected to monotonically increasing out-of-plane load till desired out-of-plane load (1113-kN) was achieved. The out-of-plane load was then maintained constant and monotonically increasing in-plane displacement was applied. Figure 8.21 presents the comparison of experimental and numerical (FE) backbone curves. Experimental backbone curve is corrected for base slip and rotation to obtain the net drift of the wall. The curve is based on push (+) half-cycles. The shell element formulation used for faceplates (SEF 16) employed full integration. However, the model had convergence issues due to large out-of-plane deformations in faceplates. The shell element formulation was then changed to SEF -16, which is a fully-integrated shell element modified for higher accuracy. Backbone curves for FE models with both the shell formulations are presented in Figure 8.21.

The stiffness of the finite element models agrees well with that observed experimentally. The experimental strength of SC-T-2.5Vn corresponded to $0.85M_{yc}$. Peak strength for FE model with SEF 16 is within 10% of that observed experimentally. FE model with SEF -16 matches the peak-strength for the experiments, and continues to gain strength up to about 5% higher than experimental strength. SC-T-2.5Vn specimen had failed abruptly due to concrete crushing, extensive diagonal shear cracking, and sliding on the diagonal shear plane (Figure 4.47 and Figure 4.48). However, the concrete model is not capable of simulating a crushing failure, therefore, the strength and deformation of the FE model increase beyond the peak values observed experimentally. The strength increase is less than 10%. Therefore, the SC wall piers subjected to out-of-plane forces significantly higher than the nominal out-of-plane shear strengths do not reach their in-plane compression yield moment capacity (M_{yc}).

Figure 8.22 and Figure 8.23 present the faceplate normal vertical strains for out-of-plane loading. The faceplates experienced a compressive strain of 200 με and tensile strain of 1000 με. This is consistent with faceplate strains observed experimentally (as shown in Figure 4.39), where the faceplates experienced tensile strains of magnitude 700-900 με and compressive strains of magnitude 100-300 με for out-of-plane loading cycle of 1113-kN. The high magnitude of out-of-plane force (and the corresponding moment) results in high tensile stresses in the faceplates (about 60% of the yield stress). Figure 8.24 shows the concrete cracking and principal compressive stresses due to the out-of-plane loading applied. Significant flexural cracking close to the base was observed. Additionally, diagonal shear cracks were observed. Concrete compression strut with an average stress of 20MPa was observed (compared to the compressive strength of 35 MPa). The diagonal cracks observed in FE model are consistent with those observed experimentally (Figure 4.38). The shear cracks engaged the bottom row of tie bars (confirmed experimentally by Figure 4.40). In the FE model, high axial stresses in ties were observed [about 20 ksi (138 MPa)]. However, the FE model tie stresses did not reach Von-Mises Stress (yielding was observed in ties for specimen SC-T-2.5Vn, Figure 4.40). The difference in tie stresses between the model and experiment may be due to different crack orientation in the FE model, and the element size for ties used in the model (100 mm length elements used). High tensile stresses in the tie bars, and significant concrete cracking due to out-of-plane loading, significantly affected the in-plane response of the specimen. The specimen strength was $0.85M_{yc}$, as compared to SC-T-C which reached a peak strength of $1.15M_{yc}$. The in-plane response of SC-T-2.5Vn is evaluated in detail through the stress states of faceplates, concrete and ties in the model.

Figure 8.26 presents the Von-Mises stresses in the faceplates at the time step corresponding to the displacement at which the peak load was observed experimentally. There was significant tension

yielding in the faceplates. However, localized compression yielding was caused by concrete compression strut (due to out-of-plane force) bearing against the faceplates. The strut combined with in-plane compressive loads on the faceplates resulted in bulging out (and initiation of buckling) of the faceplate. No extensive buckling is observed on the corresponding corner of the other faceplate. The FE model behavior is similar to that observed experimentally (Figure 4.47 and Figure 4.48). For specimen SC-T-2.5Vn, faceplate buckling at base and concrete crushing at out-of-plane loading location was observed. Concrete infill slid on the shear crack plane as the compression strut could not be anchored on the buckled faceplates. This led to amplified out-of-plane deformation of the compression faceplate and failure of the specimen.

Figure 8.27 presents the state of concrete infill at peak in-plane load. The concrete response is dominated by out-of-plane loading. For SC-T-C and SC-T-Vn (Figure 8.9 and Figure 8.18), in-plane compression strut developed and flexural shear cracking was observed through the height of the specimens. However, SC-T-2.5Vn FE models indicate that the in-plane compression strut was not fully developed, and in-plane shear cracking was limited. Instead, the concrete cracked extensively due to out-of-plane flexure and shear. Extensive diagonal shear cracking was observed and the concrete slid along the diagonal shear crack plane. Thus, out-of-plane shear significantly greater than the strength hinders the in-plane contribution of concrete. This results in a lower in-plane strength and negligible post-peak strength and deformation capacity.

Ties for SC-T-2.5Vn were spaced at 305 mm. The engagement of ties will depend on the angle at which diagonal shear cracks are formed. As observed in Figure 8.27, some of the diagonal cracks engaged the ties. Figure 8.28 shows the tie effective plastic strain (PEEQ) at peak in-plane load. Yielding was observed in the bottom row of ties. However, no rupture was observed, with peak plastic strains less than 0.1%. Figure 8.29 shows the specimen state at peak load. Sliding of

concrete over the diagonal shear crack plane is apparent. The concrete compression strut pushes the faceplates (with pre-existing buckling), leading to excessive out-of-plane deformation of the faceplates, and specimen failure. Significant out-of-plane deformation of the specimen, above the diagonal shear crack plane, is also visible in the figure.

8.1.3.4 SC-0.5T-Vn

Out-of-plane load for SC-0.5T-Vn was equal to the nominal out-of-plane shear strength of the specimen. Since SC-0.5T-Vn had ties spaced at half the section thickness, the nominal out-of-plane shear strength included both steel and concrete contributions and was equal to approximately 2.4 times the nominal out-of-plane strength for SC-T-2.5Vn. Therefore, the magnitude of out-of-plane force for SC-0.5T-Vn (1070-kN) was approximately equal to that for SC-T-2.5Vn (1113-kN). Specimen SC-0.5T-Vn was subjected to incremental cyclic out-of-plane loading till the desired out-of-plane force was reached (1070-kN). The out-of-plane load was then maintained constant and cyclic in-plane loading was applied. Experimental results for SC-0.5T-Vn were discussed in Section 4.2. The specimen was modeled in LS-DYNA using the parameters discussed previously, and was subjected to monotonically increasing out-of-plane load till desired out-of-plane load (1070-kN) was achieved. The out-of-plane load was then maintained constant and monotonically increasing in-plane displacement was applied. Figure 8.30 presents the comparison of experimental and numerical (FE) backbone curves. Experimental backbone curve is corrected for base slip and rotation to obtain the net drift of the wall. The curve is based on push (+) half-cycles. Since the faceplates were expected to undergo large out-of-plane deformations (similar to those in SC-T-2.5Vn), fully integrated shell with formulation modified for higher accuracy (SEF -16) was used. Additionally, the ties were expected to experience high axial forces due to diagonal shear cracking (tie rupture was observed for specimen SC-0.5T-Vn, as shown in Figure 4.15). To

better capture the response of ties, mesh size for tie beam elements was changed to 12.5 mm. Mesh size of 25 mm was also tried, and the results were similar to those for 12.5 mm mesh size. FE models for SC-0.5T-Vn with fine tie mesh captured the tie response (and overall response) better than the models with tie mesh size of 100 mm. FE backbone curve in Figure 8.30 employed a tie mesh size of 12.5 mm.

Initial stiffness of the FE model is marginally higher than the experimental stiffness. This may be due to flexural cracking in the specimen caused by out-of-plane loading cycles. Secant stiffness of the FE model is higher than experimental stiffness. This is consistent with observations for SC-T-C and SC-T-Vn (Figure 8.5 and Figure 8.12). The FE model was loaded monotonically, and the concrete model was elastic-perfectly plastic. The experimental strength of SC-0.5T-Vn corresponded to $1.06M_{yc}$. In-plane load for FE model at displacement corresponding to experimental peak strength was 5% lower than experimental strength ($1.01M_{yc}$). In-plane load for FE model increases marginally (5% increase) till the model fails due to rupture in multiple ties. As discussed previously, the concrete model does not consider concrete crushing and spalling, therefore the strength increases marginally till steel failure (faceplate or tie) occurs. SC-0.5T-Vn specimen had a flexural failure, with both the faceplates buckling and extensive concrete cracking, crushing and spalling (Figure 4.12 to Figure 4.14). The high magnitude of out-of-plane shear (and flexure) reduces the in-plane strength of the wall pier. However, the wall pier reached its compression moment capacity (M_{yc}).

Figure 8.31 and Figure 8.32 present the faceplate normal vertical strains for out-of-plane loading. The faceplates experienced a compressive strain of 300 $\mu\varepsilon$ and tensile strain of 1000 $\mu\varepsilon$. Similar strains due to out-of-plane loading were observed for SC-T-2.5Vn (Figure 8.22 and Figure 8.23) The strains are also consistent with SC-0.5T-Vn faceplate strains observed experimentally (as

shown in Figure 4.2), where the faceplates experienced tensile strains of magnitude 1000-1100 $\mu\varepsilon$ and compressive strains of magnitude 200-300 $\mu\varepsilon$ for out-of-plane loading cycle of 1070-kN. The high magnitude of out-of-plane force (and the corresponding moment) results in high tensile stresses in the faceplates (about 60% of the yield stress). Figure 8.33 shows the concrete cracking and principal compressive stresses due to the out-of-plane loading applied. Significant flexural cracking close to the base was observed. Additionally, diagonal shear cracks were observed. However, the extent of diagonal cracking and the magnitude of average stress for concrete compression strut are lower than those for SC-T-2.5Vn (Figure 8.24). Ties spaced at 152 mm for SC-0.5T-Vn (in comparison to 305 mm for SC-T-2.5Vn) arrest the diagonal shear cracking, and contribute to out-of-plane shear strength. The diagonal shear cracks observed in FE model are consistent with those observed experimentally (Figure 4.3). The shear cracks engaged the bottom two rows of tie bars (confirmed experimentally by Figure 4.4). Ties in specimen SC-0.5T-Vn experienced tensile strains upon cracking of concrete. Strains in ties reached the yield strain for 1070-kN out-of-plane cycle. In the FE model, yielding was observed in the bottom row of ties (Figure 8.34). Thus, ties with a finer mesh size better replicate the experimentally observed response.

Figure 8.35 presents the Von-Mises stresses in the faceplates at time step corresponding to the displacement at which peak load was observed experimentally. Faceplate region close to the base underwent compression and tension yielding (similar to SC-T-C and SC-T-Vn, Figure 8.7 and Figure 8.17). Compression buckling was observed on both the faceplates (consistent with experimental observations, Figure 4.12 and Figure 4.13). However, the buckling was more pronounced on the faceplate corner subjected to compression stress due to both out-of-plane and in-plane loadings.

Figure 8.36 presents the state of concrete infill at peak in-plane load. Similar to FE models for SC-T-C and SC-T-Vn (Figure 8.9 and Figure 8.18), in-plane compression strut developed and flexural shear cracking was observed through the height of the specimens. Flexural cracking due to in-plane and out-of-plane moments was observed. Diagonal shear cracking in the out-of-plane direction was observed (similar to that for SC-T-2.5Vn). However, the presence of ties along the shear crack arrested the crack growth and prevented the sliding of concrete on the shear plane. Concrete sliding on the shear plane had led to the failure of the specimen SC-T-2.5Vn.

Ties for SC-0.5T-Vn were spaced at 154 mm. The ties were engaged by out-of-plane shear cracks (Figure 4.4 and Figure 8.34). Widening of shear cracks due to combined in-plane and out-of-plane loading resulted in additional stresses in ties. Tie rupture was observed experimentally at specimen failure (Figure 4.15 and Figure 4.16). Rupture of ties was also observed in the FE model (Figure 8.37). The FE model failed due to rupture of multiple ties. Figure 8.38 shows the specimen state at peak load. There is extensive diagonal cracking, but the concrete does not slide on the shear crack plane [consistent with experimental observations at failure (Figure 4.12 to Figure 4.14)]. Sliding of concrete over the diagonal shear crack plane was apparent in SC-T-2.5Vn (Figure 4.48 and Figure 8.29). Thus, spacing of ties at half the section thickness increases the out-of-plane strength of the specimen and thereby improves the in-plane behavior of SC wall piers (for similar magnitudes of out-of-plane loads) by arresting the out-of-plane shear cracks.

8.1.4 Discussion

FE models reasonably predict the experimentally observed response of the specimens. Comparison of FE results with experimental observations has been discussed in the previous section (Section 8.1.3). Initial stiffnesses observed from the FE models and the experiments compare well. However, the FE models overestimate the secant stiffness of the specimens. This is partly because

the concrete model used is elastic-perfectly plastic. Additionally, the model was loaded monotonically whereas the experiments employed cyclic loading protocol. This would result in the FE model not adequately capturing the concrete cracking and steel yielding due to multiple cycles. Strength results obtained from FE models are consistent with experimental observations. The response of FE wall pier models for biaxial loading was flexure controlled, and the peak strengths for FE models (except SC-T-2.5Vn) reached or exceeded V_{Myc}. Specimen SC-T-2.5Vn failed in vector shear due to the magnitude of out-of-plane force being 2.5 times the out-of-plane strength. Flexural yielding and buckling of the faceplates were observed in the models. The low aspect ratio of the specimens enabled the concrete compression strut to form. However, the compression strut cannot anchor in at the base, and therefore its effectiveness is limited. Based on the experimental and finite element results, the interaction of in-plane and out-of-plane moments can be defined using a cross-section based fiber model (as discussed in Chapter 7).

The benchmarked finite element models developed can be employed to conduct parametric studies for biaxial loadings on SC walls. Other concrete models may need to be explored to improve the simulation of compression behavior of concrete infill in the models. The cyclic response of FE models can then be evaluated. The parametric studies and cyclic analysis will provide more information into the biaxial interaction of the specimens, and can be employed to validate the proposed axial force-biaxial moment-shear interactions in Chapter 7.

8.2 SC Wall and Wall Piers: In-plane and Thermal Loading

Chapter 6 presents the experimental evaluation of SC wall and wall pier specimens subjected to combined in-plane and accident thermal loading. Control SC wall pier specimen (SC-T-C) was also the control specimen for this series of tests (SC-WP-C). One heated SC wall pier specimen (SC-WP-H) was tested. One heated SC wall specimen (SC-W-H) was tested. The heated

specimens were subjected to surface temperatures of 149˚C and 232˚C, and heating durations of 1 hour and 3 hours. Finite element model for SC-WP-C (SC-T-C) was discussed in Section 8.1.3.1. This section discusses the finite element models for specimens subjected to combined in-plane and accident thermal loadings.

8.2.1 Model Geometry

Detailed 3D finite element models were developed in LS-Dyna [91] to simulate the response of SC walls and wall pier specimens. FE model geometry for SC-WP-H was the same as for SC-0.5T-Vn and has been discussed in Section 8.1.1. FE model geometry for SC wall is presented in Figure 8.39. As for wall pier models, the baseplate-to-specimen weld was not modeled (discussed in Section 8.1.1). Since corrected specimen displacements were obtained from the experiments, foundation block was not modeled. Steel, concrete, studs and tie elements were consistent with those used for SC wall pier model (shown in Figure 8.2).

Faceplates and flangeplates were joined together (the weld was not modeled). Monotonic in-plane loading was applied at 876 mm from the base. For models with thermal loading, bottom 610 mm region of the specimen was subjected to thermal loading.

8.2.2 Material Models

Concrete infill was modeled using Winfrith concrete model (MAT 85). Definition of material parameters and material limitations were previously discussed in Section 8.1.2.1. Measured day-of-test concrete strength (Table 5.1) was used to define the concrete model parameters. Steel plates were modeled using "Plasticity_with_damage" material model discussed previously in Section 8.1.2.2. For SC-WP-H, uniaxial stress-strain curve was modeled based on tension coupon tests (shown in Figure 8.3). The input effective stress-strain curve for faceplates was presented in Figure 8.4. Measured steel (faceplate and flangeplate) properties for SC-W-H specimen were used

(presented in Table 5.1) to define the wall FE models. 12 GA Gr 50 material was used for faceplates (webplates) with a yield strength of 395 MPa, tensile strength of 453 MPa, and elongation of 32%. A572 Gr 50 steel was used for flangeplates, with a measured yield strength of 413 MPa, tensile strength of 596 MPa, and elongation of 25%. Input effective stress-strain curves for faceplates and flangeplates were built using measured properties, considering power law coefficient of 3, yield plateau length of $8\varepsilon_y$, and strain ductility factor of 85. These values are typical values for A572 Gr. 50 steel. Input effective stress-strain curves for flangeplates and faceplates are presented in Figure 8.40 and Figure 8.41 respectively. For 12 GA Gr 50 faceplates, similar stress-strain curves were used by Bruhl [132].

Thermal properties for steel and concrete based on Eurocode [114] were used for FE models. These properties have been discussed previously in Section 2.6.1. As discussed, there is not a significant reduction in mechanical properties of steel and concrete for surface temperatures of 149˚C. Therefore, temperature dependent mechanical properties are not considered for 149˚C. The effect of temperature dependent mechanical properties for surface temperature of 232˚C is evaluated in the FE models. The concrete and steel models used were not capable of temperature dependent material properties. However, for the concrete and steel temperatures in consideration, the reduction in strength is not significant. The reduction in elastic modulus was incorporated by reducing the tangent modulus values for steel and concrete models. Steel modulus of elasticity was reduced by 13% and concrete modulus was reduced by 20%. The basis of this reduction was experimentally observed temperature distribution through the thickness (as discussed in Section 6.2).

8.2.3 Model Results and Comparisons

This section presents the results of finite element (FE) models for specimens (SC-WP-H) and SC-W-H. FE model results are compared with experimental observations. FE models are then employed to evaluate the individual response of concrete infill and steel plates.

8.2.3.1 SC-WP-H

Specimen SC-WP-C (same as SC-T-C) was subjected to just in-plane loading (no thermal loading). FE model results for the specimen were discussed in Section 8.1.3.1. FE model results for specimen SC-WP-H are presented in this section. The specimen had tie spacing of half the section thickness (similar to SC-0.5T-Vn) and was subjected to cyclic in-plane loading in combination with accident thermal loading. The response of SC-WP-H was evaluated for the following loading conditions:

- Ambient: The FE model was subjected to monotonically increasing in-plane displacement (no thermal loading) to obtain the response at ambient temperatures.

- 149˚C-no preload: FE analysis was conducted to evaluate the effect of accident thermal loads on the initial stiffness of the specimens. Accident thermal loading was applied before in-plane loading. Sequentially coupled thermal-structural analysis was performed. The thermal FE model was subjected to surface temperatures of 149˚C. The surface temperatures were increased from ambient temperatures (considered as 21˚C) to 149˚C in 45 minutes. Heat transfer analysis was conducted using the thermal FE model. Nodal temperatures from the thermal analysis were input into the structural model, and structural analysis was conducted by applying monotonically increasing in-plane loading (load control). In-plane loading protocol was changed to load control to be consistent with models with pre-load, where the in-plane load was maintained

constant while accident temperatures were applied (discussed in the following paragraph). The loading rate was set to ensure that through thickness temperature gradients at the time step when the FE model reached its peak strength were similar to those observed experimentally (Figure 6.4).

- 149˚C-preload: Typically, the structural walls will be cracked due to existing service loads when a thermal accident occurs. Additionally, the loading and heating protocol for experiments conducted comprised of ambient load cycles before thermal loading was applied (Figure 5.6). To simulate this scenario, an in-plane load of magnitude $0.54V_{Mp}$ was applied before accident thermal loading was applied. The thermal-structural analyses were sequentially coupled. After the pre-loading, the surface temperatures were increased from ambient temperatures (considered as 21˚C) to 149˚C in 45 minutes, with the in-plane load maintained constant. The in-plane load was then increased monotonically till failure. Since a pre-load needed to be applied and maintained during the heating, the loading protocol was changed to load control. Additionally, the load was applied to the interior region (leaving out 125 mm from each edge) to ensure that the edge concrete elements do not deform excessively post-cracking.

- 232˚C-no preload: The peak surface temperature in FE models for case '149˚C-no preload' was updated to evaluate the specimen response for surface temperature of 232˚C. The surface temperatures were increased from ambient temperatures (considered as 21˚C) to 232˚C in 45 minutes. The loading rate was set to ensure that through thickness temperature gradients at the time step when the FE model reached its peak strength were similar to those observed experimentally (Figure 6.5).

- 232˚C-preload: The peak surface temperature in FE models for case '149˚C-preload' was updated to evaluate the specimen response for surface temperature of 232˚C. In-plane load of magnitude $0.54V_{Mp}$ was applied before accident thermal loading was applied. The thermal-structural analyses were sequentially coupled. After the pre-loading, the surface temperatures were increased from ambient temperatures (considered as 21˚C) to 232˚C in 45 minutes, with the in-plane load maintained constant. The in-plane load was then increased monotonically till failure.

- 232˚C-no preload-TD: The FE models for case '232˚C-no preload' were employed to evaluate the effect of reduced modulus of elasticity of concrete and steel due to elevated temperatures. The reduction was based on discussion in Sections 8.2.2 and 6.2.

- 232˚C-preload-TD: The FE models for case '232˚C-preload' were employed to evaluate the effect of reduced modulus of elasticity of concrete and steel due to elevated temperatures. Since the FE model was pre-loaded at ambient temperatures, using reduced steel and concrete moduli may result in marginally lower stiffness pre-heating.

Results for these FE models are evaluated in this section, and compared with experimental observations. Figure 8.42 presents the comparison of experimental and numerical (FE) backbone curves. Experimental backbone curve is corrected for base slip and rotation to obtain the net drift of the wall. The curve is based on the average of push and pull cycle force and displacement values. Average values were used so that the average reduction in experimental stiffness due to accident thermal loading can be compared with the reduction in FE model stiffness. As discussed in Chapters 5 and 6, the SC wall pier specimen was subjected to ambient and heated (149˚C and 232˚C) cycles at a force level of $0.75F_n$. The displacements corresponding to these cycles have been included in the backbone curve, to enable comparisons with FE models. FE models for

ambient temperatures and surface temperatures of 149˚C and 232˚C (with preload) are also plotted in the figure.

In Figure 8.42, ambient secant stiffness of the FE models is higher than experimental ambient secant stiffness. However, the experimental backbone curve is obtained from cyclic loading history of SC-WP-C. Cyclic loading is expected to result in reduced stiffness (in comparison to monotonic loading) due to additional concrete cracking and faceplate yielding. Additionally, considering the average push and pull cycle values for experimental backbone curve reduced the stiffness (pull cycles were less stiff than corresponding push cycles). Peak strength for FE models matches well with experimentally observed strength. Specimen SC-WP-H had reached a peak strength corresponding to $1.07V_{Mp}$ ($1.25V_{Myc}$). The FE models reached similar peak strengths. Therefore, the FE models confirm the experimental observation that typical accident temperatures do not significantly reduce the strength of SC wall pier specimens. A comparison of ambient and heated FE models indicates that accident thermal loading results in significant reduction in stiffness of the specimen. Heated FE models reach peak strength at drift ratios significantly higher than the ambient model. The heated FE backbone curves are highly non-linear as thermal loading results in concrete cracking, reducing the stiffness of the specimens. Experimentally observed stiffness reduction due to accident thermal loading was discussed in Section 6.2. There was 20% reduction for 149˚C and 40% reduction for 232˚C, in comparison to normalized ambient $0.75F_n$ cycle stiffness. The magnitude of reduction in stiffness in FE models is similar to that observed experimentally. Percentage reduction in comparison with the ambient stiffness is higher because the ambient stiffness of the FE models is higher. Additionally, the post-heating response of FE models is less stiff in comparison to experimental response. This may be because of a more

widespread thermally induced concrete cracking and steel yielding in the faceplates for the FE model, in comparison with that observed experimentally.

Figure 8.43 shows the comparison of backbone curves for FE models with/without pre-loading. The initial stiffness of models with no preload reduces, as the specimen is pre-cracked due to thermal loading. However, the post-heating response of models with pre-heating is similar to those with no pre-heating. Figure 8.44 presents the comparison of backbone curves for FE models with/without reduced elastic moduli of steel and concrete. Reduction in initial stiffness due to reduced elastic moduli is marginal. However, the reduction increases for higher loads, as the extent of concrete cracking and steel yielding increases.

Thermal loading is expected to reduce the concrete resistance to lateral loads, due to thermal induced cracking. Steel contribution may also reduce marginally as thermal loads may hasten steel yielding. Figure 8.45 presents the overall force-drift response of FE models for ambient and accident thermal loadings (cases with pre-load are considered). Steel and concrete contributions to overall lateral resistance are presented in Figure 8.46 and Figure 8.47 respectively. As seen in Figure 8.47, thermal loading leads to concrete cracking, and the concrete contribution drops even as the total lateral force remains constant (drift ratios of 0.1% to 0.2%, initial 45 minutes of heating with constant pre-load). The concrete cracking results in an increased contribution of faceplates for the same lateral force (initial 45 minutes of heating, drift ratios of 0.1% to 0.2%, Figure 8.46). The reduction in concrete contribution is higher for 232˚C as higher temperatures (and higher thermal gradient) lead to more cracking in concrete. While the concrete contribution post-heating increases as lateral loading is increased, it does reach the peak contribution for ambient temperature conditions. The steel contribution increases during the initial 45 minutes of heating (with pre-load maintained constant). For 232˚C, the steel contribution drops marginally as

additional concrete cracking may be resulting in yielding of the faceplates. The steel contribution never reaches shear yield strength ($0.6A_sF_y$), thus confirming that the response of SC wall piers is flexure-dominated.

The loading rate was designed to ensure that through-thickness thermal gradients at peak load were similar to those observed experimentally (Figure 6.4 and Figure 6.5). Figure 8.48 and Figure 8.49 present the temperature profile at peak load, and evolution of through-thickness temperatures for FE models with surface temperatures of 149˚C and 232˚C respectively. A non-linear thermal gradient exists through the thickness of the wall, and the extent of non-linearity decreases as the duration of heating increases. At the instance of peak lateral load, center of the wall is at 94˚C for surface temperature of 149˚C (the corresponding temperature observed experimentally was 110˚C). For 232˚C surface temperature, the center temperature at peak load is 120˚C (the corresponding temperature observed experimentally was 125˚C). Thus, the temperature profiles observed in FE models are similar to those observed experimentally, with FE profiles marginally lower than experimental profiles.

To better understand the reduction in stiffness due to thermal loading, the progression of concrete cracking and steel yielding due to thermal and mechanical loads can be evaluated. Figure 8.50, Figure 8.51 and Figure 8.52 present the concrete cracking for different SC-WP FE models. For FE models with no pre-loading, thermal loading results in symmetric concrete cracking (Figure 8.50). The cracks are primarily horizontal and vertical, with some diagonal shear cracks. The extent of concrete cracking is higher for surface temperature of 232˚C in comparison to that for surface temperature of 149˚C. A pre-load corresponding to $0.54V_{Mp}$ results in flexural cracking at the base, and some flexural-shear cracking at the base (Figure 8.51a and Figure 8.52a). When thermal loading is applied, with pre-load maintained constant, significant additional flexural and flexural-

shear cracks develop (Figure 8.51b and Figure 8.52b). The extent of concrete cracking is higher for surface temperature of 232˚C in comparison to that for surface temperature of 149˚C. Thus, a structure with pre-existing cracks due to mechanical loads will develop concrete cracks based on the pre-existing cracks and stress states. For structures with no pre-existing cracking, thermally induced cracks will depend on the external and internal restraints. Figure 8.53 to Figure 8.56 present the faceplate stress state due to thermal and mechanical loading. For specimens with no pre-loading, thermal loading results in stress concentration and yielding at the bottom region of the faceplates (Figure 8.53a and Figure 8.54a). The stress concentration at base is due to external restraint to thermal expansion imposed by the baseplate. Higher thermal strains for the model with surface temperature of 232˚C result in more yielding at the base of the faceplates. FE models with no-preload failed with extensive faceplate yielding, compression buckling and tension rupture of the faceplates (Figure 8.53b and Figure 8.54b). The response is consistent with that observed experimentally (Figure 6.13 to Figure 6.16). The mechanical pre-load (magnitude corresponding to $0.54V_{Mp}$) did not result in yielding of the faceplates (Figure 8.55a and Figure 8.56a). Thermal loading resulted in stress concentration and yielding at the bottom region of the faceplates (Figure 8.53b). The stress concentration at base is due to external restraint to thermal expansion imposed by the baseplate. Higher thermal strains for the model with surface temperature of 232˚C result in more yielding at the base of the faceplates. This behavior is similar to that observed for FE models with no pre-loading. However, thermal loading for specimens with pre-load also results in flexural yielding along the tension edge of the faceplates. This is because the concrete cracking resulting in additional stresses in faceplates (since the lateral load is maintained constant). Failure for FE models with pre-load was similar to that for models with no pre-load. The models failed with extensive faceplate yielding and compression buckling.

8.2.3.2   SC-W-H

Specimen SC-W-H was subjected to cyclic in-plane loading in combination with accident thermal loading. Experimental results for SC-W-H were discussed in Section 6.3. FE model results for the specimen are presented in this section. The response of SC-WP-H was evaluated numerically for the following loading conditions:

- Ambient: The FE model was subjected to monotonically increasing in-plane displacement (no thermal loading) to obtain the response at ambient temperatures.

- 149˚C-preload: Typically, the walls will be cracked due to existing service loads when a thermal accident occurs. Additionally, the loading and heating protocol for experiments conducted comprised of ambient load cycles before thermal loading was applied (Figure 5.7). To simulate this scenario, an in-plane load of magnitude $0.50V_n^{AISC}$ was applied before the application of accident thermal loading. The thermal-structural analyses were sequentially coupled. After the pre-loading, the surface temperatures were increased from ambient temperatures (considered as 21˚C) to 149˚C in 45 minutes, with the in-plane load maintained constant. The in-plane load was then increased monotonically till failure. Since a pre-load needed to be applied and maintained during the heating, the loading protocol was changed to load control. Additionally, the load was applied to the interior region (leaving out 100 mm from each edge) to ensure that the edge concrete elements do not deform excessively post-cracking.

- 232˚C-preload: The FE models for case '149˚C-preload' were employed to evaluate the specimen response for surface temperature of 232˚C. In-plane load of magnitude $0.50V_n^{AISC}$ was applied before accident thermal loading was applied. The thermal-

structural analyses were sequentially coupled. After the pre-loading, the surface
temperatures were increased from ambient temperatures (considered as 21˚C) to 232˚C
in 45 minutes, with the in-plane load maintained constant. The in-plane load was then
increased monotonically till failure.

Results for these FE models are evaluated in this section, and compared with experimental
observations. Figure 8.57 presents the comparison of experimental and numerical (FE) backbone
curves. Experimental backbone curve is corrected for base slip and rotation to obtain the net drift
of the wall. The curve is based on the average of push and pull cycle force and displacement values.
Average values were used so that the average reduction in experimental stiffness due to accident
thermal loading can be compared with the reduction from FE models. As discussed in Chapters 5
and 6, the specimen was subjected to ambient and heated (149˚C and 232˚C) cycles at a force level
of $0.75F_n$. The displacements corresponding to these cycles have been included in the backbone
curve, to enable comparisons with FE models. FE models for ambient temperatures and surface
temperatures of 149˚C and 232˚C (with preload) are also plotted in the figure.

In Figure 8.57, initial stiffness of the FE models agrees well with experimentally observed
stiffness. Secant stiffness of the ambient FE model is marginally higher than experimental ambient
secant stiffness. However, the experimental backbone curve is obtained from cyclic loading history
of SC-W-H. Cyclic loading is expected to result in reduced stiffness (in comparison to monotonic
loading) due to additional concrete cracking and faceplate yielding. Peak strength for FE models
matches well with experimentally observed strength. SC-W-H had reached a peak strength
corresponding to $1.30V_n^{AISC}$. Peak strengths for ambient and heated FE models are similar.
Therefore, the finite element models confirm the experimental observation that typical accident
temperatures do not significantly reduce the strength of SC wall specimens. A comparison of

ambient and heated FE models indicates that accident thermal loading results in significant reduction in stiffness of the specimen. Heated FE models reach peak strength at drift ratios significantly higher than the ambient model. The heated FE backbone curves are highly non-linear as thermal loading results in concrete cracking, reducing the stiffness of the specimens. Experimentally observed stiffness reduction due to accident thermal loading was discussed in Section 6.3. There was 28% reduction for 149°C and 43% reduction for 232°C, in comparison to normalized ambient $0.75F_n$ cycle stiffness. The magnitude of reduction in stiffness in FE models is similar to that observed experimentally. Percentage reduction in comparison with ambient stiffness is higher for FE models because the ambient stiffness of the FE models is higher. Additionally, the post-heating response of FE models is less stiff in comparison to experimental response. This may be because of a more widespread thermally induced concrete cracking and steel yielding in the faceplates for the FE model, in comparison with that observed experimentally. Thermal loading is expected to reduce the concrete resistance to lateral loads, due to thermally induced cracking. Steel contribution may also reduce marginally as thermal loads may hasten steel yielding. Figure 8.58 presents the overall force-drift response of FE models for ambient and accident thermal loadings. Steel and concrete contribution to overall lateral resistance are presented in Figure 8.59 and Figure 8.60 respectively. As seen in Figure 8.60, thermal loading leads to concrete cracking, and the concrete contribution drops even as the total lateral force remains constant (drift ratios of 0.1% to 0.2%, initial 45 minutes of heating with constant pre-load). The concrete cracking results in an increased contribution of faceplates for the same lateral force (initial 45 minutes of heating, drift ratios of 0.1% to 0.2%, Figure 8.59). The reduction in concrete contribution is higher for 232°C as higher temperatures (and higher thermal gradient) lead to more cracking in concrete. The concrete contribution post-heating increases as lateral loading

is increased and reaches the peak contribution for ambient temperature conditions. The steel contribution increases during the initial 45 minutes of heating (with pre-load constant). Faceplates for heated FE models reach the peak shear contribution (corresponding to steel shear yield strength, $0.6A_sF_y$) before the faceplates for the ambient model. This is because additional concrete cracking due to thermal loads results in higher stresses in faceplates.

Since no control specimen (at ambient conditions) was tested for SC-W, it is valuable to evaluate the response of concrete infill and steel plates at ambient temperatures. As seen in Figure 8.57, peak strength for ambient FE model matches the strength observed experimentally, and for heated FE models. Figure 8.61a presents the concrete cracking at force levels close to the peak (3070-kN). Response of the concrete infill is shear dominated, with shear and flexural-shear cracks. Flexural cracking is also observed on the tension side. Figure 8.61b presents the Von-Mises stresses in steel plates at force levels close to the peak load (3070-kN). There is significant yielding in the faceplates. No yielding was observed in the flangeplates. However, the compression strut anchoring in to the flangeplate resulted in high localized stresses in the bottom region of the faceplates. As discussed in Section 6.3, concrete compression strut had resulted in bulging of the flangeplates, ultimately leading to baseplate-faceplate-flangeplate weld rupture (Figure 6.25, Figure 6.27 and Figure 6.28).

For heated FE models, the loading rate was adjusted to ensure that through-thickness thermal gradients at peak load were similar to those observed experimentally (Figure 6.21). Figure 8.62a and Figure 8.62b present the temperature profiles at peak load for FE models with surface temperatures of 149˚C and 232˚C respectively. The evolution of non-linear gradient was similar to that observed for SC-WP models. However, since the wall models were heated on the flange and web (only the faceplates were heated for SC-WP models), a thermal gradient existed through

the length of the specimen too. The temperature profiles observed in FE models are similar to those observed experimentally, with FE profiles marginally lower than experimental profiles.

To better understand the reduction in stiffness due to thermal loading, the progression of concrete cracking and steel yielding due to thermal and mechanical loads can be evaluated. Figure 8.63 and Figure 8.64 present the concrete cracking for heated SC-W FE models. A pre-load corresponding to $0.50V_n^{AISC}$ results in flexural-shear cracking at the base on the tension side (Figure 8.63a and Figure 8.64a). When thermal loading is applied, with pre-load maintained constant, significant additional flexural and flexural-shear cracks develop in the specimen (Figure 8.63b and Figure 8.64b). The extent of concrete cracking is higher for surface temperature of 232˚C in comparison to that for surface temperature of 149˚C. Thus, a structure with pre-existing cracks due to mechanical loads will develop concrete cracks based on the pre-existing cracks and stress states. Figure 8.65 and Figure 8.66 present the faceplate stress state due to thermal and mechanical loading. The mechanical pre-load (magnitude corresponding to $0.50V_n^{AISC}$) did not result in yielding of the faceplates (Figure 8.65a and Figure 8.66a). Thermal loading resulted in stress concentration and yielding at the restrained region (bottom and top corners) of the faceplates (Figure 8.53b). The stress concentration is due to external restraint to thermal expansion. Higher thermal strains for the model with surface temperature of 232˚C result in more yielding in the faceplates. Failure for FE models with thermal loading was similar to that for the ambient model. Steel stress for heated models at failure is shown in Figure 8.67. There is extensive yielding in the faceplates. Additionally, the concrete compression strut results in localized flangeplate yielding.

8.2.4   Discussion

FE models reasonably predict the experimentally observed response of the specimens. Comparison of FE results with experimental observations has been discussed in the previous section (Section

8.2.3.2). Ambient stiffness of SC wall FE models compares well with experimentally observed stiffness. Ambient SC wall pier FE models overestimate the stiffness in comparison to experimentally observed stiffness. This is partly because the concrete model used is elastic-perfectly plastic. Additionally, the model was loaded monotonically whereas the experiments employed cyclic loading protocol. This would result in the FE model not adequately capturing the concrete cracking and steel yielding due to multiple cycles. Strength results obtained from FE models are consistent with experimental observations. SC wall pier FE models subjected to accident thermal loadings reached a peak strength marginally greater than the force corresponding to plastic moment capacity (V_{Mp}). SC wall models reached a peak strength of 1.30 times the nominal in-plane shear strength of the wall (V_n^{AISC}). Peak strengths for ambient and heated FE models were similar. Accident thermal loads resulted in significant reduction in the stiffness. Reduced stiffness leads to heated SC FE models reaching peak strengths at drift ratio significantly larger than that for ambient FE models. The magnitude of reduction in stiffness observed in FE models was consistent with that observed in the experiments. Reduction in stiffness is primarily due to cracking of concrete caused by non-linear thermal gradient through the cross-section of the wall. Concrete cracking results in reduced contribution of concrete to lateral strength, which increases the stress in steel at similar force levels. This leads to hastening of steel yielding in the specimen. For the range of accident temperatures, the contribution of reduced steel and concrete elastic moduli to stiffness reduction is marginal.

The benchmarked finite element models developed can be employed to conduct parametric studies for a combination of thermal and lateral loadings on SC walls and wall piers. Other concrete models need to be explored to improve the simulation of compression behavior of concrete infill in the models. The cyclic response of FE models can then be evaluated. The parametric studies

and cyclic analysis will provide more information regarding the effects of accident thermal loadings on the lateral load response of SC structures, and can be employed to validate the proposed equations for effective in-plane flexural and shear stiffness of SC walls and wall piers subjected to combination of in-plane and accident thermal loads (discussed in Section 6.4).

8.3 Chapter Summary

This chapter presents the results from finite element analysis. Detailed finite element (FE) analysis models were built to simulate the experiments presented in this dissertation. Details and limitations of the material models employed were discussed. FE results were compared to experimental results.

FE models for biaxially loaded SC wall pier specimens agreed reasonably with experimental results. The FE peak strengths were within 5% of the experimental strengths. Monotonically loaded FE models had a marginally stiffer response in comparison to experiments. The response of FE wall pier models was flexure controlled, and the models (except SC-T-2.5Vn) reached strengths higher than their compression yield moment capacity, V_{Myc}. Specimen SC-T-2.5Vn failed in vector shear due to the magnitude of out-of-plane force being 2.5 times the out-of-plane strength. Flexural yielding and buckling of the faceplates was observed in the models. The low aspect ratio of the specimen enabled the concrete compression strut to form. However, the compression strut cannot anchor in at the base, and therefore its effectiveness is limited.

FE analyses for SC wall pier and wall specimens subjected to combined in-plane and accident thermal loading were conducted. The analysis results agreed reasonably with experiments. The ambient stiffness of SC wall FE models compares well with experimentally observed stiffness. Ambient SC wall pier FE models marginally overestimate the stiffness in comparison to experimentally observed stiffness. SC wall pier FE models subjected to accident thermal loadings

reached a peak strength marginally greater than the force corresponding to plastic moment capacity (V_{Mp}). SC wall models reached a peak strength of 1.30 times the nominal in-plane shear strength of the wall (V_n^{AISC}). Peak strengths for ambient and heated FE models were similar. Accident thermal loads resulted in significant reduction in the stiffness. Reduced stiffness leads to heated SC FE models reaching peak strengths at drift ratio significantly larger than that for ambient FE models. The magnitude of reduction in stiffness observed in FE models was consistent with that observed in the experiments. Reduction in stiffness is primarily due to cracking of concrete caused by non-linear thermal gradient through the cross-section of the wall. Concrete cracking results in reduced contribution of concrete to lateral strength, which increases the stress in steel at similar force levels. This leads to hastening of steel yielding in the specimen

Since the FE model results are consistent with experiments, these benchmarked models can be used to conduct parametric studies and further validate the recommendations provided (based on experimental results).
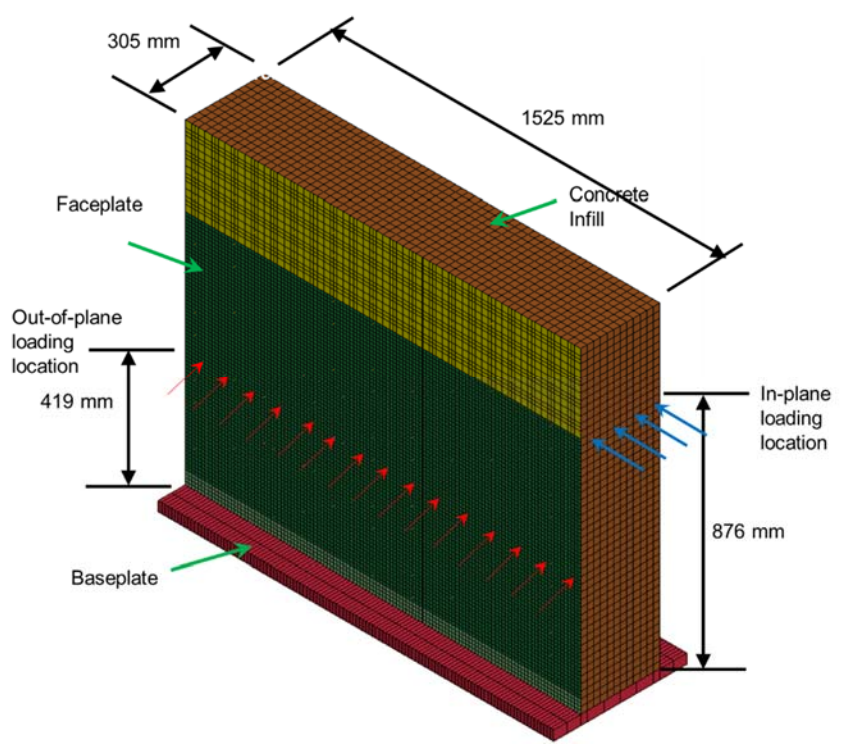
Figure 8.1 Details of SC wall pier model
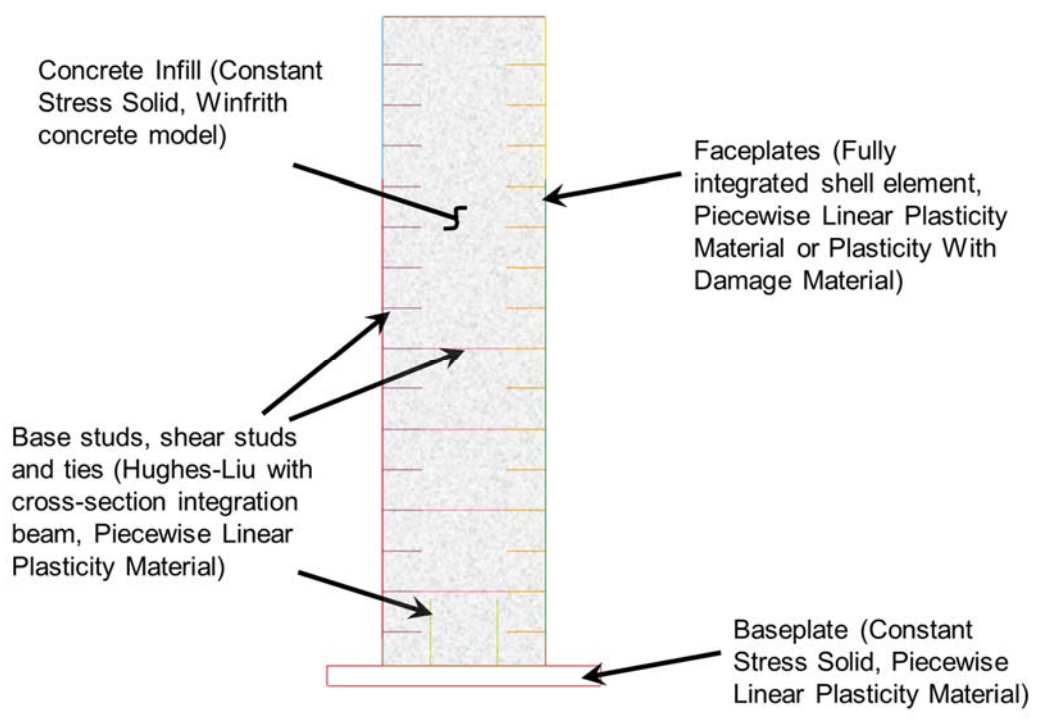
Figure 8.2 Details of SC wall pier model (element type and material model)
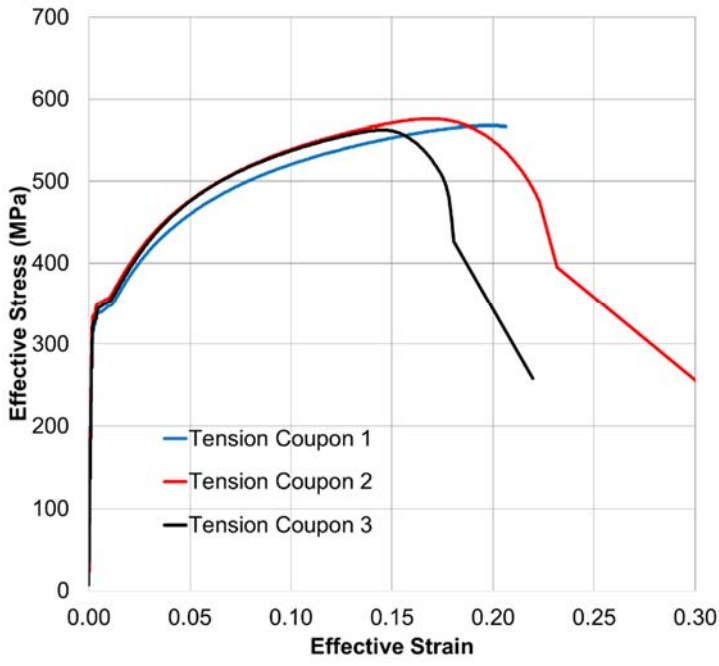
Figure 8.3 Data from faceplate tension coupons (Specimens SC-0.5T-Vn, SC-T-Vn, SC-T-2.5Vn and SC-WP-H)
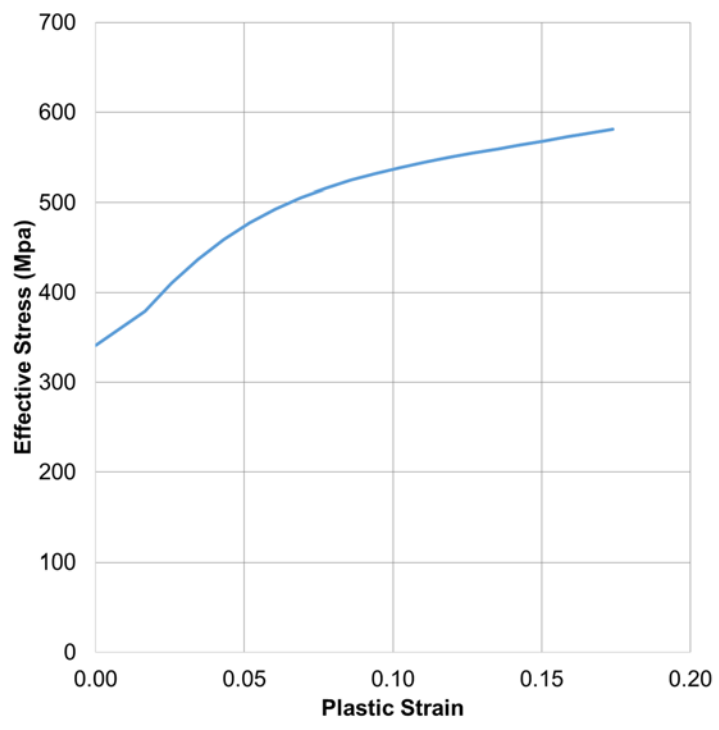
Figure 8.4 Faceplate effective stress-plastic strain input for LS-DYNA (specimens SC-0.5T-Vn, SC-T-Vn, SC-T-2.5Vn and SC-WP-H)
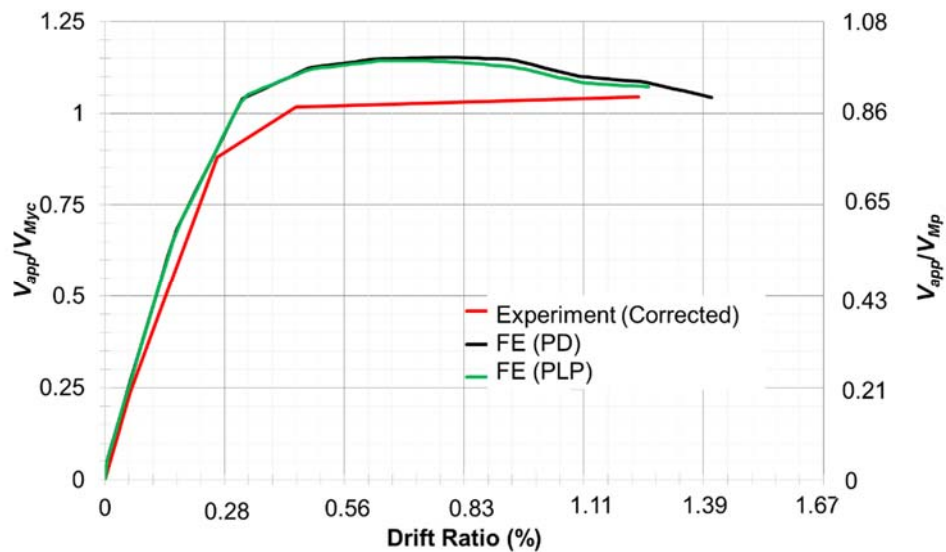
Figure 8.5 SC-T-C: Comparison of experimental and finite element backbone curves
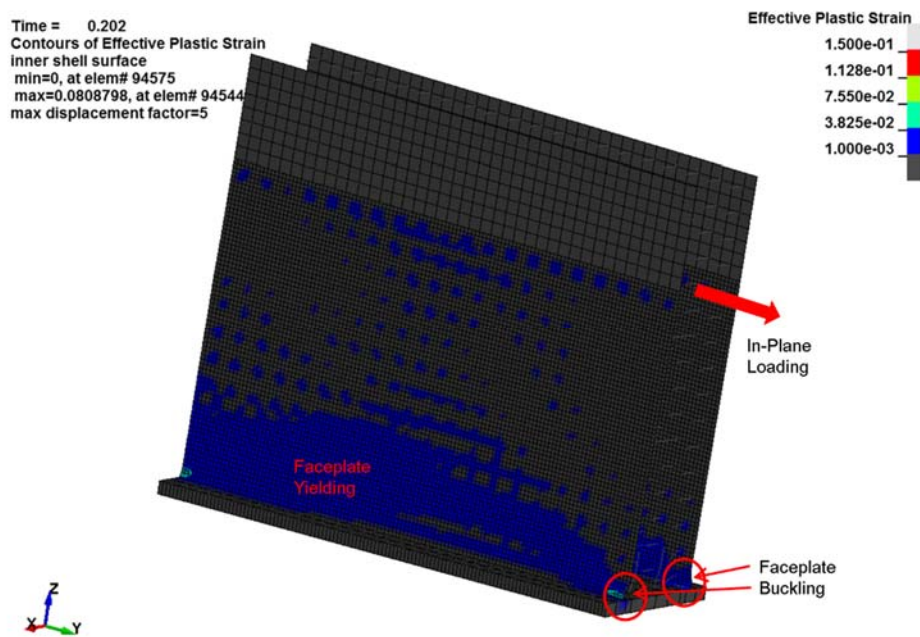
Figure 8.6 SC-T-C: Faceplate PEEQ strain at peak load
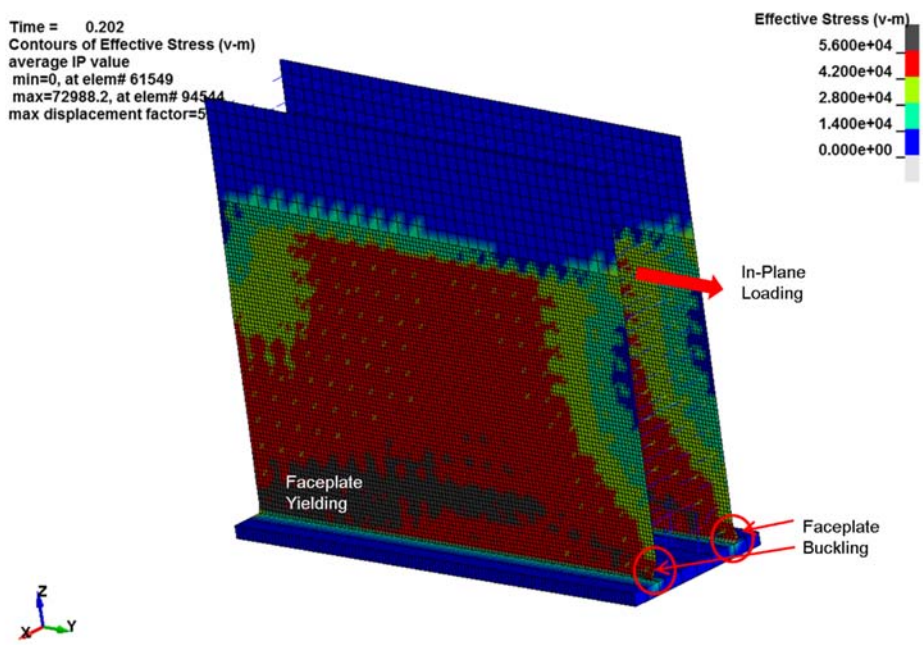
Figure 8.7 SC-T-C: Faceplate Von-Mises stress at peak load (in psi units, 1 psi=6.9 kPa)
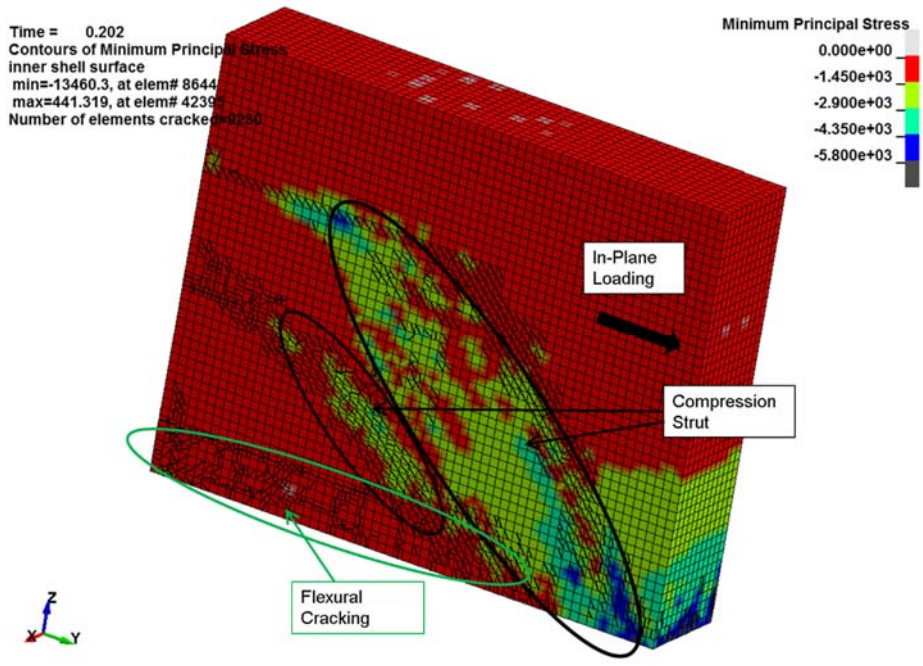
Figure 8.8 SC-T-C: Concrete principal compression stress at peak load (in psi units, 1 psi=6.9 kPa)
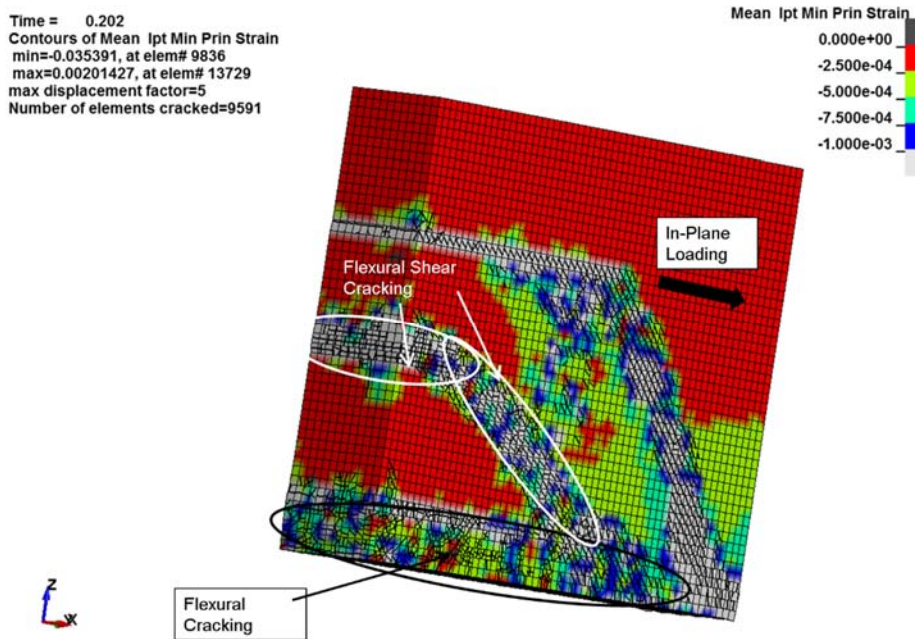
Figure 8.9 SC-T-C: Concrete cracking at peak load
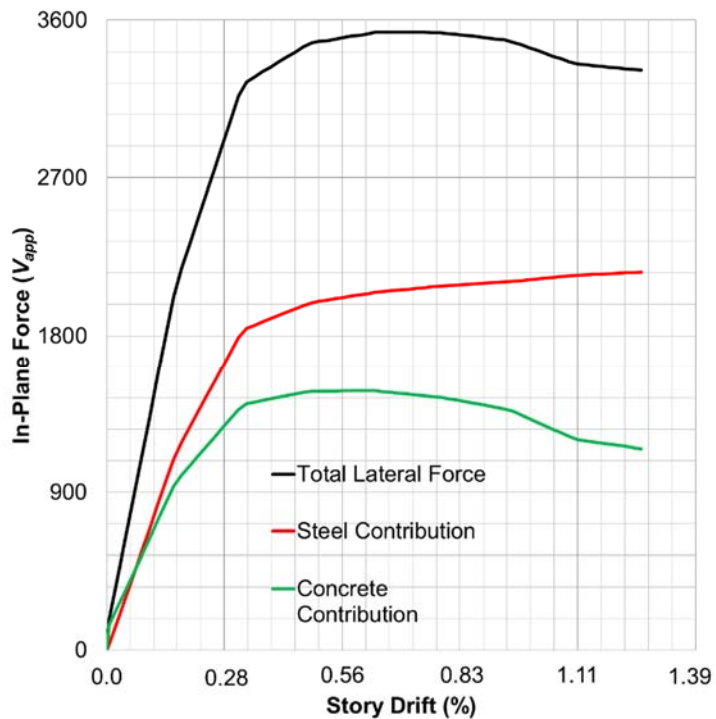
Figure 8.10 SC-T-C: Distribution of in-plane force in steel faceplates and concrete infill
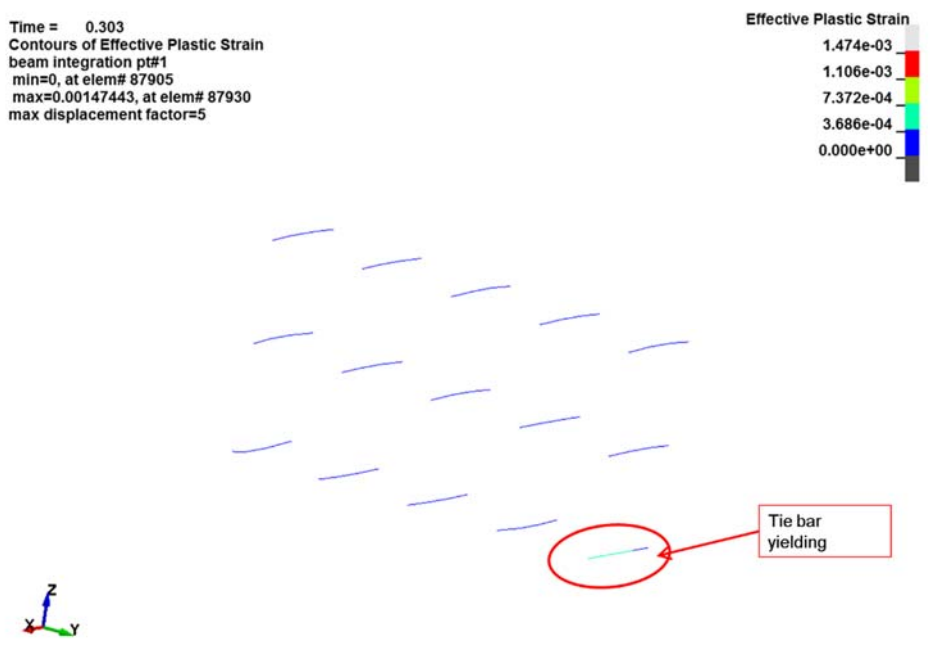
Figure 8.11 SC-T-C: Tie bar PEEQ at failure
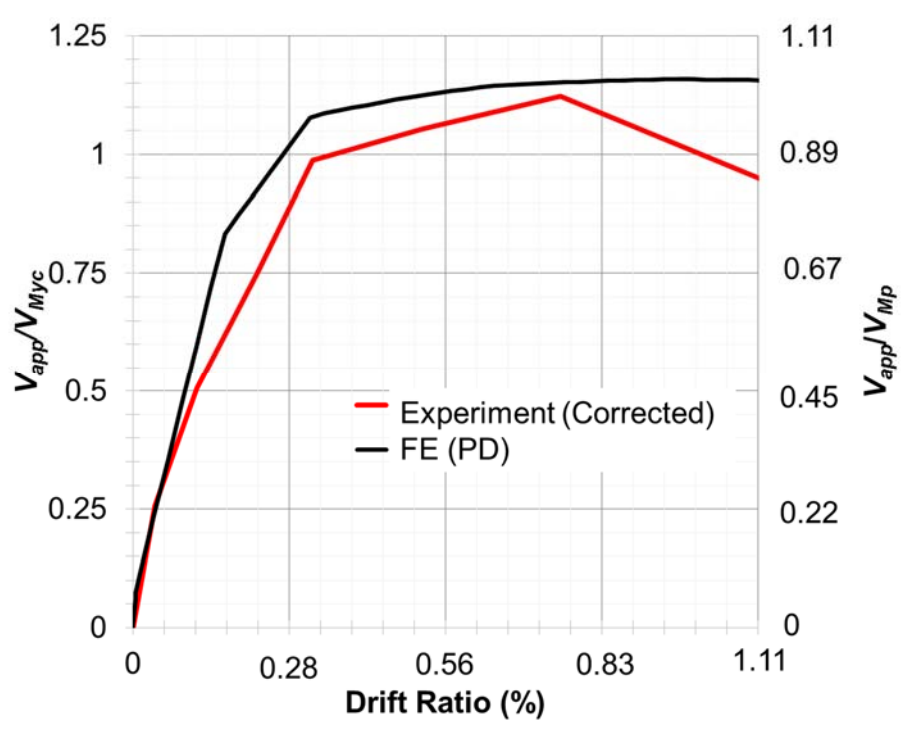
Figure 8.12 SC-T-Vn: Comparison of experimental and finite element backbone curves
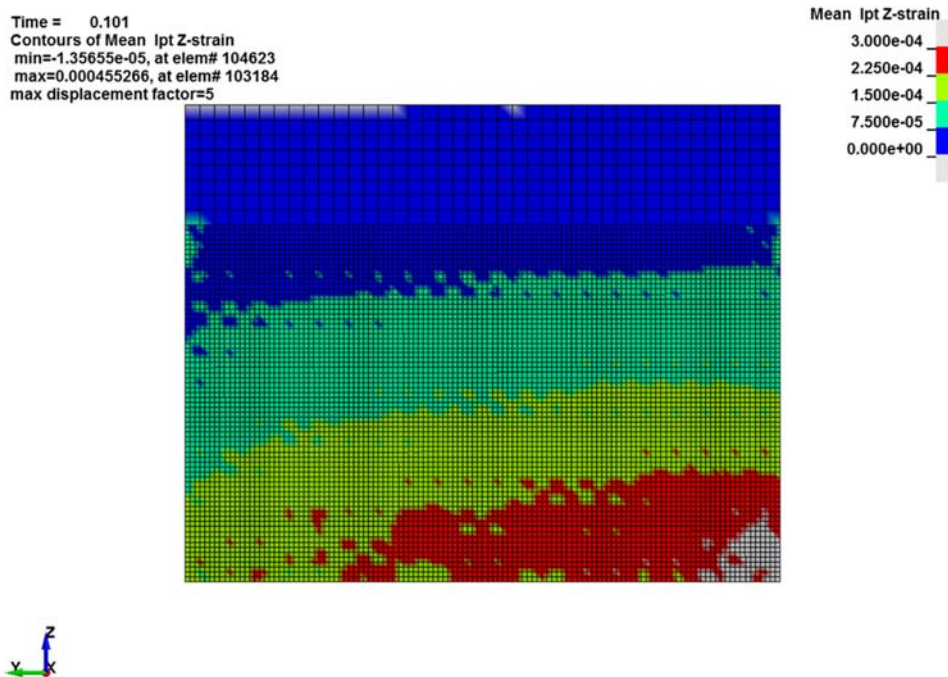
Figure 8.13 SC-T-Vn: Tensile strain in faceplate due to out-of-plane loading
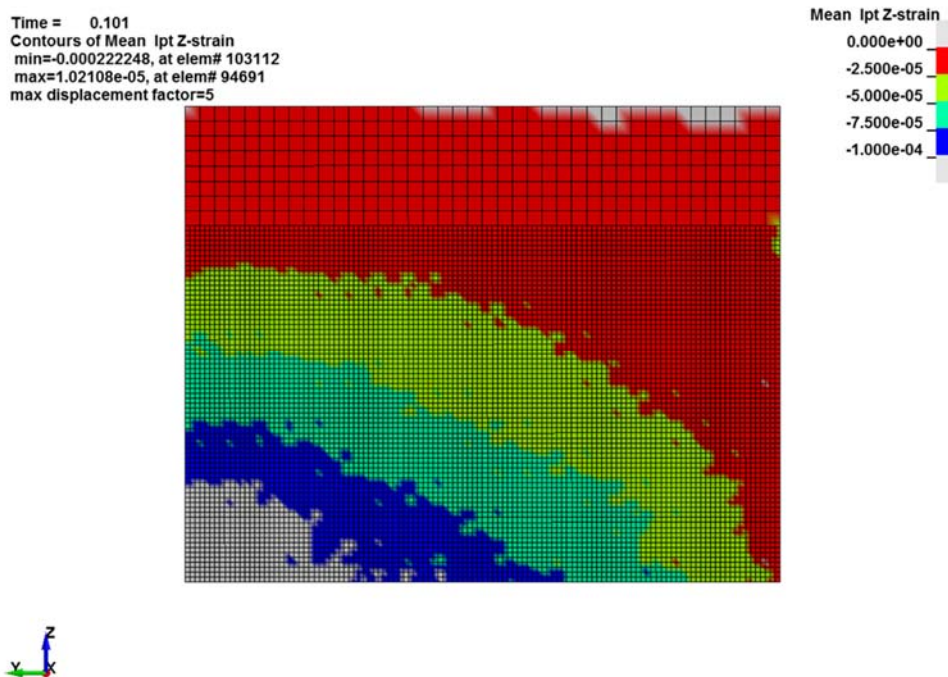
Figure 8.14 SC-T-Vn: Compressive strain in faceplate due to out-of-plane loading
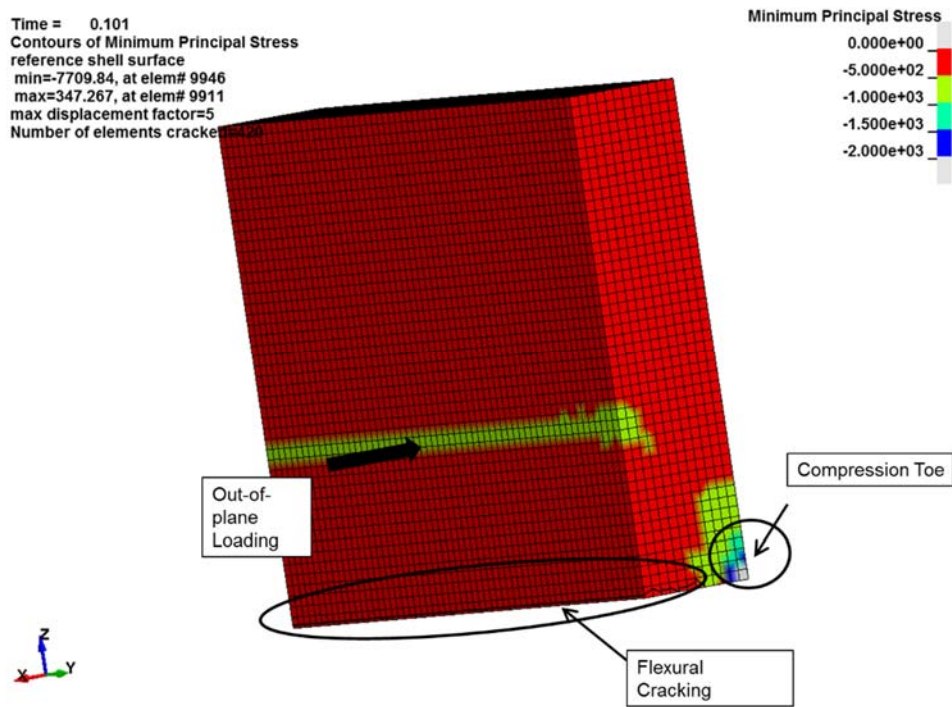
Figure 8.15 SC-T-Vn: Concrete cracking and principal compressive stress due to out-of-plane loading (in psi units, 1 psi=6.9kPa)
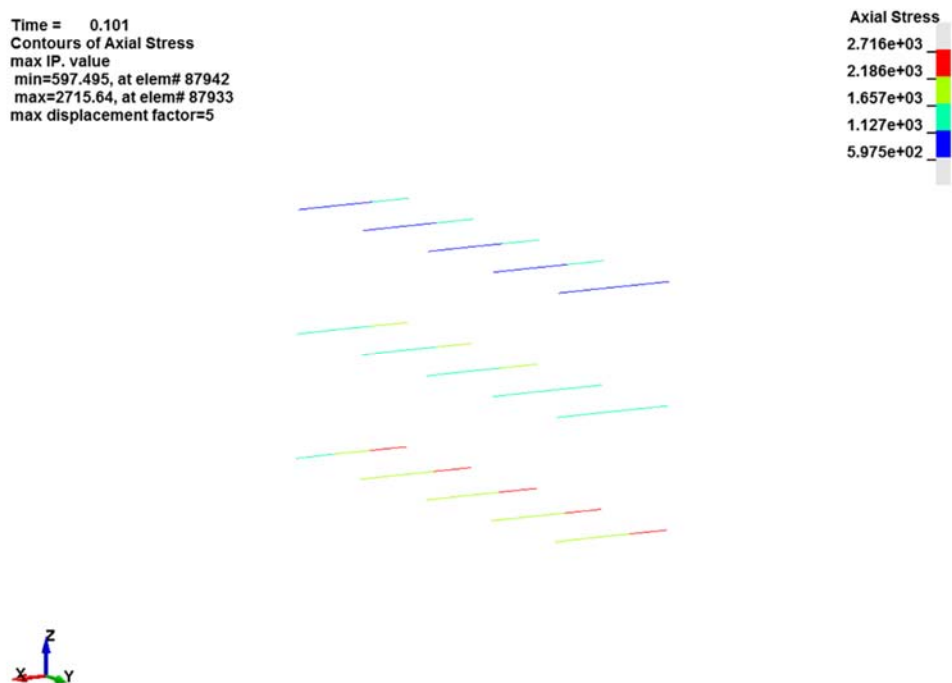
Figure 8.16 SC-T-Vn: Tie stress due to out-of-plane loading (in psi units, 1psi=6.9kPa)
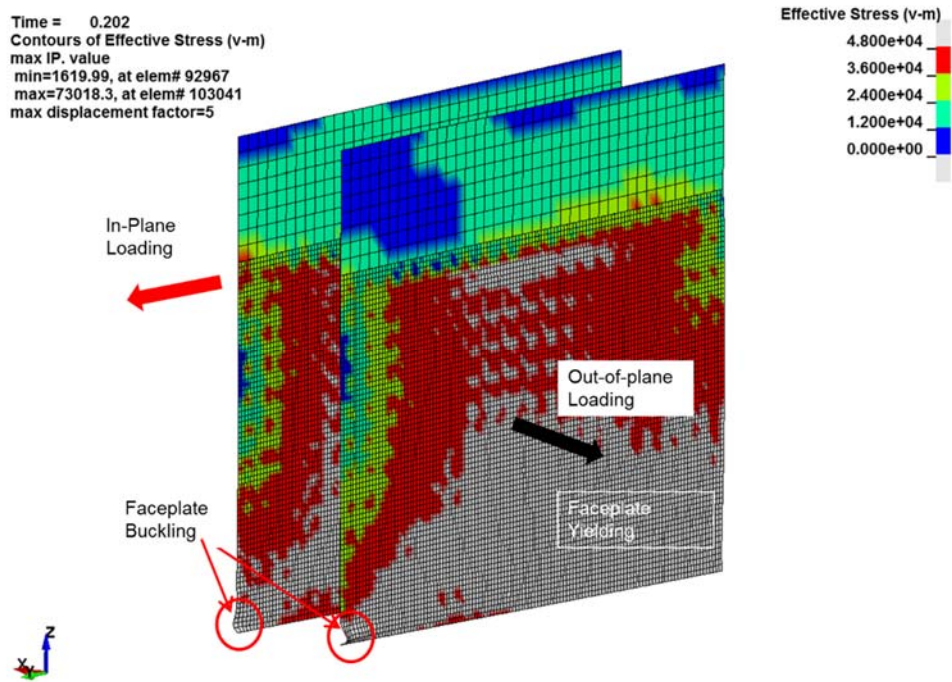
Figure 8.17 SC-T-Vn: Faceplate Von-Mises stress at peak in-plane load (in psi units, 1 psi=6.9 kPa)
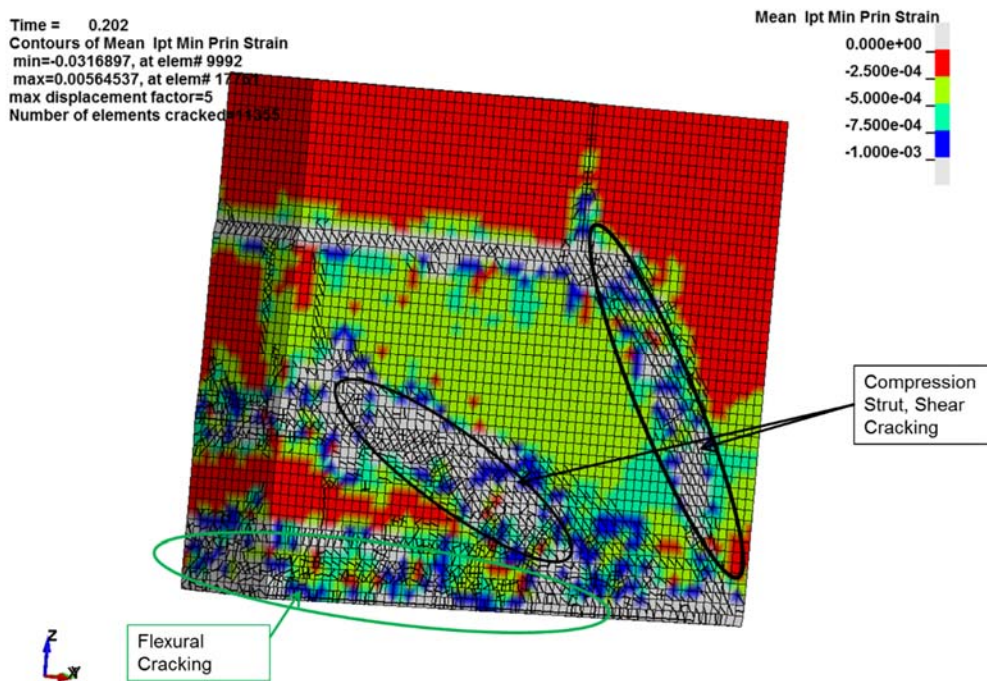
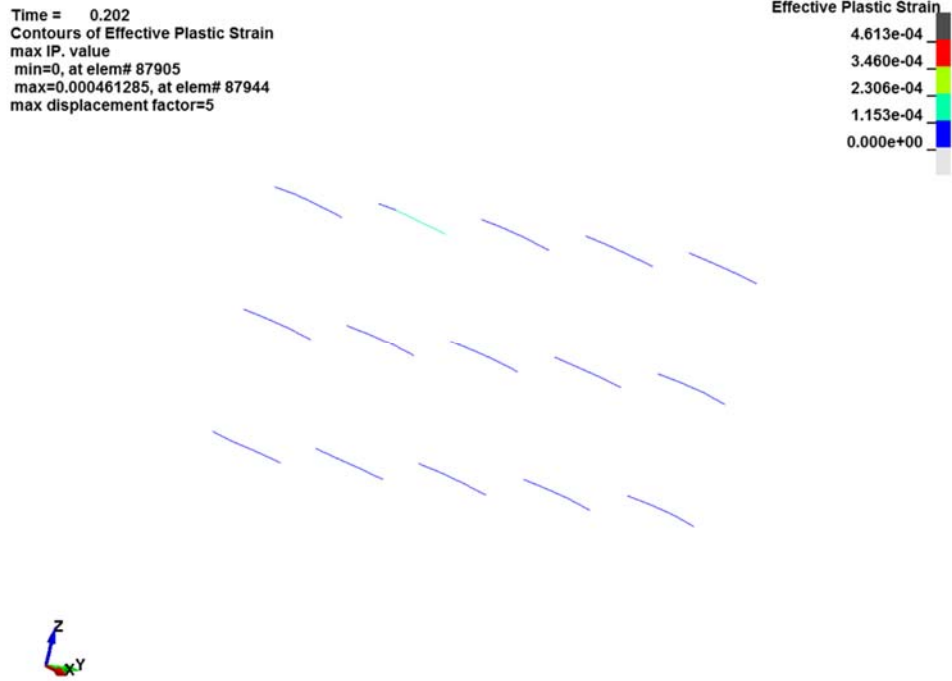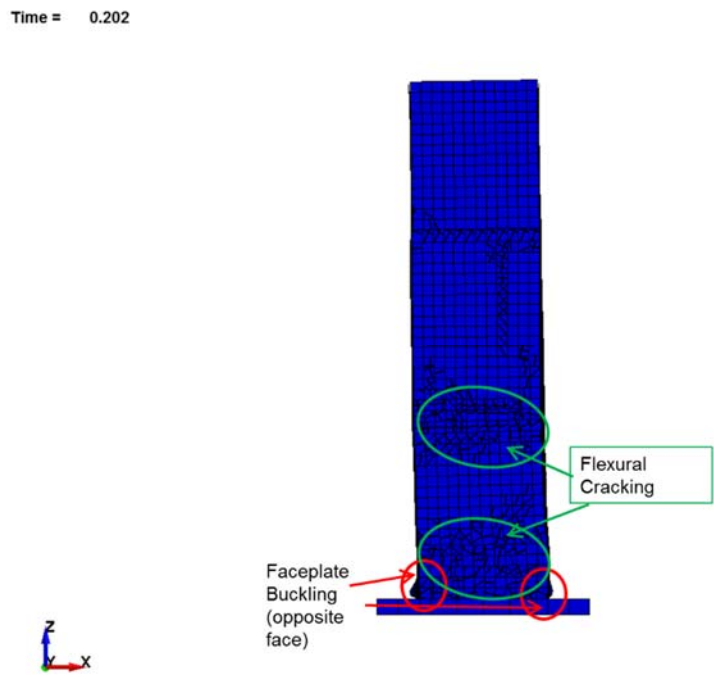Figure 8.18 SC-T-Vn: Concrete cracking at peak in-plane load

Time = 0.202
Contours of Effective Plastic Strain
max IP. value
 min=0, at elem# 87905
 max=0.000461285, at elem# 87944
max displacement factor=5

Effective Plastic Strain

4.613e-04
3.460e-04
2.306e-04
1.153e-04
0.000e+00

Figure 8.19 SC-T-Vn: Tie strain at peak in-plane load

Time = 0.202

Flexural
Cracking

Faceplate
Buckling
(opposite
face)

Figure 8.20 SC-T-Vn: Specimen at peak load
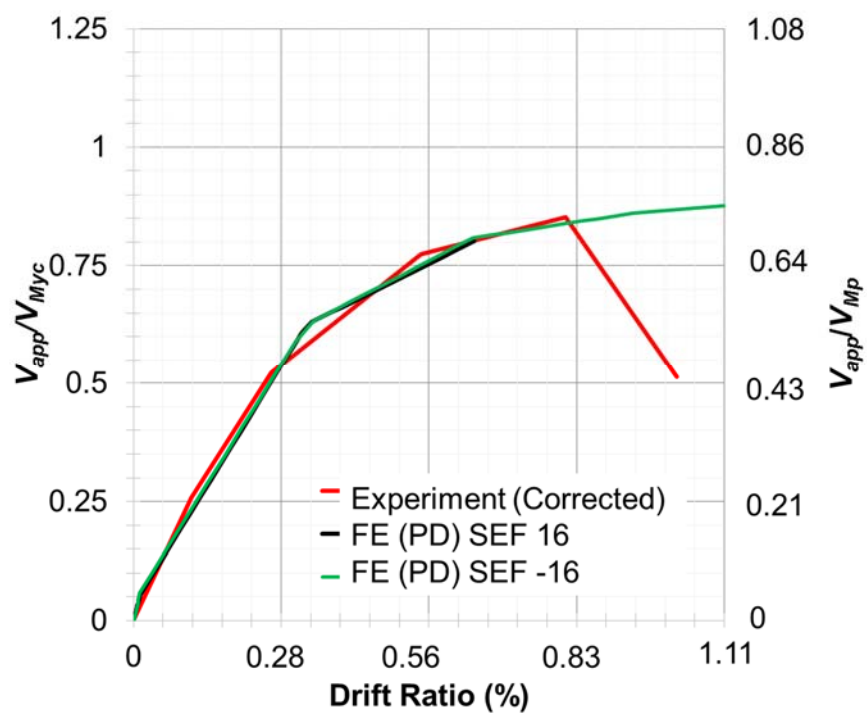
Figure 8.21 SC-T-2.5Vn: Comparison of experimental and finite element backbone curves
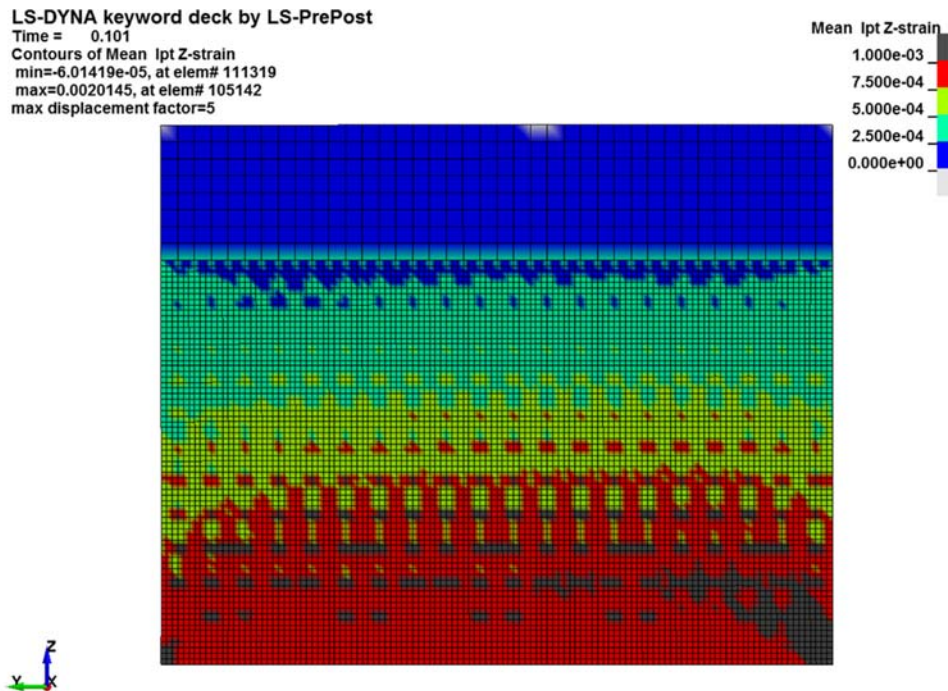
Figure 8.22 SC-T-2.5Vn: Faceplate tensile strains due to out-of-plane loading
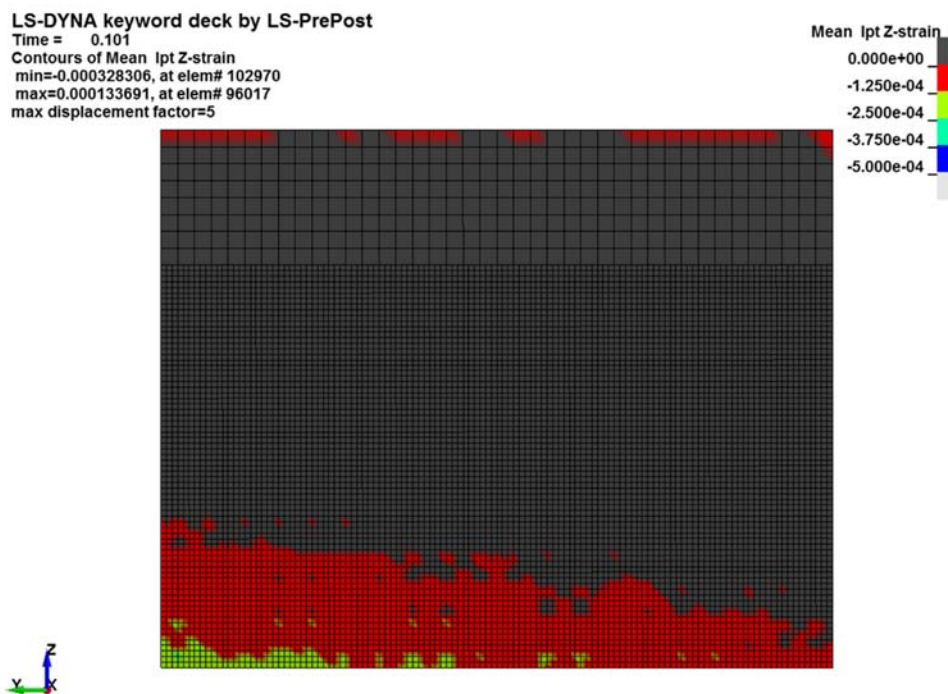

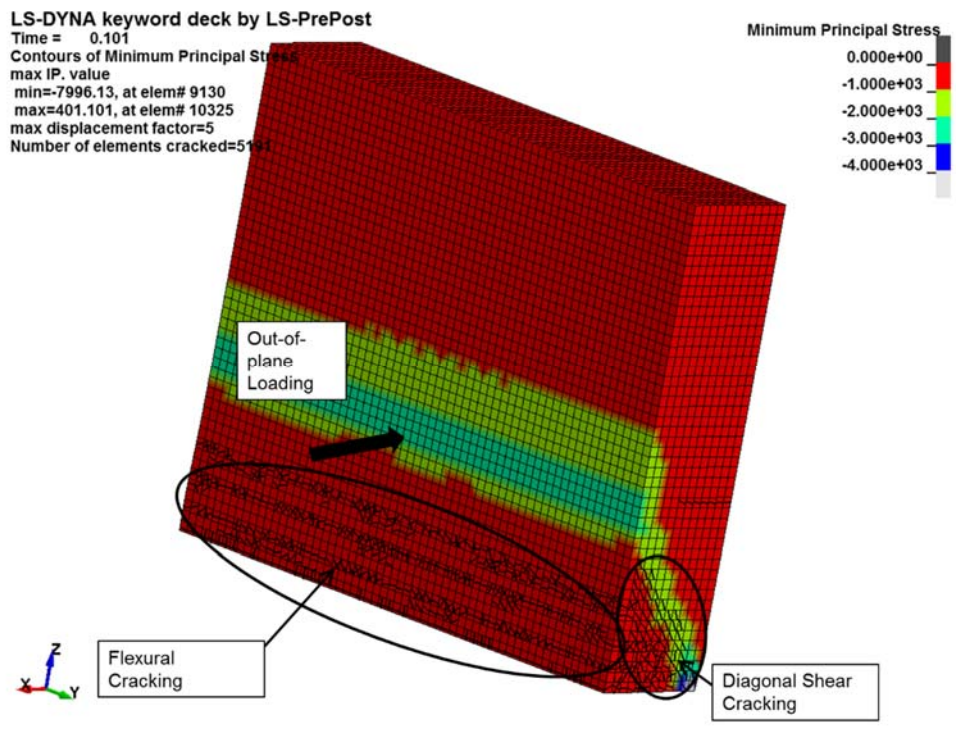Figure 8.23 SC-T-2.5Vn: Faceplate tensile strains due to out-of-plane loading

Figure 8.24 SC-T-2.5Vn: Concrete cracking and compressive principal stress due to out-of-plane loading (in psi units, 1 psi=6.9kPa)
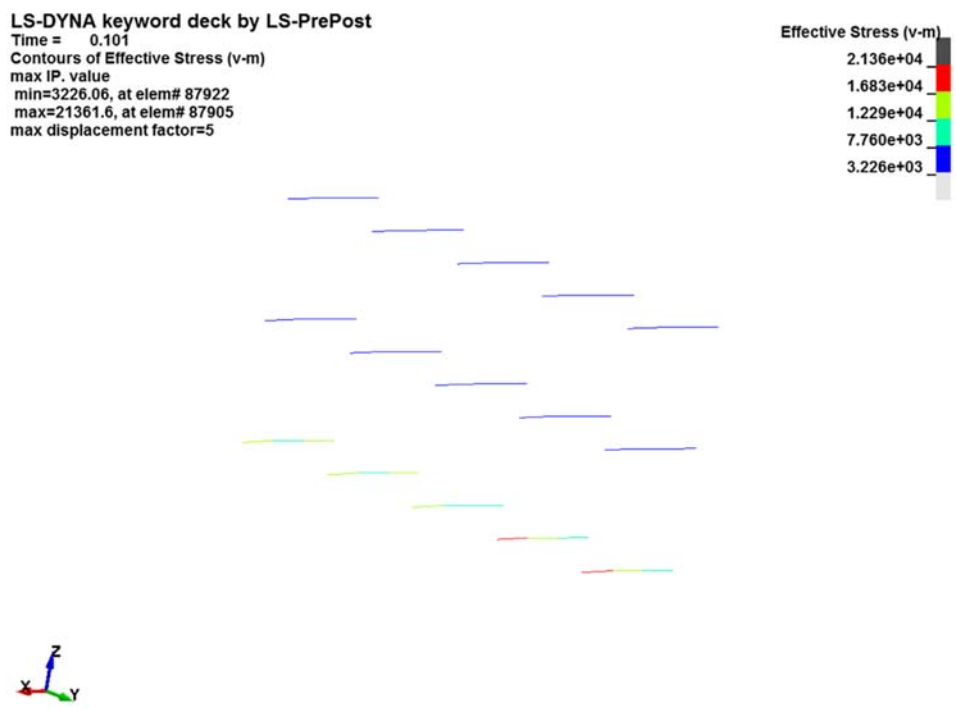

Figure 8.25 SC-T-2.5Vn: Von-Mises stress in ties due to out-of-plane loading (in psi units, 1 psi=6.9kPa)
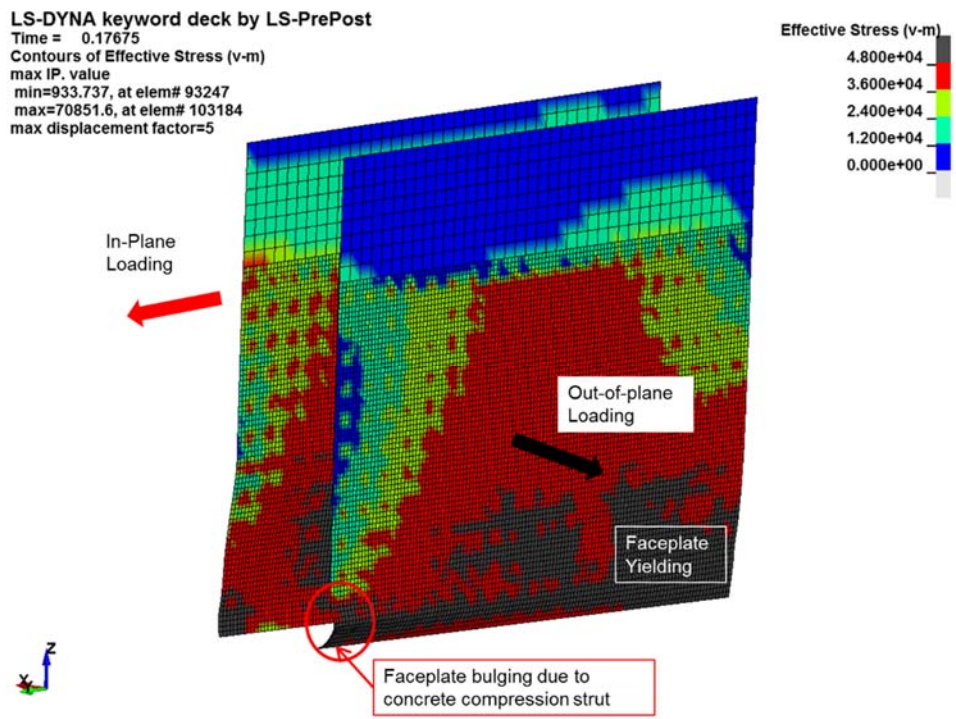
Figure 8.26 SC-T-2.5Vn: Faceplate yielding and bulging at peak in-plane load (in psi units, 1 psi=6.9 kPa)
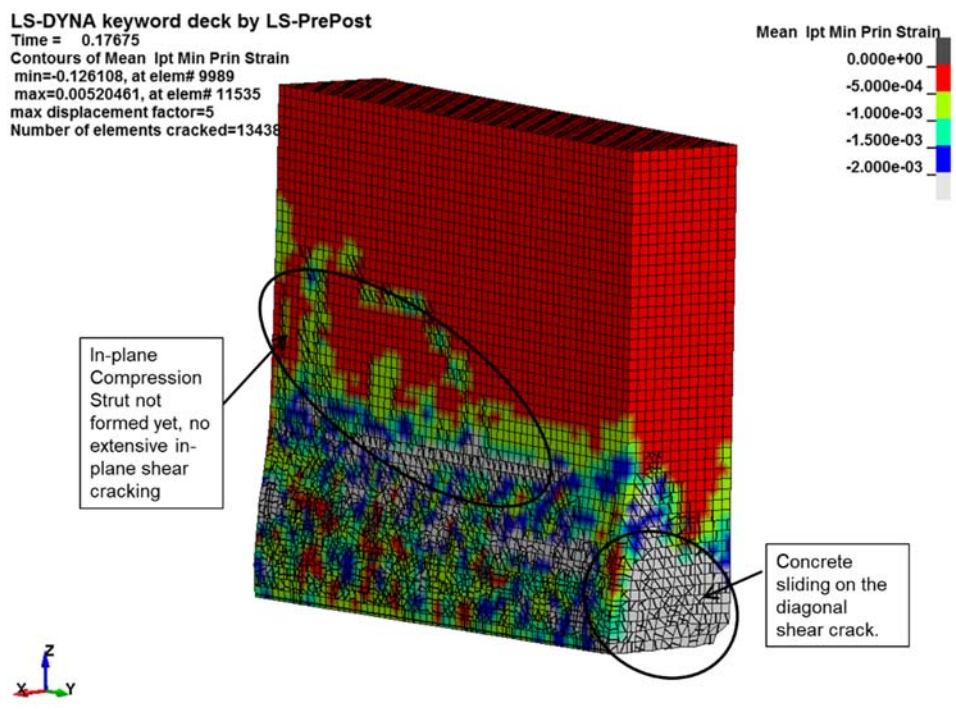
Figure 8.27 SC-T-2.5Vn: Concrete cracking at peak in-plane load

Figure 8.28 SC-T-2.5Vn: Tie yielding at peak in-plane load

Figure 8.29 SC-T-2.5Vn: Specimen state at peak in-plane load
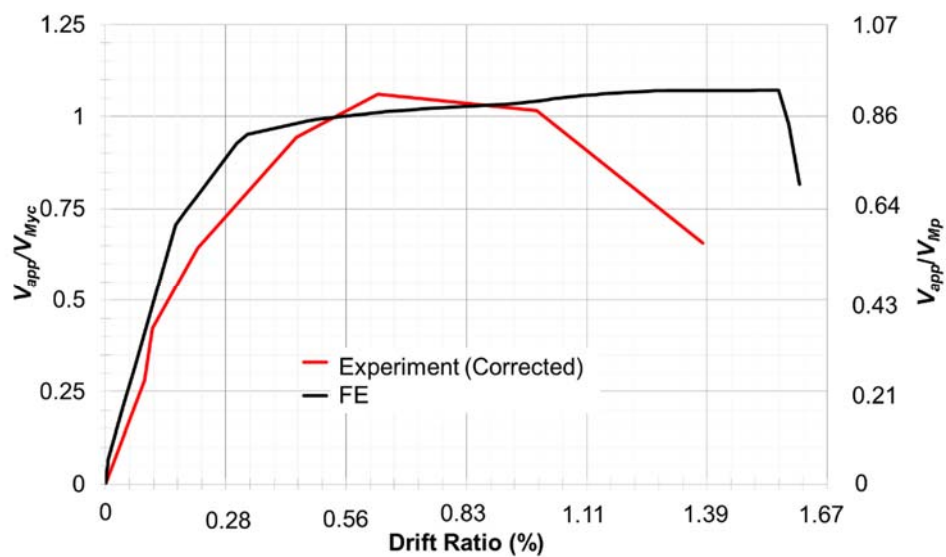
Figure 8.30 SC-0.5T-Vn: Comparison of experimental and finite element backbone curves
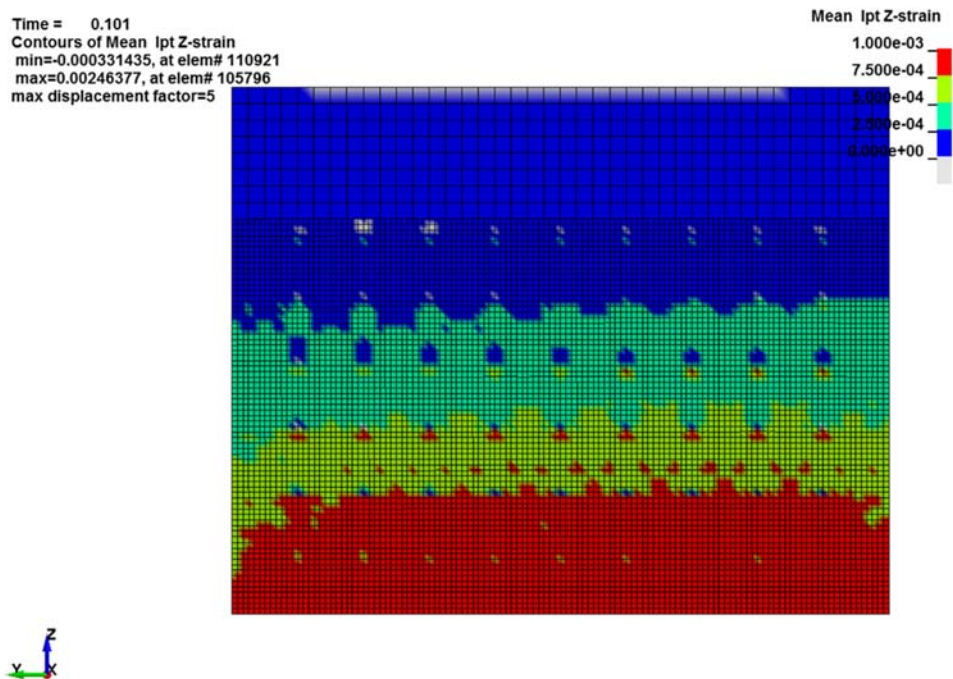
Figure 8.31 SC-0.5T-Vn: Faceplate tensile strain due to out-of-plane loading
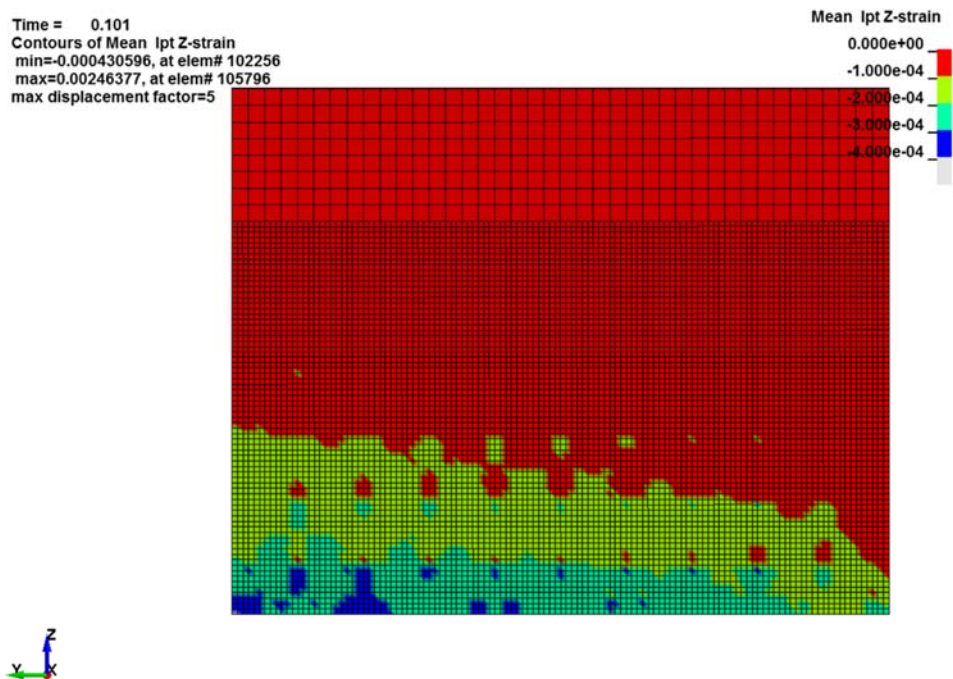
Figure 8.32 SC-0.5T-Vn: Faceplate compressive strains due to out-of-plane loading
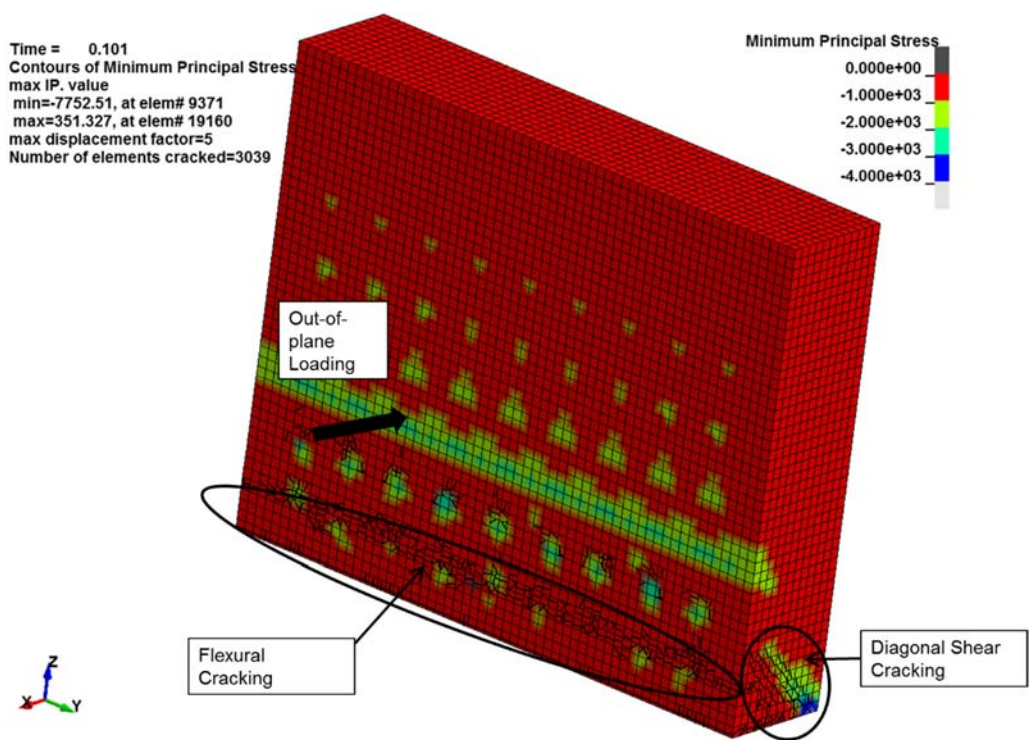
Figure 8.33 SC-0.5T-Vn: Concrete cracking and principal compressive stress due to out-of-plane loading (in psi units, 1 psi=6.9 kPa)
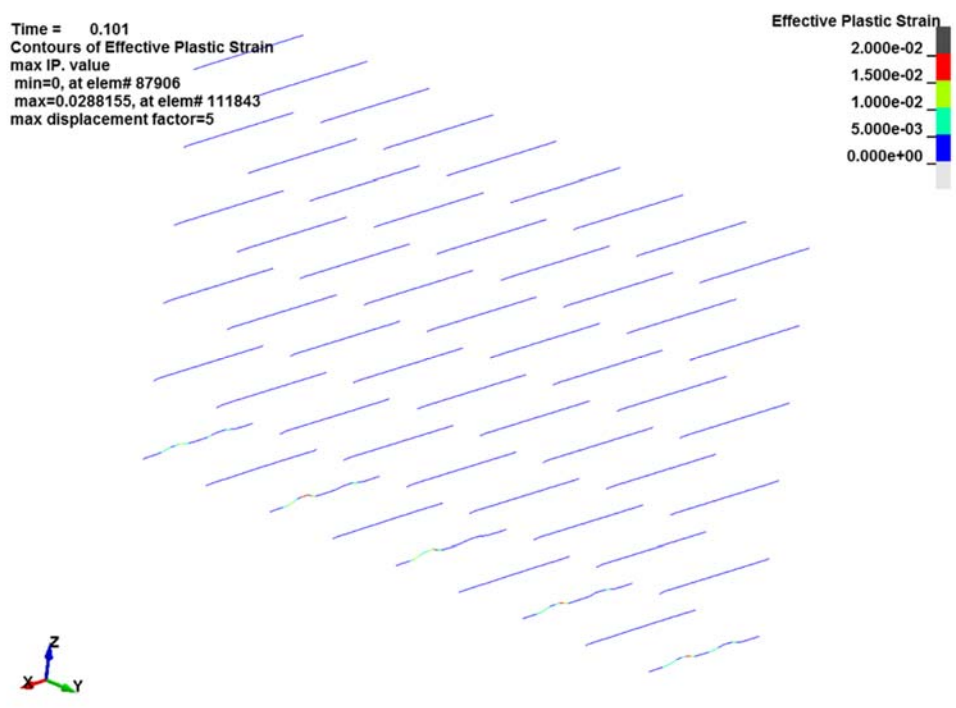
Figure 8.34 SC-0.5T-Vn: Tie yielding due to out-of-plane loading
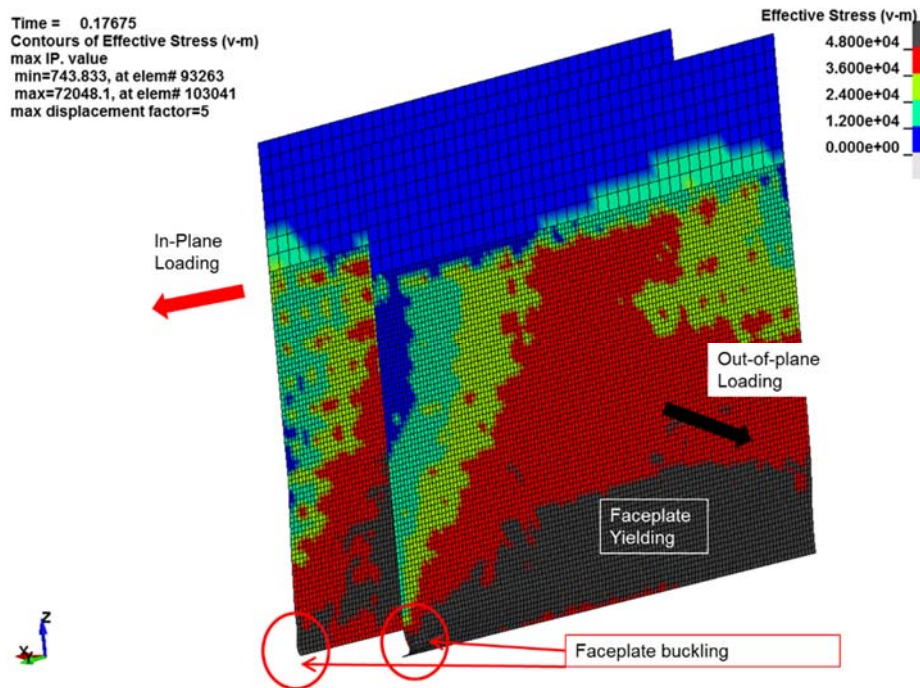
Figure 8.35 SC-0.5T-Vn: Faceplate yielding and buckling at peak in-plane load (in psi units, 1 psi=6.9 kPa)
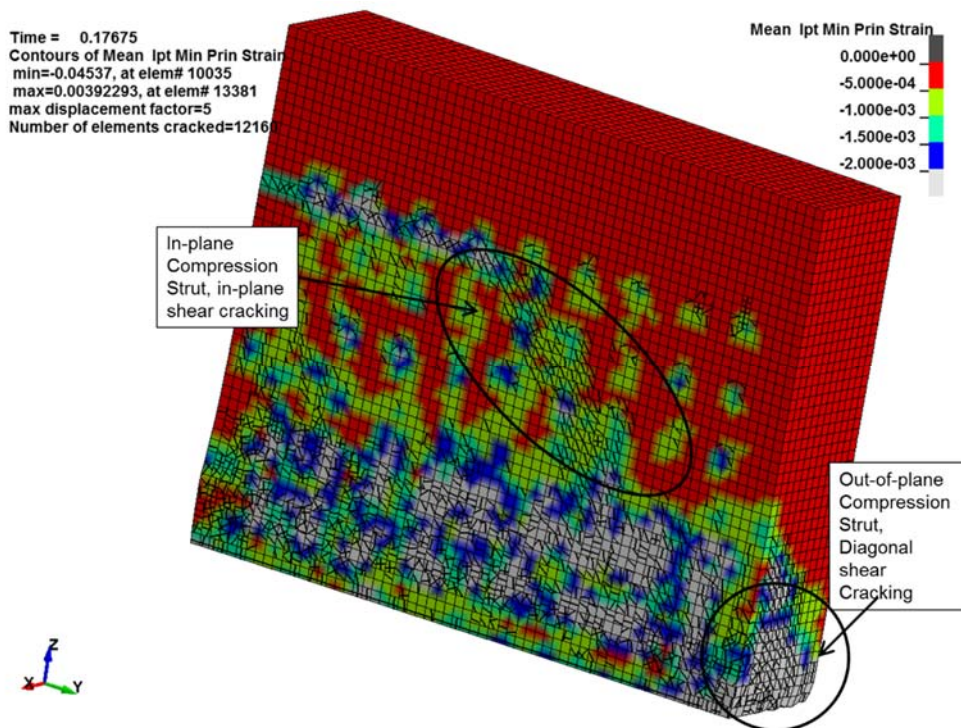
Figure 8.36 SC-0.5T-Vn: Concrete cracking and principal compressive stress at peak in-plane load
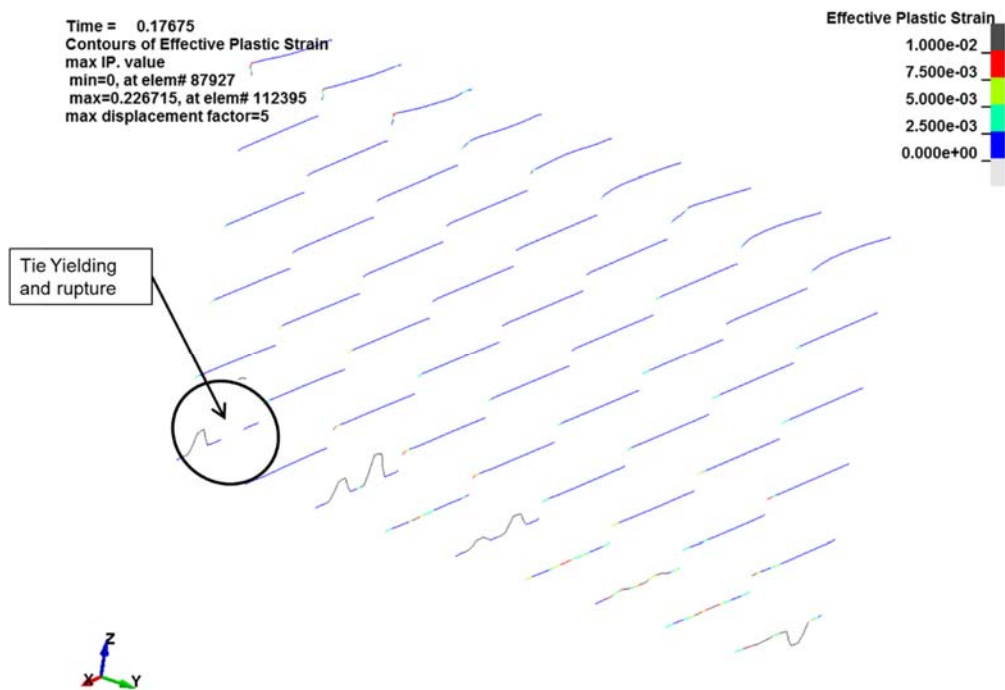
Figure 8.37 SC-0.5T-Vn: Tie yielding and rupture at peak in-plane load
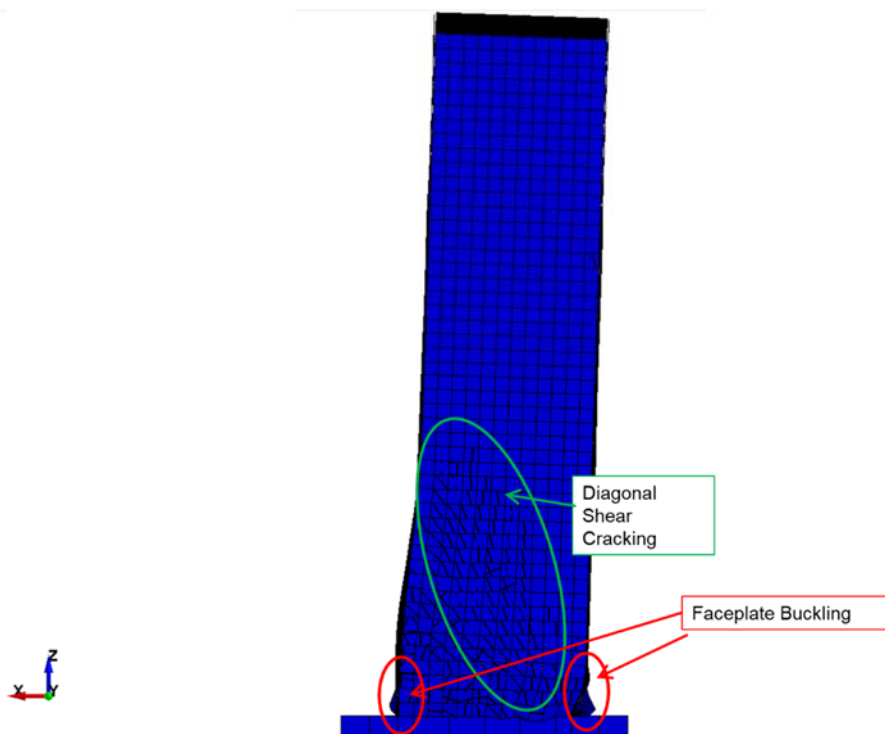
Figure 8.38 SC-0.5T-Vn: Specimen state at peak in-plane load
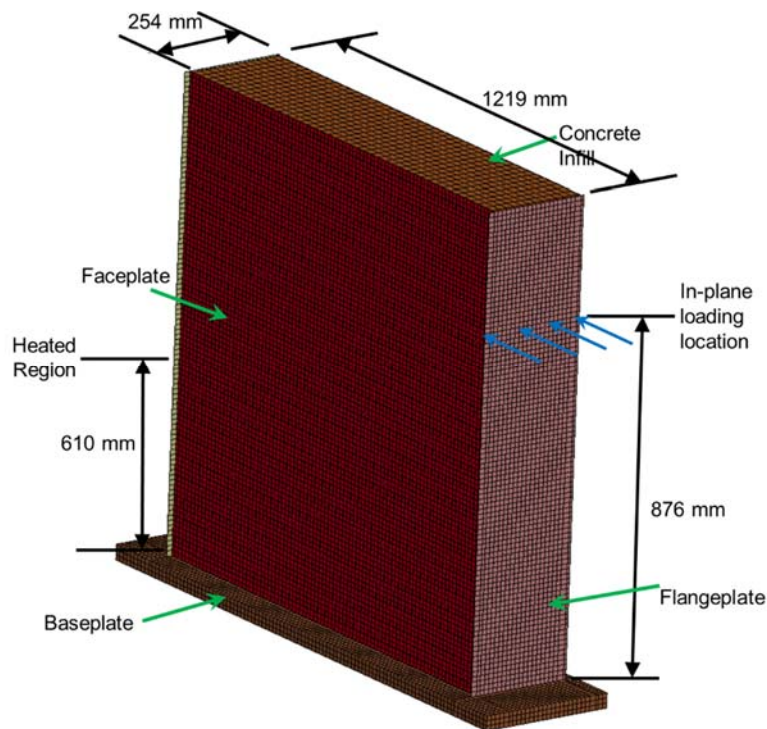
Figure 8.39 SC Wall model details
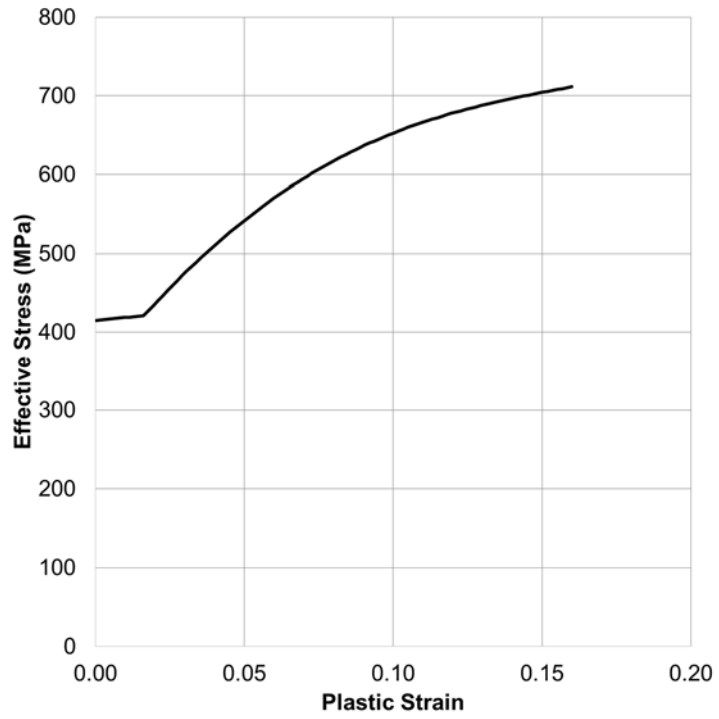
Figure 8.40 SC Wall Model: input stress-strain curve for flangeplates
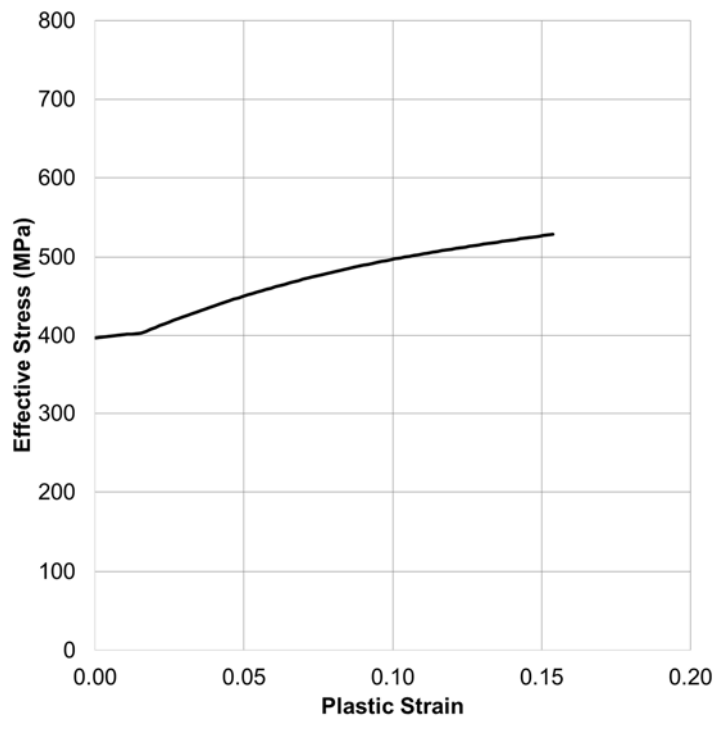
Figure 8.41 SC Wall Model: input stress-strain curve for faceplates
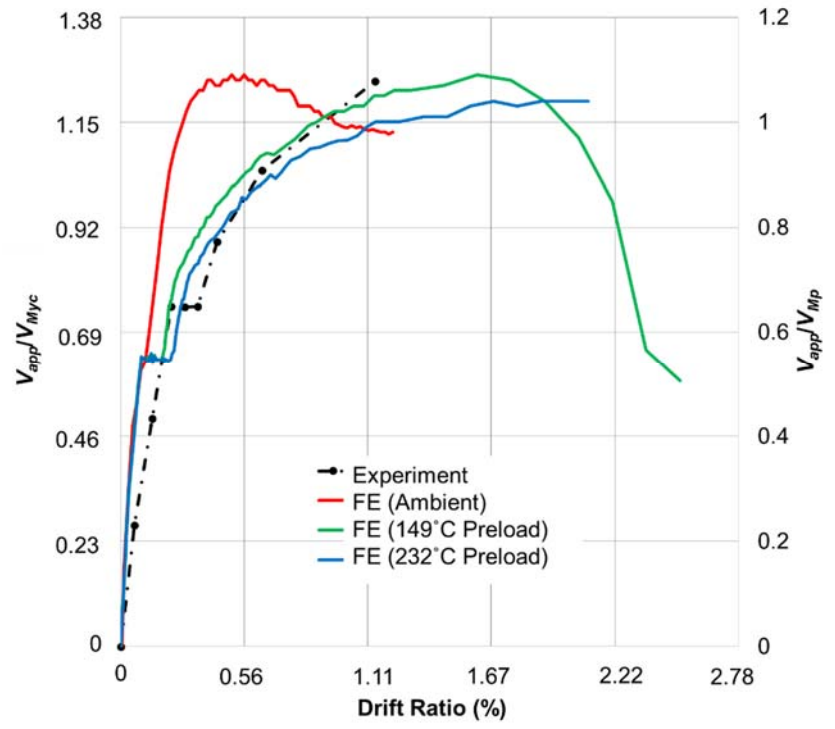
Figure 8.42 SC-WP-H: Comparison of experimental and finite element backbone curves
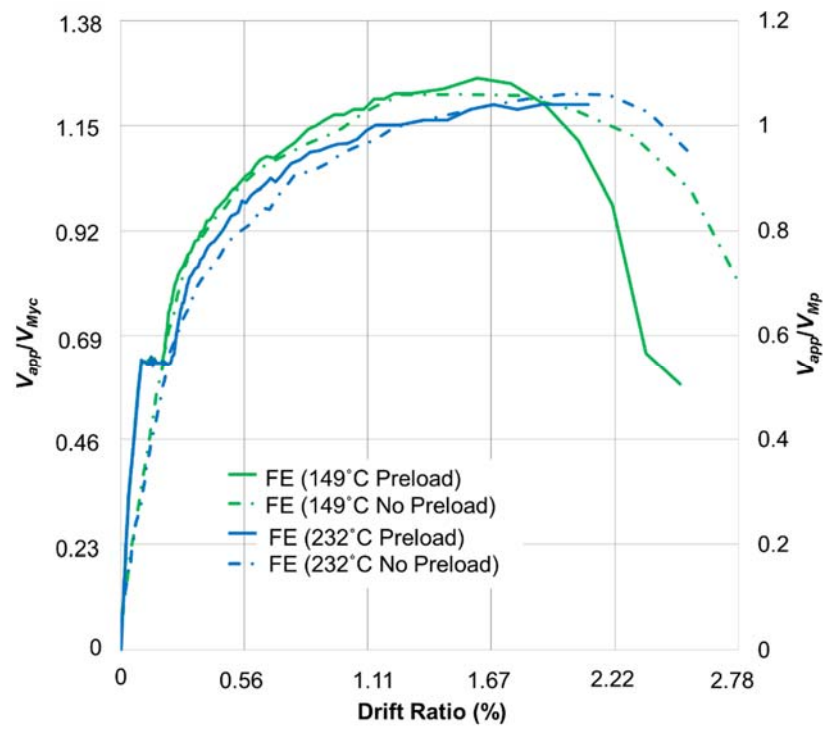
Figure 8.43 SC-WP-H: Comparison of FE backbone curves for cases with and without pre-loading (before heating)
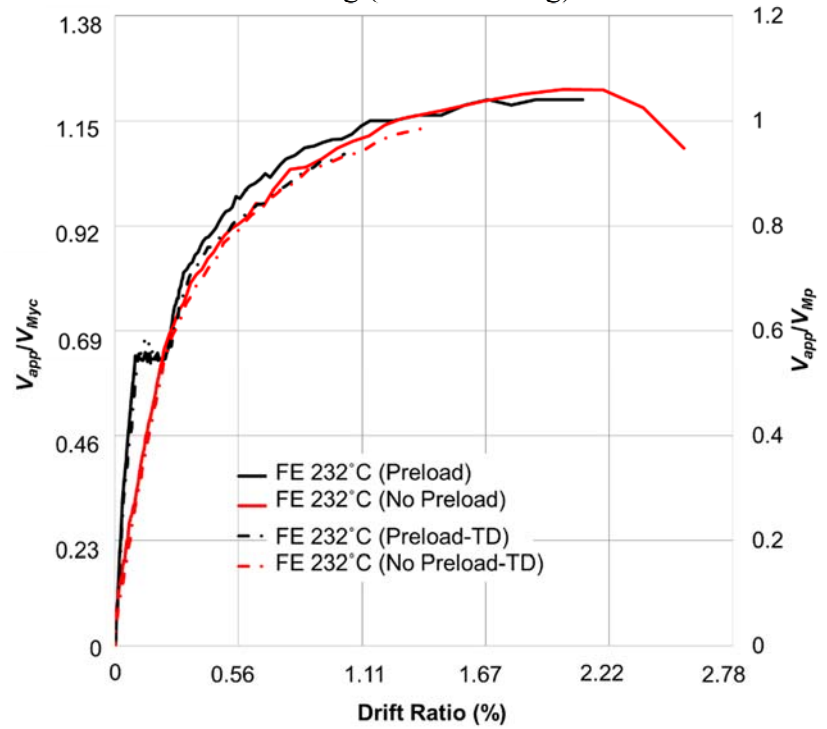
Figure 8.44 SC-WP-H: Comparison of FE backbone curves for cases with and without temperature dependent (TD) elastic moduli
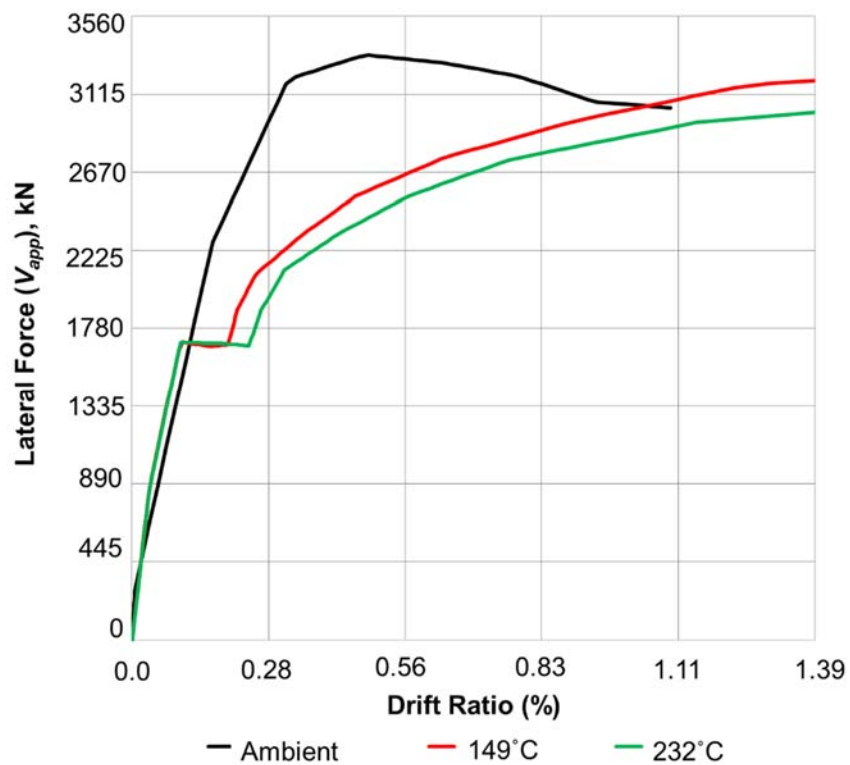
Figure 8.45 SC-WP-H: FE model overall force drift response
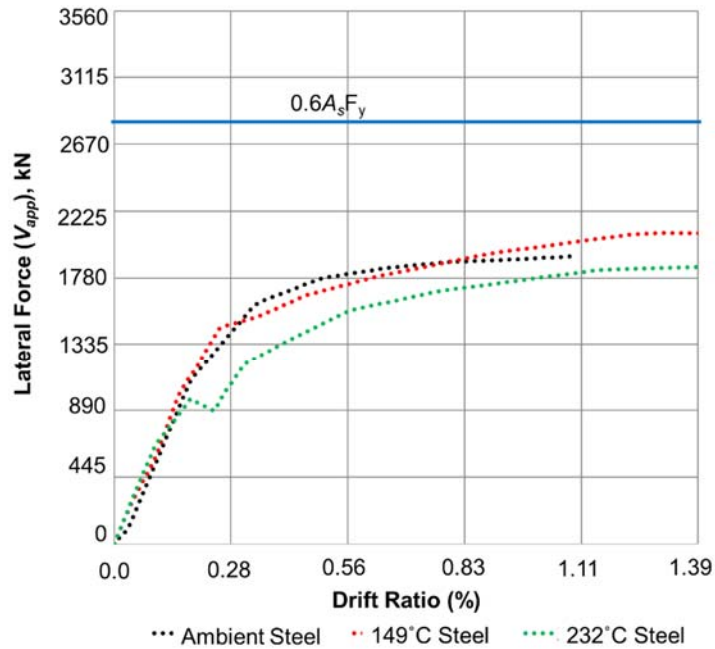
Figure 8.46 SC-WP-H: FE model comparison of lateral force resisted by steel faceplates
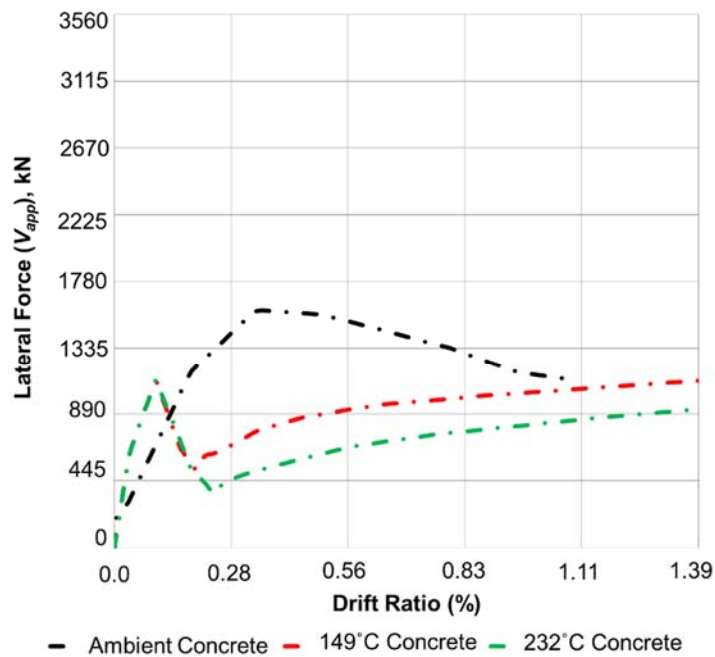
Figure 8.47 SC-WP-H: FE model comparison of lateral force resisted by concrete infill
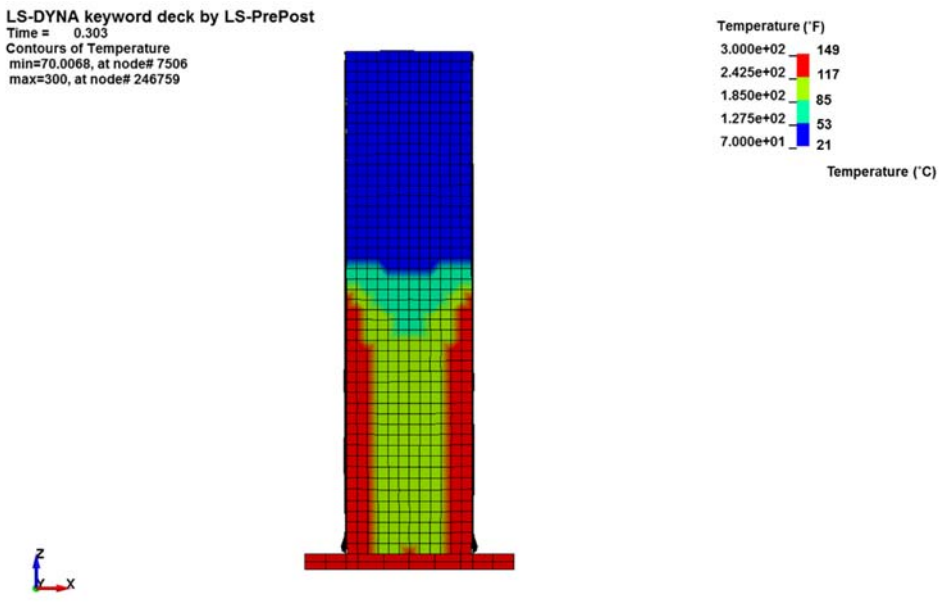
a) Temperature profile at peak load
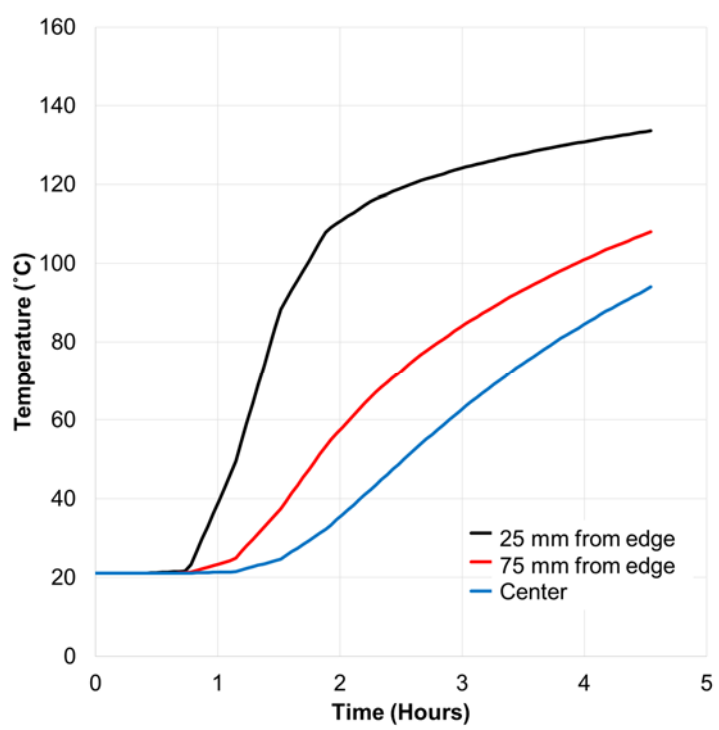
b) Evolution of temperature through the thickness

Figure 8.48 SC-WP-H: FE model temperature distribution for surface at 149˚C
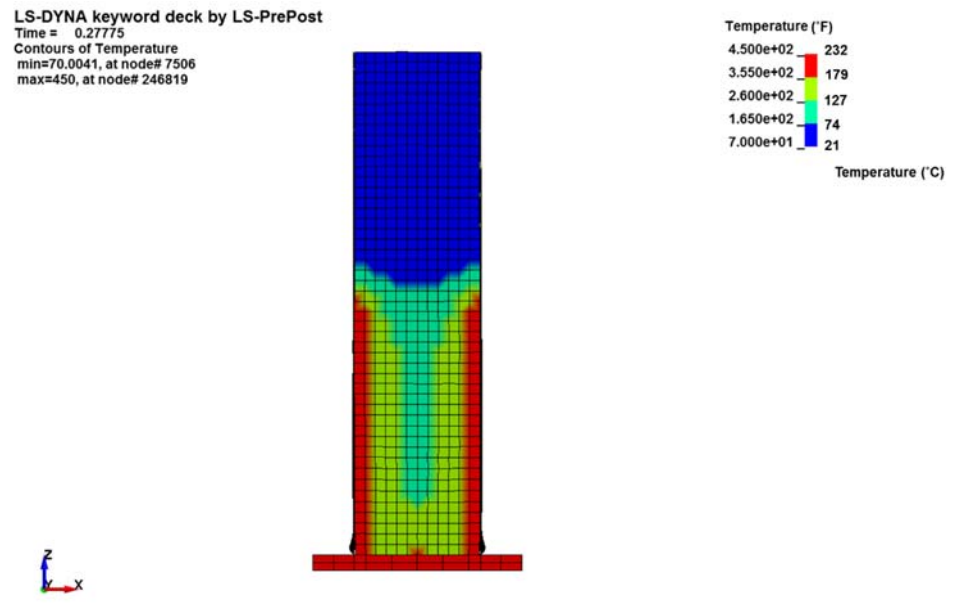
a) Temperature profile at peak load
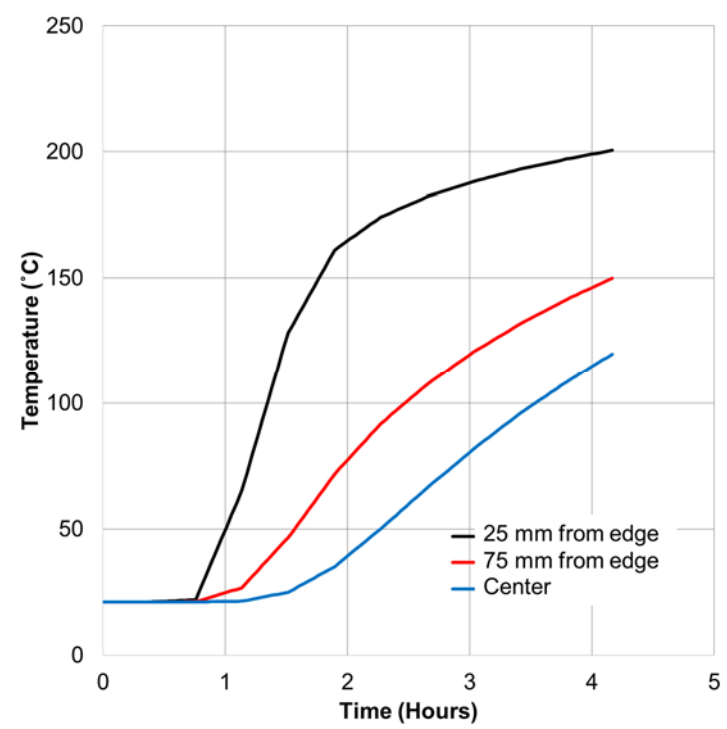
b) Evolution of temperature through the thickness

Figure 8.49 SC-WP-H: FE model temperature distribution for surface at 232˚C

LS-DYNA keyword deck by LS-PrePost
Time =   0.101
Contours of Mean Ipt Max Prin Strain
  min=-9.22565e-06, at elem# 29881
  max=0.0436969, at elem# 17309
Number of elements cracked=6161

Mean Ipt Max Prin Strain
2.000e-03
1.500e-03
1.000e-03
5.000e-04
0.000e+00

a)   Surface temperature of 149˚C

Time =   0.101
Contours of Mean Ipt Max Prin Strain
  min=-1.42734e-05, at elem# 30887
  max=0.0517243, at elem# 17302
Number of elements cracked=11996

Mean Ipt Max Prin Strain
2.000e-03
1.500e-03
1.000e-03
5.000e-04
0.000e+00

b)   Surface temperature of 232˚C

Figure 8.50 SC-WP-H: Concrete cracking at 45 minutes of heating for FE models with no pre-loading
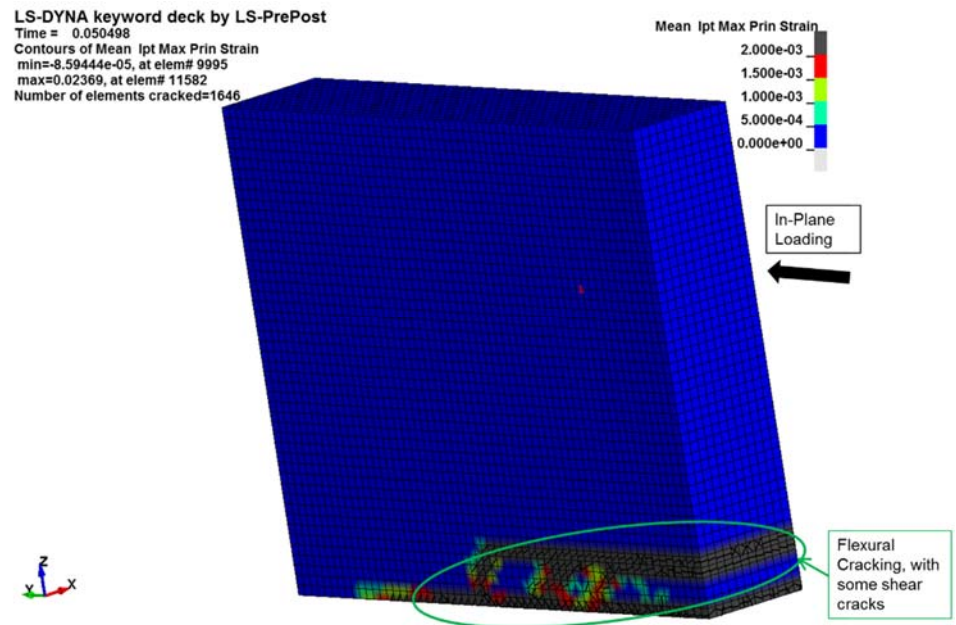
a) Before heating (Lateral load of 0.54 V_{Mp})
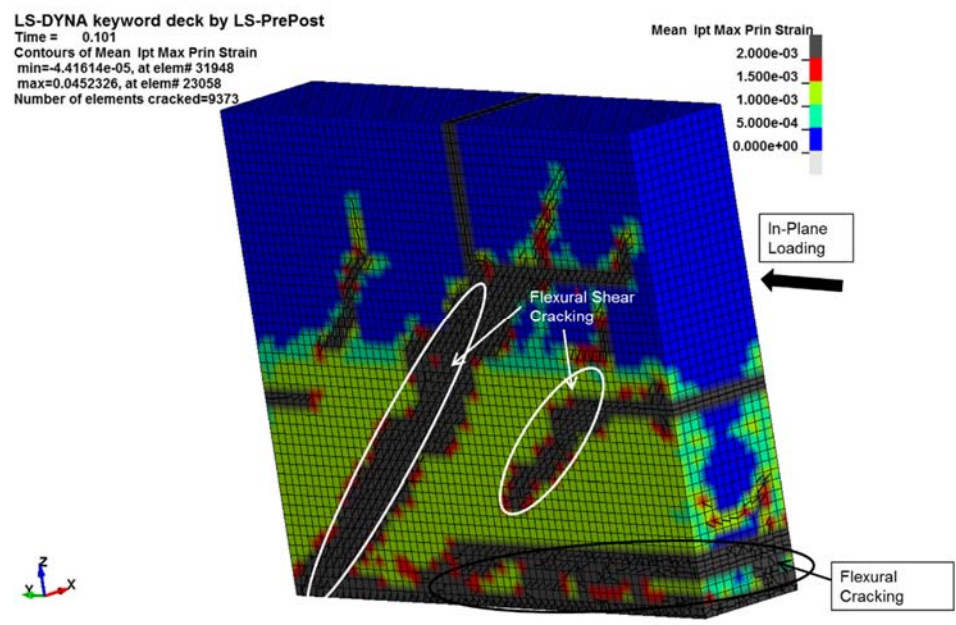
b) At 45 minutes of heating (Lateral load of 0.54 V_{Mp})

Figure 8.51 SC-WP-H: Concrete cracking for FE models with pre-loading and surface temperature of 149˚C
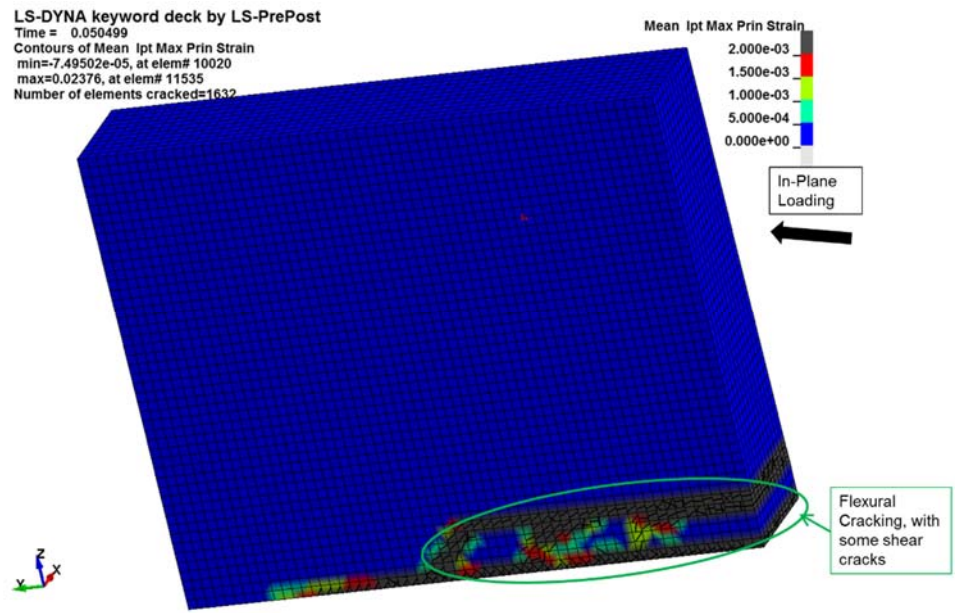
a) Before heating (Lateral load of 0.54 V_{Mp})
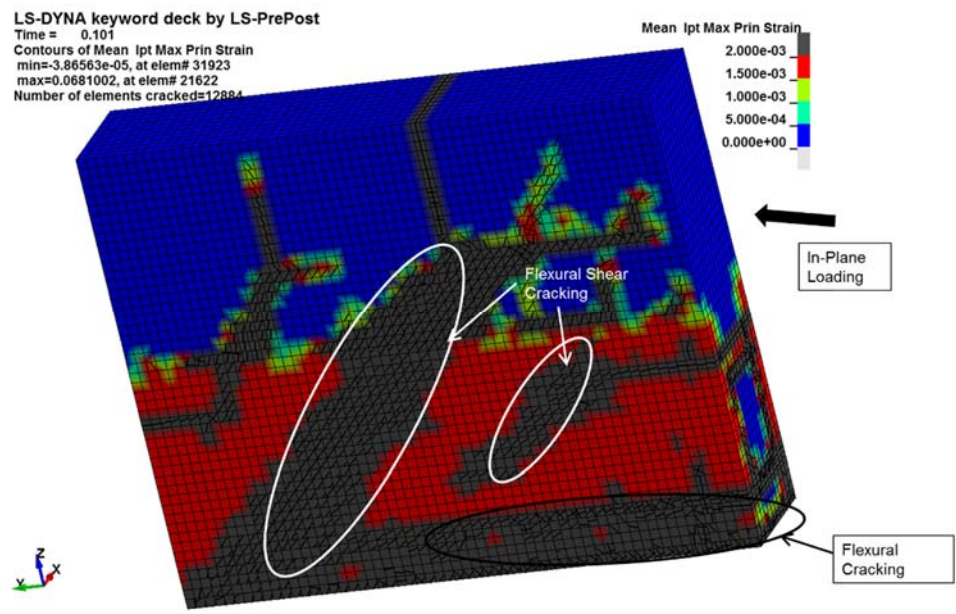
b) At 45 minutes of heating (Lateral load of 0.54 V_{Mp})

Figure 8.52 SC-WP-H: Concrete cracking for FE models with pre-loading and surface temperature of 232˚C
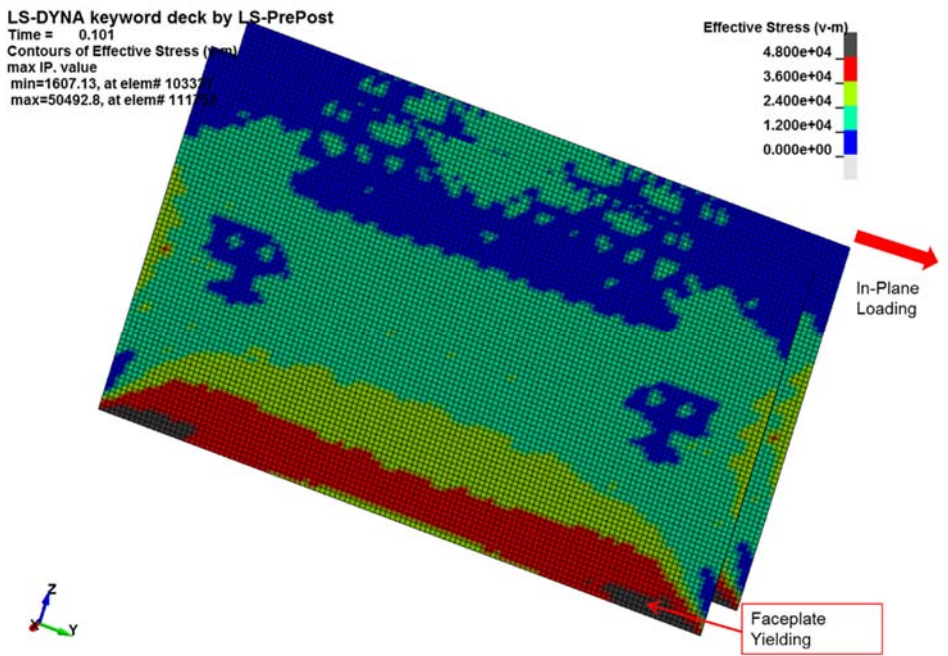
a) At 45 minutes of heating
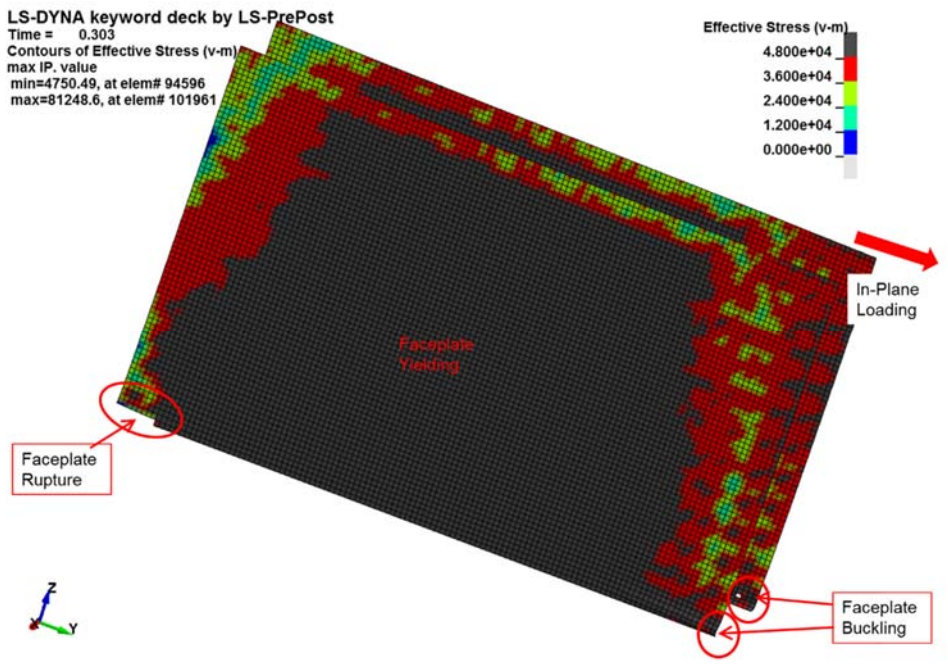
b) At failure

Figure 8.53 SC-WP-H: Faceplate Von-Mises stresses for FE model with no pre-loading and surface temperature of 149°C (in psi units, 1 psi=6.9 kPa)
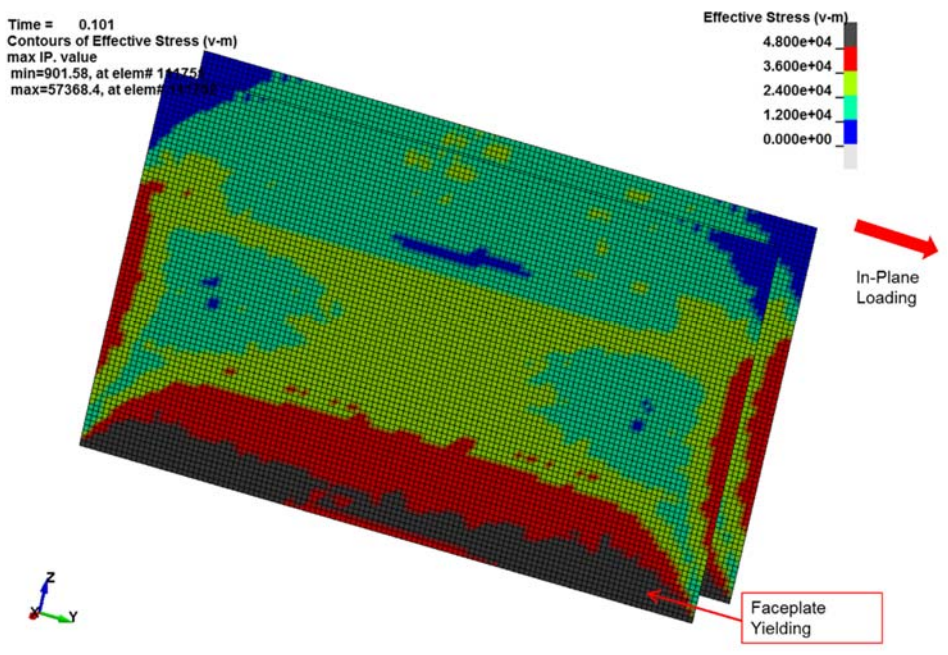
a) At 45 minutes of heating
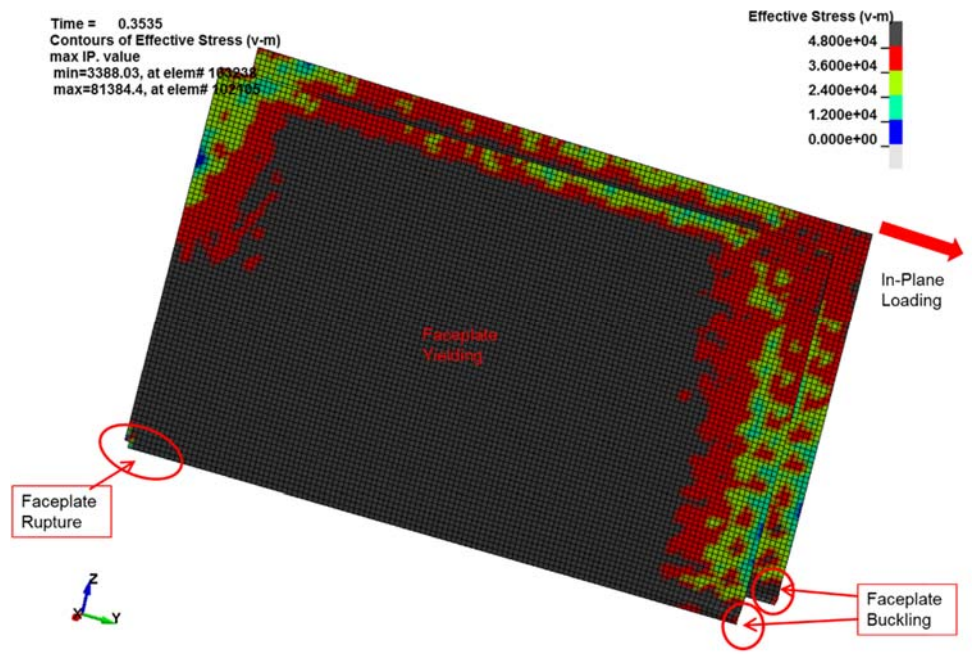
b) At failure

Figure 8.54 SC-WP-H: Faceplate Von-Mises stresses for FE model with no pre-loading and surface temperature of 232˚C (in psi units, 1 psi=6.9 kPa)
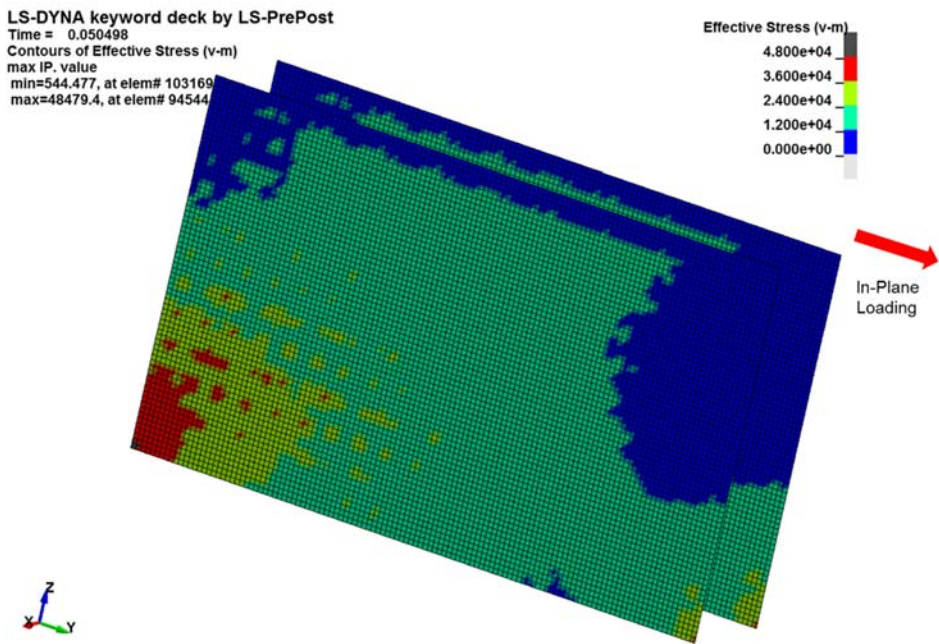
a) Before heating (Lateral load of 0.54 V_{Mp})
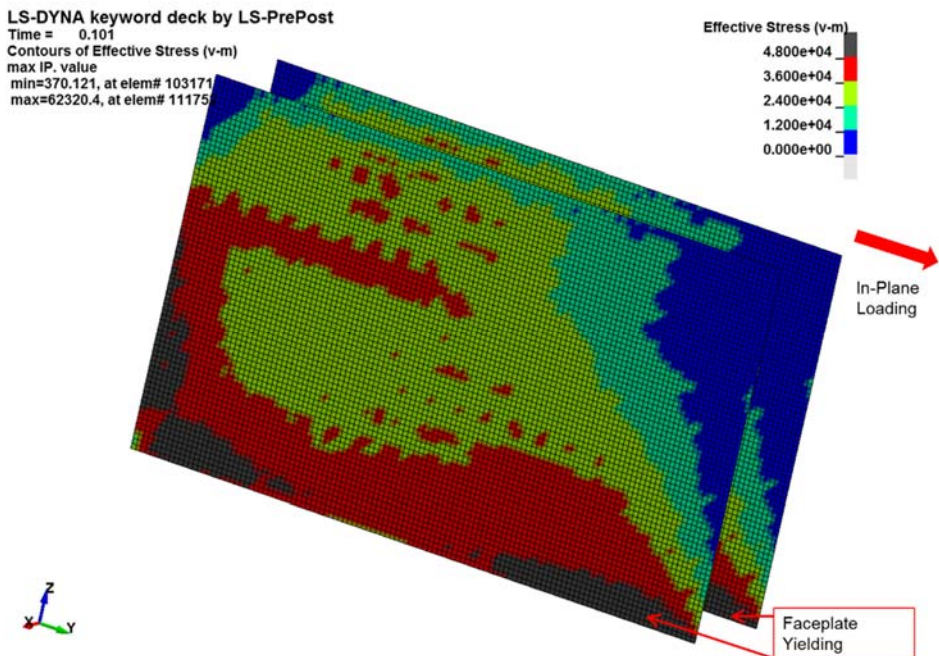
b) At 45 minutes of heating (Lateral load of 0.54 V_{Mp})

Figure 8.55 SC-WP-H: Faceplate Von-Mises stress for FE models with pre-loading and surface temperature of 149°C (in psi units, 1 psi=6.9 kPa)
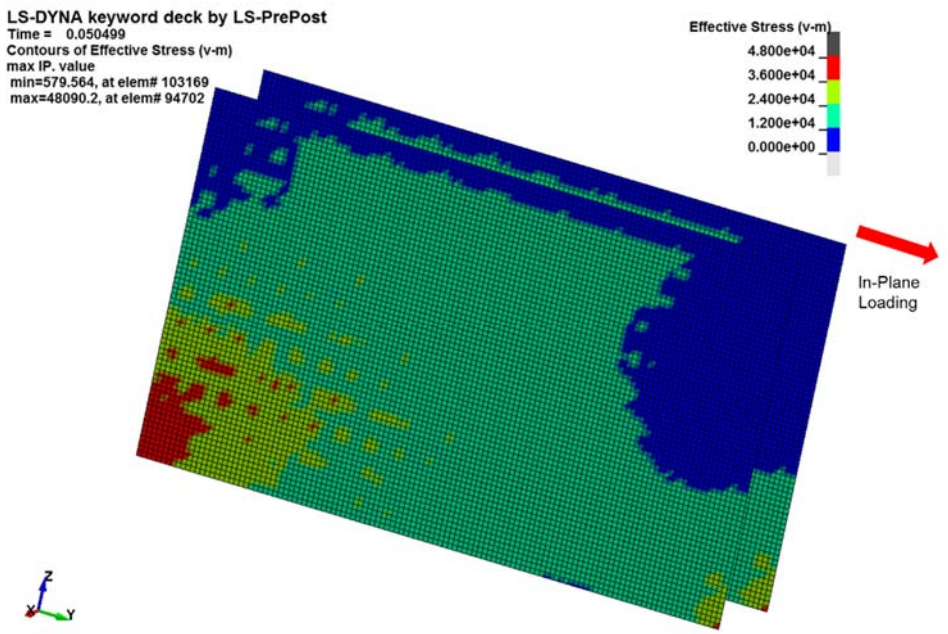
a) Before heating (Lateral load of 0.54 V_{Mp})
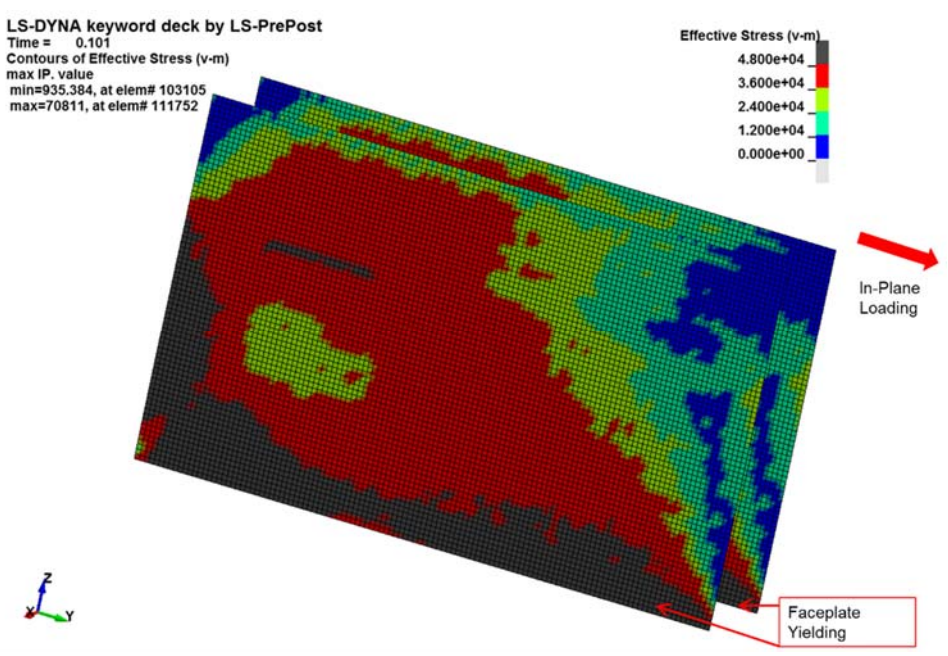
b) At 45 minutes of heating (Lateral load of 0.54 V_{Mp})

Figure 8.56 SC-WP-H: Faceplate Von-Mises stress for FE models with pre-loading and surface temperature of 232˚C (in psi units, 1 psi=6.9 kPa)
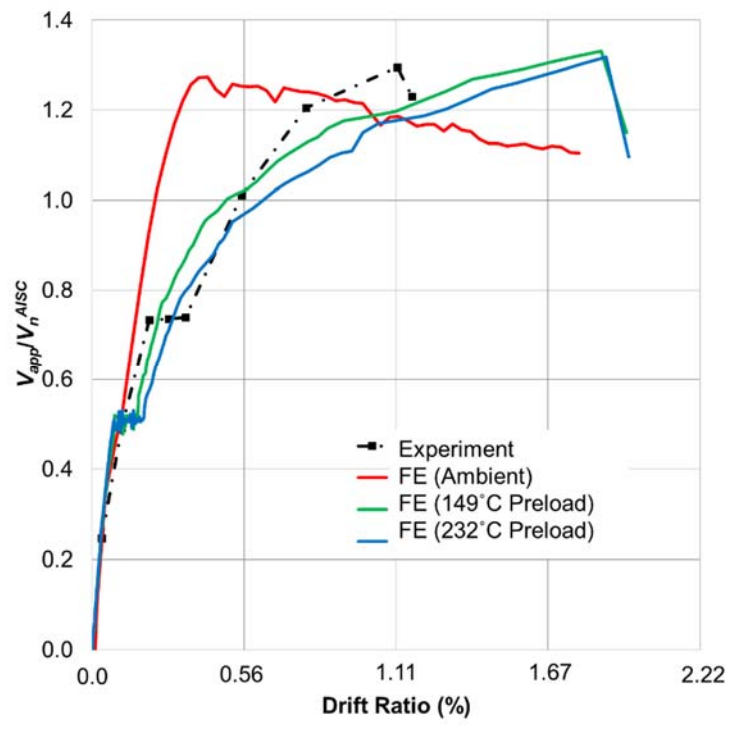
Figure 8.57 SC-W-H: Comparison of experimental and finite element backbone curves
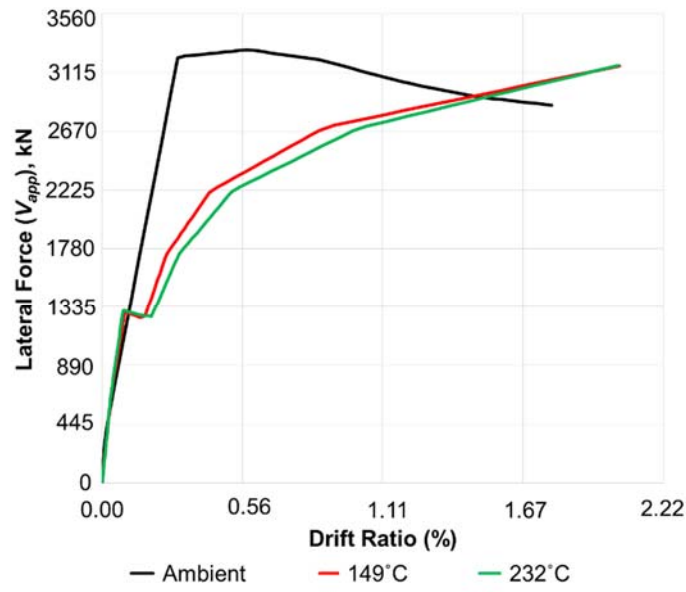
Figure 8.58 SC-W-H: FE model overall force drift response
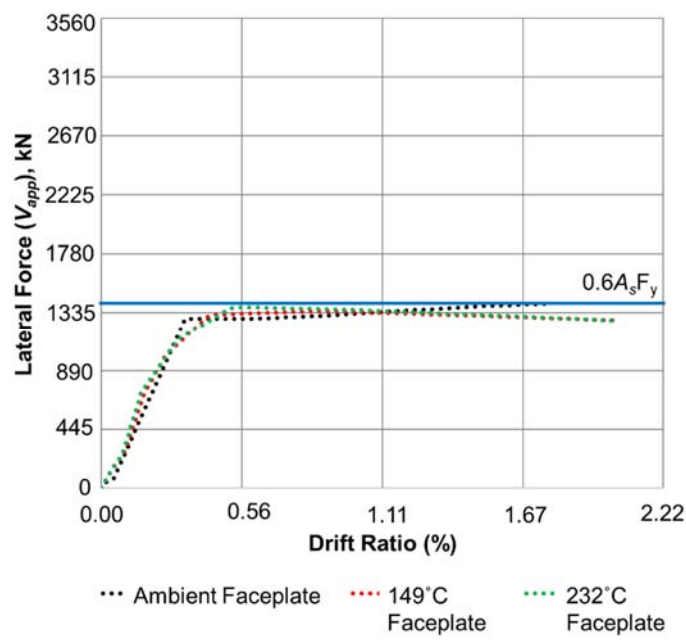
Figure 8.59 SC-W-H: FE model comparison of lateral force resisted by steel faceplates
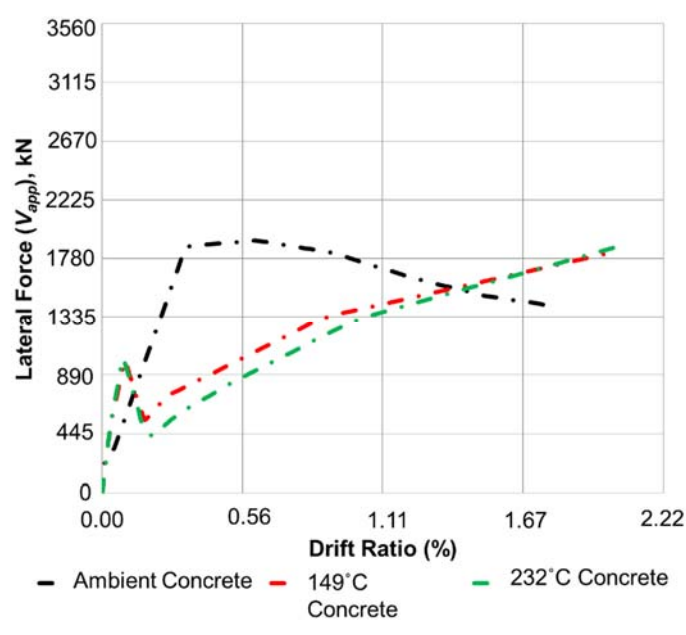
Figure 8.60 SC-WP-H: FE model comparison of lateral force resisted by concrete infill
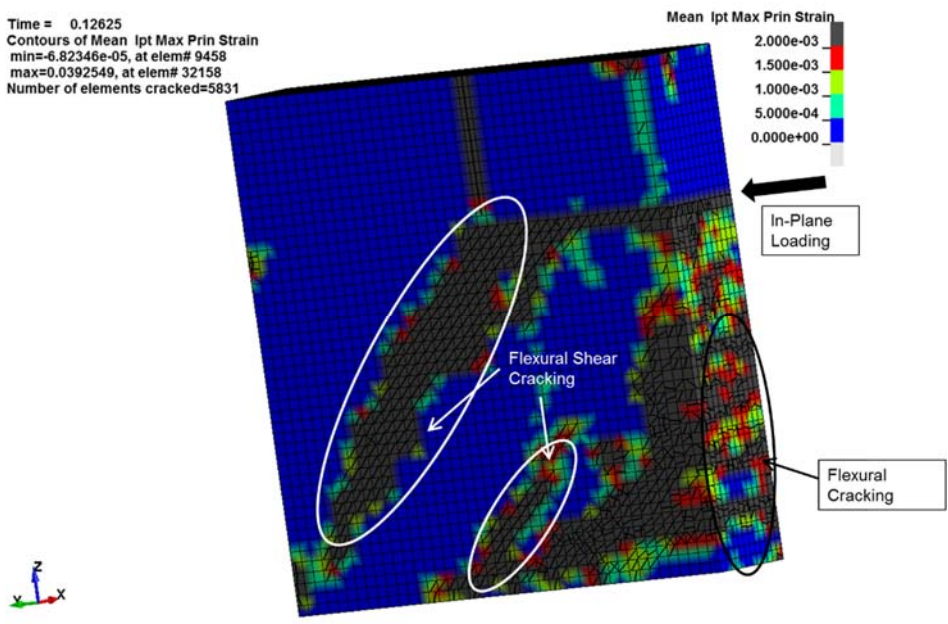
a) Concrete infill
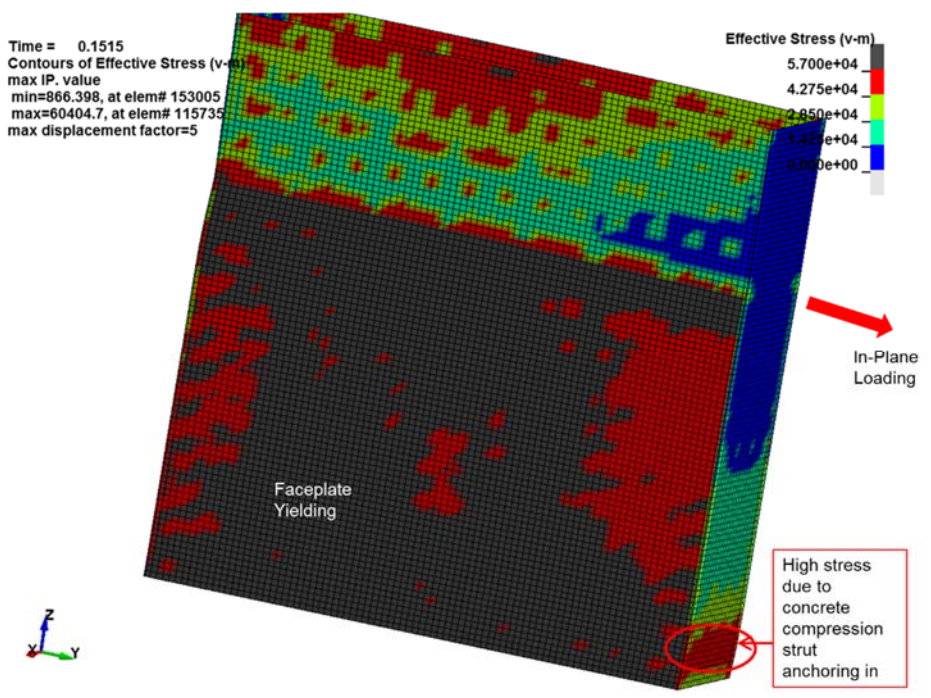
b) Steel plates

Figure 8.61 SC-W-H: Ambient FE model state at lateral force close to peak load (3070-kN), in psi units (1psi=6.95kPa)
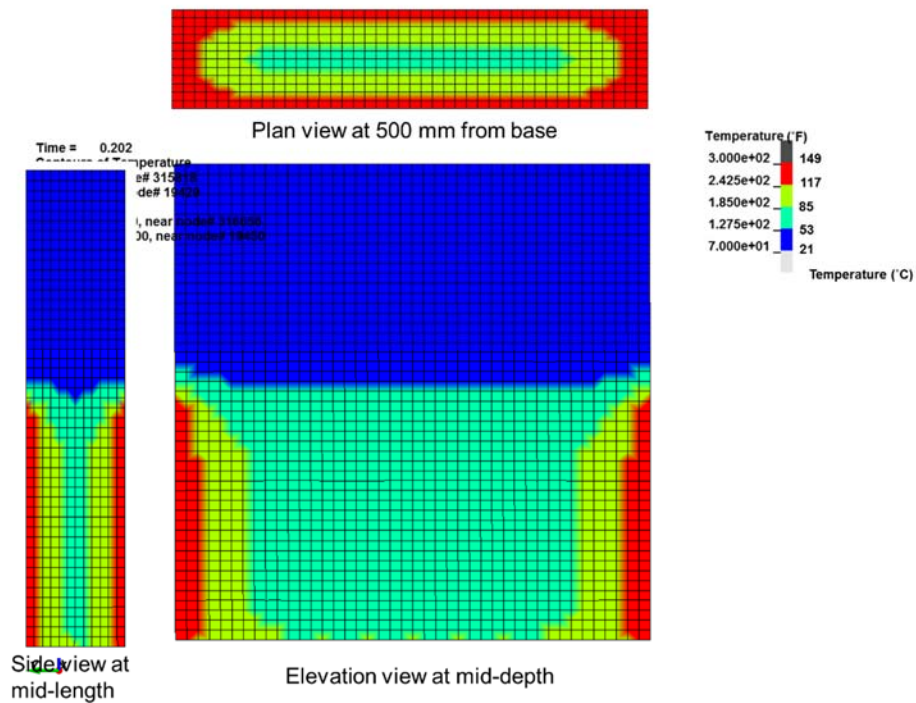
a) Surface temperature of 149°C
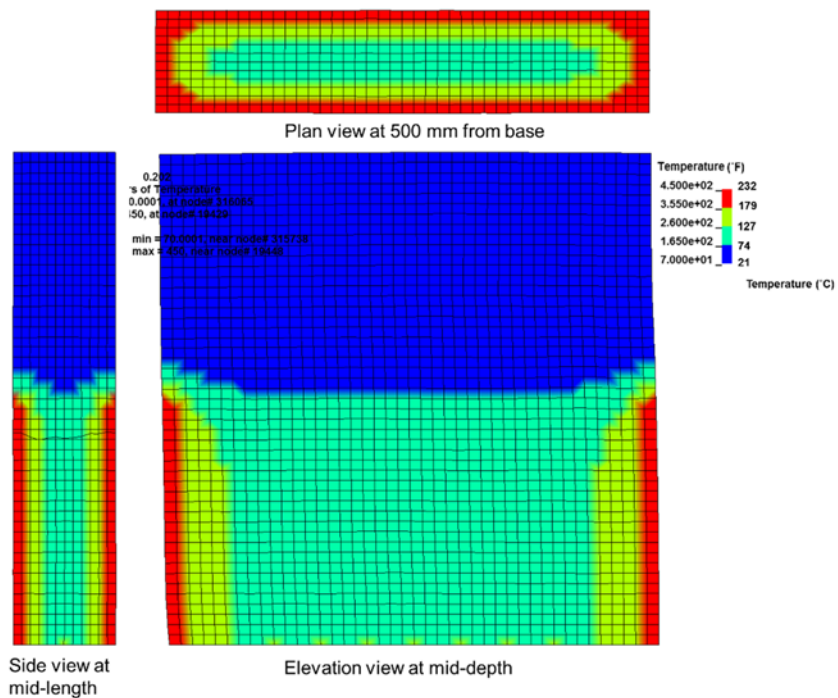
b) Surface temperature of 232°C

Figure 8.62 SC-W-H: Temperature profile for FE models at peak load
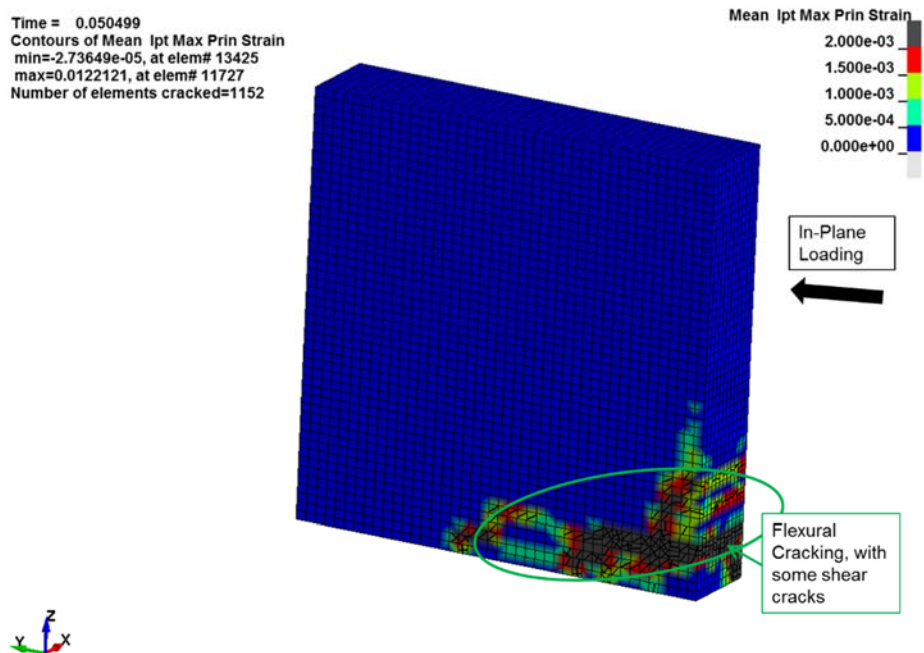
a) Before heating (Lateral load of 0.50 V_n^{AISC})
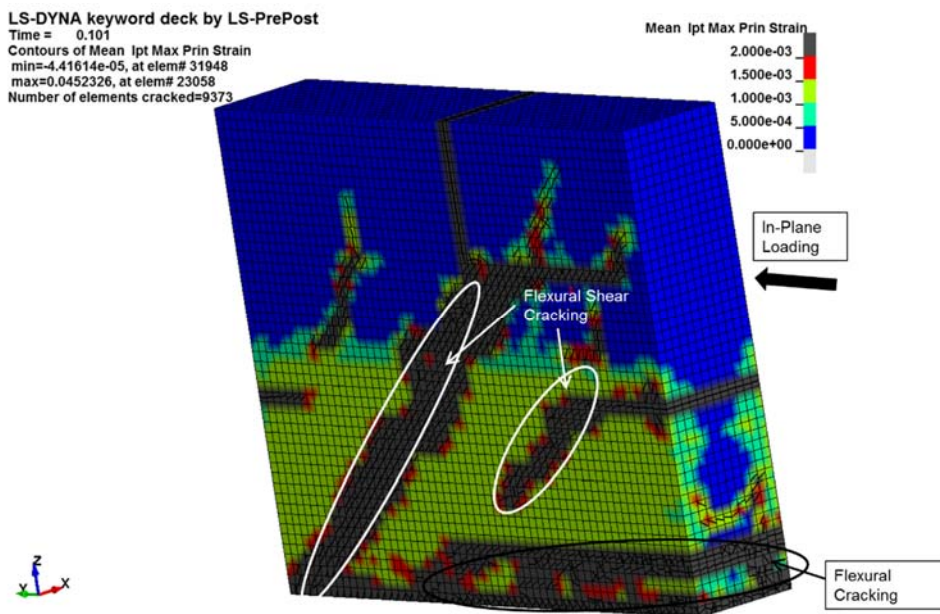
b) At 45 minutes of heating (Lateral load of 0.50 V_n^{AISC})

Figure 8.63 SC-W-H: Concrete cracking for FE models with pre-loading and surface temperature of 149°C (in psi units, 1 psi=6.9 kPa)

Time = 0.050499
Contours of Mean Ipt Max Prin Strain
min=-4.36556e-06, at elem# 136298
max=0.0119145, at elem# 11778
Number of elements cracked=1027

Mean Ipt Max Prin Strain
2.000e-03
1.500e-03
1.000e-03
5.000e-04
0.000e+00

In-Plane Loading

Flexural Cracking, with some shear cracks

a) Before heating (Lateral load of 0.50 V_n^{AISC})

Time = 0.101
Contours of Mean Ipt Max Prin Strain
min=-4.4603e-06, at elem# 136843
max=0.0275954, at elem# 12069
Number of elements cracked=12336

Mean Ipt Max Prin Strain
2.000e-03
1.500e-03
1.000e-03
5.000e-04
0.000e+00

Extensive Shear Cracking

In-Plane Loading

Extensive Flexural-shear Cracking

b) At 45 minutes of heating (Lateral load of 0.50 V_n^{AISC})

Figure 8.64 SC-W-H: Concrete cracking for FE models with pre-loading and surface temperature of 232°C (in psi units, 1 psi=6.9 kPa)
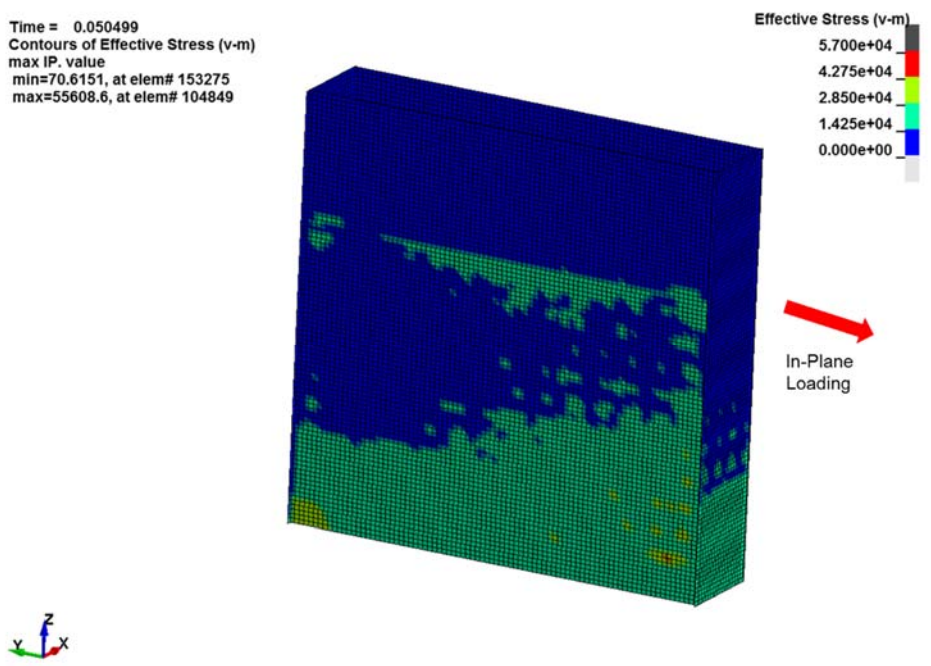
a) Before heating (Lateral load of 0.50 V_n^{AISC})
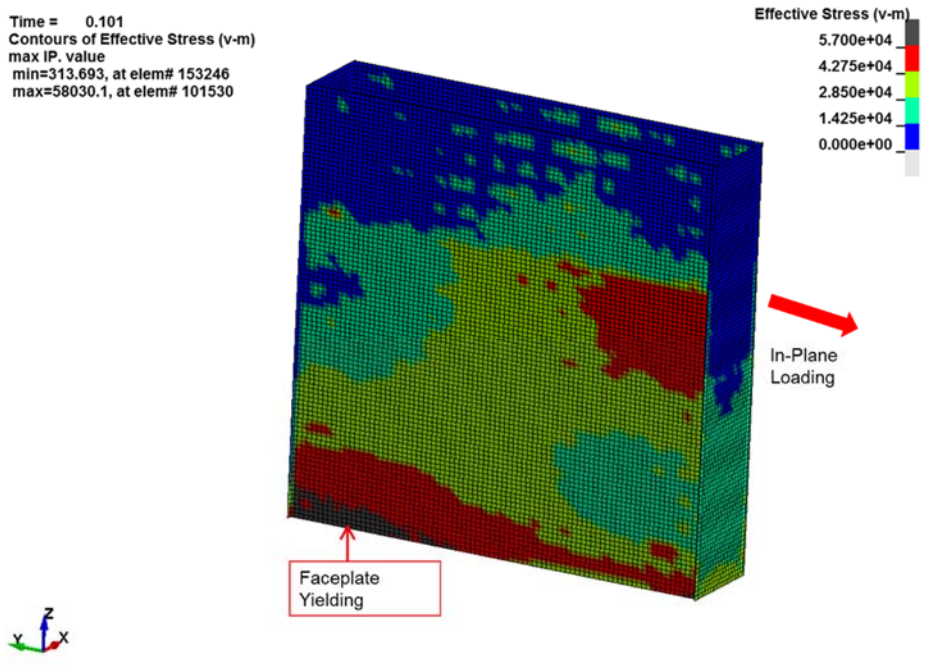
b) At 45 minutes of heating (Lateral load of 0.50 V_n^{AISC})

Figure 8.65 SC-W-H: Faceplate Von-Mises stress for FE models with pre-loading and surface temperature of 149˚C (in psi units, 1 psi=6.9 kPa)
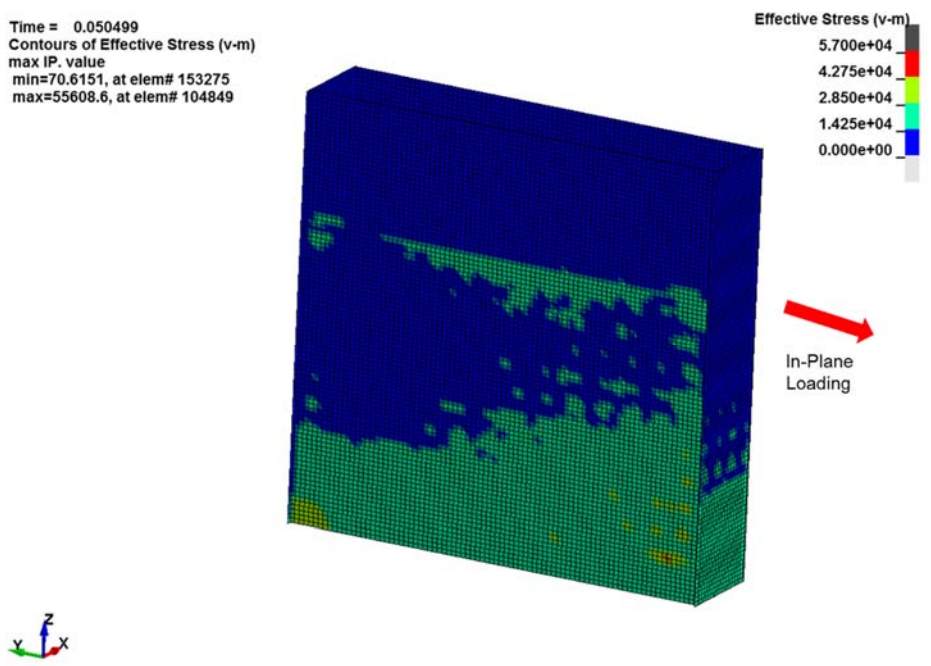
a) Before heating (Lateral load of 0.50 V_n^{AISC})
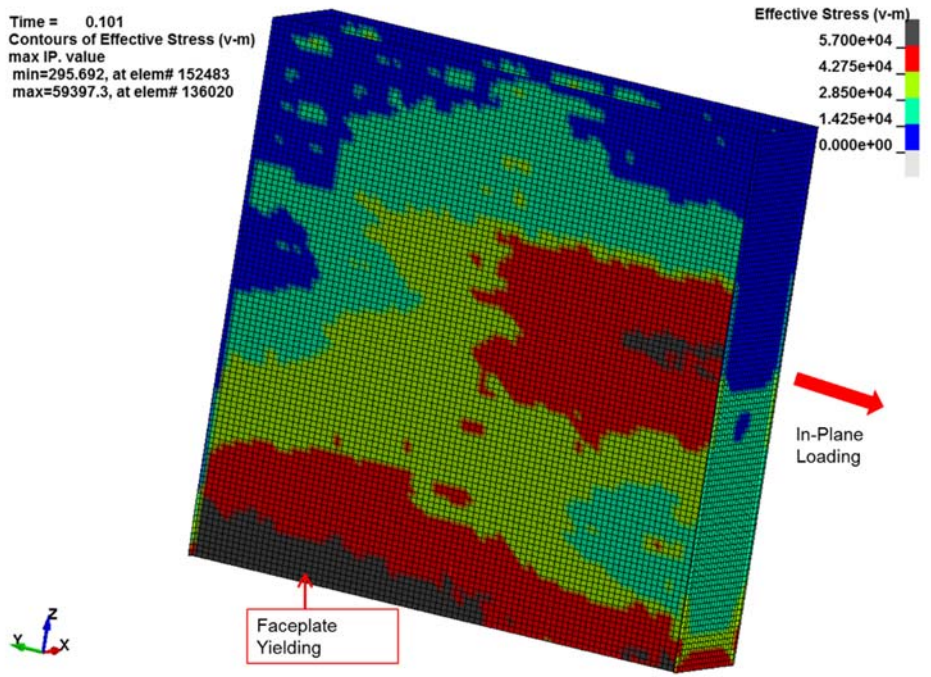
b) At 45 minutes of heating (Lateral load of 0.50 V_n^{AISC})

Figure 8.66 SC-W-H: Faceplate Von-Mises stress for FE models with pre-loading and surface temperature of 232˚C (in psi units, 1 psi=6.9 kPa)
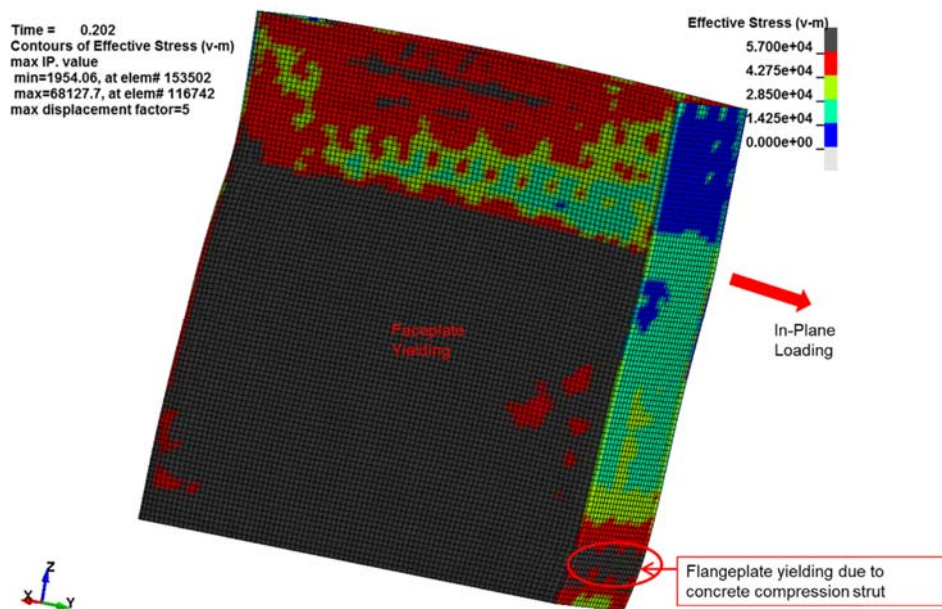
a)   Surface temperature of 149˚C
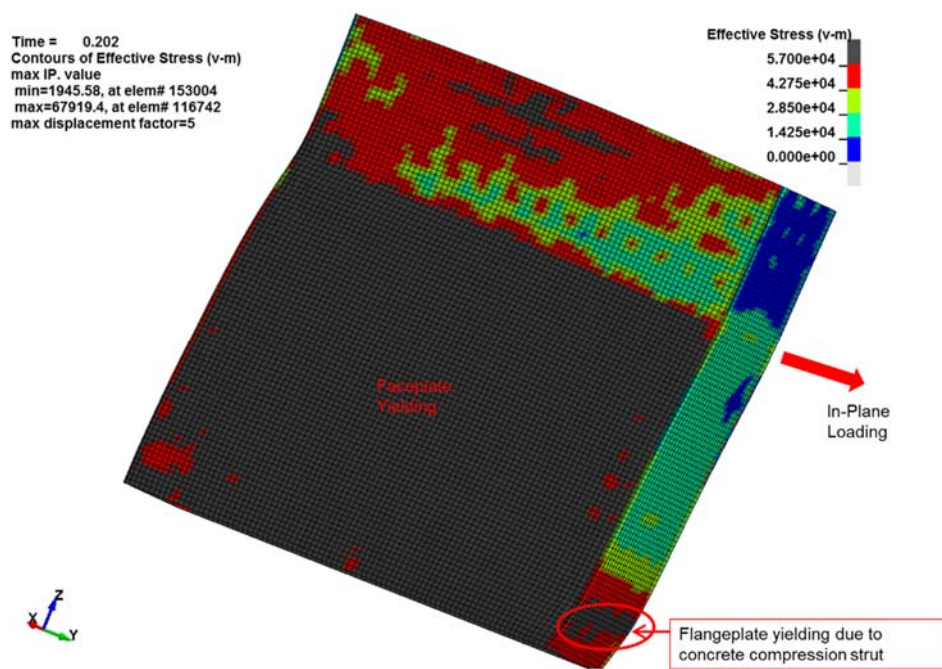
b)   Surface temperature of 232˚C

Figure 8.67 SC-W-H: Faceplate Von-Mises stress at peak load for FE models with pre-loading
(in psi units, 1 psi=6.9 kPa)

9. SUMMARY, CONCLUSIONS, RECOMMENDATIONS, LIMITATIONS AND DIRECTIONS FOR FUTURE RESEARCH

This chapter summarizes the research presented in this dissertation. Conclusions and recommendations based on the experimental and numerical observations are enlisted. In the end, directions for future research are described.

9.1 Summary

SC walls (with boundary elements) and wall piers (without boundary elements) may be subjected to a combination of demands due to cascading hazards. This dissertation presents research conducted to evaluate the in-plane response of SC structures subjected to out-of-plane and accident thermal loading. Two series of experimental and numerical studies were conducted.

9.1.1 Experimental Investigations

First series of experiments comprised of four SC wall pier specimens. One control specimen was subjected to in-plane loading (no out-of-plane loading). Three specimens were subjected to different magnitudes of out-of-plane loading in combination with in-plane loading. The test matrix was designed to evaluate the effect of magnitude of out-of-plane loading, and tie spacing on the in-plane response of wall piers. The test setup was designed based on the magnitude of out-of-plane force and expected the in-plane strength of the specimens. Clevises with press-fit spherical plain bearings were designed and fabricated to enable orthogonal deformations of the specimens without resulting in stresses in the loading rams. Biaxially loaded specimens were subjected to incremental cyclic out-of-plane loading till the desired out-of-plane force magnitude was achieved. The out-of-plane force magnitude was then maintained, and incremental in-plane cyclic loading was applied up to failure.

Experimental results indicate that the in-plane response of wall piers with aspect ratios greater than or equal to 0.6 was flexure dominated, with specimens failing due to excessive faceplate yielding, compression buckling, and concrete spalling. Introducing an out-of-plane force resulted in out-of-plane shear and moment in the wall piers. The out-of-plane response of wall pier specimens was flexure controlled with concrete cracking. Out-of-plane flexural stiffness can be reasonably estimated using the provisions of AISC N690s1. Diagonal shear cracking of the wall piers depended on the magnitude of out-of-plane force in comparison to concrete contribution to shear strength (V_c). SC wall pier with ties spaced at half the section thickness developed diagonal shear cracks when subjected to out-of-plane shear equal to the nominal shear strength. No diagonal shear cracking was observed for wall pier specimen with ties spaced at section thickness and subjected to out-of-plane shear equal to nominal shear strength. Wall piers subjected to out-of-plane shear equal to their nominal shear strength (per US codes) develop flexural yielding and failure due to the interaction between the in-plane and out-of-plane moments. Shear failure does not occur for these wall piers. The in-plane flexural strength of the specimens was influenced by the magnitude of out-of-plane moments. The wall pier specimen subjected to an out-of-plane shear force that is 2.5 times the nominal shear strength (per US codes) was forced into a shear failure mode by the interaction of in-plane shear and out-of-plane shear. Specimens subjected to biaxial loading exhibited asymmetric response with the twisting of the specimens, and tie rupture for SC-0.5T-Vn. The second series of experiments involved subjecting one SC wall and one SC wall pier specimen to different magnitudes and durations of accident temperatures in combination with in-plane loading. Control specimen for the first series of tests was also used as control wall pier specimen for this series. The test matrix was designed to evaluate the effect of magnitude and duration of accident temperatures on the in-plane response of wall piers. Wall pier specimen was designed to

have a flexure-controlled response (aspect ratio of 0.6). The wall specimen was designed to undergo in-plane shear failure. Two temperature magnitudes (149°C and 232°C) and two heating durations (1-hour and 3 hours) were selected. The specimens were subjected to heating and loading cycles. SC wall pier specimen was subjected to heating on the faceplates. SC wall specimen was subjected to heating on the faceplates (web plate) and flangeplates. The test setup was designed based on the expected in-plane capacity of the specimens. Accident thermal loading was applied using high-temperature ceramic-fiber radiant heating panels. Each heater was controlled individually and operated on a feedback control loop that referenced a thermocouple attached to the heated surface of the specimens. Surface thermocouples and through-thickness thermocouple trees were used to obtain the evolution of thermal gradient in specimens with time.

Experimental results indicate that accident thermal loading resulted in non-linear thermal gradients through the thickness of the specimens. The non-linearity of thermal gradients was higher for higher surface temperatures. The gradient reduced as the duration of heating increased. The measured in-plane strength of heated wall pier specimen was 1.25 times the in-plane force corresponding to compression yield moment capacity. Similarly, the measured in-plane strength of heated wall specimen was 1.29 times the nominal in-plane shear strength (using measured properties) per AISC N690s1. Therefore, typical accident thermal temperatures do not significantly reduce the strength of SC walls. The strength can be calculated using current strength equations (per US codes) for ambient temperatures.

However, non-linear thermal gradients lead to concrete cracking due to external and self-restraint. Concrete cracking results in significant reduction in the stiffness of SC walls. The extent of the reduction in stiffness depends on the temperature magnitude and duration of the thermal accident. Secant stiffness (and shear stiffness) of SC wall specimen reduces by about 25% for 149°C and

40% for 232˚C, in comparison to secant (and shear) stiffness at ambient temperatures. For SC wall piers, the reduction is about 20% for 149˚C and 40% for 232˚C. The in-plane shear and flexural stiffnesses of SC walls can be considered to linearly reduce from cracked stiffness to steel only (fully cracked) stiffness for temperature increments (ΔT) of 0˚C to 150˚C. The recommended stiffnesses compare reasonably with experimentally observed stiffness for heated cycles. Since the recommendations provide a lower bound stiffness, they eliminate the need for considering temperature-dependent properties for typical accident temperatures.

9.1.2   Numerical Investigations

Results from the first series of experiments (SC wall piers subjected to a combination of in-plane and out-of-plane loadings) indicated a biaxial flexure interaction exists for SC wall piers. A finite-difference based cross-section fiber analysis model was developed for evaluating axial force-biaxial moment-shear interaction for SC wall piers. The model iteratively establishes equilibrium for axial forces and biaxial moments. Shear interaction is considered by incorporating Mohr-Coulomb based shear failure for concrete and Von-Mises yielding for steel. The model was validated using experimental results for wall pier specimens subjected to biaxial loadings. *P-M* interaction for wall piers is evaluated using the fiber model. The biaxial moment interaction was updated to consider *P-M* interaction. A tri-linear design interaction for biaxial moments was developed. The design interaction surface compares conservatively with fiber model, finite element model results, and experimental results. For shear controlled SC wall piers, the biaxial interaction surface is updated to consider vector shear failure of concrete, and Von-Mises yielding of faceplates. The fiber model can be employed to obtain axial force-biaxial moment-shear interaction for SC wall piers.

Three-dimensional finite element models were also developed to simulate the two series of experiments. FE models for biaxially loaded SC wall pier specimens agreed favorably with experimental results. The FE peak strengths were within 5% of the experimental strengths. Monotonically loaded FE models had a marginally stiffer response in comparison to experiments. The response of FE wall pier models was flexure controlled, and the models (except SC-T-2.5Vn) reached their compression yield moment capacity, V_{Myc}. Specimen SC-T-2.5Vn failed in vector shear due to the magnitude of out-of-plane force being 2.5 times the out-of-plane strength. Flexural yielding and buckling of the faceplates were observed in the models. The low aspect ratio of the specimen enabled the concrete compression strut to form. However, the compression strut cannot anchor in at the base, and therefore its effectiveness would be limited.

FE analyses for SC wall pier and wall specimens subjected to combined in-plane and accident thermal loading results agreed reasonably with experiments. The ambient stiffness of SC wall FE models compared well with experimentally observed stiffness. Ambient SC wall pier FE models marginally overestimated the stiffness in comparison to experimentally observed stiffness. SC wall pier FE models subjected to accident thermal loadings reached a peak strength marginally greater than the force corresponding to plastic moment capacity (V_{Mp}). SC wall models reached a peak strength of 1.30 times the nominal in-plane shear strength of the wall (V_n^{AISC}). Peak strengths for ambient and heated FE models were similar. The FE strengths were within 5% of the experimentally observed strengths. Accident thermal loads resulted in significant reduction in the stiffness. Reduced stiffness led to heated FE models reaching peak strengths at drift ratios significantly larger than that for ambient FE models. The magnitude of reduction in stiffness observed in FE models was consistent with that observed in the experiments. Reduction in stiffness is primarily due to cracking of concrete caused by non-linear thermal gradient through the cross-

section of the wall. Concrete cracking results in reduced contribution of concrete to lateral strength, which increases the stress in steel at similar force levels. This may hasten the steel yielding in SC walls and wall piers.

Since the FE model results are consistent with experiments, these benchmarked models can be used to conduct parametric studies and further validate the recommendations provided (based on experimental results).

9.2   Conclusions

The following conclusions are drawn based on the experiments, finite element analysis, and fiber analysis for SC wall pier specimens subjected to combined in-plane and out-of-plane loading.

1. In-plane response of SC wall piers with aspect ratio greater than or equal to 0.6 is flexure controlled. Nominal in-plane strength of SC wall piers can be calculated as the lateral force corresponding to initiation of compression yielding in the faceplates (V_{Myc}).

2. SC wall pier failure for combined in-plane and out-of-plane loadings is due to interaction of in-plane and out-of-plane flexure. Biaxial moment interaction needs to be considered in the design of SC wall piers.

3. SC wall pier specimen subjected to an out-of-plane force of magnitude 2.5 times its nominal out-of-plane strength failed in vector shear. For SC wall piers with shear dominated response (due to an in-plane aspect ratio less than 0.5, or high magnitude of out-of-plane shear), the biaxial moment interaction needs to account for vector shear failure of the wall piers.

4. Tie spacing plays an important role in the response of SC wall piers for biaxial loading once diagonal shear cracks form due to out-of-plane loads. Adequately designed ties spaced at half the section thickness can arrest the diagonal shear cracks. The wall pier would then

have a flexure controlled failure. However, ties spaced at section thickness do not provide adequate out-of-plane shear resistance. The wall pier may undergo a vector shear failure, with significant reduction in in-plane strength, and almost no post-peak response.

5. Biaxial loading results in an asymmetric response of the wall piers. There was extensive twisting and out-of-plane deformation of the specimens. The ties need to be adequately designed for additional forces due to this asymmetric response.

6. Out-of-plane flexural stiffness of SC wall piers can be estimated using the provisions of AISC N690s1. The stiffness will be uncracked or cracked-transformed depending on the magnitude of out-of-plane force.

7. In-plane stiffness of the wall piers can be reasonably estimated based on cracked flexural stiffness (calculated for neutral axis location corresponding to compression yield moment) and cracked shear stiffness (calculated as the sum of steel shear stiffness and 0.25 times the shear stiffness of uncracked portion of concrete).

8. A cross-section based fiber model can be employed to obtain the axial force-biaxial moment-shear interaction for SC wall piers. The model accounts for axial force-moment (*P-M*) interaction, vector shear failure of concrete, and Von-Mises yielding of faceplates. The design interaction recommended is conservative with respect to the fiber model, experiments, and finite element results.

9. FE model results for the specimens are consistent with experimental observations. The models reasonably predict the experimental strength and stiffness of the specimens. Stress states in steel and concrete, and failure modes of the specimens agree with those observed experimentally. The benchmarked finite element models can be employed to conduct parametric studies that will validate the recommendations based on experiments.

10. The test setup designed for experiments was successfully employed to apply high magnitudes of simultaneous orthogonal loading. The test setup can be used for testing RC shear walls or SC walls for biaxial loading.

The following conclusions are drawn based on the experiments and finite element analysis for SC wall and wall pier specimens subjected to combined in-plane and accident thermal loadings.

1. The nominal in-plane shear strength of SC walls at ambient temperatures can be conservatively estimated using the provisions of AISC N690s1. As discussed previously, the nominal in-plane strength of SC wall piers can be calculated as the lateral force corresponding to initiation of compression yielding in the faceplates (V_{Myc}).

2. Ambient secant stiffness of SC walls can be reasonably estimated considering cracked flexural (EI_{cr}) and shear stiffnesses (GA_{cr}). EI_{cr} can be calculated from the moment-curvature relationship, and GA_{cr} can be calculated as the tangent shear stiffness (GA_{cr}^{TAN}) based on composite plate theory.

3. Typical accident temperature loads for safety-related nuclear facilities range from 150˚C to 230˚C. Accident temperatures may be maintained for up to few days after the accident. Highly non-linear thermal gradients exist through the cross-section for first few hours after the accident. The extent of non-linearity reduces as concrete temperatures increase with time.

4. Typical accident temperatures and durations do not significantly reduce the strength of SC wall and wall piers. The strength for accident thermal loading combinations can be calculated using strength equations for ambient temperatures (discussed in Conclusion 1).

5. Typical accident temperatures and durations result in significant reduction in stiffness of walls and wall piers. The reduction is stiffness depends on the magnitude of surface

temperature. The SC wall pier specimen underwent secant stiffness reduction of 20% and 40% (in comparison to ambient secant stiffness) for surface temperatures of 149˚C and 232˚C. The corresponding reduction in secant stiffness (and shear stiffness) for SC wall was 25% for 149˚C and 40% for 232˚C.

6. Reduction in stiffness of wall structures is primarily caused by cracking of concrete due to non-linear thermal gradients. Concrete cracking results in higher stress in steel plates, which may hasten the yielding of steel plates.

7. The effect of accident thermal temperatures on specimen stiffness can be addressed by calculating effective flexure and shear stiffnesses. The effective stiffnesses can be assumed to linearly reduce from cracked stiffness to steel-only stiffness for surface temperature change (ΔT) from 0˚C to 150˚C.

8. Concrete cracking pattern due to thermal loads depends on the pre-existing cracks. If there are no pre-existing cracks, concrete would crack symmetrically in regions with no external restraints. Typically, structures subjected to thermal loads will be pre-cracked, in which case thermally induced cracking will be along the pre-cracks and high-stress regions.

9. The test setup designed for experiments was successfully employed to apply simultaneous thermal and mechanical loading. Since the heaters are capable of simulating fire temperatures, the setup can be used to conduct fire tests on SC walls. Fire or thermal tests can also be conducted for RC walls or beams.

9.3   Analysis and Design Recommendations

Typical analysis procedures in the industry employ elastic finite element models to obtain the design demands for the structure. The model parameters are calibrated to match the model stiffness with an effective stiffness value. The effective stiffness value is generally provided in codes and

specifications or may be obtained from experimental studies or benchmarked non-linear finite element models. Demands obtained from finite element analysis are compared with design strengths. Biaxial interaction and effect of thermal loads need to be considered while calculating design strength. Based on the experimental results, stiffness and strength recommendations for walls and wall piers are provided in this section. These recommendations compare favorably with experimental and numerical investigations presented in this dissertation. However, further research is needed to confirm the validity of these recommendations for a range of parameters not considered in this research.

9.3.1 Out-of-plane Flexural Stiffness (EI_{eff}^{oop})

Effective out-of-plane flexural stiffness for SC walls and wall piers can be reasonably estimated using the provisions of AISC N690s1.

9.3.2 In-plane Flexural Stiffness (EI_{eff}^{ip})

EI_{eff}^{ip} can be calculated using Equation 6.1 (repeated here), where EI_{cr} is the cracked flexural stiffness, and ΔT is the maximum increase in surface temperatures (in ˚C). For SC walls, EI_{cr} can be calculated from the moment-curvature relationship. For SC wall piers, EI_{cr} can be calculated using neutral axis location for M_{yc} (Equation 2.4).

$$EI_{eff}^{ip} = EI_{cr} - \frac{\left(EI_{cr} - E_s I_s\right)}{150}\Delta T \geq E_s I_s \qquad \text{Equation 9.1}$$

9.3.3 In-plane Shear Stiffness (GA_{eff})

GA_{eff} can be calculated using Equation 6.2 (repeated here), where GA_{cr} is the cracked shear stiffness, and ΔT is the maximum increase in surface temperatures (in ˚C). For SC walls, GA_{cr} can be calculated as tangent shear stiffness (GA_{cr}^{TAN}) using Equation 2.12 (repeated here). AISC N690s1 provisions may also be used for calculating GA_{cr}, but they may result in higher shear

stiffnesses. For SC wall piers, GA_{cr} can be calculated as the sum of steel stiffness (G_sA_s) and $0.25G_cA_c^{uncr}$, where A_c^{uncr} is the concrete area under compression for neutral axis location corresponding to M_{yc} (Equation 2.4).

$$GA_{eff} = GA_{cr} - \frac{(GA_{cr} - G_sA_s)}{150}\Delta T \geq G_sA_s \qquad \text{Equation 9.2}$$

$$GA_{cr}^{TAN} = G_sA_s + \frac{1}{\dfrac{4}{0.7E_cA_c} + \dfrac{2(1-\nu_s)}{E_sA_s}} \qquad \text{Equation 9.3}$$

9.3.4 In-plane Strength

Nominal in-plane strength of flexure controlled SC wall piers can be calculated corresponding to compression yield moment (M_{yc}) using Equations 2.4 and 2.5. For SC walls, the provisions of AISC N690s1 can be used. These strength equations are applicable for ambient and accident thermal conditions (for typical accident temperatures up to 232˚C).

9.3.5 Biaxial Moment Interaction

For flexure-controlled SC wall piers subjected to biaxial (in-plane and out-of-plane loading), biaxial interaction needs to be checked. The interaction can be checked against the tri-linear design interaction surface (discussed in Chapter 7) anchored at in-plane compression yield moment capacity (0, M_{yc}), nominal out-of-plane moment capacity (M_n^{AISC}, 0), (0.4M_n^{AISC}, M_{yc}), and (M_n^{AISC}, 0.4M_p), where M_p is the in-plane plastic moment capacity (calculated using Equations 2.2 and 2.3).

9.4 Limitations of Results

The conclusions, and analysis and design recommendations presented in this chapter are based on a limited number of experimental and benchmarked finite element studies. Experimental studies have an inherent variability associated with them. This section enlists potential limitations of the conclusions and recommendations presented in this chapter. The recommendations should be

applied while being cognizant of the limitations. Some of the limitations can be addressed by future research discussed in the following section.

Identical specimens may sometimes have variability in experimentally observed strength and stiffness values. The variability is expected to be higher for limit strengths controlled by concrete, in comparison to steel. Additionally, the specimens tested were scaled, and scaling effects have been observed in the past, especially in concrete limit states. As discussed in Section 1.5, scaling of the specimens was necessary to enable laboratory testing of these specimens. While measures were taken to address the effect of scaling, the results may still be influenced by scaling.

Due to these limitations, the conclusions may need to be validated against additional experimental studies (with a different range of parameters) before they can be applied in the design space. Benchmarked finite element models may be employed to conduct parametric studies and validate the conclusions. The analysis and design recommendation provided in this chapter may also need to be validated using benchmarked numerical models. Reliability studies may be needed to establish desired conservatism for the proposed recommendations.

Performance of specimens may vary between different research programs. The variation may be due to different fabrication and testing methods employed. Since this dissertation discusses the evaluation of SC walls for nuclear applications, and nuclear structures are typically designed for first onset of significant inelastic deformation (FOSID), the design of structures can be checked for lower bound strength estimates. Uniformity in fabrication and testing protocols for SC walls is desired to obtain more reliable results from experiments conducted by different research programs. An important aspect of fabrication is welding of the specimens. As discussed in Section 6.3, SC-W-H specimen failed due to weld fracture at the constrained weld location. This may be a potential issue in physical structures, where larger specimen and weld sizes may result in higher constraints.

Alternative details for flangeplate-webplate-baseplate weld need to be evaluated experimentally. Pre-qualified weld procedures for industry application and laboratory testing will standardize the fabrication procedures and eliminate potential variation in response due to differences in fabrication details.

9.5   Directions for Future Research

The experimental and numerical research presented in this dissertation fills some critical gaps in the existing database for SC walls. However, the research also paves the path for future directions of research.

9.5.1   Experimental Studies

- Experiments for biaxial loading were limited to SC wall piers (without boundary elements) because of the challenges discussed previously in Chapter 1. However, the successful design and implementation of the test setup means it can be employed for testing of SC walls (with boundary elements) and RC walls subjected to biaxial loading. This is especially important as shear walls in commercial construction, and labyrinthine walls in safety-related nuclear facilities are typically SC or RC. These experiments will provide valuable information about the interaction of in-plane and out-of-plane loadings for these walls.

- SC wall and wall pier tests for combined thermal and in-plane loading establish the successful use of heating setup for wall tests. Since the heaters are capable of temperatures up to 1100˚C, the next step would be using the setup for fire testing of SC walls. Research is currently underway at Purdue University to investigate the in-plane behavior of concrete filled-composite plate shear walls (CF-CPSWs) for potential application in high rise commercial construction. Since the fire hazard is a major concern for commercial construction, fire tests

for CF-CPSWs will provide critical information for applicability evaluation of the system for commercial application.

- Failure of SC wall specimen was initiated by weld fracture. The weld detail was highly constrained, and may potentially result in a degraded response of full-scale walls, with higher weld and basemetal sizes. Different weld details can be experimentally evaluated. Pre-qualified weld details and weld procedures can be developed to reduce the potential for weld fracture, and standardize the fabrication procedure for SC walls.

9.5.2   Numerical Studies

- While the benchmarked finite element models provide valuable supplementary information about the experiments, there are some inherent limitations that can be addressed. A major improvement would be the implementation of a concrete model that has better multiaxial compression plasticity formulation. Also, the hysteretic response of the concrete model used is not satisfactory. A recently developed triaxial constitutive model for cyclic loading [135] is currently being explored by the research team. A better concrete model will enable more confidence in the post-peak response, and cyclic analyses for the specimens.

- The benchmarked finite element models compare favorably with experimental results. Since the recommendations provided in this dissertation are primarily based on experiments that covered a limited number of parameters, benchmarked numerical models can be employed to explore the validity of recommendations for a variety of parameters. Reliability studies based on benchmarked finite element analyses can be performed to establish desired conservatism for the proposed recommendations.

- The fiber model for biaxial moment interaction has some simplifying assumptions. The model can be refined to improve the precision of results obtained, e.g., effective compressive stress-

strain curves obtained from detailed finite element analyses can be used to incorporate a more precise post-buckling response for the faceplates. The fiber model can also be updated to include accident thermal effects on biaxial moment interaction for the cross-section.

REFERENCES

[1]   K. Zhang, A. H. Varma, S. R. Malushte, and S. Gallocher, "Effect of shear connectors on local buckling and composite action in steel concrete composite walls," *Nucl. Eng. Des.*, vol. 269, pp. 231–239, 2014.

[2]   K. C. Sener, A. H. Varma, and D. Ayhan, "Steel-plate composite (SC) walls: Out-of-plane flexural behavior, database, and design," *J. Constr. Steel Res.*, vol. 108, pp. 46–59, 2015.

[3]   K. C. Sener and A. H. Varma, "Steel-plate composite walls: Experimental database and design for out-of-plane shear," *J. Constr. Steel Res.*, vol. 100, pp. 197–210, 2014.

[4]   K. C. Sener, A. H. Varma, and J. Seo, "Experimental and numerical investigation of the shear behavior of steel-plate composite (SC) beams without shear reinforcement," *Eng. Struct.*, vol. 127, pp. 495–509, 2016.

[5]   J. Seo, A. H. Varma, K. Sener, and D. Ayhan, "Steel-plate composite (SC) walls: In-plane shear behavior, database, and design," *J. Constr. Steel Res.*, vol. 119, pp. 202–215, 2016.

[6]   A. H. Varma, K. Zhang, H. Chi, P. N. Booth, and T. Baker, "In-Plane Shear Behavior of SC Walls: Theory vs. Experiment," in *Transactions of the 21st International Association for Structural Mechanics in Reactor Technology Conference*, 2011.

[7]   M. Ozaki, S. Akita, H. Osuga, T. Nakayama, and A. Naoyuki, "Study on Steel Plate Reinforced Concrete Panels Subjected to Cyclic In-Plane Shear," *Nucl. Eng. Des.*, vol. 228, pp. 225–244, 2004.

[8]   A. H. Varma, S. R. Malushte, K. C. Sener, and Z. Lai, "Steel-plate composite (SC) walls for safety related nuclear facilities: Design for in-plane forces and out-of-plane moments," *Nucl. Eng. Des.*, vol. 269, pp. 240–249, 2014.

[9]   S. R. Bhardwaj, A. H. Varma, and S. R. Malushte, "Minimum requirements and section detailing provisions for steel-plate composite (SC) walls in safety-related nuclear facilities," *Eng. J.*, vol. Second Qua, pp. 89–108, 2017.

[10]   S. R. Bhardwaj and A. H. Varma, "Seel Design Guide 32-Design of Modular Steel-Plate Composite Walls for Safety-Related Nuclear Facilities," Amrican Institue of Steel Construction, 2017.

[11]   A. H. Varma, S. R. Malushte, and Z. Lai, "Modularity & innovation using steel-plate composite (SC) walls for nuclear and commercial construction," in *Proceedings of the 11th International Conference on Advances in Steel-Concrete Composite Structures (ASCCS)*, 2015.

[12]   K. C. Sener, A. H. Varma, P. N. Booth, and R. Fujimoto, "Seismic behavior of a containment internal structure consisting of composite SC walls," *Nucl. Eng. Des.*, vol. 295, pp. 804–816, 2015.

[13]   P. N. Booth, A. H. Varma, K. C. Sener, and S. R. Malushte, "Flexural behavior and design of steel-plate composite (SC) walls for accident thermal loading," *Nucl. Eng. Des.*, vol. 295, pp. 817–828, 2014.

[14]   A. H. Varma, K. C. Sener, and S. R. Bhardwaj, "Investigation of Accident Thermal Effects of Reinforced Concrete Beams," in *Transactions of the 24th International Association for Structural Mechanics in Reactor Technology Conference*, 2017.

[15]   J. C. Bruhl, A. H. Varma, and W. H. Johnson, "Design of composite SC walls to prevent perforation from missile impact," *Int. J. Impact Eng.*, vol. 75, pp. 75–87, 2015.

[16]   J. C. Bruhl and A. H. Varma, "Missile impact behavior and design of composite SC walls," in *Proceedings of the Structures Con*, 2015.

[17] S. R. Malushte and A. H. Varma, "Rethinking steel-plate composite (SC) construction for improved sustainability and resiliency of nuclear power plants," *Nuclear Power International*, 2015.

[18] M. Bruneau, Y. Alzeni, and P. F. Fouché, "Seismic behavior of concrete-filled steel sandwich walls and concrete-filled steel tube columns," in *Steel Innovations 2013 Conf*, 2013.

[19] R. Selvarajah, "Behavior and design of earthquake-resistant dual-plate composite shear wall systems," Purdue University, 2013.

[20] X. Ji, X. Cheng, X. Jia, and A. H. Varma, "Cyclic in-plane shear behavior of double-skin composite walls in high-rise buildings," *J. Struct. Eng.*, vol. 143, no. 6, pp. 1–12, 2017.

[21] A. H. Varma, Z. Lai, and J. Seo, "An Introduction to coupled composite core wall systems for high-rise construction," in *Proceedings of the 8th International Conference on Composite Construction in Steel and Concrete*, 2017.

[22] ASCE, *ASCE/SEI 7-10: Minimum design loads for buildings and other structures*. 2010.

[23] American Institute of Steel Construction, "Seismic Provisions for Structural Steel Buildings, ANSI/AISC 341–16," 2016.

[24] U.S. Nuclear Regulatory Commision, "Combining Modal Responses and Spatial Components in Seismic Response Analysis," *RG 1.92*, Office of Nuclear Regulatory Research, 2006.

[25] American Concrete Institute, *ACI 349: Code Requirements for Nuclear Safety-Related Concrete Structures and Commentary*. 2006.

[26] American Institute of Steel Construction, *AISC N690s1: Specification for Safety-Related Steel Structures for Nuclear Facilities Including Supplement No. 1*. 2015.

[27] L. Choe, A. H. Varma, A. Agarwal, and A. Surovek, "Fundamental behavior of steel beam-columns and columns under fire loading: Experimental evaluation," *J. Struct. Eng.*, vol. 137, no. 9, pp. 954–966, 2011.

[28] E. I. Wellman, A. H. Varma, R. Fike, and V. Kodur, "Experimental evaluation of thin composite floor assemblies under fire loading," *J. Struct. Eng.*, vol. 137, no. September, pp. 1002–1016, 2011.

[29] L. Choe, A. Agarwal, and A. H. Varma, "Steel columns subjected to thermal gradients from fire loading: Experimental evaluation," *J. Struct. Eng.*, vol. 142, no. 7, pp. 1–9, 2016.

[30] K. L. Selden, "Structural behavior and design of composite beams subjected to fire," Purdue University, 2014.

[31] E. C. Fischer, "Fire behavior of simple (shear) connections in steel-frame buildings," Purdue University, 2015.

[32] C. Schlaseman and J. Russell, "Application of advanced construction technologies to new nuclear power plants," *MPR*-2610, *Rev.* 2, Prepared for U.S. Department of Energy, 2004.

[33] E. G. Kurt, "Steel-plate composite (SC) walls and their basemat connections: Seismic behavior, analysis and design," Purdue University, 2016.

[34] R. Narayanan and T. M. Roberts, "Double skin composite construction for submerged tube tunnels," in *Proceedings of an Engineering Foundation Conference*, 1992, pp. 351–365.

[35] P. F. Adams, T. J. E. Zimmerman, and J. G. MacGregor, *Design and Behavior of Composite Ice-Resisting Walls*, vol. 109. 1987.

[36] Dai X. X. and Liew J. R., "Steel-concrete-steel sandwich system for ship hull construction," in *Proceedings of International Colloquium on Stability and Ductility of Steel Structures*, 2006, pp. 877–84.

[37] T. M. Roberts, D. N. Edwards, and R. Narayanan, "Testing and analysis of steel-concrete-steel sandwich beams," *J. Constr. Steel Res.*, vol. 38, no. 3, pp. 257–279, 1996.

[38] T. O. S. Oduyemi and H. D. Wright, "An experimental investigation into the behaviour of double-skin sandwich beams," *J. Constr. Steel Res.*, vol. 14, no. 1989, pp. 197–220, 1989.

[39] O. Dogan and T. M. Roberts, "Comparing experimental deformations of steel-concrete-steel sandwich beams with full and partial interaction theories," *Int. J. Phys. Sci.*, vol. 5, no. 10, pp. 1544–1557, 2010.

[40] B. McKinley and L. F. Boswell, "Behaviour of double skin composite construction," *J. Constr. Steel Res.*, vol. 58, no. 10, pp. 1347–1359, 2002.

[41] M. Xie, N. Foundoukos, and J. C. Chapman, "Static tests on steel-concrete-steel sandwich beams," *J. Constr. Steel Res.*, vol. 63, no. 6, pp. 735–750, 2007.

[42] N. Foundoukos and J. C. Chapman, "Finite element analysis of steel–concrete–steel sandwich beams," *J. Constr. Steel Res.*, vol. 64, no. 9, pp. 947–961, 2008.

[43] H. A. H. Sekimoto, M. Tanaka, K. Inoue, M. Fukihara, and Y. Okuta, "1/l0th Scale model test of inner concrete structure composed of concrete filled steel bearing wall," in *Transactions of the 10th International Conference on Structural Mechanics in Reactor Technology*, 1989, pp. 1–6.

[44] N. Kato, M., Watanabe, Y., Takeda, T., Yamaguchi, T., Ito, M. and Furuya, "Horizontal Loading Tests on 1/10 Scale Model of Inner Concrete Structure for PWR-Type Nuclear Power Plant," in *Transactions of the 9th International Conference on Structural Mechanics in Reactor Technology*, 1987, pp. 133–142.

[45] M. Takeuchi, M. Narikawa, I. Matsuo, K. Hara, and S. Usami, "Study on a concrete filled structure for nuclear power plants," *Nucl. Eng. Des.*, vol. 179, no. 2, pp. 209–223, 1998.

[46] R. Takeuchi, M., Fujita, F., Funakoshi, A., Shohara, R., Akira, S. and Matsumoto, "Experimental study on steel plate reinforced concrete structure, part 2: Response of SC members subjected to out-of-plane load (outline of the experimental program and the results)," in *Proceedings of the Annual Conference of Architectural Institute of Japan (in Japanese)*, 1999, pp. 1037–1038.

[47] M. Ozaki, S. Akita, M. Takeuchi, H. Oosuga, T. Nakayama, and H. Niwa, "Experimental study on steel- plate-reinforced concrete structure part 41: Heating tests (outline of experimental program and results," in *Annual Conference of Architectural Institute of Japan, Part 41-43*, 2000, pp. 1127–1132.

[48] M. Ozaki, S. Akita, N. Niwa, I. Matsuo, and S. Usami, "Study on steel plate reinforced concrete bearing wall for nuclear power plants part 1: Shear and bending loading tests of SC walls," in *Transactions of the 16th International Conference on Structural Mechanics in Reactor Technology, SMiRT-16*, 2001, pp. 1–8.

[49] X. Song, M. Chu, H. Ge, and H. Wang, "A failure criterion for steel-concrete composite walls," in *International Conference on Sustainable Development of Critical Infrastructure*, 2014, pp. 324–331.

[50] Y.-B. Leng, X.-B. Song, M. Chu, and H.-H. Ge, "Experimental study and theoretical analysis of resistance of steel-concrete-steel sandwich beams," *J. Struct. Eng.*, vol. 141, no. 2, pp. 4014113-1–11, 2015.

[51] Y. B. Leng, X. B. Song, and H. L. Wang, "Failure mechanism and shear strength of steel–concrete–steel sandwich deep beams," *J. Constr. Steel Res.*, vol. 106, pp. 89–98, 2015.

[52] I. H. Moon, S. M. Kim, W. B. Kim, and W. K. Kim, "The use of steel plate concrete for structural module of NPP structures," *J. Korean Soc. Steel Constr. (in Korean)*, vol. 19, no. 2, pp. 740–745, 2007.

[53] I. H. Moon, T. Y. Kim, and S. T. You, "Nuclear power plant structure and SC structure design," *J. Korean Soc. Steel Constr. (in Korean)*, vol. 20, no. 2, pp. 14–23, 2008.

[54] W. K. Kim, W.B. and Kim, "Status and Background in Developing SC Structure Specifications for Nuclear Power Plants," *J. Korean Soc. Steel Constr. (in Korean)*, vol. 2, no. 9–13, 2008.

[55] U. W. Lee, K. K. Kim, T. Y. Mun, and W. S. Sun, "Nuclear power plant construction and SC structures," *J. Korean Soc. Steel Constr. (in Korean)*, vol. 20, no. 2, 2008.

[56] S. J. Lee, B. J. Choi, and T. K. Kim, "An experimental study on the behavior of steel plate concrete wall with vertical ribs," *J. Korean Soc. Steel Constr. (in Korean)*, vol. 21, no. 3, pp. 277–287, 2009.

[57] D. Hong, S., Kim, W., Lee, K., Hong, N. K. and Lee, "Out-of-Plane Shear Strength of Steel Plate Concrete Walls Dependent on Bond Behavior," in *Transactions of the 20th International Conference on Structural Mechanics in Reactor Technology, SMiRT-20*, 2009.

[58] JEA (Japan Electric Association), *Technical Guidelines for Aseismic Design of Nuclear Power Plants*, *JEAG 4601*, 2005.

[59] K. E. A. Board of KEPIC Policy, Structural Committee, *Specification for Safety-Related Steel Plate Concrete Structures for Nuclear Facilities, KEPIC-SNG*. 2010.

[60] P. N. Booth, A. H. Varma, S. R. Malushte, and W. H. Johnson, "Response of modular composite walls to combined thermal and mechanical loads," in *Transactions of the 19th International Association for Structural Mechanics in Reactor Technology Conference, SMiRT-19*, 2007, pp. 1–8.

[61] A. H. Varma, S. R. Malushte, K. C. Sener, and P. N. Booth, "Analysis and design of modular composite walls for combined thermal and mechanical loadings," in *Transactions of the 20th International Association for Structural Mechanics in Reactor Technology Conference, SMiRT-20*, 2009, pp. 1–11.

[62] A. H. Varma, K. Zhang, and S. R. Malushte, "Local buckling of SC composite walls at ambient and elevated temperatures," in *Transactions of the 22nd International Conference on Structural Mechanics in Reactor Technology, SMiRT-22*, 2013, pp. 1–10.

[63] P. N. Booth, A. H. Varma, K. C. Sener, and S. R. Malushte, "Flexural behavior and design of steel-plate composite (SC) walls for accident thermal loading," *Nucl. Eng. Des.*, vol. 295, pp. 817–828, 2014.

[64] A. H. Varma, K. C. Sener, K. Zhang, K. Coogler, and S. R. Malushte, "Out-of-plane shear behavior of SC composite structures," in *Transactions of the 21st International Association for Structural Mechanics in Reactor Technology Conference, SMiRT-21*, 2011, pp. 1–8.

[65] K. C. Sener, A. H. Varma, and J. Seo, "Experimental and numerical investigation of the shear behavior of steel-plate composite (SC) beams without shear reinforcement," *Eng. Struct.*, vol. 127, pp. 495–509, 2016.

[66] J. Seo, A. H. Varma, K. Sener, and D. Ayhan, "Steel-plate composite (SC) walls: In-plane shear behavior, database, and design," *J. Constr. Steel Res.*, vol. 119, pp. 202–215, 2016.

[67]   S. Epackachi, A. S. Whittaker, A. H. Varma, and E. G. Kurt, "Finite element modeling of steel-plate concrete composite wall piers," *Eng. Struct.*, vol. 100, pp. 369–384, 2015.

[68]   S. Epackachi, N. H. Nguyen, E. G. Kurt, A. S. Whittaker, and A. H. Varma, "In-plane seismic behavior of rectangular steel-plate composite wall piers," *J. Struct. Eng.*, vol. 141, no. 7, pp. 1–10, 2014.

[69]   E. G. Kurt, A. H. Varma, P. Booth, and A. S. Whittaker, "In-plane behavior and design of rectangular SC wall piers without boundary elements," *J. Struct. Eng.*, vol. 142, no. 6, pp. 1–16, 2016.

[70]   K. Zhang, "Axial compression behavior and partial composite action of SC walls in safety-related nuclear facilities," Purdue University, 2014.

[71]   S. R. Bhardwaj and A. H. Varma, "Effect of imperfections on the compression behavior of SC walls," in *Structural Stability Research Council Annual Stability Conference 2016, SSRC 2016*, 2016.

[72]   S. R. Bhardwaj and A. H. Varma, "SC wall compression behavior: Interaction of design and construction parameters," in *Proceedings of the Annual Stability Conference Structural Stability Research Council 2017*, 2017.

[73]   A. H. Varma, S. R. Malushte, K. Sener, and Z. Lai, "Steel-plate composite walls for safety related nuclear facilities: Design for combined in-plane and out-of-plane demands," in *Transactions of the 21st International Association for Structural Mechanics in Reactor Technology Conference, SMiRT-21*, 2011, pp. 1–8.

[74]   J. C. Bruhl, A. H. Varma, and J. M. Kim, "Static resistance function for steel-plate composite (SC) walls subject to impactive loading," *Nucl. Eng. Des.*, vol. 295, pp. 843–859, 2015.

[75] J. C. Bruhl and A. H. Varma, "Summary of blast tests on steel-plate reinforced concrete walls," in *Proceedings of the SEI Structures Congress, ASCE*, 2015, pp. 151–159.

[76] J. C. Bruhl and A. H. Varma, "Experimentally-validated analysis methods for steel-plate composite walls subjected to blast and impact loads," in *Proceedings of the Geotechnical and SEI Congress, ASCE*, 2016, pp. 25–34.

[77] A. H. Varma, J. Seo, H. Chi, and T. Baker, "Behavior of SC wall lap splice anchorages," in *Transactions of the 21st International Association for Structural Mechanics in Reactor Technology Conference, SMiRT-21*, 2011, pp. 1–8.

[78] J. Seo, and A. H. Varma, "Experimental behavior and design of steel plate composite-to-reinforced concrete lap splice connections," *J. Struct. Eng.*, vol. 143, no. 5, pp. 1–14, 2017.

[79] E. G. Kurt, A. H. Varma, and Y. M. Sohn, "Direct shear strength of rebar-coupler anchor systems for steel-plate composite (SC) walls," *Int. J. Steel Struct.*, vol. 16, no. 4, pp. 1397–1409, 2016.

[80] J. Seo, A. H. Varma, and D. Winkler, "Preliminary investigations of the joint shear strength of SC wall- to-wall T-joints," in *Transactions of the 22nd International Association for Structural Mechanics in Reactor Technology Conference, SMiRT-22*, 2013, pp. 1–9.

[81] J. Seo, "Design of steel concrete composite wall-to-wall joints for safety related nuclear facilities," Purdue University, 2014.

[82] J. Seo and A. H. Varma, "Behaviour and design of corner or L-joints in SC walls," in *Transactions of the 23rd International Association for Structural Mechanics in Reactor Technology Conference, SMiRT-23*, 2015, pp. 1–10.

[83] P. N. Booth, A. H. Varma, K. C. Sener, and K. Mori, "Seismic behavior and design of a primary shield structure consisting of steel-plate composite (SC) walls," *Nucl. Eng. Des.*, vol. 295, pp. 829–842, 2015.

[84] S. R. Bhardwaj, A. H. Varma, and T. Al-Shawaf, "Outline of specification for composite SC walls in nuclear facilities," in *International Conference on Nuclear Engineering, Proceedings, ICONE, 2016*, 2016.

[85] A. H. Varma, S. R. Bhardwaj, and S. R. Malushte, "Design of SC walls and connections in nuclear facilities," in *International Conference on Nuclear Engineering, Proceedings, ICONE*, 2016, vol. 1, pp. 1–10.

[86] H. Akiyama, H. Sekimoto, M. Fukihara, K. Nakanishi, and K. Hara, "A compression and shear loading tests of concrete filled steel bearing wall," in *Transactions of the 11th Structural Mechanics in Reactor Technology, SMiRT-11*, 1991, pp. 323–328.

[87] S. Usami, H. Akiyama, M. Narikawa, K. Hara, M. Takeuchi, and N. Sasaki, "Study on a concrete filled steel structure for nuclear plants (part 2). Compressive loading tests on wall members," in *Transactions of the 13th International Structural Mechanics in Reactor Technology Conference, SMiRT-13*, 1995, pp. 21–26.

[88] M. Kanchi, "Experimental study on a concrete filled steel structure: Part 2 compressive tests (1)," in *Summary of Technical Papers of Annual Meeting, Architectural Institute of Japan, Structures*, 1996.

[89] B. J. Choi and H. S. Han, "An experiment on compressive profile of the unstiffened steel plate-concrete structures under compression loading," *Steel Compos. Struct.*, vol. 9, no. 6, pp. 519–534, 2009.

[90] American Concrete Institute, *ACI 318: Building Code Requirements for Structural Concrete and Commentary*. 2014.

[91] J. Hallquist, *LS-DYNA theory manual*, March, Livermore, CA; Livermore Technology Software Corporation, 2006.

[92] Dassault Systèmes Simulia, *ABAQUS documentation*, Privudence, RI, 2013.

[93] A. H. Varma, K. C. Sener, K. Zhang, K. Coogler, and S. R. Malushte, "Out-of-plane shear behavior of SC composite structures," in *Transactions of the 21st International Association for Structural Mechanics in Reactor Technology Conference, SMiRT-21*, 2011.

[94] M. Chu, X. Song, and H. Ge, "Structural performance of steel-concrete-steel sandwich composite beams with channel steel connectors," in *Proceedings of 22nd International Conference on Structural Mechanics in Reactor Technology (SMiRT-22)*, 2013, pp. 1–10.

[95] K. C. Sener, A. H. Varma, S. R. Malushte, and K. Coogler, "Experimental database of SC composite references specimens tested under out-of-plane shear loading," in *Proceedings of 22nd International Conference on Structural Mechanics in Reactor Technology (SMiRT-22)*, 2013, pp. 1–10.

[96] M. Chu, X. Song, and H. Ge, "Structural performance of steel-concrete-steel sandwich composite beams with channel steel connectors," in *Proceedings of 22nd International Conference on Structural Mechanics in Reactor Technology (SMiRT-22)*, 2013, pp. 1–10.

[97] M. Lee, B. Choi, S. Hong, and E. Lee, "In-plane shear behavior of composite steel concrete walls," in *The 5th International Symposium on Steel Structures*, 2009.

[98] A. Funakoshi, S. Akita, H. Matsumoto, K. Hara, N. Matsuo, and N. Hayashi, "Experimental study on a concrete filled steel structure part. 7 bending shear tests (outline of the experimental program and the results)," in *Summaries of Technical Papers Annual Meeting, Architectural Institute of Japan*, 1998, pp. 1063–1064.

[99] T. Fujita, A. Funakoshi, S. Akita, N. Hayashi, I. Matsuo, and H. Yamaya, "Experimental study on a concrete filled steel structure part. 16 bending shear tests (Effect of bending strength)," in *Summaries of Technical Papers of Annual Meeting, Architectural Institute of Japan*, 1998.

[100] P. Booth, A. H. Varma, and J. Seo, "Lateral load capacity of steel plate composite wall structures," in *Transactions of the 23rd International Conference on Structural Mechanics in Reactor Technology, SMiRT-23,* 2015.

[101] K. C. Sener, A. H. Varma, and S. R. Bhardwaj, "Accident thermal loading effects on seismic behaviour of safety-related nuclear structures," in *Transactions of the 23rd International Association for Structural Mechanics in Reactor Technology Conference, SMiRT-23*, 2015.

[102] U.S. Nuclear Regulatory Commission, "Design Control Document for the AP1000," Revision 19, 2011.

[103] U.S. Nuclear Regulatory Commission, "Design Control Document for the US-APWR," Revision 4, 2012.

[104] S. R. Bhardwaj, A. H. Varma, and K. Sener, "On the calculation of design demands for accident thermal loading combination," in *Transactions of the 23rd International Association for Structural Mechanics in Reactor Technology Conference, SMiRT-23*, 2015.

[105] S. Hong and A. H. Varma, "Analytical modeling of the standard fire behavior of loaded CFT columns," *J. Constr. Steel Res.*, vol. 65, no. 1, pp. 54–69, 2009.

[106] S. Hong and A. H. Varma, "Predicting fire behavior of composite CFT columns using fundamental section behavior," *J. ASTM Int.*, vol. 1517, no. 1, pp. 78–110, 2008.

[107] U. Schneider, "Concrete at high temperatures - A general review," *Fire Saf. J.*, vol. 13, no. 1, pp. 55–68, 1988.

[108] D. J. Naus, "A compilation of elevated temperature concrete material property data and information for use in assessments of nuclear power plant reinforced concrete structures. US NRC," Oak Ridge, TN, 2010.

[109] F. Elmohandes, "Advanced three-dimensional nonlinear analysis of reinforced concrete structures subjected to fire and extreme loads," University of Toronto, 2013.

[110] G. A. Khoury, "Effect of fire on concrete and concrete structures," *Prog. Struct. Eng. Mater.*, vol. 2, no. 4, pp. 429–447, 2000.

[111] M. Takeuchi, M. Hiramoto, N. Kumagai, N. Yamazaki, A. Kodaira, and K. Sugiyama, "Material properties of concrete and steel bars at elevated temperatures," in *Transactions, SMiRT12*, 1993, pp. 133–138.

[112] G. M. E. Cooke, "An introduction to the mechanical properties of structural steel at elevated temperatures," *Fire Saf. J.*, vol. 13, no. 1, pp. 45–54, 1988.

[113] V. Kodur, M. Dwaikat, and R. Fike, "High temperature properties of steel for fire resistance modeling of structures," *J. Mater. Civ. Eng.*, vol. 22, no. May, pp. 423–434, 2010.

[114] B. R. Kirby and R. R. Preston, "High temperature properties of hot-rolled, structural steels for use in fire engineering design studies," *Fire Saf. J.*, vol. 13, no. 1, pp. 27–37, 1988.

[115] Z. P. Bazant and P. C. Prat, "Effect of temperature and humidity on fracture energy of concrete," *ACI Materials Journal*, vol. 85, no. 4. pp. 262–271, 1988.

[116] American Institute of Steel Construction, *AISC 360: Specification for Structural Steel Buildings*. 2016.

[117] American Concrete Institute, "Code requirements for determining fire resistance of concrete and masonry construction assemblies (ACI/TMS 216.1-14).," 2014.

[118] American Society of Civil Engineers, "Structural fire protection ASCE committee on fire protection, Manual No. 78," 1992.

[119] European Committee for Standardization, *Eurocode 3: General rules— Structural fire design, EN1993-1-2*. 2005.

[120] Comite Euro-international du Beton, "CEB-FIP Model Code 1990." 1993.

[121] F. J. Vecchio and J. A. Sato, "Thermal gradient effects in reinforced concrete frame structures," *ACI Struct. J.*, vol. 87, no. 3, pp. 262–275, 1990.

[122] Y. Kitajima, T. Miyagawa, S. Hirako, I. Kojima, T. Hirama, and T. Akase, "Applicability evaluation of steel plate reinforced concrete structure to primary containment vessel of bwrs (4) shear loading test of steel plate reinforced concrete structure under high temperature," in *23rd Conference on Structural Mechanics in Reactor Technology*, 2015, pp. 1–9.

[123] S. R. Bhardwaj, E. G. Kurt, B. Terranova, A. H. Varma, S. Whittaker, Andrew, and N. Orbovic, "Preliminary investigation of the effects of out-of-plane loading on the in-plane behavior of SC walls," in *23rd Conference on Structural Mechanics in Reactor Technology*, 2015, pp. 1–10.

[124] Applied Technology Council, "Guidelines for cyclic seismic testing of components of steel structures, ATC-24," 1992.

[125] ASTM International, *ASTM C39: Standard Test Method for Compressive Strength of Cylindrical Concrete Specimens*. 2016.

[126] T. D. Canonsburg, "SpecView User Manual," vol. 3304, pp. 724–746, 2009.

[127] S. R. Bhardwaj and A. H. Varma, "Design of wall structures for in-plane and out-of-plane forces: An exploratory evaluation," in *Proceedings of Structures Congress*, 2017.

[128] S. R. Bhardwaj, P. Wazalwar, A. H. Varma, and T. Tseng, "Interaction of axial, in plane, and out-of-plane forces in structural walls," in *Proceedings, NCEE 11*, 2018.

[129] S. Popovics, "A numerical approach to the complete stress-strain curve of concrete," *Cem. Concr. Res.*, vol. 3, no. 5, pp. 583–599, 1973.

[130] O. Mohr, "Abhandlungenaus dem Gebiete der Technischen," in *second edition, W. Ernst und Sohn, Berlin, Germany*, 1914.

[131] C. A. Coulomb, "In Memories de Mathematique et de Physique," *Acad. R. Sci. par Divers.*, vol. 7, pp. 343–382, 1773.

[132] S. Pul, A. Ghaffari, E. Öztekin, M. Hüsem, and S. Demir, "Experimental determination of cohesion & internal friction angle on conventional concretes," *ACI Struct. J.*, vol. 114, no. 3, pp. 407–416, 2017.

[133] J. C. Bruhl, "Behavior and design of steel-plate composite (SC) walls for blast loads," Purdue University, 2014.

[134] L. Schwer, "An introduction to the Winfrith concrete model," *Schwer Eng. Consult. Serv.*, April, pp. 1–28, 2010.

[135] M. Moharrami, and I. Koutromanos, "Triaxial Constitutive Model for Concrete under Cyclic Loading," *J. Struct. Engineering*, vol. 142, no. 7, p. 4016039, 2016.

VITA

Saahastaranshu R. Bhardwaj completed his undergraduate studies in 2007 at Punjab Engineering College, Chandigarh, India. Upon graduation, he worked as a structural engineer at Fluor Daniel India Pvt. Ltd., and subsequently at Delhi Metro Rail Corporation (DMRC) Limited. During his stay at DMRC, he earned a Post-Graduate Diploma in Metro Construction and Technology at Indian Institute of Technology, Delhi, India.

In 2013, he started his graduate studies in structural engineering at Purdue University, West Lafayette, U.S.A. He earned a Master of Science in Civil Engineering in 2014 and began pursuit of a Doctor of Philosophy in Civil Engineering. He has conducted fundamental experimental and numerical research on the multi-hazard response of steel-plate composite (SC) and reinforced concrete (RC) wall structures.